UNIVERSITY OF NAPLES FEDERICO II

DEPARTMENT OF PHARMACY

PhD programme in Pharmaceutical Sciences

Multitarget-directed drugs: design, synthesis and pharmacological evaluation of ligands targeting G protein-coupled and nuclear receptors

PhD student
Pasquale Rapacciuolo

Coordinator
Prof.
ROSARIA MELI

Tutor
Prof.
VALENTINA SEPE

XXXV CYCLE (2019-2022)

Io pensavo ad un'altra morale, più terrena e concreta, e credo che ogni chimico militante la potrà confermare: che occorre diffidare del quasi-uguale (il sodio è quasi uguale al potassio: ma col sodio non sarebbe successo nulla), del praticamente identico, del pressappoco, dell'oppure, di tutti i surrogati e di tutti i rappezzi. Le differenze possono essere piccole, ma portare a conseguenze radicalmente diverse, come gli aghi degli scambi; il mestiere del chimico consiste in buona parte nel guardarsi da queste differenze, nel conoscerle da vicino, nel prevederne gli effetti. Non solo il mestiere del chimico.

Primo Levi, "Potassio", Il Sistema periodico

To my beloved and proud grandparents:

Nonno Pasquale - Nonna Lina – Nonno Luigi – Nonna Rosa

COLLABORATIONS

My research project was conducted under the supervision of Prof. Valentina Sepe in the research group headed by Prof. Angela Zampella at the Department of Pharmacy of the University of Naples "Federico II".

The pharmacological evaluations were performed in collaboration with Prof. Stefano Fiorucci's group (Department of Surgery and Biomedical Sciences, Perugia) whereas the group of Prof. Vittorio Limongelli (Institute of Computational Science Center for Computational Medicine in Cardiology, Università della Svizzera Italiana) and Dr Bruno Catalanotti (Department of Pharmacy, University of Naples "Federico II") performed the computational studies.

SUMMARY

Abstract

Given the rise in the number of people conducting a sedentary lifestyle along with unhealthy diets on a global scale, the increase of dysmetabolic conditions mostly involving the liver, the intestine and the cardiovascular system has been steady in the last decades. As for the liver, two emerging conditions are non-alcoholic fatty liver disease (NAFLD) and non-alcoholic steatohepatitis (NASH). These two terms stand for a range of pathological conditions determined by an excessive fat build-up in the liver, whenever said build-up cannot be traced back to any secondary cause such as alcohol abuse. Although several pharmaceutical approaches have been investigated, NASH remains devoid of any effective drug therapy. Another non-communicable pathological condition is intestinal bowel disease (IBD). This term also withholds two main chronic inflammatory intestinal conditions: Crohn's disease and ulcerative colitis. Both diseases present complex pathogenesis, and the symptoms can heavily impact the life quality of the patients. Together with these two enterohepatic conditions, it is very well known that dysmetabolism comes with a series of comorbidities mostly involving the cardiovascular system.

Over the whole PhD work, all these conditions were the starting point for the identification of several small molecules which could be potentially applied to therapeutical protocols. Many molecular targets are involved in these multifactorial diseases. Considering the complexity of the molecular network underlying these conditions, the possibility of designing multi-target-oriented drugs represents a valid and potent tool to address these diseases. Starting from the long-standing expertise of my research group on the G protein-coupled bile acid receptor 1 (GPBAR1) and its involvement in liver and intestinal homeostasis, the aim of this PhD project

was combining the pivotal structural information for GPBAR1 agonism with those allowing the modulation of interesting new targets also involved in pro-inflammatory conditions, such as leukotrienes receptors (CysLTRs), retinoic acid receptor-related orphan receptor gamma t (RORγt) and angiotensin-converting enzyme 2 (ACE2). Many chemical moieties have been studied during the design of new multi-target small molecules, ranging from heterocyclic quinoline derivatives to several semi-synthetic steroid-like compounds. A large family of dual GPBAR1 agonist and $CysLT_1R$ antagonist compounds was identified with the lead compound showing great effects on different models of inflamed liver. The identification of GPBAR1 agonists/RORγt inverse agonists proved instead very successful on a murine colitis model representing a potential class for the treatment of IBD.

Furthermore, the identification of an in-house library of selective GPBAR1 agonists as ACE2 activators also allowed us to further investigate the activation mechanism of ACE2 itself and the effects of its activation on the interaction with SARS-CoV-2 Spike protein.

In the end, the advancement to Phase I clinical trial of a potent FXR/GPBAR1 agonist, BAR502, determined the need to study its metabolic profile in animals and humans. To this end, several metabolites were synthesised to be used as standards for the qualitative and quantitative-oriented analysis of the products of BAR502 metabolic transformations.

1. INTRODUCTION

1.1 Drug discovery and development

Ever since ancient times, humankind has been tackling the emergence of new diseases. Several efforts have been made to identify possible cures to avoid bad complications and thus improve the quality of the life. At the very beginning, priests, shamans, or medicine men were the first to gather knowledge about remedies by acutely observing that the consumption of certain types of plant parts had a positive effect on the sick, thus laying the foundations for what we define today as the drug discovery (DD) process. Whilst this activity began many centuries ago, the twentieth century has undoubtedly been the apogee of drug discovery, in terms of productivity, considering that most of the remedies available nowadays have then been produced.[1] The deeper understanding of biological and pathological processes together with the development of effective synthetic strategies facilitated and accelerated the way medicines can be discovered, thus enabling humans to constantly face unmet medical needs.[2] Since the late 80s, the quantity of pharmaceutical R&D projects has increased notably; interestingly, the number of drugs that made it into the market has not followed the same trend. A very detailed review has shown that the number of potential drugs reaching the clinic phase is one over ten thousand.[3] The hypothesis could be that the scientifical community has already used up the low-hanging fruits of pharmaceutical R&D; therefore, the efforts to develop new drug candidates must be bigger and more conscientious. The issue of stricter evaluation parameters emitted by the existing regulatory institutions, such as the FDA or EMA, contributed to a reduction of granted marketing authorisations as a drawback of the increased safety levels.[4]

Nowadays a large set of therapeutical approaches are available to most diseases, yet others have almost no efficient means to be treated, such as Alzheimer's and Crohn's diseases, non-alcoholic fatty liver conditions, several cancers, pluri-resistant bacteria, neglected tropical diseases, and so on. All these certainly leave a great space for investigating and identifying new remedies.

The process of drug discovery can be considered a scientifical journey fraught with obstacles; first, comes the choice of the target of interest; the latter being an enzyme, a receptor, or any biological entity, whose involvement in the pathogenesis of a certain disease has been demonstrated. At the same time proper *in vitro* and *in vivo* models are required to reliably assess the pharmacological significance of the putative drug candidates in the pre-clinical phase. Once both requirements are satisfied, the actual drug design process can start; the techniques available to do so have increased in the late years, thanks to the integration of databanks and automated software. Among these, two main strategical approaches can be specified: target-based (TDD) and ligand-based (LDD) drug design. The former is based on several computational studies performed on the 3D virtual model of the X-ray crystal structure of the chosen target, if available; once the points of interaction in the active site of the such target are identified, a model of a possible set of hit-compounds is derived. If the target's structure has not been elucidated, LDD can be employed instead. As its name reveals, this technique starts by building *in silico* the target's possible interaction pocket starting from its ligand's structure. One may predict the putative types of interactions that could take place by analysing each functional group or moiety of the selected ligand. Both techniques are rational and allow the screening of vast existing chemical libraries which are usually coupled to high-throughput screening

(HTS) assays. After the process of hit identification, lead optimisation follows by harnessing the structure of the hit compound.[5,6]

During the DD process, many drugs developed to address specific targets might be successfully applied in a different therapeutical area that was initially without the scope of interest. This process is referred to as drug repurposing (Fig. 1), and its application has emerged as a valid tool to cut the costs and the time expense of the traditional drug discovery process.[7]

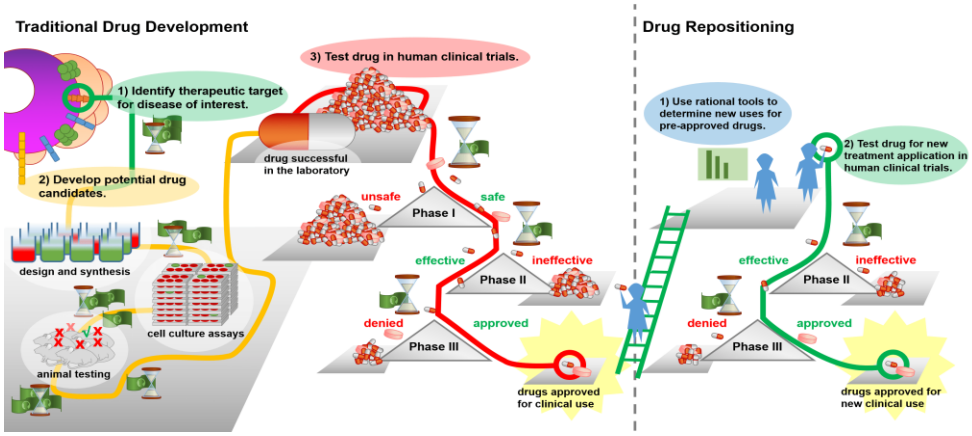

Figure 1. Generic outline of traditional drug discovery and drug repurposing/repositioning.

The identification of hit compounds can be carried out through *in silico* virtual high-throughput screenings; in this case, although the data results represent a potential starting point to find "hits", they come with a share of limitations. *In silico* data originate from predictions based on a virtual model; therefore, their reliability depends on both the quality of the model and that of the X-ray crystal structure of the selected target. The exact correspondence between the crystal structure and the real active form of the biological target cannot be taken for granted; in fact, the actual in-cell condition of the target may be far from that observed by crystallography since they are usually included in very complex systems like the cellular membrane or the cytoplasm. Given these limitations, every virtual "hit"

must be tested in physical HTS assays to substantiate the predicted activity and thus the possibility of follow-up modifications to achieve the hit-to-lead transition. The latter stage is the real first chokepoint of the whole process, the number of “hits”, which can easily exceed 50000 units, is drastically lessened and only 0.1% of them are endowed with encouraging biological properties. Nonetheless, once the "hit" is identified, the lead optimisation cycle starts. The principle it follows is that a set of new analogues is generated by adjusting the hit structure and every structural modification of the hit compound associated with improved potency is kept, thus exploring the chemical space linked to an overall improvement of the activity of the small molecules. This cycle is repeated several times as long as the candidate with the desired properties is identified. High potency values are obviously of utter importance even though this might not be sufficient. The role of DD is the identification of a candidate endowed with the right equilibrium between several desirable properties, such as efficacy, novelty, selectivity, stability, solubility, pharmacokinetic profile, and no toxicity. It is fairly understood that juggling all these properties is no simple process, even though various ways of predicting the drug-likeness have been described such as Lipinski’s rule. When the desired candidate complies with the correct requisites, the process moves forward to the *in vivo* assays. The pre-clinical stage relies on robust animal models of the selected disease and dictates whether the candidate can reach the clinical phase eventually. Human clinical trials represent the most delicate and important phase of the whole process; every single parameter that has been previously modulated in detail stands to reason at this point, the entire DD pipeline serves the final purpose of safely administering the right candidate to healthy human volunteers at first. Phase I of the clinical trials allows the evaluation of the real response of the human organism to

the potential drug; such information can only be partially predicted by animal models due to the great difference between each organism. The clinical studies can go onward once the drug candidate complies with every safety requirement. Finally, the drug candidate can be administered to subjects suffering from the selected disease, thus providing crucial information about the efficacy of the therapy, its proper quantitative parameters like dosage and frequency, and eventual adverse effects. In case everything goes smoothly, the request for the marketing authorisation is eventually forwarded to a regulatory institution, i.e., Food and Drug Administration (FDA) or European Medicines Agency (EMA). The meticulous evaluation of every single property of the drug candidate and its risk-benefit ratio will determine whether the drug can enter the market. The monitoring of the authorised drug will not stop once it is allowed to be sold, pharmacovigilance will constantly collect data regarding any adverse effect reported by the patients.[8]

1.2 Chronic inflammatory diseases

Inflammation is a critical evolutionary feature developed for survival in case of physical injury and infection; the activation of acute inflammatory pathways happens in a restricted period of time until the source of the insult or threat has been solved or removed.[9,10] The resolution of the inflammatory event is of great relevance to re-establish the physiological conditions of a tissue; when the resolution fails, the persistent inflammation response determines a decline of the immune tolerance, a major rearrangement of the tissue structure and gradual damage associated with a loss of the specific functions. The shift from a short to a long-lasting inflammatory event is referred to as chronic inflammation.[11]

Latest studies have proven that certain social, environmental and lifestyle factors can promote systemic chronic inflammation (SCI).[12] SCI leads to several diseases that overall represent the main causes of disability and mortality across the world, such as cardiovascular disease, cancer, diabetes mellitus, inflammatory liver disease, non-alcoholic fatty liver disease and autoimmune and neurodegenerative disorders.[13]

My PhD project has focused on developing novel multitarget compounds to address different inflammatory-based enterohepatic diseases.

1.3 NAFLD and NASH

Non-alcoholic fatty liver disease (NAFLD) is a non-communicable condition characterised by excessive fat accumulation in the liver parenchyma. It is an umbrella term that includes any liver steatosis that cannot be related to a secondary cause such as alcohol abuse, viral infection, or drug adverse effect.[14] NAFLD is one of the fastest emerging pathological conditions among the known metabolic dysfunctions worldwide. Its increased manifestations are paralleling the global upsurge of metabolic syndrome, obesity, and diabetes, thus delineating their close correlation.[15] Numbers speak for themselves, the estimated global prevalence of NAFLD is currently around 30%[16] and constantly growing at an alarming rate (from 25.5% in 2005 to 37.8% in 2016 or later).[17] The overall prevalence of the condition was also estimated to be higher in men than women.[18] NAFLD can evolve in 4 consecutive stages. The first is hepatic steatosis, the direct consequence of triglycerides building up in the liver and characterised by the formation of small liposomes that can grow into larger fat vacuoles which give the typical signet ring look to hepatocytes. Eventually, large vacuoles can coalesce and form cysts as irreversible damage. Usually, steatosis has no related symptoms, it can be reversed by changing diet and lifestyle and is usually diagnosed by chance when performing abdominal imaging for other medical reasons.[19] The second stage is non-alcoholic steatohepatitis (NASH), which is the phenotypical form of NAFLD.[20] Many molecular mechanisms underlie the onset of inflammation in a fatty liver; the whole picture has not been yet described completely.[21] First, it had been proposed that a second insult to a fatty liver, often referred to as the “second hit”, was responsible for the transition from steatosis to NASH; this “two-hits” theory is now regarded as obsolete due to the greater complexity of the molecular processes

coming along with the onset of NASH.[22] Nonetheless, the effects of the continuous inflammatory status on hepatocytes are serious, cell ballooning degeneration is a typical histological sign and is due to the swelling of damaged cells; other characteristic elements are the presence of Mallory-Denk bodies, polymorphonucleate infiltrations and apoptotic bodies.[23] Up until this stage, the whole condition is still reversible and can be treated by adjusting the lifestyle and dietary habits of the patient.[24] The persistent damage to the liver parenchyma determines the deposition of connective tissue by fibroblasts causing fibrosis. These fibrotic scars can increase and alter the normal parenchymal tissue organisation determining a loss of function.[25] Over time, the accumulation of fibrotic tissue results in the stiffening of the whole organ and more importantly the impairment of its functions. This stage is known as cirrhosis, a cirrhotic liver heavily affects the quality of life of the patient and is usually related to the emergence of severe complications like hepatic encephalopathy or hepatocellular carcinoma (HCC).[26,27]

The NAFLD spectrum presents a multifaceted aetiology connected to genetic and environmental causes. Notably, several epidemiological studies from the population, family clusters or twins[28–31] underline the probable existence of an inheritable trait for NASH ranging from 35% to 61%. Many gene loci have been associated with the onset of NAFLD/NASH, all encoding proteins involved in the regulation of liver fat metabolism.[32] The most frequently associated gene is PNPLA3, subject to single nucleotide polymorphism (SNP). The variant, whose isoleucine 148 is changed with a methionine, has no native hydrolase activity towards triglycerides, thus contributing to their accumulation.[33,34] Other genetic SNPs have been correlated to a higher risk of NASH such as transmembrane 6 superfamily member 2 (TM6SF2) involved in very low-

density lipoproteins (VLDL) secretion[35], and glucokinase regulator (GCKR) gene regulating *de novo* lipogenesis.[36] Some data about epigenetic factors related to this clinical condition are also emerging even though they are still in their early stage.[37]

NASH first-line treatment follows the same therapeutic protocol used for type 2 diabetes and obesity, encouraging changes of habits such as exercise, a healthy diet, and weight loss.[38] However, promoting a better lifestyle is not completely successful in fighting the illness; a group of the affected population can sometimes come upon problems sustaining healthier habits, and sometimes the sole weight loss does not suffice for late-stage patients. Identifying the molecular targets involved in NASH pathogenesis is of utmost importance in assisting the development of new pharmacological approaches. Over time, a large group of receptors has been identified whose dysregulated activity was tightly linked to the inflammation onset in a fatty liver.

The molecular events leading to this are complex, and multifaceted and involve many pro-inflammatory mediators with the respective receptors. Targeting these to quench the ongoing inflammatory process has been an important focus until today.

Many receptors have been correlated with NAFLD/NASH: peroxisome proliferator-activated receptors (PPARs) are a family of nuclear receptors, and their endogenous ligands are short to medium-chain fatty acids and can thus regulate their metabolism other than inflammation *via* transcriptional regulation.[39] PPARs act as transcriptional factors; once activated, heterodimerisation with RXR occurs and their DNA binding domain (DBD) can recognise several gene promoters called PPAR responsive elements (PPREs).[40] Several PPARs agonists have been

successfully introduced in the treatments of type 2 diabetes[41] or dyslipidaemias.[42]

Glucagon-like peptide-1 receptor (GLP-1R) is a G protein-coupled receptor.[43,44] Its endogenous ligand is glucagon-like peptide 1 (GLP-1), part of the gut hormones called incretins. It can stimulate insulin secretion and has a very short half-life. External administration of GLP-1 to patients determined an overall improvement of the energy metabolism with a decrease in food intake leading to weight loss. These findings prompted the development of more stable derivatives of GLP-1.[45]

Apoptosis signal-regulating kinase 1 (ASK1) is a serine/threonine-specific protein kinase, that belongs to the mitogen-activated protein kinase kinase kinase (MAP3K) enzyme family and influences Jun N-terminal kinase (JNK) and p38's activity.[46] Tumor necrosis factor α (TNFα), lipopolysaccharide, endoplasmic reticulum stress, calcium influx, and oxidative stress are all capable of activating ASK1.[47–49] Without any external stress source, ASK1 forms dimers and binds its N-terminal non-catalytic region to thioredoxin (TRX), a regulatory redox protein. The production of reactive oxygen species determines the oxidation of TRX; thus, it dissociates from ASK1 which is in turn activated. The JNK and p38 pathways in hepatic cells lead to apoptosis, inflammation, and fibrosis. The identification of ASK1 inhibitors has been already explored for several indications even though no drug candidate made it to the market.[50,51] Lately, studies of ASK1 inhibitors in rodent NASH models have renewed the interest in potentially using them for NASH treatment.[52]

Over time, many other targets have been identified to address the need for a new therapeutical approach to NASH. The high complexity of the molecular pathways that constitute the whole hepatic system reflects the intricate pathogenesis process; thus, the number of molecular targets to

investigate is still large.[53] Sugars and lipids metabolism in the liver is regulated by bile acids (BAs).[54]

BAs are amphipathic steroids produced in the liver starting from cholesterol and excreted as the main component of bile.[55] Lately, the exploration of their functions has changed their pharmacological relevance; BAs do not only play a marginal role in aiding the emulsion and absorption of fats, as previously thought. Many studies over the last decades proved that they act as signalling molecules interacting with several receptors and are capable of heavily influencing sugar, lipid, and energy metabolism.[56]

BA-activated receptors include different nuclear receptors, such as farnesoid X receptor (FXR), pregnane X receptor (PXR), vitamin D receptor (VDR), and G protein-coupled receptors like G protein-coupled bile acid receptor 1 (GPBAR1 aka TGR5) and sphingosine 1 phosphate receptor 2 (S1PR2).[57] GPBAR1 is one of the selected targets to be addressed as part of this PhD project and thus, it will be further described in detail afterwards.

1.4 Inflammatory bowel diseases

Among the existent chronic inflammatory diseases, another condition that was addressed during this PhD work is inflammatory bowel disease. Inflammatory bowel disease (IBD) is a conventional term that includes two types of idiopathic gastrointestinal diseases, ulcerative colitis (UC) and Crohn's disease (CD).[58,59]

Both diseases' incidence has been steadily increasing worldwide, especially in Europe and North America and each one presents a distinguished phenotype in its manifestation. UC is usually limited to the rectal or colic portion and consists of continuous inflammation and erosion of the sole mucosal layer. In contrast, CD can discontinuously affect the ileum and the colon and presents deeper lesions of the intestinal walls like fistulas, strictures, and granulomas.

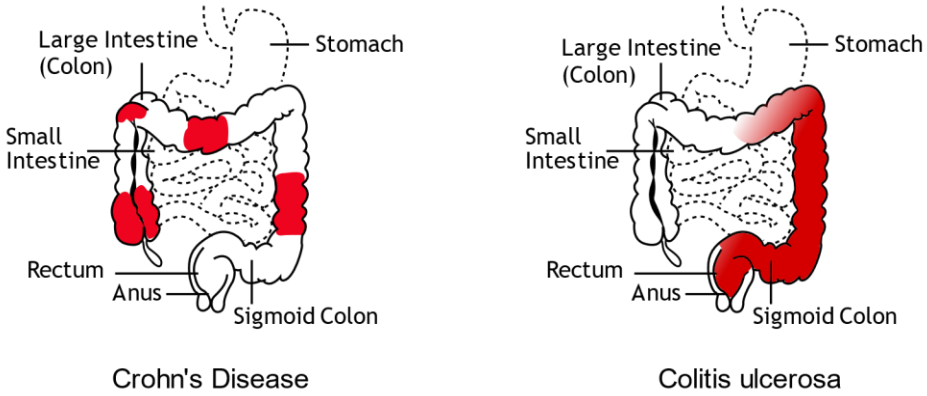

Figure 2. Inflammatory Bowel Disease – Crohn's Disease and Ulcerative Colitis

Both IBDs present similar general symptoms like fatigue, fever, abdominal cramps, and altered bowel movements (diarrhoea); the symptoms can progress and regress over time with intense flare-ups followed by temporary remissions, which can sometimes prevent a fast diagnosis.[60,61] The exact etiopathogenesis has not been yet clarified but

what emerged from the first studies is its indisputable multifactorial nature.

Lately, the presence of a genetic contribution associated with a higher susceptibility to this kind of disease has been suggested. The most evident gene association is a frameshift mutation of the NOD2 gene[62] encoding for the nucleotide-binding oligomerization domain-containing protein 2, responsible for the recognition of muramyl dipeptide (MDP) present in the bacterial peptidoglycan in the gut to control bacterial growth[63,64] and autophagy, and for stimulation of the immune response in the intestine.[65,66] Many other gene modifications have been linked to an increased IBD susceptibility, interestingly all of these seem to be involved in controlling autophagy processes.[67,68] Even though the number of discovered gene loci linked to IBD pathogenesis is increasing and, thus, producing more insights into its molecular mechanisms, the hereditariness is not justified; in fact, the loci discovered now only account for at least 20% of it. Another important role is played by environmental factors; smoke is the most studied factor, and heavy smoking has been associated with a decreased risk of developing UC.[69,70] In contrast to this, smoking increases the risk of CD development.[71] Other than tobacco dependence, vitamin D deficiency, stress and antibiotics assumption have also been linked to a higher risk of IBD to a certain extent.[72–74] Gut microbiome and mucosal cells' activities are so tightly intertwined that a change in the flora composition in IBD patients can be easily anticipated. The diversity and stability of the bacterial pool are lower than that of a healthy person.[75,76] The anomalous intestinal inflammatory response has also been related to the mucosal T-cells response dysfunction. UC and CD present different T-cell activation profiles in their pathogenesis; Crohn's disease is characterized by excessive production of IFN-γ and IL-2 by type 1 helper

T cells[77] while in ulcerative colitis some studies described an increased production of IL-13, a typical Th2 cells' cytokine, by atypical NK T cells.[78,79] The association of these immune characteristics for each type of IBD remains uncertain, subsequent studies have shown a different and more complex scenario where the types and quantity of produced cytokines change during the disease progress which is now considered to have a "dynamic" inflammatory profile.[80] Another noteworthy pro-inflammatory cytokine that has been associated with IBD is interleukin-17. Different IL-17s (IL-17A, IL-17F) are mostly produced by Th17 cells together with IL-22 and IL-6.[81,82]

If left unchecked, IBDs can determine serious complications with time such as internal haemorrhage, fatty liver, erythema nodosum, primary sclerosing cholangitis, intestinal perforation, polyps' growth and a higher risk of GI malignancies. Considering the complex and partially undiscovered causes of IBD together with the highly debilitating symptoms, IBDs represent another important medical need to be addressed. The therapeutical approaches available today are few and merely based on the interruption of the inflammation rather than the interaction of specific targets and some patients fail to respond to the protocolar therapy. The first-in-line drugs prescribed for IBD are aminosalicylates like 5-ASA or sulfasalazine. The overall ability of 5-ASA to repress the production of pro-inflammatory cytokines like IL-1 and TNF-α is very useful in preventing UC relapse[83] while its efficacy in treating CD is lower.[84] Aminosalicylates can be detrimental especially in IBD treatment because their side effects mainly affect the GI trait other than myelosuppression. Another important drug category is corticosteroids. They can be administered alone or together with a suitable aminosalicylate formulation.[85] Patients can be divided into three

categories depending on their response to steroids: steroid-responsive when patients experience a long-lived remission even after the doses of steroids are lowered; steroid-dependent when the remission only stays if steroids are administered and steroid-unresponsive when no improvement is brought by protracted steroids doses.[86] However, glucocorticoid therapy is not resolutive because the total remission cannot be maintained if the administration stops, moreover long-term steroid therapy is associated with severe side effects. Therefore, steroidal anti-inflammatory drugs do not represent the best pharmacological approach for IBDs. Due to the strong immune component of IBD, the application of several immunomodulators has also been successful in some cases. The earliest immunosuppressant was azathioprine, even though it usually requires a period of at least three months to see remission.[87] This drug category is also associated with many severe side effects so the decision of applying them to treat IBD is usually taken after a careful evaluation of the risk-to-benefit ratio. The most recent therapeutical approach regards the use of biological agents, i.e., monoclonal antibodies. To be more precise, the main Ig targets are TNF-α, IL-12/23 and integrins.[88–90] Many clinical studies are still ongoing nowadays but there are still many limitations in using monoclonal antibodies like high production costs, potential side effects and immunogenicity. In conclusion, the therapeutical outlook of IBDs nowadays still lacks a safe and very well-tolerated strategy. Any existing protocol fails to completely remove or attenuate the causes generating both CD and UC. Given the circumstances, the opportunities to further investigate any potential specific target are still aplenty. A new emerging target for the treatment of IBD is Retinoic Acid Receptor-Related Orphan Receptor gamma T (RORγT), a nuclear hormone receptor whose endogenous ligand is yet to be identified. RORγT strongly regulates

the differentiation of Th17 cells, thus holding an important position in IBD pathogenesis.[91] More details about RORγT will be given subsequently.

2. GPBAR1 – CysLT$_1$R as targets for NAFLD/NASH

2.1 G protein-coupled bile acid receptor 1 (GPBAR1)

G protein-coupled bile acid receptor 1 (GPBAR1), also known as Takeda G protein-coupled receptor 5 (TGR5), is a metabotropic membrane receptor with the typical seven transmembrane domains; for the sake of coherence, this receptor will always be referred to as GPBAR1 throughout this thesis.[92] As the name suggests, primary and secondary bile acids (BA) are endogenous ligands.

Their potency depends on some structural features, mainly influencing the hydrophobicity of the cholane scaffold or the presence of conjugation. The most potent natural agonist is taurolithocholic acid (TLCA). GPBAR1 is expressed in several tissues, such as the liver, gallbladder, small intestine, central nervous system, and spleen.[93–95] More specifically in the liver the highest expression levels are those of Kupffer cells (KCs), sinusoidal endothelial cells (LSECs), biliary epithelial cells and activated stellate cells (HSCs) while no expression was observed in their quiescent state.[96,97] Natural or synthetic BA derivatives activate GPBAR1; in LSECs (Fig. 3) the activation of the G protein promotes the activity of adenylate cyclase to produce cAMP.

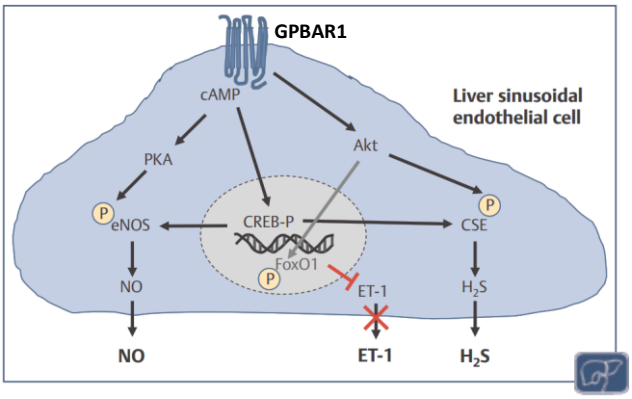

Figure 3. Effects of GPBAR1 activation on liver sinusoidal endothelial cells. [95]

The cAMP in turn activates protein kinase A (PKA) that can phosphorylate different proteins like cAMP response element binding protein (CREB-P). CREB promotes the transcription of endothelial nitric oxide synthase (eNOS) that gets phosphorylated by PKA to then produce NO. Furthermore, protein kinase B, also known as Akt, is also activated and represses the transcription of endothelin-1 (ET-1). In brief, GPBAR1's role in LSECs is to control the portal blood pressure.

In KCs (Fig. 4), higher levels of cAMP determine the inhibition of IκB kinase (IKK); thus, IκB transmigration in the nucleus is prevented.

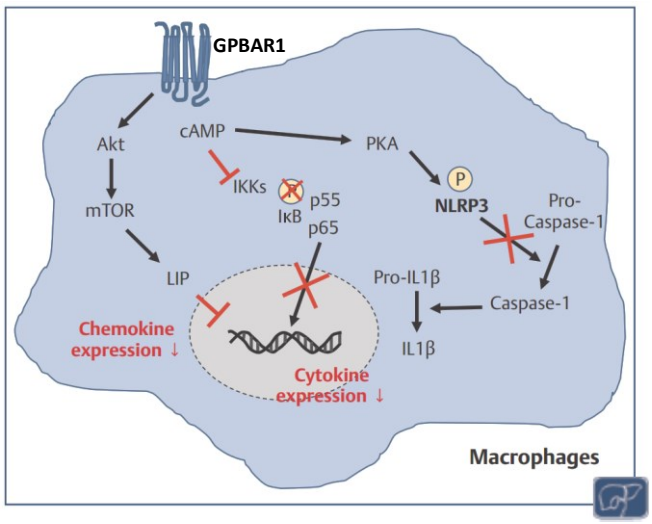

Figure 4. Effects of GPBAR1 activation on macrophages.[95]

At the same time, the reduction of both NF-κB translocation in the nucleus and its transcriptional activity lowers the expression of pro-inflammatory cytokines genes.[98,99]

All these effects also determine the inhibition of the inflammasome NLRP3 which in turn lowers the activation of Caspase-1 limiting the production of pro-inflammatory cytokines like interleukin-1β and -18.[100]

In the end, Akt and mTOR activation also upregulates the CCAAT/enhancer-binding protein β (C/EBPβ) isoform liver-enriched

inhibitory protein (LIP) suppressing the production of inflammatory chemokines. In conclusion, BAs activation of GPBAR1 exerts important anti-inflammatory effects both in monocytes and macrophages.[101,102]

To sustain this assumption, murine GPBAR1-deficient models were consistently found more susceptible to LPS-induced damage to the liver with higher alanine and aspartate aminotransferases and inflammatory cytokines levels in the serum.[103]

Moreover, high-fat diet-induced liver steatosis in mice was attenuated by administering a GPBAR1 agonist. Besides the anti-inflammatory effect, the treatment with an agonist was linked to increased glucagon-like peptide 1 (GLP-1) production by entero-endocrine L-type cells in the intestine.[99,104,105] All these findings prompted the identification of novel and better GPBAR1 agonists for the treatment of NAFLD/NASH.

GPBAR1 ligands can be chemically classified into steroidal (both natural and semisynthetic) and non-steroidal derivatives.

The most potent steroidal agonist is taurolithocholic acid (Fig. 5) with EC_{50} of 0.33 μM. Other endogenous bile acids bind GPBAR1 with decreasing potency like lithocholic (LCA), deoxycholic (DCA), cholic (CA) and chenodeoxycholic acids (CDCA).

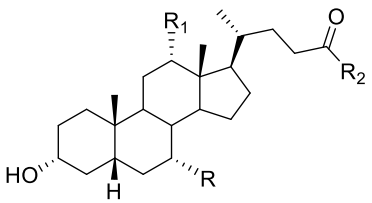

1 TLCA	R=H	R_1=H	R_2=$NHCH_2CH_2SO_3Na$
2 LCA	R=H	R_1=H	R_2=OH
3 DCA	R=H	R_1=OH	R_2=OH
4 CA	R=OH	R_1=OH	R_2=OH
5 CDCA	R=OH	R_1=H	R_2=OH

Figure 5. Natural bile acids.

These natural BAs were the starting point for the discovery of new semisynthetic compounds with improved efficacy and potency. Harnessing the steroidal scaffold, a large group of hit compounds was

found, since together with GPBAR1 another important and extensively studied receptor is FXR, most of the hits presented a dual affinity towards both receptors. The most important modification was the introduction of an ethyl group at the C-6 position of chenodeoxycholic acid furnishing the most potent agonist ever discovered, obeticholic acid (OCA) with an EC_{50} of 99 nM towards FXR and 0.9 μM towards GPBAR1.[106–108] A Phase III clinical trial for OCA was started in 2012 and completed in 2018 (https://clinicaltrials.gov/ct2/show/record/NCT01473524).

The drug candidate performed great in treating PBC but unfortunately, 23% of patients developed cholestatic itching which was unbearable enough to induce drug discontinuation in 40% of patients. OCA was approved for the treatment of (ursodeoxycholic acid)-resistant patients with PBC (primary biliary cholangitis).[109,110]

GPBAR1 selectivity was achieved by some modifications on the OCA scaffold, the introduction of an (S)-methyl at C-23 gave INT-777 with an EC_{50} of 0.8 μM and a successful pharmacological profile on both pancreas and liver in db/db mice (Fig. 6).[111,112] Another GPBAR1 selective compound was BAR501 (EC_{50} = 1.03 μM), a triol with β-configuration of both the ethyl group at C-6 and the hydroxy at C-7.[113]

BAR501 was able to reverse insulin resistance, improve liver histology, and BAT functionality to promote energy expenditure and the browning of epWAT in a murine NASH model.[114] Moreover, BAR501 has been affirmed as a promising lead compound in IBD. In a trinitrobenzene sulfonic acid (TNBS)-induced colitis model in mice, BAR501 also reduced inflammation and immune dysfunction by modulating the inflammatory phenotype of colonic macrophages.[115]

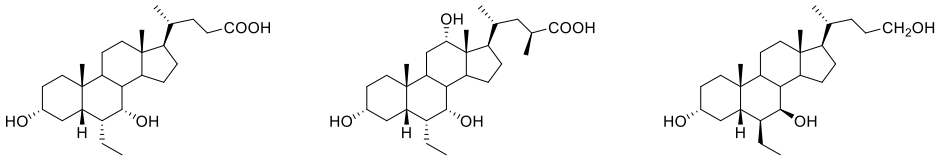

Figure 6. GPBAR1 agonists.

Apart from these last derivatives, a large effort was put into the identification of alternative non-steroidal scaffolds endowed with the same activity towards GPBAR1. In the last decades, many potent agonists were also discovered, thus amplifying the known chemical assets able to bind this receptor. These can be briefly classified as follows (Fig. 7):

- 3-Aryl-4-isoxazolecarboxamides (compound 9)
- 3-Aminomethylquinolines (compounds 10a and b)
- 2-Phenoxynicotinamides (compounds 11a and b)
- 4-Phenylpyridines and pyrimidines (compounds 12a and b)
- 3,4,5-Trisubstituted 4,5-dihydro-1,2,4-oxadiazoles (compounds 13a and b)
- Nipecotamide derivatives (compound 14)
- Oximes (compounds 15a and b)
- Diazepine (SB-756050 – compound 16)
- Thioamino-1*H*-imidazole (compound 17)

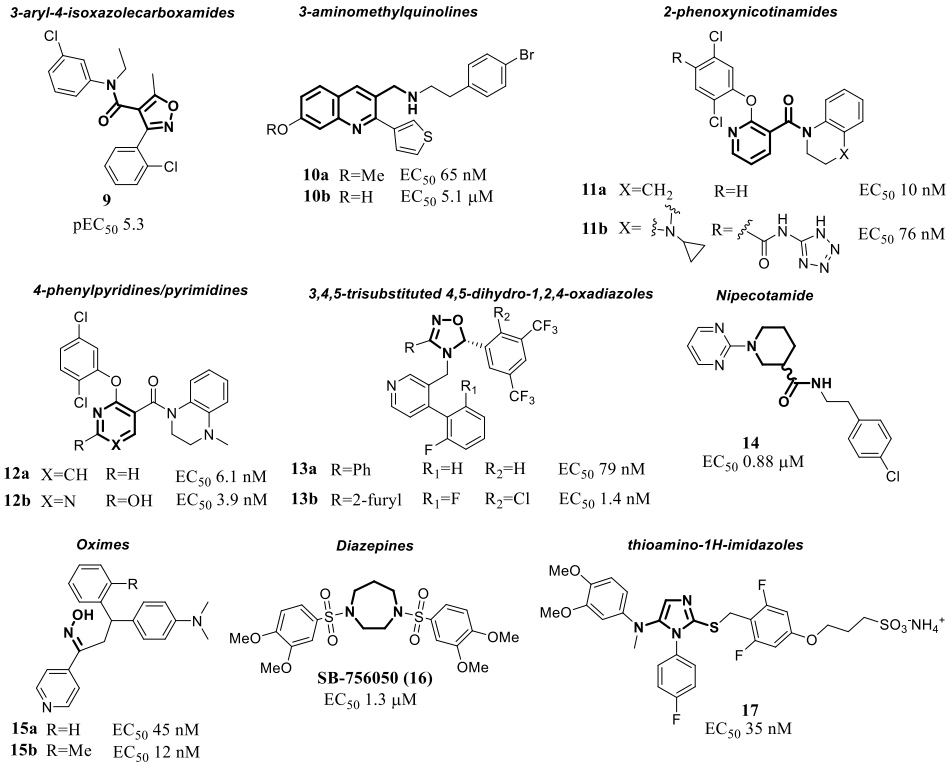

Figure 7. Non-steroidal GPBAR1 selective agonists.

Of all the reported molecules, SB-756050 is noteworthy as it reached Phase I clinical trials to treat type 2 diabetes mellitus even though its pharmacodynamic profile proved inconsistent. Thus, a further attempt to optimise the druggability of these compounds led to compound **17**, the most potent derivative (Fig. 7).[116]

A recent project based on drug repositioning was able to identify a new group of GPBAR1 agonists by testing known cysteinyl-leukotriene receptor 1 antagonists. Docking calculations suggested the possible overlap of the binding interactions between CysLTR1 and GPBAR1 binding sites. Such assumptions were then strongly confirmed by performing a set of *in vitro* and *in vivo* assays to validate the activity towards GPBAR1. The most successful candidate was REV5901, alpha-pentyl-3-[2-quinolinylmethoxy] benzyl alcohol.[117] It has been largely

studied without any clinical development for the treatment of asthma; its off-target effect on GPBAR1 determined a renewed interest in REV5901 as a hybrid modulator, thus prompting a new whole project which took a large part of this PhD work. Before discussing the aim of the project, an introduction to cysteinyl-leukotriene receptor 1 is deserved.

2.2 Cysteinyl leukotrienes receptors (CysLTRs)

Cysteinyl leukotrienes receptors are a family of G protein-coupled receptors (GPCRs) and bind indeed the cysteinyl leukotrienes.[118] These are a group of lipid mediators, also known as eicosanoids, endogenously produced by 5-lipoxygenase (5-LOX) starting from the arachidonic acid. The common precursor of all leukotrienes is LTA_4 which can be converted into LTB_4 or LTC_4 (Fig. 8).

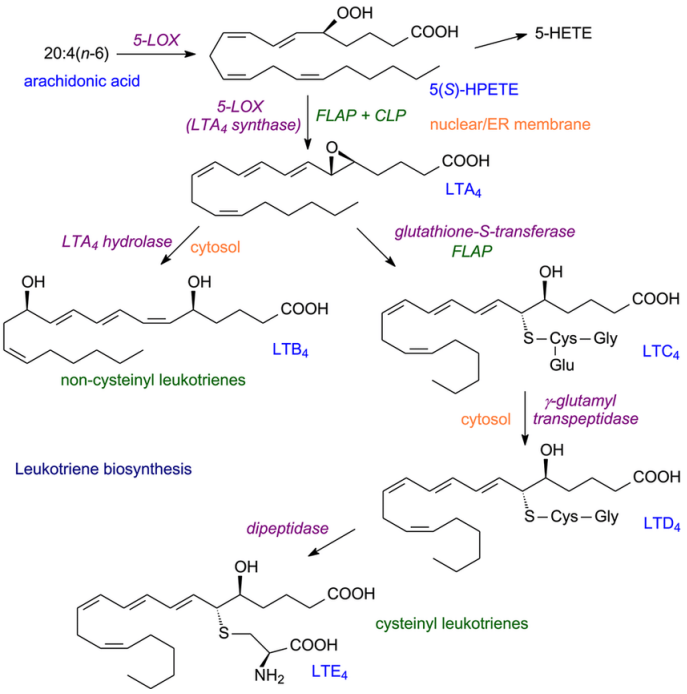

Figure 8. Leukotrienes biosynthesis.[119]

The latter is the result of a glutathione conjugation reaction by LTC_4 synthase and is converted first into LTD_4 which in turn loses the glutamate moiety to give LTE_4. Leukotrienes C_4, D_4 and E_4 all have a cysteinyl moiety and represent the endogenous ligands of CysLTRs.

Three isoforms have been identified up to date: type 1 and type 2 CysLTRs, both recognising cysteinyl leukotrienes with different affinities and recently also type 3 CysLTR, also known as GPR99 receptor.[120]

The differences between the two subtypes do not only concern the affinity to different LTs, their expression in the tissues and especially their activation effect differ. $CysLT_1R$ is mostly expressed in the respiratory system, leukocytes, spleen, heart, and gastrointestinal system while $CysLT_2R$ is highly present in the heart, vascular tissues, different parts of the brain, and the adrenal gland.[121]

$CysLT_1R$ is coupled to a tissue-dependent G protein, a pertussis toxin (PTX)-sensitive $G_{i/o}$ protein able to reduce intracellular cAMP levels and a PTX-insensitive G_q protein which can induce the increment of intracellular free Ca^{2+} concentration whereas $CysLT_2R$ is only coupled with a PTX-insensitive G_q protein.[122]

The different localisation of both receptors reflects their biological functions:

- ✓ $CysLT_1R$ determines bronchoconstriction, increased vascular permeability, higher mucus production, collagen deposition, and fibrosis, and plays an important role in the inflammatory chemotaxis.
- ✓ $CysLT_2R$ is related to the release of vasoactive factors and modulates the migration and proliferation of smooth vascular muscle cells.

Upon interaction of LTs with $CysLT_1R$, several downstream signalling pathways are activated. PI3K-Akt signalling is activated resulting in β-catenin nuclear translocation and activation of target genes including cyclin D1, COX-2, and c-Myc.[123] Akt/PKB complex activates the IKK complex with subsequent degradation of IκB protein leading to the NF-kB translocation and activation.[124] $CysLT_1R$ signalling can activate phospholipase C (PLC) and the Ras-Raf-MEK-ERK pathway.[123,125,126] This leads to the nuclear translocation of Erk 1/2 resulting in the activation

of genes involved in proliferation, migration, and survival. Moreover, CysLT receptor ligation can also activate PKC and the transcription factor cAMP response element-binding protein (CREB). Crosstalk occurs between CysLT and epidermal growth factor (EGF) signalling pathways; EGF signalling also activates Rac and the Ras-Raf-MEK-ERK pathway. EGF signalling induces the production of 5-LOX, resulting in leukotrienes synthesis and consequential potentiation of CysLT receptor signalling, while LOX/CysLT1 also regulate EGF-induced migration.[127]

Many $CysLT_1R$ antagonists have been identified, like Montelukast, Pranlukast, Zafirlukast, and REV5901, all successfully active in asthma therapy (Fig. 9).

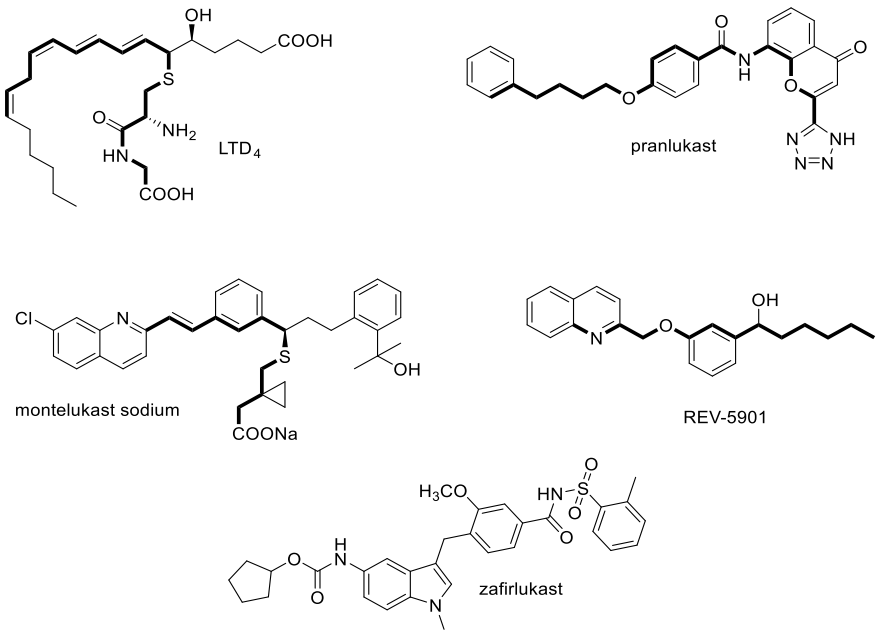

Figure 9. LTD_4 vs CysLTR1 antagonists.

All the above antagonists present a similar structural backbone to that of LTD_4. Montelukast has been the most successful candidate and is now also used as a reference compound in pharmacological assays. Apart from the

well-established use in the therapy of asthma, montelukast has been also found capable of preventing liver damage induced by acetaminophen.[128]

3. Hybrid modulators of GPBAR1 and CysLT$_1$R

3.1 Project presentation

As briefly described in the last chapter, the research group I joined during my PhD studies has investigated whether a selection of CysLT$_1$R antagonists had any off-target affinity in a drug repurposing fashion. In particular, the focus was given to two bile acid receptors: GPBAR1 and the farnesoid X receptor (FXR), both already well-known as selected targets for several projects in my team. The putative crosstalk between GPBAR1 and CysLT$_1$R represents an interesting starting point for the identification of promising hybrid modulators for the treatment of enterohepatic inflammatory conditions like NASH or IBD.

The set of antagonists included levocetirizine, a second-generation histamine H$_1$-receptor antagonist, zafirlukast, pranlukast, LY171883, REV5901 and montelukast, all CysLT$_1$R antagonists (Fig. 10).

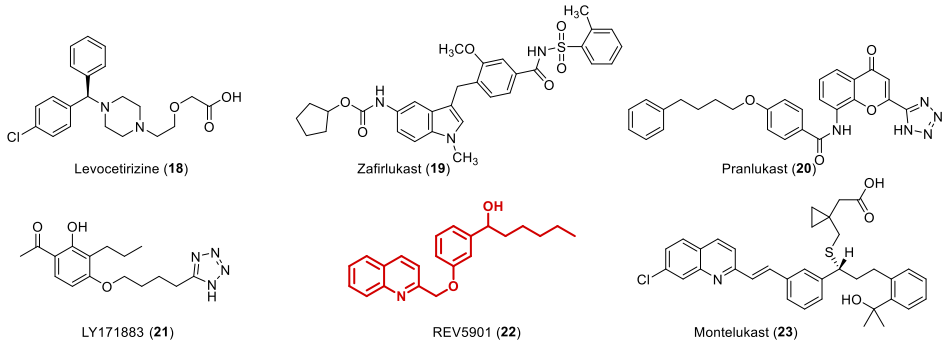

Figure 10. Known CysLT$_1$R antagonists.

REV5901 was the only compound of the set to present interesting results: it acted as a GPBAR1 agonist in a concentration-dependent fashion with an EC$_{50}$ of 2.5 μM, a result that is consistent with the docking predictions. In the transactivation assay, REV5901 was almost as potent as taurolithocholic acid while it failed to transactivate FXR thus showing a relative specificity towards GPBAR1. The use of silenced Gpbar1 gene

macrophages confirmed the interaction between REV5901 and the receptor (Fig. 11). All the *in vitro* assay data were corroborated by two *in vivo* models: TNBS-induced colitis and DSS-induced colitis using Gpbar1 knockout mice (Fig. 12).

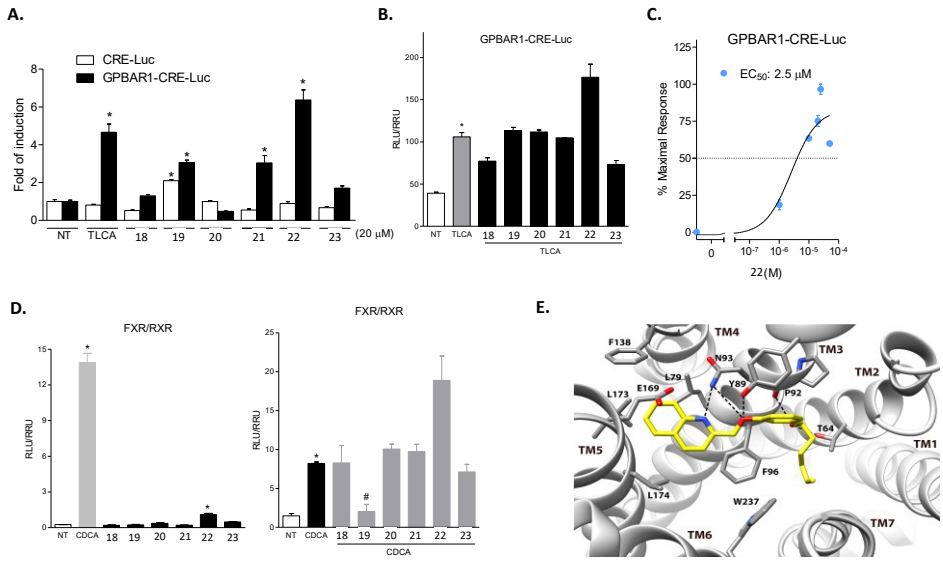

Figure 11. (A) Measure of induction of luciferase activity in cells transfected with CRE-Luc or GPBAR1-CRE-Luc and incubated with **TLCA** (10 μM) or compounds **18-23** (20 μM); (B) Antagonistic activity of compounds **18-23** towards GPBAR1 (TLCA = 10 μM, compounds 18-23 = 20 μM). Results are shown as mean ± standard error. ∗p < 0.05 versus not treated cells (NT). (C) Dose-response curve of compound **20** (REV5901) to evaluate the activity on GPBAR1; cells were stimulated with different concentrations of **20** from 1 μM to 50 μM. (D) FXR transactivation on HepG2 cells transfected with pSG5-FXR, pSG5-RXR, PGL4.70-Renilla, and p(hsp27) TKLUC vectors, and with compounds **18-23** (20 μM) alone or with CDCA (10 μM). Results are shown as mean ± standard error. ∗p < 0.05 versus not treated cells (NT). (E) Binding mode of REV5901. The ligand is in yellow, whereas the interacting leavings of the receptor are shown in grey. Oxygen atoms are in red and nitrogens are in blue. GPBAR1 is represented as grey ribbons. Hydrogens are omitted and H-bonds are displayed as dashed lines.

A rather detailed immunologic analysis has also been performed in the DSS-induced colitis model; mice treated with REV5901 showed a reduction in the production of many inflammatory cytokines. The consistency of this data was confirmed by the complete abrogation of the positive effects in silenced Gpbar1 gene mice.

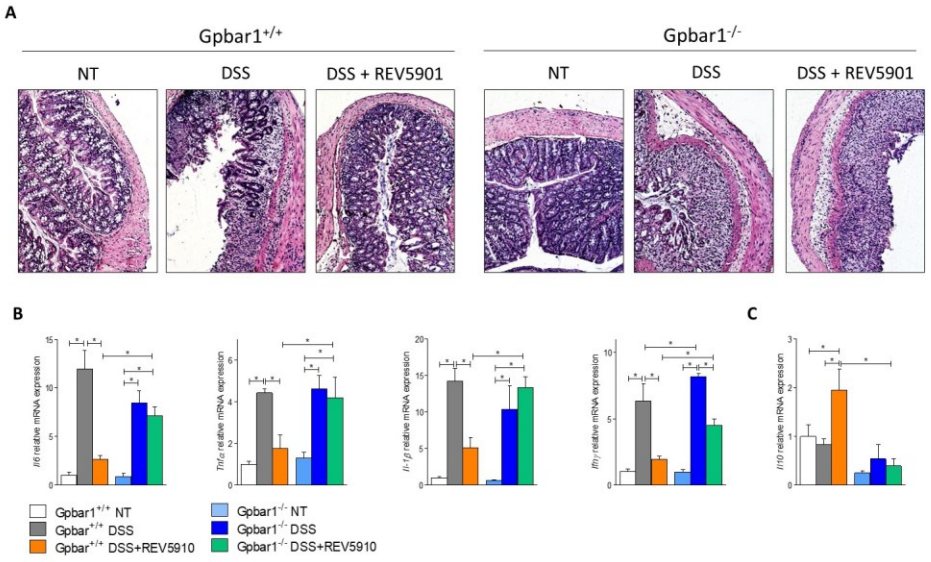

Figure 12. Gpbar1$^{+/+}$ and Gpbar1$^{-/-}$ mice were treated with DSS and then administered with REV5901 (30 mg/kg/day) or Montelukast (10 mg/kg/day) by gavage for 8 days. (A) H&E staining of colon sections from control mice, mice treated with DSS, and mice treated with TNBS plus REV5901 or Montelukast (original magnification ×10). Relative mRNA expression of (B) pro-inflammatory cytokines (Il-6, Tnf-α, Il-1β, Ifn-γ), (C) anti-inflammatory cytokine (Il-10) in the colon of Gpbar1$^{+/+}$ and Gpbar1$^{-/-}$ mice was evaluated by real-time PCR. The data are normalized to Gapdh mRNA. Results are the mean ± SEM of 6–10 mice per group from two independent experiments. *$p < 0.05$.

This report was one of the first to identify an off-target activity of shelved $CysLT_1R$ antagonists towards GPBAR1. REV5901 dual activity encouraged the further investigation of its structural features to obtain better hybrid compounds suitable for the treatment of NASH or IBD.[117]

3.2 Synthesis of REV5901 derivatives

According to the results of the docking prediction of REV5901 towards both $CysLT_1R$ and GPBAR1, the quinoline moiety appears required in both interaction models. Therefore, we decided to retain the heterocyclic ring and apply most of the modification on the alkyl side chain. The possibility for a strongly polar interaction on the extremity of the binding site of both receptors also influenced the choice of introducing highly polar substituents such as alcohols or carboxylic acids. The entire library of compounds is displayed in Figure 13.

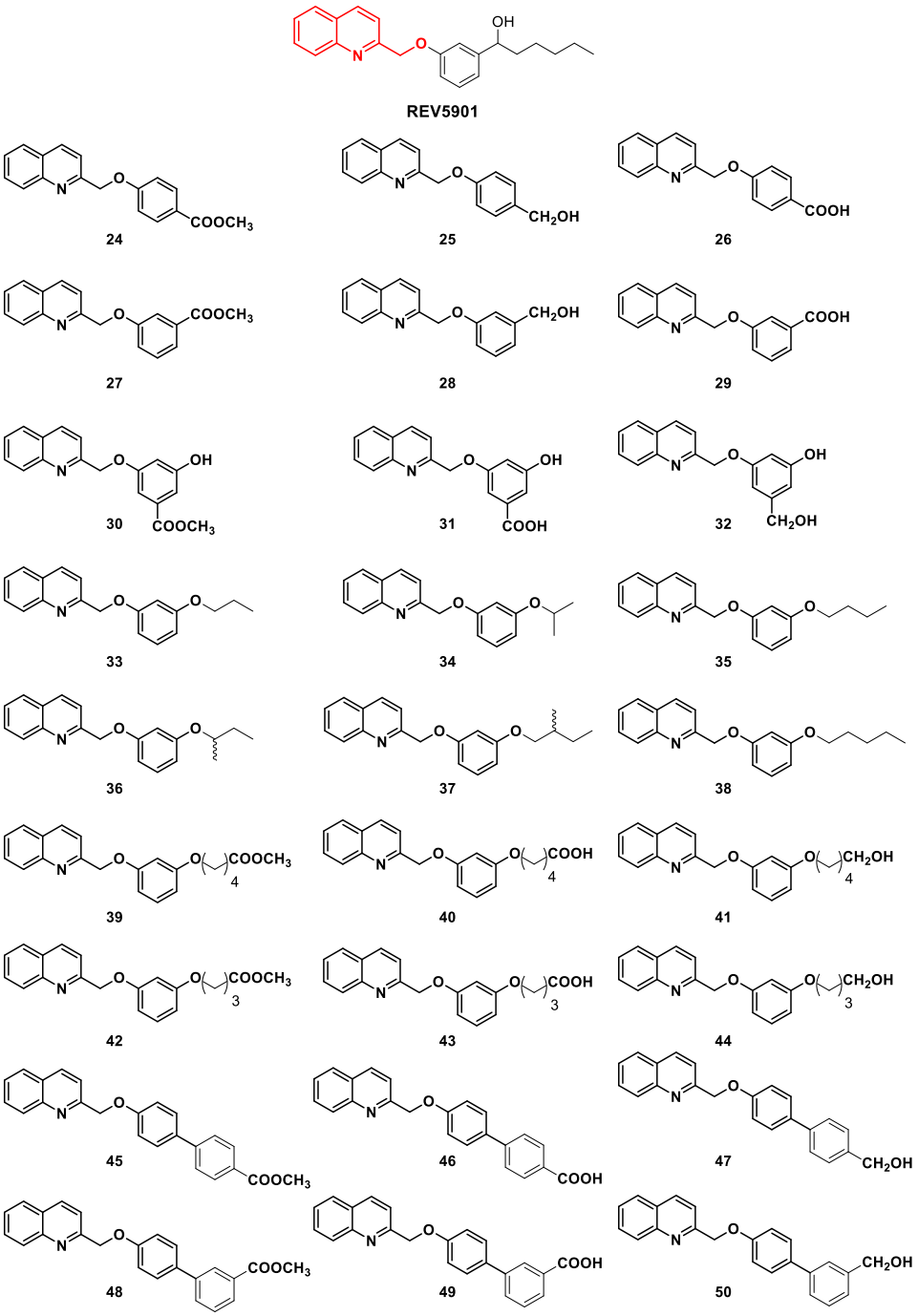
REV5901
24
25
26
27
28
29
30
31
32
33
34
35
36
37
38
39
40
41
42
43
44
45
46
47
48
49
50

Figure 13.

A concise retrosynthetic analysis revealed the modularity of the synthetic strategy thanks to the common presence of the quinoline ring. All the designed molecules could be easily divided into two synthons, one being the quinoline ring itself and the other being a phenol-like ring.

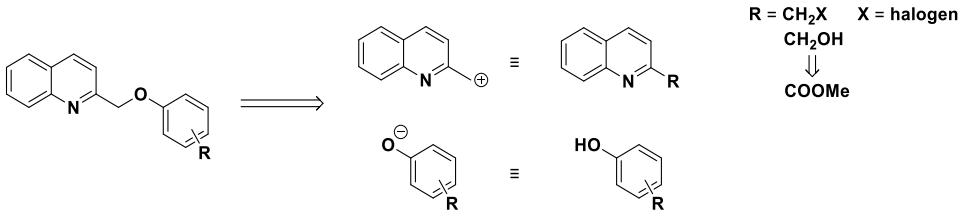

Figure 14. Retrosynthetic analysis

The synthetic equivalent of the 2-methyl quinoline synthon used for the synthesis of compounds **24-32** was the commercially available methyl quinoline-2-carboxylate (**51**) that was subjected to a mild reduction with di-isobutyl aluminium hydride (DIBAL-H) to afford the corresponding alcohol derivative (**52**). The other half of the molecules was then introduced by coupling the respective phenol derivative *via* Mitsunobu reaction. Methyl 4-hydroxybenzoate was used to afford the ester **24** (76%) while methyl 3-hydroxybenzoate gave the ester **27** (78%). Each ester was respectively hydrolysed with NaOH or reduced with DIBAL-H to obtain the corresponding acids **26** (43%) and **29** (68%) and the alcohols **25** (68%) and **28** (60%) (Scheme 1).

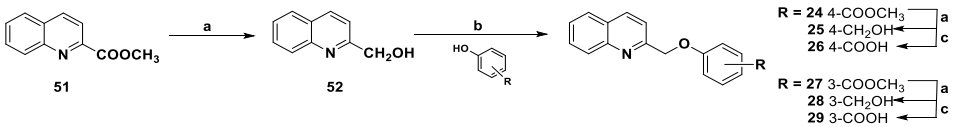

Scheme 1 *Reagents and conditions:* a) DIBAL-H 1M in THF dry, 0°C; b) phenol, PPh_3, DIAD, dry THF, 0° C; c) NaOH, MeOH/H_2O 1:1 v/v, reflux

The synthesis of compounds **30-32** (Scheme 2) required a slightly longer procedure because of the insertion of the methyl 3,5-dihydroxybenzoate (**55**), a modification that we performed to explore a larger chemical space.

The direct coupling of the purchased compound **55** with the mesylate **53** always gave a very low yield no matter the attempts of optimisation because of the fast decomposition of the methyl 3,5-dihydroxybenzoate in the basic conditions required by the Williamson synthesis step. An improvement was obtained through the mono protection of **55** with t-butyldimethylsilylchloride (TBS-Cl); the corresponding silylether **56** was successfully coupled with the mesylate intermediate **53** to afford compound **54** with 87% yield. The Mitsunobu reaction was not compatible with the presence of the TBS group in our experimental conditions; therefore, we performed a mesylation of the alcohol **52**, followed by a classic Williamson ether synthesis. Deprotection with tetrabutylammonium fluoride (TBAF) of compound **54** furnished the ester derivative **30** (85%). Again, basic hydrolysis and reduction with DIBAL-H of **30** afforded respectively the acid **31** (92%) and the alcohol **32** (quantitative yield).

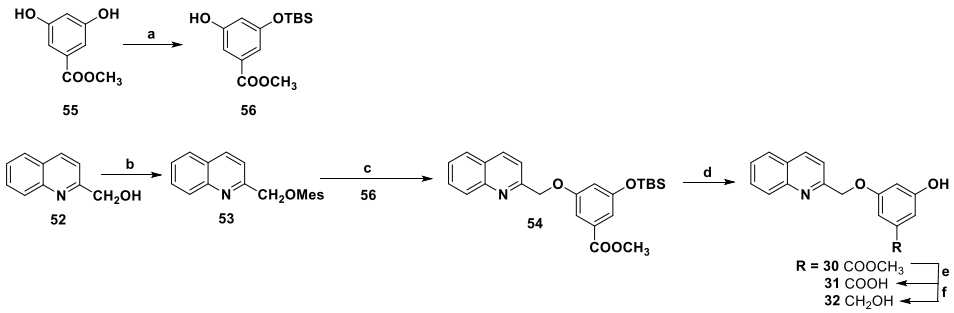

Scheme 2 *Reagents and conditions:* a) TBS-Cl, imidazole, dry DMF; b) Ms-Cl, lutidine, dry diethylether, 0°C; c) K_2CO_3, **56**, dry DMF; d) TBAF 1M in THF; e) NaOH, MeOH/H_2O 1:1 v/v, reflux; f) DIBAL-H 1M in THF dry, 0°C

With the third subset of molecules, a wider chemical space was explored by removing any polar substituent on the side chain of the scaffold. Thus, allowing us to verify how this would affect the overall activity together with different lengths and degrees of the alkyl chain ramification. Compounds **33**-**38** (Scheme 3) were synthesised by coupling the mesylate

53 with the corresponding alkoxy phenols **60a-f**. These were synthesised starting from the purchasable resorcinol **57** which was first mono protected with TBSCl and then coupled with the corresponding alcohol *via* the Mitsunobu reaction. The treatment with TBAF to cleave the silylether afforded the final ethers **60a-f** (47−84% yield over the last two steps).

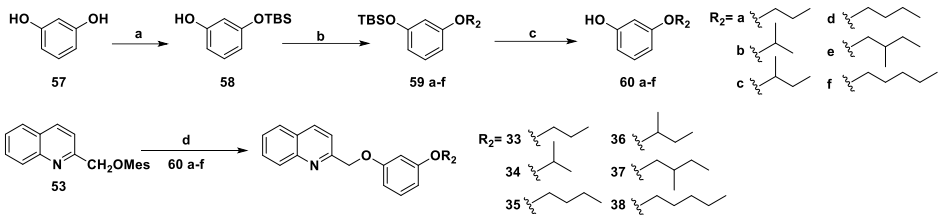

Scheme 3 *Reagents and conditions:* a) TBS-Cl, imidazole, dry DMF; b) alcohol, PPh_3, DIAD, dry THF, 0° C; c) TBAF 1M in THF; d) K_2CO_3, **60a-f**, dry DMF

Afterwards, I revised the synthetic protocol to achieve a much simpler and cheaper strategy. We observed the short-term stability of the quinoline-2-ylmethanol **52**, even when freshly made. Thus, the synthetic protocol was adjusted by substituting the methyl quinoline-2-carboxylate (**51**) with 2-(chloromethyl)quinoline hydrochloride (**62**). The use of compound **62** allowed us to skip two synthetic steps as it is suitable for a direct Williamson reaction with the phenolic building block, and the overall synthesis yield rose notably.

A different distance between the quinoline ring and the polar group was also evaluated. This was performed by inserting a flexible linear propyl or butyl chain carrying either an alcohol or a carboxylic acid on the last carbon. The synthesis of compounds **39-44** (Scheme 4) started with the monofunctionalisation of resorcinol (**57**) with methyl 5-bromopentanoate or 4-bromobutanoate to give the respective products **61a** and **b** (64% and 43% yield respectively).

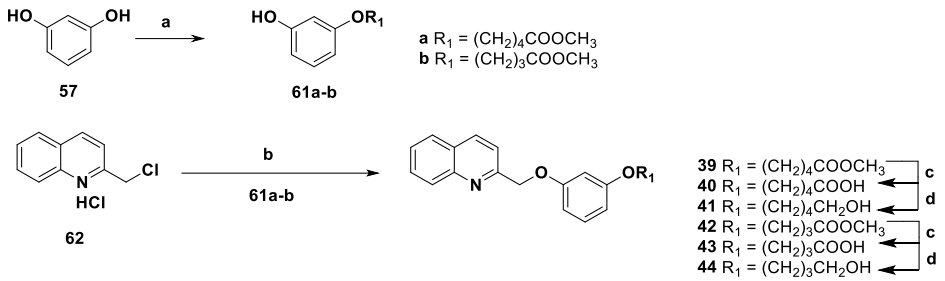

Scheme 4 *Reagents and conditions:* a) $Br(CH_2)_nCOOMe$, K_2CO_3, dry DMF; b) **62a-b**, K_2CO_3, dry DMF; c) NaOH, MeOH/H_2O 1:1 v/v, reflux; d) $LiBH_4$, dry MeOH, dry THF, 0°C

These were coupled with 2-(chloromethyl)quinoline to afford compounds **39** (75% yield) and **42** (72% yield). The corresponding carboxylic acids **40** and **43** were synthesised by basic hydrolysis with 68% and 97% yield respectively. The reduction of **39** and **42** with $LiBH_4$ furnished alcohols **41** and **44** (80% yield for both).

The last subset of molecules was planned to investigate the effects of the presence of a rigid lipophilic group like the biphenyl moiety keeping a polar group at its very end in the *meta* or *para* position.

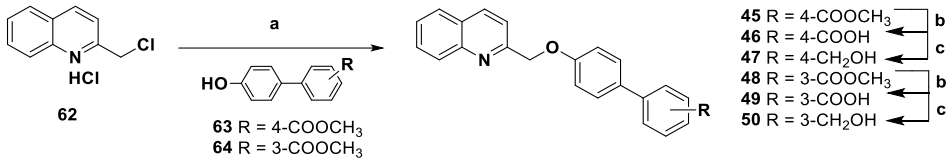

Scheme 5 *Reagents and conditions:* a) **63** or **64**, K_2CO_3, dry DMF; b) NaOH, MeOH/H_2O 1:1 v/v, reflux; c) $LiBH_4$, dry MeOH, dry THF, 0°C

The synthesis of compounds **45-50** is very concise (Scheme 5). The Williamson coupling between **62** and methyl 4′-hydroxy-[1,1′-biphenyl]-4-carboxylate (**63**) or methyl 4′-hydroxy-[1,1′-biphenyl]-3-carboxylate (**64**) afforded the esters **45** (87% yield) and **48** (quantitative yield), both were subjected to basic hydrolysis to furnish acids **46** and **49** (quantitative yield for both) and $LiBH_4$ reduction to produce alcohols **47** and **50** (92% and quantitative yield respectively).

3.3 *In vitro* preliminary pharmacological evaluation

The GPBAR1 agonistic activity of compounds **24-50** was evaluated in a luciferase reporter assay with HEK-293T cells transfected with GPBAR1. Their antagonism towards human $CysLT_1R$ expressed in transfected CHO cells was determined *via* a fluorimetric detection method and measuring the effect on cytosolic Ca^{2+} production induced by an agonist. The cellular antagonist effect was calculated as a % inhibition of control reference agonist (LTD4) response for each target whilst GPBAR1 agonism was compared to that of the reference compound taurolithocholic acid (TLCA) set as 100%.

Table 1 Efficacy and potency for compounds **24-38**.

Compounds	GPBAR1[a]	EC_{50}[b] (µM)	$CysLT_1R$[c]	IC_{50}[b] (µM)
REV5901	136.74 ± 27.80	2.50 ± 1.20	116.80 ± 0.21	1.10 ± 0.50
24	20.7 ± 8.45	nd	48 ± 4.60	nd
25	12.63 ± 4.11	nd	85 ± 3.32	2.10 ± 1.50
26	32.15 ± 3.29	16.50 ± 0.71	-11 ± 4.38	nd
27	23 ± 4.76	nd	85 ± 0.91	3.90 ± 1.50
28	**92.69 ± 0.73**	**7.40 ± 1.84**	**97 ± 0.78**	**1.20 ± 0.42**
29	**74.80 ± 3.96**	**3 ± 0.30**	**71 ± 2.05**	**2.80 ± 0.38**
30	17.58 ± 1.37	nd	59 ± 3.25	nd
31	29.80 ± 0.89	20 ± 0.71	3 ± 7.42	nd
32	72.92 ± 1.57	23 ± 1.41	26 ± 14.30	nd
33	112.34 ± 12.21	1 ± 0.04	66 ± 4.66	5.11 ± 1.6
34	14.99 ± 1.81	nd	79 ± 5.09	nd
35	100.50 ± 13.91[e]	0.1 ± 0.05	66 ± 0.07	9.63 ± 1.3
36	138.88 ± 11.15	0.50 ± 0.22	4 ± 8.27	nd
37	**106.43 ± 4.45**	**0.17 ± 0.07**	**15 ± 3.67**	**nd**
38	137 ± 12.93	1.80 ± 0.07	22 ± 4.38	nd

Table 2 Efficacy and potency for compounds **39-50**.

Compounds	GPBAR1[a]	EC_{50}[b] (μM)	$CysLT_1R$[c]	IC_{50}[b] (μM)
39	20.5 ± 2.4	nd	76 ± 9.6	1.68 ± 0.28
40	12 ± 1.3	nd	99.6 ± 2.0	0.90 ± 0.50
41	**30.8 ± 7.5**	**nd**	**106.9 ± 1.6**	**0.36 ± 0.58**
42	20.2 ± 4.5	nd	92.1 ± 3.4	1.55 ± 0.43
43	18.3 ± 4.8	nd	92.8 ± 2.3	0.95 ± 0.2
44	**12.8 ± 3.3**	**nd**	**108.6 ± 1.8**	**0.31 ± 0.24**
45	36.74 ± 3	nd	43 ± 4.5	nd
46	64.9 ± 13	nd	0.8 ± 1.5	nd
47	20.5 ± 2.4	nd	76 ± 9.6	nd
48	56.91 ± 7.8	nd	21 ± 6.5	nd
49	**82 ± 1.2**	**4.6 ± 1.5**	**109 ± 1.6**	**5.67 ± 0.77**
50	2.1 ± 0.06	nd	59 ± 3.6	nd

[a]Eff (%) is the maximum efficacy of the compound (10 μM) relative to TLCA (10 μM) as 100 in transactivation of a cAMP response element (CRE) on HEK293T cells; results are mean of at least two experiments ±SD. [b]Results are the mean of at least two experiments. Nd means not determined. [c]These assays were performed by Eurofins Cerep-Panlabs (France). The results are expressed as % inhibition of the control response to 0.1 nM LTD_4. The standard reference antagonist is MK-571. Results are the mean of two experiments ±standard deviations (SD). [d]These assays were performed by Eurofins Cerep-Panlabs (France). [e]Efficacy calculated with 1 μM of the compound.

As shown in **Tables 1** and **2**, compounds **28**, **29** and **49** presented the best profiles in terms of efficacy and potency towards both receptors, thus highlighting their dual activity. At the same time, highly selective derivatives for one of the receptors were discovered: compound **37** showed high selectivity towards GPBAR1 while compounds **41** and **44** selectively antagonised $CysLT_1R$.

3.4 Docking studies

The binding modes of all compounds to $CysLT_1R$ and GPBAR1[129–132] were investigated *via* molecular docking calculations employing the Glide software package.[133,134] $CysLT_1R$ crystallographic structure with PDB ID 6rz420has[135] been employed for the docking simulations, whilst for GPBAR1 the 3D model developed in-house[136], already employed in several successful projects.[137–139]

In GPBAR1 the simulations for all derivatives gave convergent results: the quinoline group places itself in the amphipathic pocket between transmembrane helices (TM) 3 and 5, reaching out to the residues involved in GPBAR1 activation like $Tyr89^{3.29}$, $Asn93^{3.33}$, $Phe96^{3.36}$, and $Trp237^{6.48}$. As for $CysLT_1R$, the quinoline portion of all molecules resides in the pocket formed by TM3, TM4, and TM5.

Next, the detailed binding modes of compounds **28, 29, 37** and **49** will be discussed.

3.4.1 Binding mode of 28 in GPBAR1

Compound **28** is placed so that the quinoline ring binds to TM3 and TM5 through an H-bond with Asn93$^{3.33}$ and several hydrophobic interactions with Phe96$^{3.36}$, Leu97$^{3.37}$, Leu100$^{3.40}$, Leu173$^{5.46}$, and Leu174$^{5.47}$ (Figure 15A). The phenyl ring engages in a T-shaped π stacking interaction with Trp237$^{6.48}$ and interacts with Leu71$^{2.60}$, Tyr89$^{3.29}$, Pro92$^{3.32}$, Glu169$^{5.42}$, and Leu266$^{7.39}$. The terminal alcohol group stretches towards TM1 and TM7, pointing to Leu68$^{2.57}$ and contacts both Ser 270$^{7.43}$ and Tyr240$^{6.51}$ with two additional H-bonds (Fig. 15, panel A).

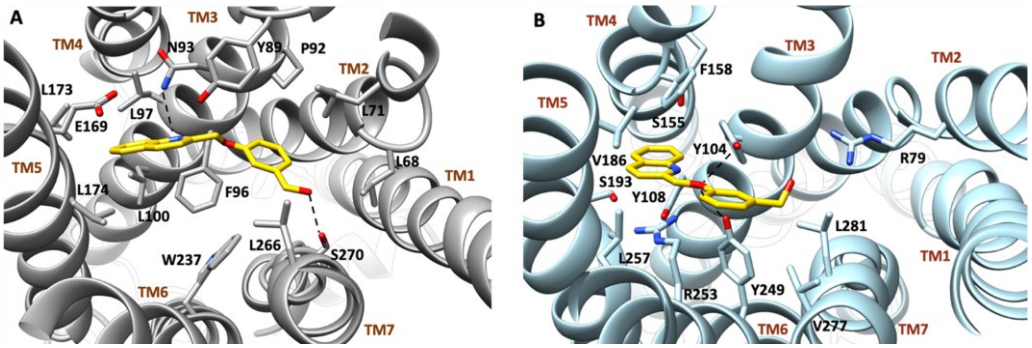

Figure 15. Binding modes of **28** in (A) GPBAR1 and (B) CysLT$_1$R were identified *via* docking calculations. The ligand is represented as gold sticks, whereas the interacting residues of the receptors are shown in grey (GPBAR1) or cyan (CysLT$_1$R) and labelled. Oxygen atoms are depicted in red, and nitrogen atoms are depicted in blue. The receptors are represented as grey (GPBAR1) or cyan (CysLT$_1$R) ribbons with their TMs labelled. Hydrogens are omitted for the sake of clarity, and H-bonds are displayed as black dashed lines.

3.4.2 Binding mode of 28 in CysLT$_1$R

The quinoline moiety of compound **28** stands perpendicular to TM3 and TM5 and sits in the pocket formed by Tyr108$^{3.37}$, Ser155$^{4.57}$, Phe158$^{4.60}$, Val186$^{5.35}$, Ser193$^{5.42}$, and Leu257$^{6.59}$ (Fig. 15, panel B). Some additional interactions further stabilise the binding mode: a cation-π interaction between the quinoline and Arg253$^{6.55}$, an H-bond with Tyr104$^{3.33}$ which in turn also forms a T-shaped π stacking interaction with the phenyl ring together with Tyr249$^{6.51}$. Finally, an H-bond between the hydroxyl group of **28** and Arg79$^{2.60}$ is mediated by a water molecule (Fig. 15, panel B).

Molecular dynamics (MD) and free-energy calculations of this binding mode strongly confirmed the predictions of the binding mode (Fig. 16, panels A and B).

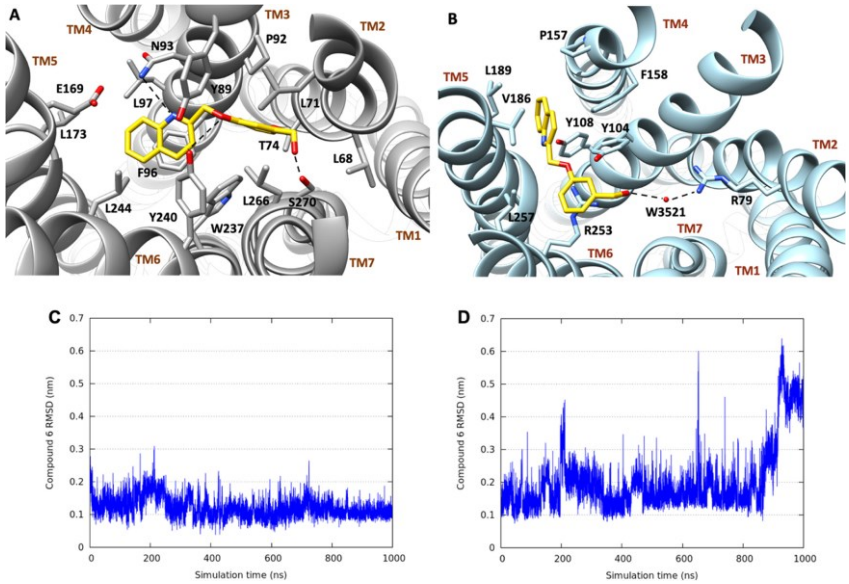

Figure 16. (A, B) Centroids of the most populated clusters of **28** in (A) GPBAR1 and (B) $CysLT_1R$ MD simulations. The ligand is represented as gold sticks, whereas the interacting residues of the receptors are shown in grey (GPBAR1) or cyan ($CysLT_1R$) and labelled. Oxygen atoms are depicted in red, and nitrogen atoms are depicted in blue. The receptors are represented as grey (GPBAR1) or cyan ($CysLT_1R$) ribbons with their TMs labelled. Hydrogen atoms are omitted for the sake of clarity, and H-bonds and salt bridges are displayed as black dashed lines. (C, D) Average RMSD of the heavy atoms of **28** in GPBAR1 (C) and $CysLT_1R$ (D) along the MD simulations. Prior to the RMSD calculations, trajectory frames were aligned on the backbone of the protein.

3.4.3 Binding mode of 29 in GPBAR1

Due to the high similarity with compound **28**, its binding mode almost overlaps that of compound **29** (Fig. 17, panel A). More specifically, the quinoline portion resides in the amphipathic box formed by TM3, TM5, and TM6 where it interacts positively with $Tyr89^{3.29}$, $Leu97^{3.37}$, $Glu169^{5.43}$, $Leu173^{5.46}$, $Tyr240^{6.51}$, $Val241^{6.52}$, and $Leu244^{6.55}$. The quinoline also forms an H-bond with $Asn93^{3.33}$ and a π-π stacking interaction with $Phe96^{3.36}$.

A T-shaped π stacking interaction happens between $Trp237^{6.48}$ and the phenyl moiety which also points toward TM2 and TM7 establishing apolar

interactions with Leu68$^{2.57}$, Leu71$^{2.60}$, Thr74$^{2.63}$, Pro92$^{3.32}$, and Leu266$^{7.39}$. In the end, the carboxyl group forms an H-bond with Ser270$^{7.43}$.

3.4.4 Binding mode of 29 in CysLT$_1$R

As previously mentioned, compound **29** binds very similarly to **28** (Fig. 17, panel B). TM4 and TM5 surround the quinoline ring very close, establishing several hydrophobic contacts with residues like Phe158$^{4.60}$, Val186$^{5.35}$, and Leu257$^{6.59}$. Moreover, Tyr104$^{3.33}$ and Arg253$^{6.55}$ are involved in a T-shaped π and cation−π interaction respectively with compound **29**. Unlike 28, the phenyl ring is located next to TM3 and TM2 and interacts with Leu103$^{3.32}$ and Leu281$^{7.39}$. Additionally, a salt-bridge interaction occurs between the carboxylic group and Arg79$^{2.60}$.

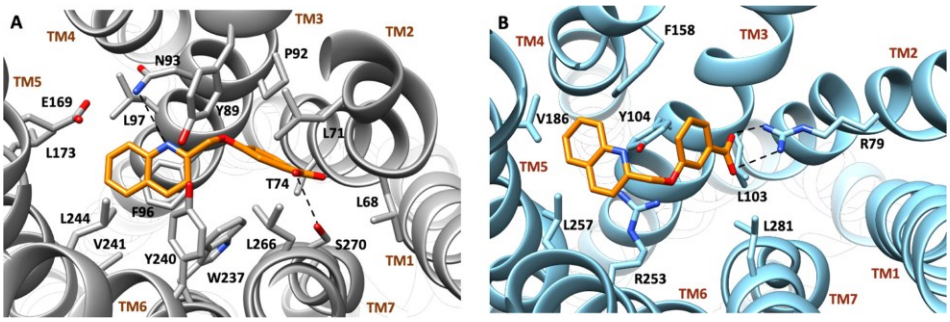

Figure 17. Binding mode of **29** in (A) GPBAR1 and (B) CysLT$_1$R. The ligand is represented as orange sticks, whereas the interacting residues of the receptors are shown in grey (GPBAR1) or cyan (CysLT$_1$R) and labelled. Oxygen atoms are depicted in red, and nitrogen atoms are depicted in blue. The receptors are represented as grey (GPBAR1) or cyan (CysLT$_1$R) ribbons with their TMs labelled. Hydrogens are omitted for the sake of clarity, and H-bonds and salt bridges are displayed as black dashed lines.

3.4.5 Binding mode of 49 in GPBAR1

In this case, the quinoline portion, positioned between TM3 and TM5, establishes polar interaction with Tyr89$^{3.29}$, Asn93$^{3.33}$, and Glu169$^{5.38}$. It also engages hydrophobic contacts with Phe96$^{3.36}$, Leu97$^{3.37}$, Leu166$^{5.40}$ Leu173$^{5.47}$, and Leu174$^{5.48}$. The ethereal oxygen forms an H-bond with Tyr240$^{6.42}$, whilst the biphenyl group stretches out through the cleft shaped by Leu71$^{2.60}$, Pro92$^{3.42}$, Trp237$^{6.39}$, Tyr240$^{6.42}$, and Leu266$^{7.39}$ letting the carboxylic group form an H-bond with the side chain of Ser270$^{7.43}$ (Fig. 18, panel A).

3.4.6 Binding mode of 49 in CysLT$_1$R

The quinoline group of **49** fills a region between TM3 and TM5, in a hydrophobic pocket formed by Tyr108$^{3.37}$, Phe158$^{4.60}$, Val 186$^{5.35}$, Ser193$^{5.40}$, and Arg253$^{6.55}$. Here, Arg253$^{6.55}$ and Phe158$^{4.60}$ form a cation-π and π-π stacking interaction with the quinoline ring respectively, further stabilizing the binding mode. The biphenyl ring points toward TM2 and interacts with Tyr249$^{6.51}$, Tyr104$^{3.33}$, and Leu281$^{7.39}$. On the other hand, the terminal carboxyl group establishes a salt bridge interaction with Arg79$^{2.60}$ and two water-mediated H-bonds, one again with Arg79$^{2.60}$ and the other with Thr109$^{3.38}$ (Fig. 18, panel B).

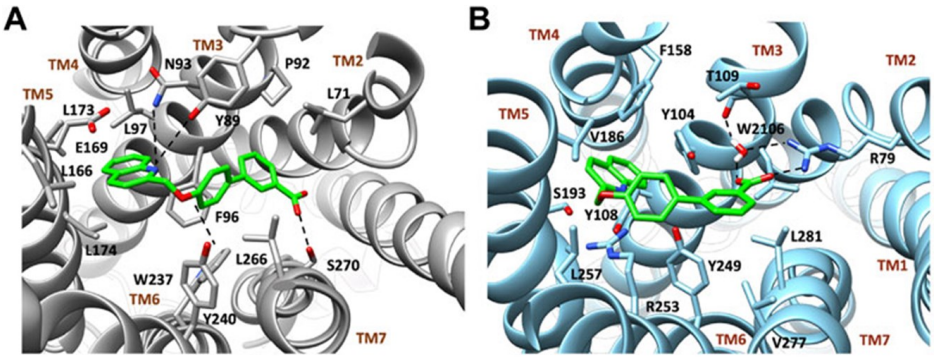

Figure 18. Binding mode in GPBAR1 and CysLT$_1$R and in vitro and in vivo evaluation of the pharmacokinetics for compound **49**. Binding mode of compound **49** (green stick) in GPBAR1 (A) (grey cartoon) and CysLT$_1$R (B) (sky-blue cartoon). The interacting residues of the receptor are shown in stick and labelled. TMs of the receptors are labelled. Oxygen atoms are depicted in red and nitrogens in blue. Hydrogens are omitted for the sake of clarity and H-bonds

are displayed as black dashed lines. The bridging water molecule is reported as red sticks with explicit hydrogens.

3.4.7 Binding mode of 37 in GPBAR1

Finally, the binding pose of **37**, the most potent selective GPBAR1 agonist discovered in this study, was also investigated. The quinoline scaffold places itself between TM3 and TM5; there, it forms an H-bond with Asn93$^{3.33}$ and interacts with the hydrophobic residues, Leu97$^{3.37}$, Leu100$^{3.40}$, Leu173$^{5.46}$, and Leu174$^{5.47}$. The phenyl group interacts with Pro92$^{3.32}$ and forms a T-shaped π interaction with Phe96$^{3.36}$.

The sec-butyl chain points toward TM1 and TM7, establishing more hydrophobic contacts with Leu68$^{2.57}$, Leu71$^{2.60}$, and Leu266$^{7.39}$ (Fig. 19).

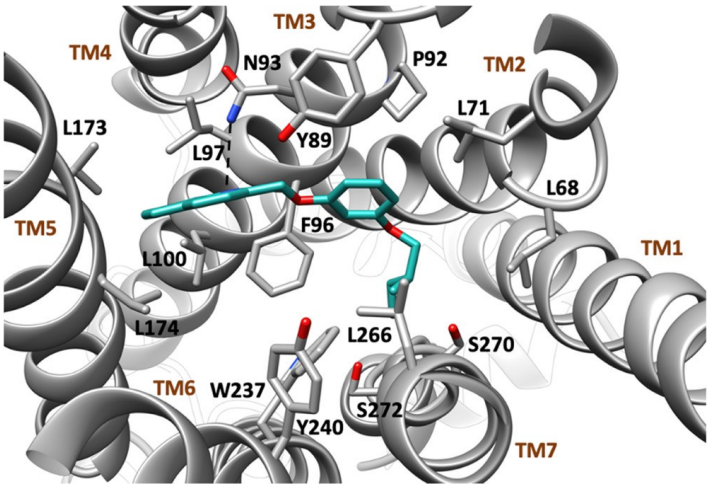

Figure 19. Binding mode of **37** in GPBAR1 from docking calculations. The ligand is represented as light sea green sticks, whereas the interacting residues of the receptor are shown in grey and labelled. Oxygen atoms are depicted in red, and nitrogen atoms are depicted in blue. The receptor is represented as grey ribbons with its TMs labelled. Hydrogens are omitted for the sake of clarity, and H-bonds are displayed as black dashed lines.

3.5 *In vitro* and *in vivo* pharmacological profiling

3.5.1 Anti-inflammatory activity of 28, 29 and 37

To further investigate their pharmacological potential, compounds **28**, **29** and **37** were tested to check if any anti-inflammatory activity would be displayed. To this effect, murine RAW264.7 macrophages were treated with lipopolysaccharides (LPS) and then co-incubated with or without compounds **28**, **29** and **37** at 0.1, 1.5, and 10 μM respectively.

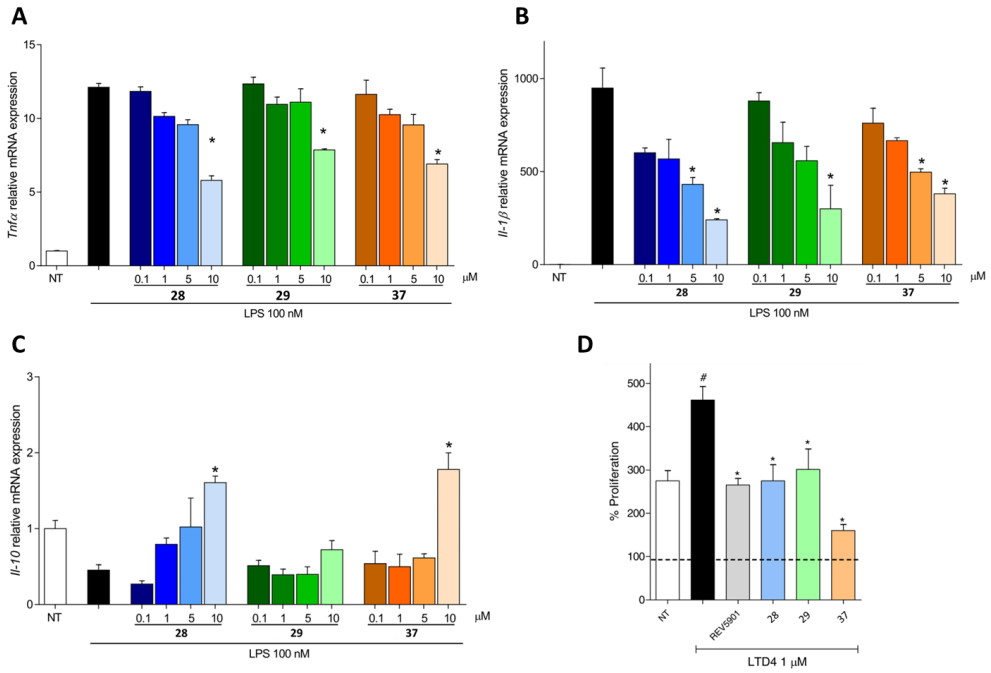

Figure 20. RAW264.7 cells were classically activated with LPS (100 nM) and exposed or not to compounds **28**, **29**, and **37** at concentrations of 0.1, 1.5, and 10 μM, respectively, for 16 h. Quantitative real-time polymerase chain reaction (PCR) analysis of expression of proinflammatory genes Tnf-α (A) and Il-1β (B), and anti-inflammatory genes Il-10 (C). These data are normalized to Gapdh/18s mRNA. Data are derived from six replicates from two independent experiments. Results represent mean ± standard error of the mean (SEM). *p < 0.05 vs LPS group. Analysis of variance (ANOVA) was used for statistical comparisons.

All three derivatives successfully decreased the levels of pro-inflammatory cytokines (TNF-α and IL-1β) while compounds **28** and **37** also stimulated IL-10, an anti-inflammatory cytokine (Fig. 20).

The ability to contrast LTD_4-induced proliferation of RAW246.7 cells was also investigated: all the compounds together with REV5901 as control successfully reversed the effect of LTD_4, yet again confirming the antagonism towards $CysLT_1R$.

GPBAR1 was recently found able to modulate adhesion proteins' production in endothelial and immune cells, thus influencing their recruitment in inflamed regions. As $CysLT_1R$ plays a key role in cell adhesion and leukocyte rolling, all compounds were tested in an adhesion assay employing human aortic endothelial (HAEC) and U937 cells (human monocytic cell line).

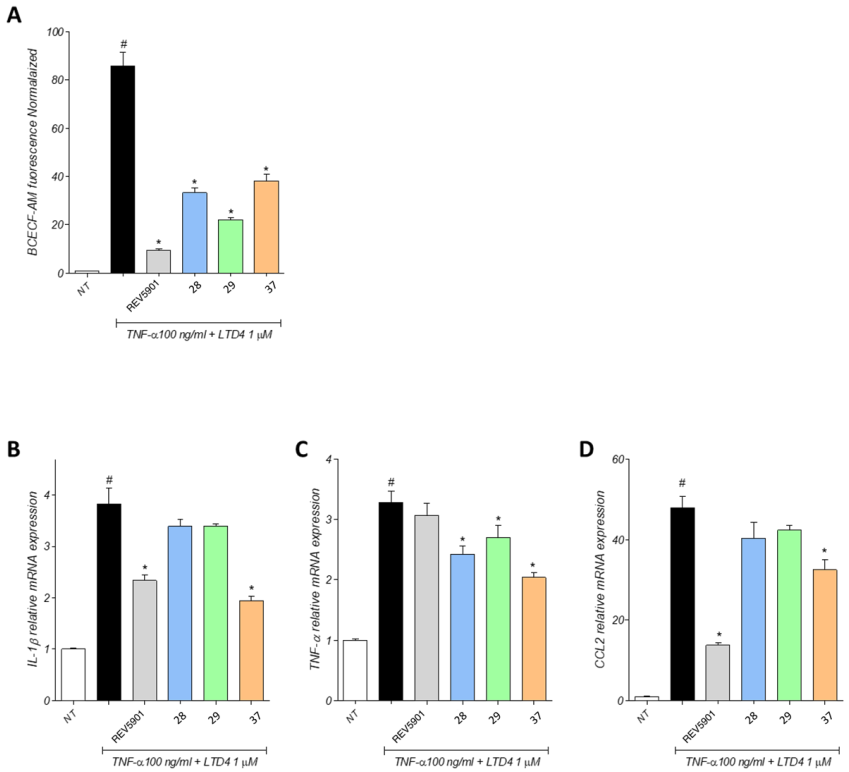

Figure 21. HAEC cells were plated on a 24-well plate and activated with TNFα (100 ng/mL) and LTD4 (1 μM) for 24 h, alone or in combination with compounds **28**, **29**, and **37** and REV5901 at 10 μM. U937 cells were treated under the same conditions. (A) For adhesion assay, U937 cells were fluorescently labelled with BCECF-AM and were incubated for 120 min with HAEC cells. Nonadherent monocytes were removed by gentle washing and fluorescence intensity was measured

(485 nm excitation and 520−560 nm emission) using a microplate reader. (B) Quantitative real-time PCR analysis of expression of proinflammatory genes Il-1β (B) and Tnf-α (C) and chemokine Ccl2 (D) in U937 cells. These data are normalized to Gapdh mRNA. Data are derived from eight replicates from two independent experiments. Results represent mean ± SEM. #p < 0.05 vs NT group and *p < 0.05 vs TNF-α + LTD4 group. Analysis of variance (ANOVA) was used for statistical comparisons.

Monocytes' adhesion to endothelial cells increases notably upon exposure to TNF-α + LTD4 (Fig. 21, panel A). Compounds **28, 29** and **37** together with REV5901 were able to decrease the adhesion of U937 cells with compound **29** being the most effective among the new derivatives and REV5901 being the most active. Since this adhesion assay determines monocyte activation, the production of additional mediators (IL-1β, TNF-α and CCL2) was also investigated. The results of the experiment showed the onset of an inflammatory state due to an increase in pro-inflammatory cytokines. Compounds **28** and **37** managed to decrease TNF-α but were less effective on IL-1β and CCL2. Besides, compound **37**, a nano-molar GPBAR1 selective agonist, was the most effective among the new compounds in reducing the expression of pro-inflammatory cytokines IL-1β and TNF-α (Fig. 21, panels B, C, D)

3.5.2 Pharmacokinetics Evaluation

The physicochemical parameters of the above-mentioned compounds were assessed by liquid chromatography−mass spectrometry (LC−MS) analysis and compared to those of the reference compound, REV5901 (Table 3). Compounds **28**, **29** and **49** present good physicochemical properties, with a better aqueous solubility than REV5901 (141, >200, and 66 respectively, vs 39 μM).

Moreover, the stability of the synthesised compounds against the human metabolizing enzymes contained in liver microsomes (responsible for phase I metabolism) and S9 (responsible for phase II metabolism) fractions was investigated *in vitro*, controlling the reduction of the non-metabolised compound by high-performance liquid chromatography (HPLC)-MS/MS.

Compounds **28**, **29** and **49** are highly stable to microsomal enzymes while compound **37** was quickly modified by phase I enzymes, as reported in **Table 3**.

Thus, the *in vitro* metabolic stability of compounds **28**, **29** and **49** in the S9 fraction was further investigated. Good $t_{1/2}$ values were observed for all the tested compounds. Among these, compound **49** presented the longest half-life times (578 min in microsomes and 385 in S9 fraction). When compared with REV5901, all three compounds showed a better pharmacokinetic profile proving their high drug-likeness.

Table 3 Efficacy and potency for compounds **39-50**.

			Microsomes		***S9 fraction***	
Compound	**Solubility (μM)[a]**	**LogD**	**$t_{1/2}$ (min)**	**C_{int}[b]**	**$t_{1/2}$ (min)**	**C_{int}**
REV5901	39.3	3.1	37	63	57	40
28	141	2.8	48	48	119	19
29	>200	0.12	210	11	247.5	9.3
37	3.5	1.01	22.3	103.3	-	-
49	66	2.0	578	4	385	6

The best PK profile was that of compound **49**; thus, its stability was also investigated *in vivo*. Mice were treated with **49** and then plasma samples were withdrawn after 1, 6 and 24h. LC-MSMS results showed that the candidate quantity in blood was still considerable and that only after 24h it would have reduced to the 20%.

3.5.3 *In vivo* pharmacological evaluation of compound 49

The aim of the project was the application of new $CysLT_1R$ antagonists/GPBAR1 agonists in the treatment of NAFLD/NASH, so studying the involvement of $CysLT_1R$ and GPBAR1 in a murine model of this condition was mandatory. To do so, the liver gene expression in both

pathways was extensively assessed in a group of patients classified as early and moderate NAFLD/NASH patients.

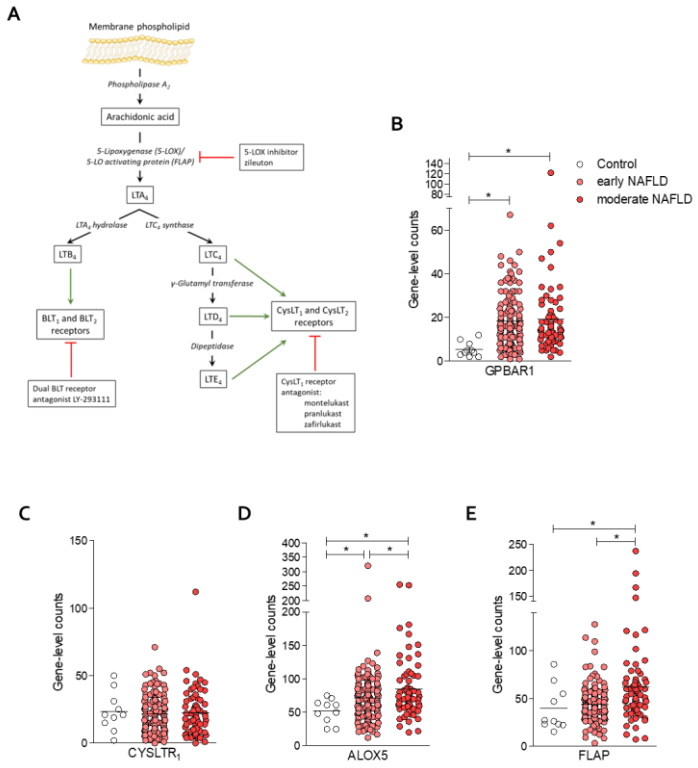

Figure 22. The synthesis of leukotrienes is upregulated in the liver of NAFLD patients. (**A**) Leukotriene synthesis pathway with the enzymes that are involved in each step of the synthesis. (**B-E**) RNA-seq analysis of liver biopsy samples from GSE135251 repository of control, early NAFLD and moderate NAFLD patients. Each dot represents a patient. Gene profile expression of (**B**) GPBAR1, (**C**) CYSLTR1, (**D**) ALOX5, and (**E**) FLAP, *p <0.05.

What emerged from this study was the robust increase in GPBAR1 expression in both early and moderate stages while $CysLT_1R$ expression did not change from that of the healthy liver. Even though $CysLT_1R$ was not upregulated, the enzymes responsible for the biosynthesis of LTs (ALOX5 and FLAP) were overexpressed indeed (Fig. 22).

As for the experimental model, mice fed a High Fat Diet (HFD-F) were chosen as these imitate the Western diet with a high-calorie intake leading to liver damage like that observed in human patients. Compound **49** emerged as the best of all candidates because it presents the right

combination of efficiency, potency, and PK profile. Therefore, compound **49** was fed orally (30 mg/kg) for 54 days to (HFD-F)-fed mice. During the experiment, HFD-F mice gained 32% of their weight in 61 days while the treatment was able to reduce this to a certain extent (Fig 23, panels A, B and C). Compound **49** also determined an increase in insulin sensitivity, observed through an oral glucose tolerance test (OGTT) (Fig. 23, panels D and E).

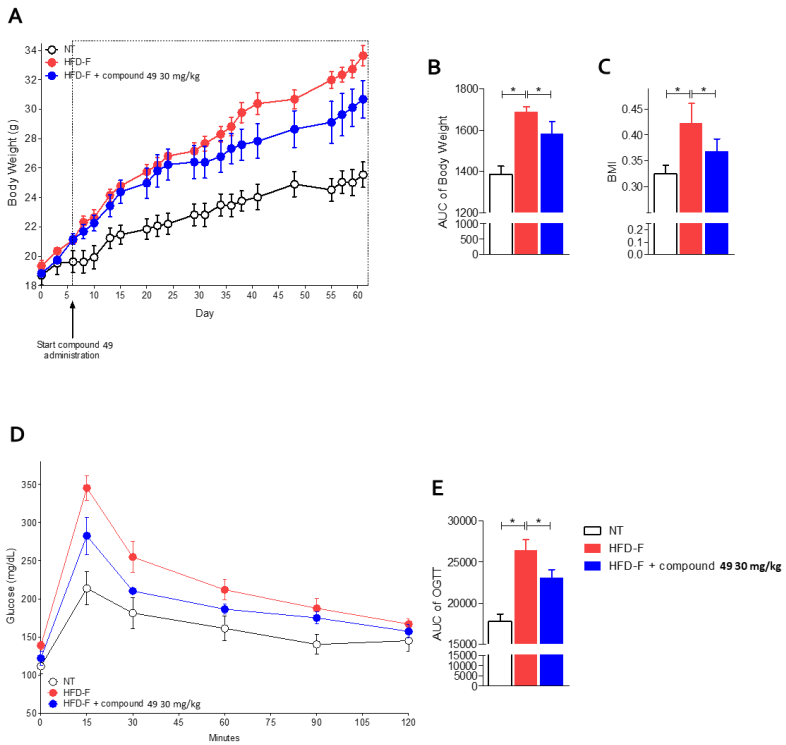

Figure 23. Beneficial effects of compound 49 on body weight gain and insulin sensitivity. C57BL/6 male mice were fed a high-fat diet and fructose (HFD-F) or normal chow diet for 61 days. From day 7 compound 49 was administered by oral gavage at the dose of 30 mg/kg/daily. (**A**) Changes in body weight (%) and (**B**) AUCs of body weight expressed in arbitrary units. (**C**) Body Mass Index (BMI) at the end of the experiment. (**D**) Glucose plasma levels in response to OGTT and (**E**) AUCs of glucose plasma levels expressed in arbitrary units. Results are the mean ± SEM of 5-7 mice per group; *p <0.05.

Decreased levels of AST and ALT in plasma were also observed together with a partial reduction of the proatherogenic profile determined by the HFD.

Histological analysis of the liver tissue was also performed to assess the macroscopic appearance of the damage. HFD mice's liver was bigger while its enlargement was reversed by compound **49**. The reversion of fat vacuoles and hepatocytes ballooning in treated livers was also robust (Fig. 24).

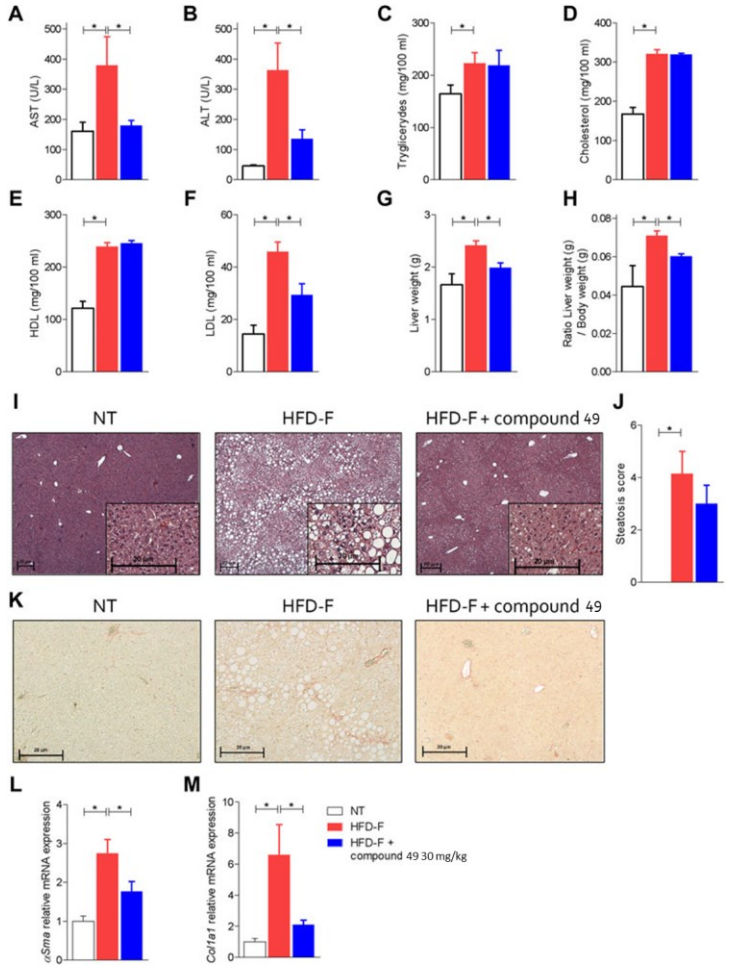

Figure 24. Beneficial effects of compound 49 on liver biochemistry and histopathology. C57BL/6 male mice were fed a high-fat diet and fructose (HFD-F) or normal chow diet for 61 days. From day 7 compound 49 was administered by oral gavage at the dose of 30 mg/kg/daily. Plasmatic levels of (**A**) AST, (**B**) ALT, (**C**) Triglycerides, (**D**) Cholesterol, (**E**) HDL and (**F**) LDL at the end of the study. Macroscopic and microscopic features of the liver: (**G**) liver weight (g), (**H**) ratio between liver weight (g) and body weight (g), (**I**) hematoxylin and eosin (H&E) staining of liver tissues obtained at the end of the study (magnification 4×, insets 10×) with (**J**) steatosis score, and (**K**) Sirius red staining of liver tissues obtained at the end of the study (magnification 10×). Results are the mean ± SEM of 5-7 mice per group; *p <0.05.

The reduction of fibrotic scars was also evident and correlated to decreased expression of pro-fibrogenic genes, αSma and Col1α1.

As for the molecular level, the liver transcriptome was also analysed in HFD-F mice with or without treatment (Fig. 25). The results showed that compound **49** heavily rearranged the transcriptome with the modulation of 647 genes, the most upregulated genes were those involved in fat metabolism like Cfd, Mogat 1 and Me1.

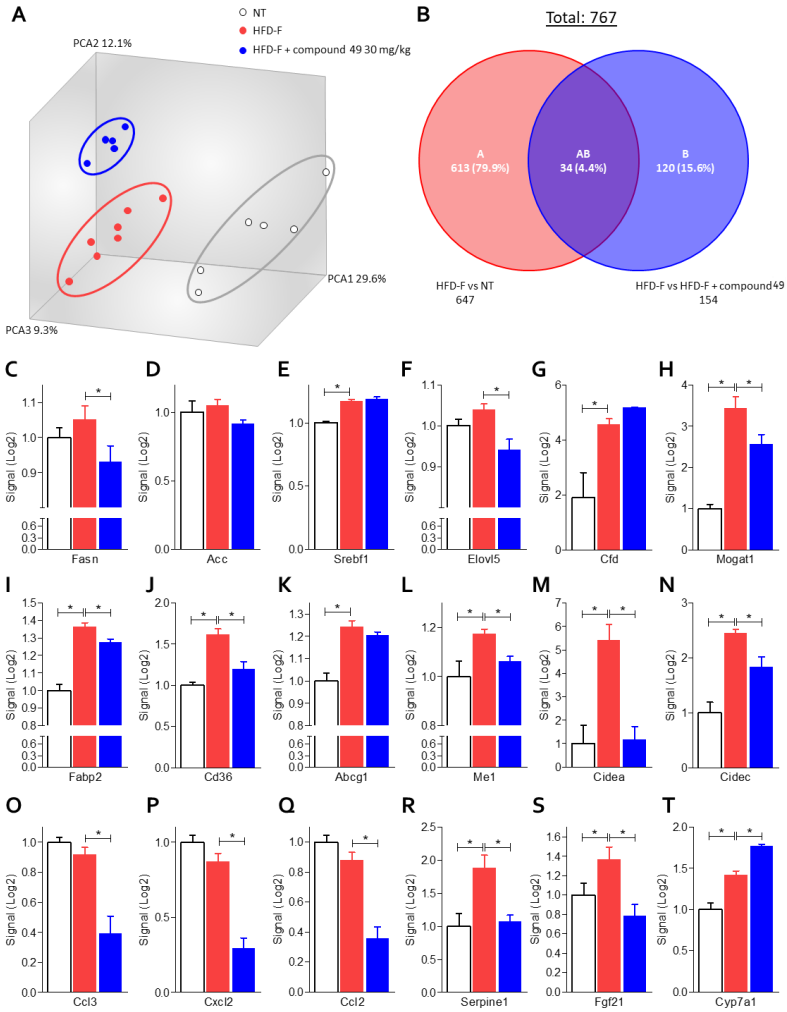

Figure 25. Liver transcriptome analysis of compound 49 in HFD-F fed mice. C57BL/6 male mice were fed a high-fat diet and fructose (HFD-F) or normal chow diet for 61 days. From day 7 compound **49** was administered by oral gavage at the dose of 30 mg/kg/daily. (A) Quantitative β analysis of PCoA that showed a major dissimilarity between the three experimental groups and (B)

Venn diagram of differentially expressed genes showing the overlapping regions between the experimental groups (fold change <−2 or >2, p-value < 0.05). Relative mRNA expression levels extract from RNA-seq analysis of (C) Fasn, (D) Acc, (E) Srebf1, (F) Elovl5, (G) Cfd, (H) Mogat, (I) Fabp2, (J) Cd36, (K) Abcg, (L) Me1, (M) Cidea, (N) Cidec, (O) Ccl3, (P) Ccl2, (Q) Cxcl2, (R) Serpine1, (S) Fgf21 and (T) Cyp7a1. Results are the mean ± SEM of 5-7 mice per group; *p < 0.05.

The treatment with **49** influenced the expression of 154 genes, the most downregulated gene was Ccl3, a chemokine whose levels are found high in NASH patients' liver and serum. Cxcl2, Ccl2 and Serpine 1 were also downregulated together with FgF21, responsible for the liver uptake of fatty acids and lipoproteins. Cyp7a1 expression was also increased with the consequent increase in cholesterol conversion and bile acids synthesis. The treatment with **49** was also able to increase the expression of Pparα, a gene linked to fatty acid oxidation, and Pparγ, a confirmed target for the treatment of NASH. No influence was ever detected on other receptors like GPBAR1, FXR and their genes, or the LTs pathway (Fig. 26).

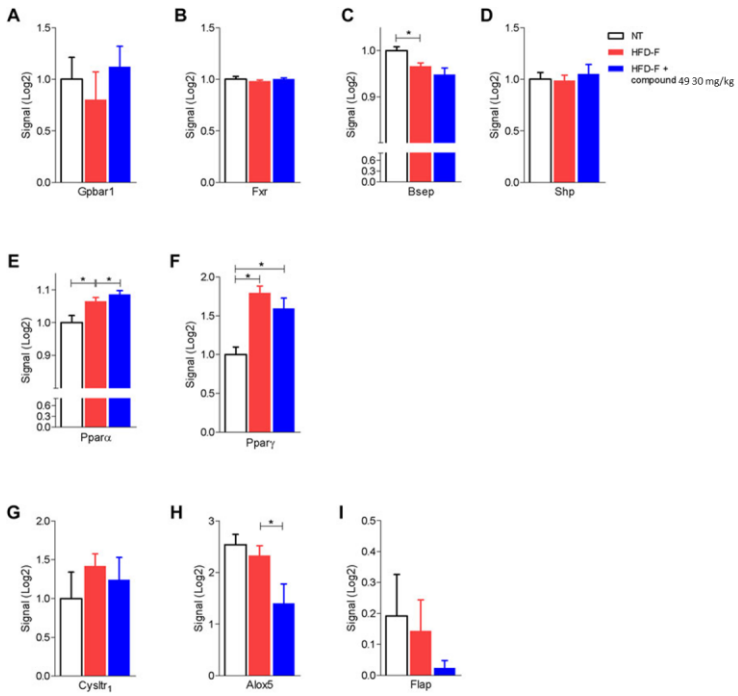

Figure 26. Effects of compound 49 on the liver expression of GPBAR1, FXR, and its target genes and nuclear transcription factors. C57BL/6 male mice were fed a high-fat diet and fructose (HFD-F) or normal chow diet for 61 days. From day 7 compound **49** was administered by oral gavage at the dose of 30 mg/kg/daily. Relative mRNA expression levels extract from RNA-seq analysis

of (A) Gpbar1, (B) Fxr, (C) Bsep, (D) Shp, (E) Pparα, (F) Pparγ, (G) $CysLT_1R$, (H) Alox5, and (I) Flap. Results are the mean ± SEM of 5-7 mice per group; *p < 0.05.

The adipose tissues are greatly intertwined with the energy management processes and present a deep interplay with liver parenchyma. Several hepatic factors were found to modulate the activity of both white and brown adipose tissues.[140]

By implication, the effects of compound **49** on white and brown adipose tissues were studied (Fig. 27).

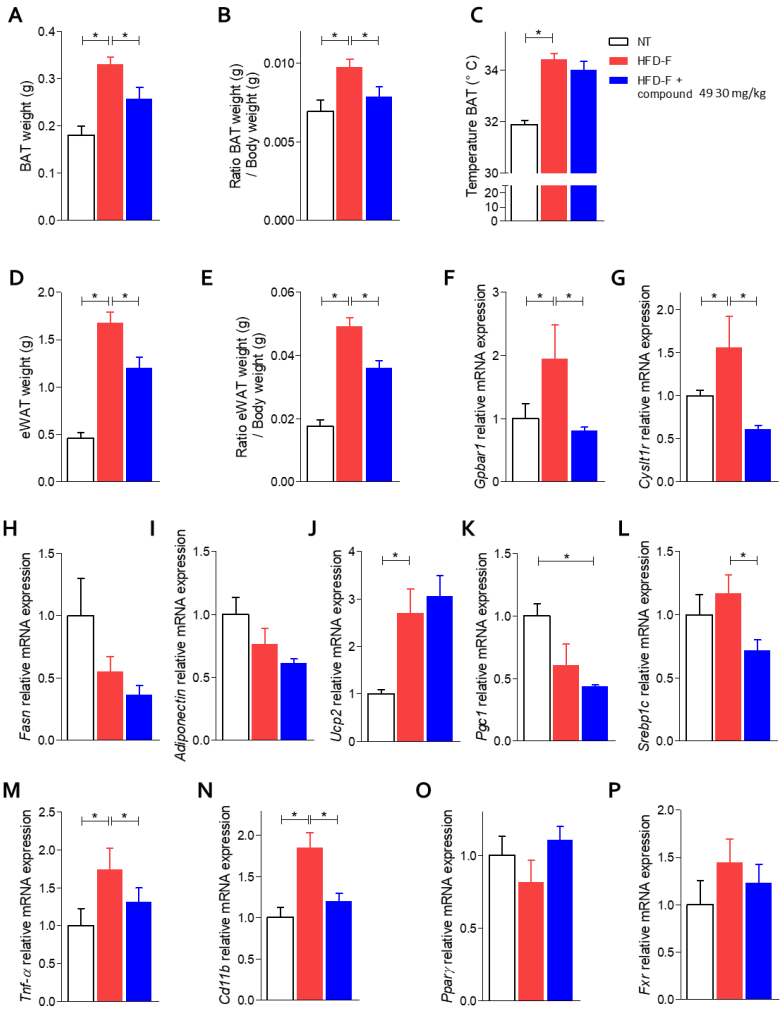

Figure 27. Effects of compound 49 on adipose tissue. C57BL/6 male mice were fed a high-fat diet and fructose (HFD-F) or normal chow diet for 61 days. From day 7 compound **49** was administered by oral gavage at the dose of 30 mg/kg/daily. (A) BAT weight, (B) ratio BAT weight

(g)/body weight (g), and (C) temperature of BAT (°C) on day 51. (D) eWAT weight and (E) ratio eWAT weight (g)/ body weight (g). Relative mRNA expression levels of (F) GPBAR1, (G) CysLT$_1$R, (H) Fasn, (I) Adiponectin, (J) Ucp2, (K) Pgc1, (L) Srebp1c, (M) Tnf-α, (N) Cd11b, (O) Pparγ, and (P) Fxr in eWAT. Results are the mean ± SEM of 5-7 mice per group; *p < 0.05.

The volume of BAT and the ratio of BAT weight/body weight were reduced partially by the treatment. The same effect was observed on the epididymal white fat (eWAT), the mouse counterpart of the visceral fat in humans. The influence on the gene expression in eWAT was investigated and GPBAR1, CysLT$_1$R, Tnf-α and Cd11b were increased by HFD-F and these effects were reversed by compound **49**. Lipogenic genes suffered no changes in their expression while HFD tended to downregulate Pparγ and Pgc1α.

As for the colon, compound **49** also upregulated the expression of Gcg, a gene encoding glucagon-like peptide 1, and the levels of the pro-inflammatory cytokine Il-1β were also decreased (Fig. 28).

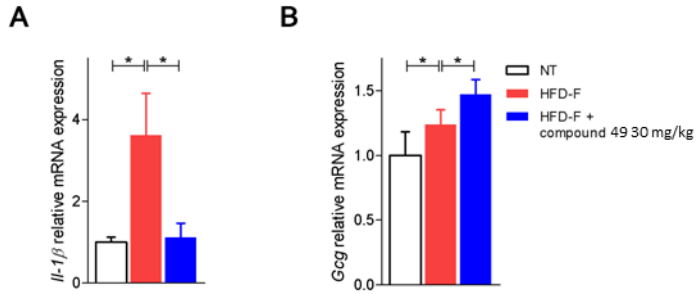

Figure 28. Effects of compound 49 on colon inflammation. C57BL/6 male mice were fed a high-fat diet and fructose (HFD-F) or normal chow diet for 61 days. From day 7 compound **49** was administered by oral gavage at the dose of 30 mg/kg/daily. Relative mRNA expression levels of (A) Il-1β, and (B) Gcg. Results are the mean ± SEM of 5-7 mice per group; *p < 0.05.

3.6 Conclusions

The synthesis and the pharmacological characterization of compound **49** are reported as the first in a class of a novel series of dual $CysLT_1R$ antagonists/GPBAR1 agonists. All the obtained derivatives are easily accessible, using commercially available low-cost starting materials and few synthetic steps with good-to-excellent yields. The structure-activity relationship (SAR) was rationalized thanks to *in silico* and pharmacological analyses. The dual activity was obtained by harnessing the scaffold of a well-characterized, yet discarded, $CysLT_1R$ antagonist, REV5901.

A flat, aromatic spacer connecting the quinoline ring to the ending polar group (i.e., carboxylic or hydroxyl group), like the biphenyl function, is of choice over a flexible spacer (alkyl chain) to maintain $CysLT_1R$/GPBAR1 affinity.

Importantly, the carboxylic group with its negative charge establishes a strong salt bridge interaction with $Arg79^{2.60}$ in the $CysLT_1R$. The same kind of interaction happens with known $CysLT_1R$ antagonists, like pranlukast, whose tetrazole group is bioisostere of the carboxylate group. Such interaction weakens indeed when the carboxylic acid is substituted with an ester or an alcohol group, the same consequence happens when the carboxylic acid is in the para position.

The key residues for the activation of GPBAR1 ($Tyr89^{3.29}$, $Asn93^{3.33}$, $Phe96^{3.36}$, and $Trp237^{6.48}$) are all contacted by compound **49**.

Moreover, an additional H-bond interaction takes place between the carboxylic group in the meta position of **49** with $Ser270^{7.43}$, as seen in other GPBAR1 agonists.[141–144]

Considering the results of the *in vitro* pharmacological and pharmacokinetic assays, the lead compound (**49**) was tested to investigate its efficacy in a preclinical model of NAFLD/NASH.

Compound **49** exerted several positive effects on the used murine model: a reduction of the body gain and the macroscopic liver damage elements together with lower levels of AST/ALT in plasma were observed.

Supporting these phenotypical effects, the liver transcriptome was heavily reshaped during the treatment influencing the expression of 154 genes.

More precisely, several genes involved in lipogenesis and energy metabolism were successfully modulated.

The treatment also largely influenced the production of several pro-inflammatory cyto and chemokines including Ccl3, Ccl2, and Cxcl2.

Furthermore, the regulation of Cyp7a1 was also influenced by **49** in this model of NAFLD[145], a result that is relevant since CYP7A1 is the rate-limiting enzyme in the synthesis of primary bile acids in the liver.[146]

An interesting consequence of HFD in mice is the increased conversion rate of cholesterol into BAs. Thus, cholesterol is excreted more in the stool preventing the process of fat accumulation in the liver. Furthermore, the induction of CYP7A1 is strongly associated with a protective effect towards the liver preventing steatosis, inflammation, and fibrosis.[147]

The effects of the treatment on adipose tissues were also studied. Indeed, compound **49** reduces BAT weight, probably due to the reduction of body weight, and it also determines some changes in the eWAT. Inflammatory genes such as Tnf-α and Cd11b were also negatively modulated, thus resolving the pro-inflammatory nature that is typical in NASH patients.

To sum up, we presented a novel family of dual $CysLT_1R$ antagonists and GPBAR1 agonists endowed with beneficial effects in a murine model of NASH. Genetic and pharmacological profiling of the lead compound of

the series, compound **49**, showed a novel approach for the modulation of multiple targets in the treatment of NASH.

Liver damage can also be caused by external factors, such as exaggerated alcohol consumption or drug misuse. To expand the pharmacological potential of compound **49**, a model of drug-induced liver damage was applied with very promising results.[148]

4 [redacted]

[redacted]

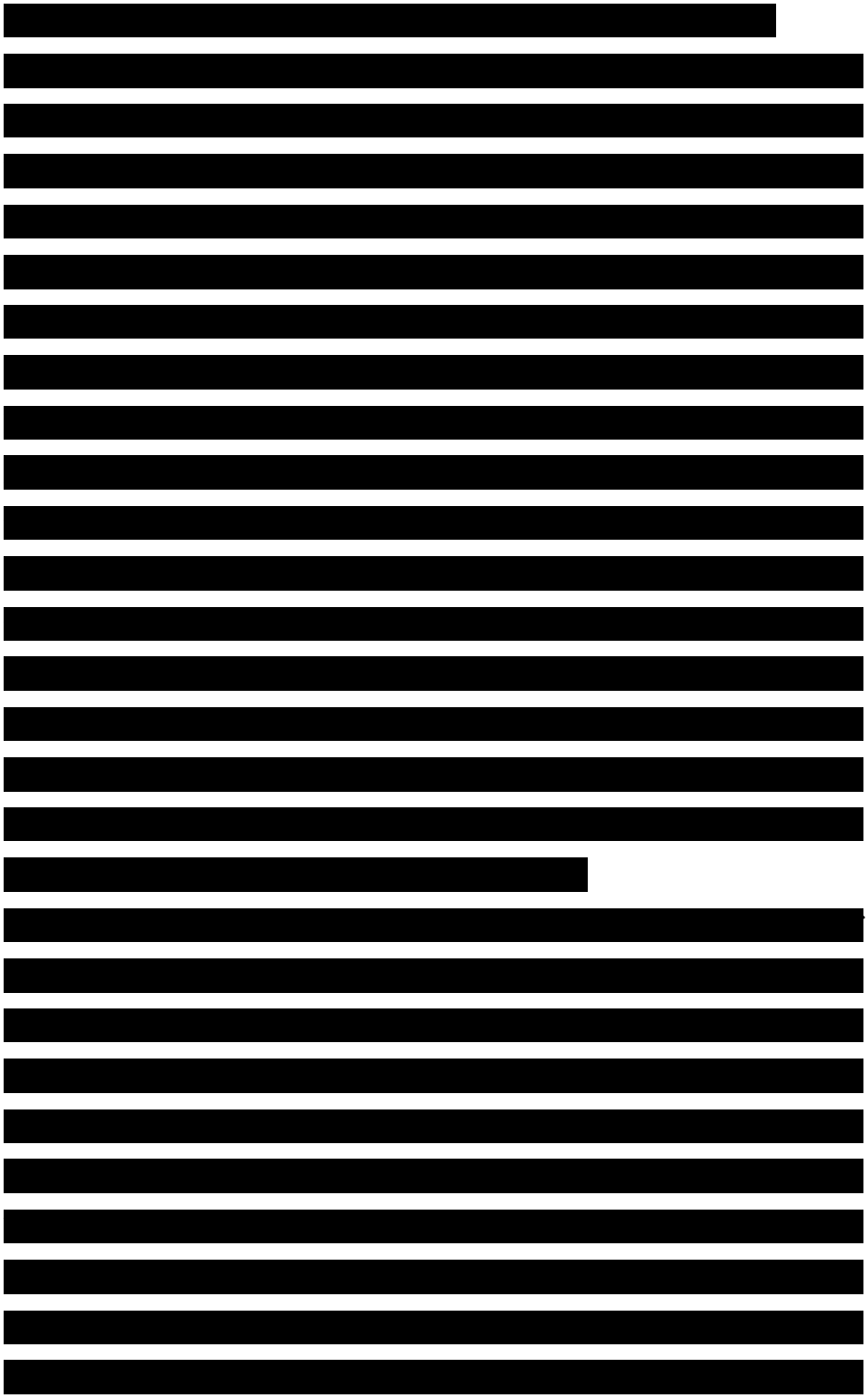

[redacted]

[redacted]

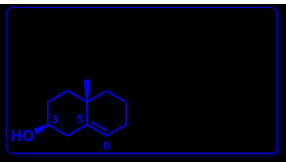
HO
3
5
6

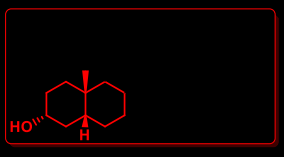
HO
H

[redacted]

[redacted]


HO
O
OH
R2
HO
O
R2
R1

[redacted]

[redacted]

[redacted]

[redacted]

[redacted]

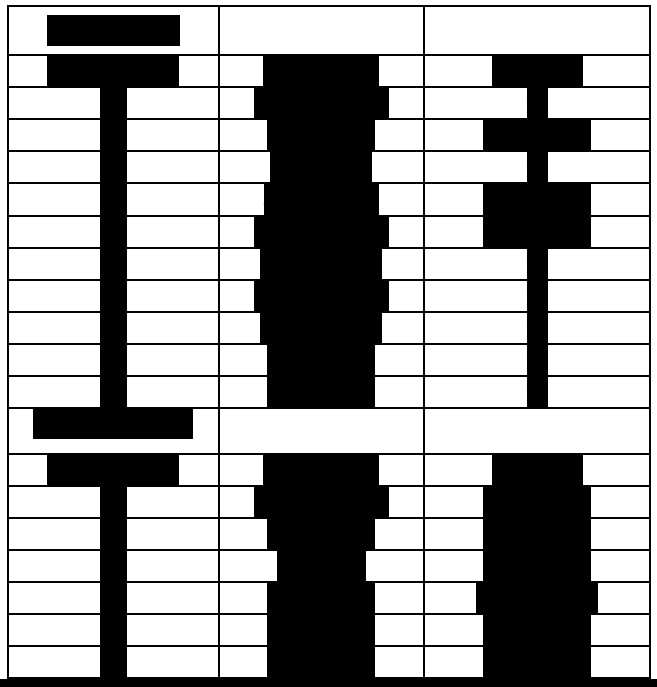

[redacted]

[redacted]

[redacted]

[redacted]

[redacted]

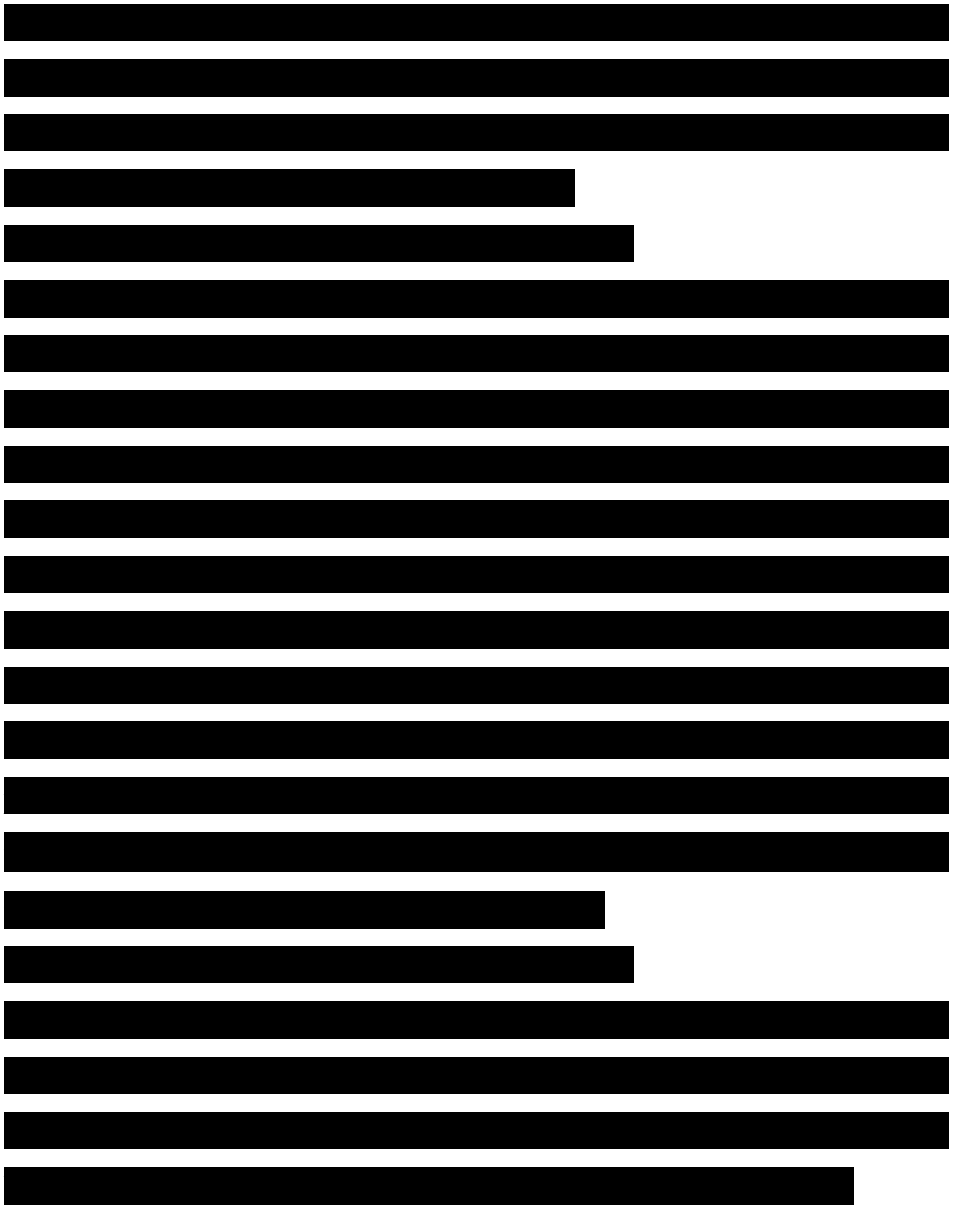

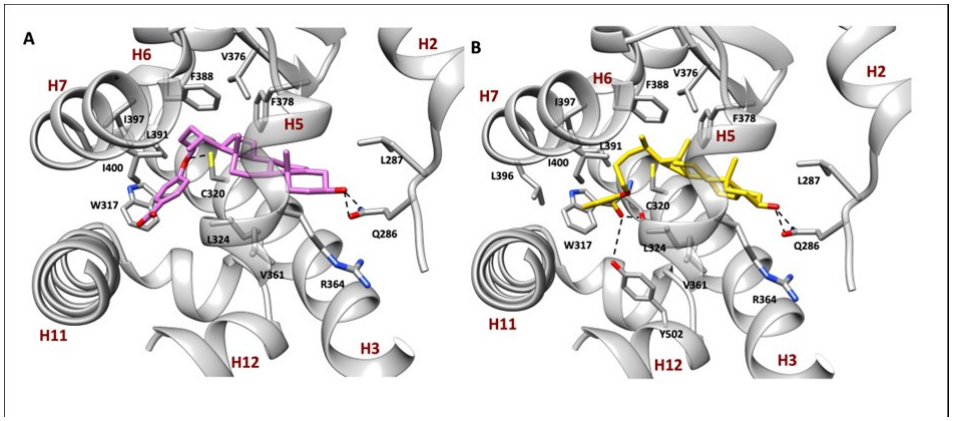
A
H6
V376
H2
H7
F388
F378
I397
H5
L391
L287
I400
W317
C320
Q286
L324
V361
R364
H11
H12
H3
B
H6
V376
H2
H7
F388
I397
F378
H5
L391
L396
I400
L287
C320
W317
Q286
L324
V361
R364
H11
Y502
H12
H3

[redacted]

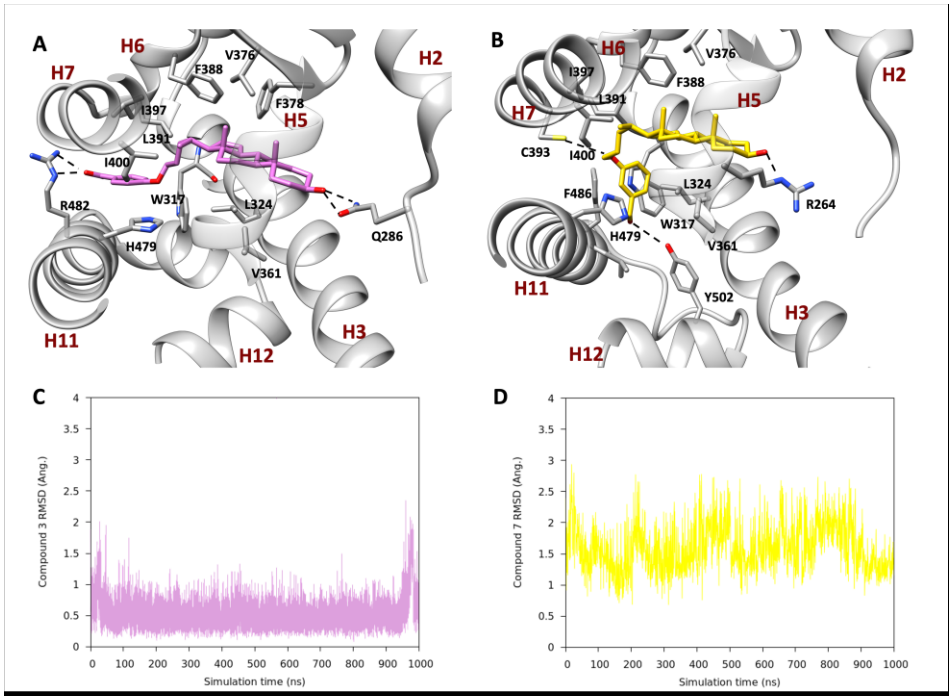
A
H6
H7
V376
F388
H2
I397
F378
H5
L391
I400
W317
L324
R482
Q286
H479
V361
H11
H12
H3
B
H6
V376
I397
F388
H2
L391
H5
H7
C393
I400
L324
F486
R264
W317
H479
V361
H11
Y502
H3
H12
C
Compound 3 RMSD (Ang.)
Simulation time (ns)
D
Compound 7 RMSD (Ang.)
Simulation time (ns)

[redacted]

[redacted]

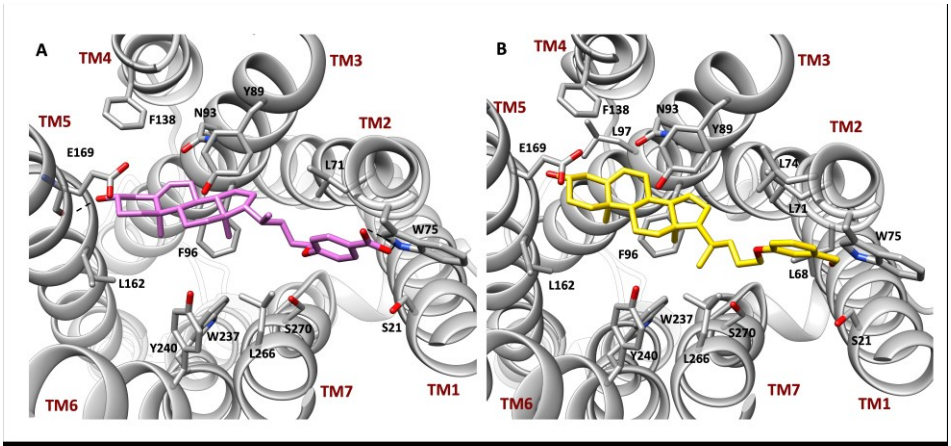

[redacted]

[redacted]

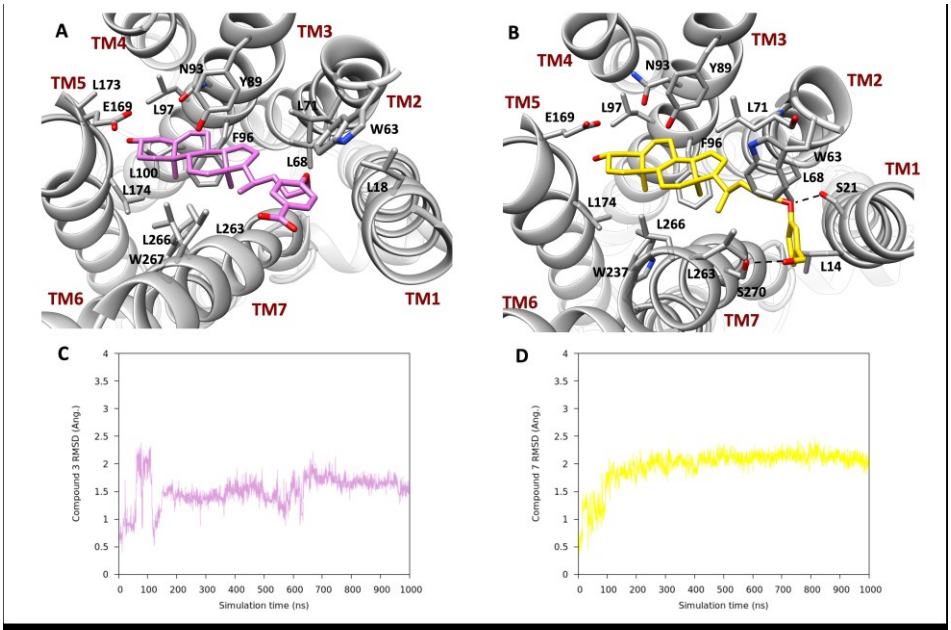
A
TM4
TM3
N93
Y89
TM5
L173
E169
L97
L71
TM2
W63
F96
L68
L100
L174
L18
L263
L266
W267
TM6
TM7
TM1
B
TM3
TM4
N93
Y89
TM2
TM5
E169
L97
L71
F96
W63
TM1
L68
S21
L174
L266
W237
L263
L14
S270
TM6
TM7
C
Compound 3 RMSD (Ang.)
Simulation time (ns)
D
Compound 7 RMSD (Ang.)
Simulation time (ns)

[redacted]

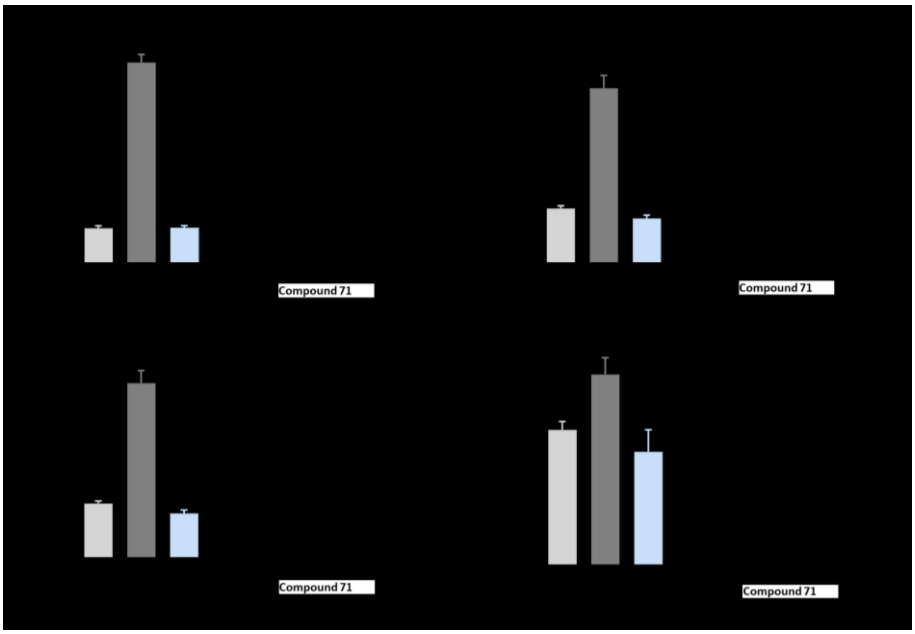

[redacted]

[redacted]

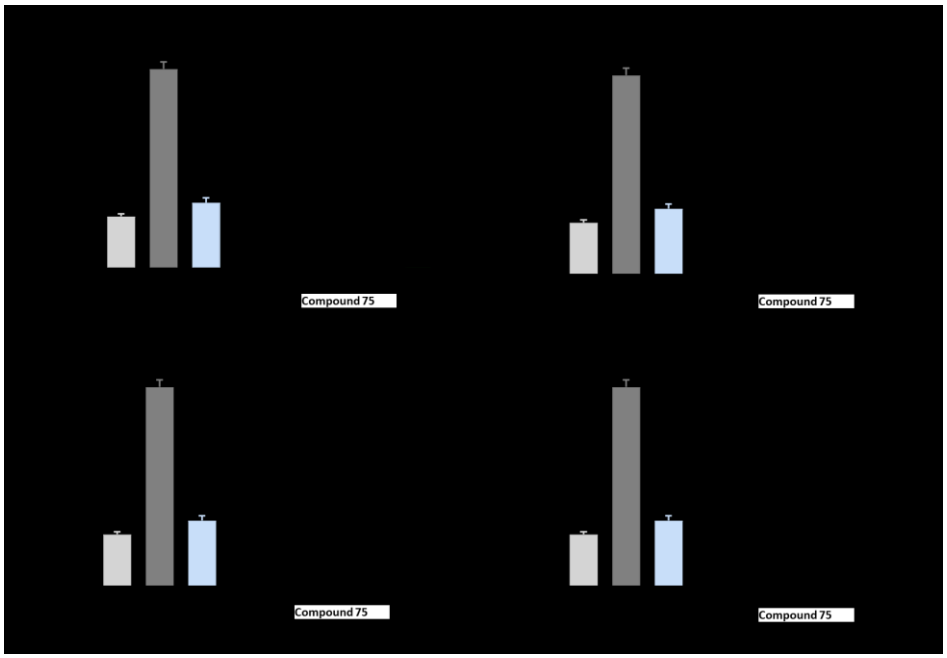

[redacted]

[redacted]

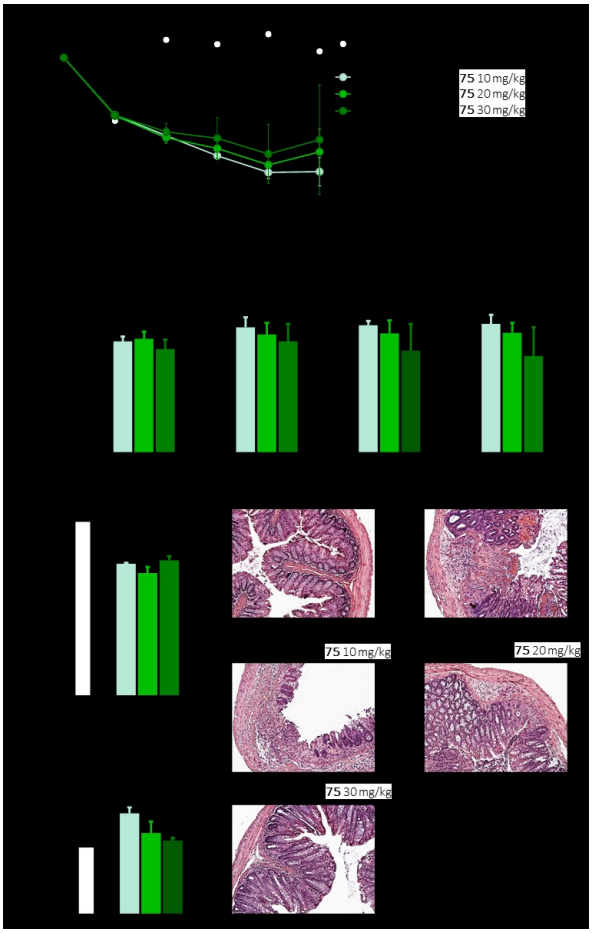

[redacted]

[redacted]

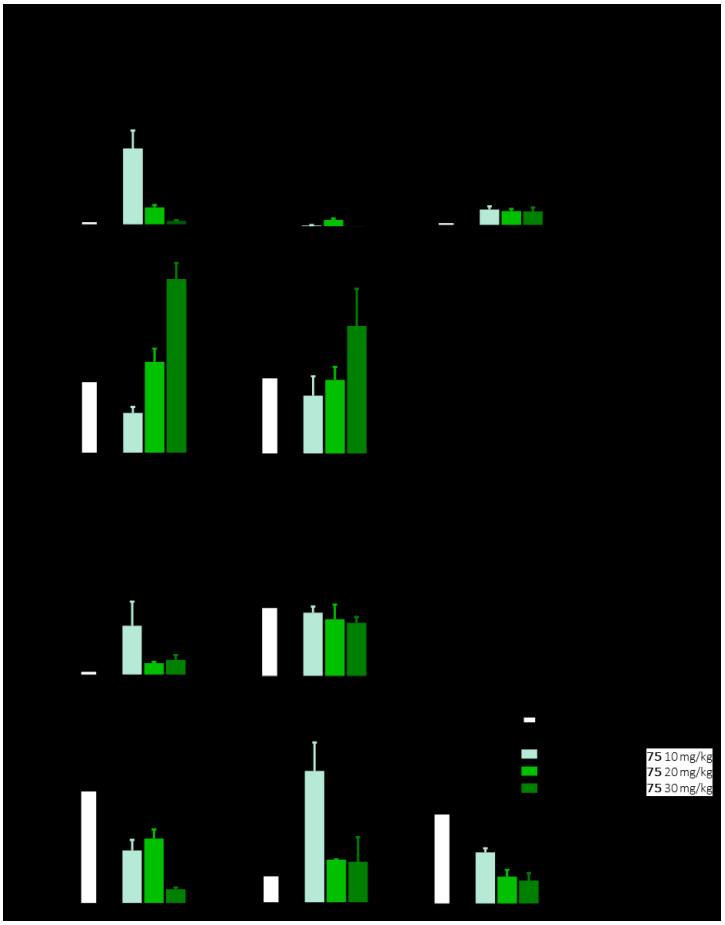

[redacted]

[redacted]

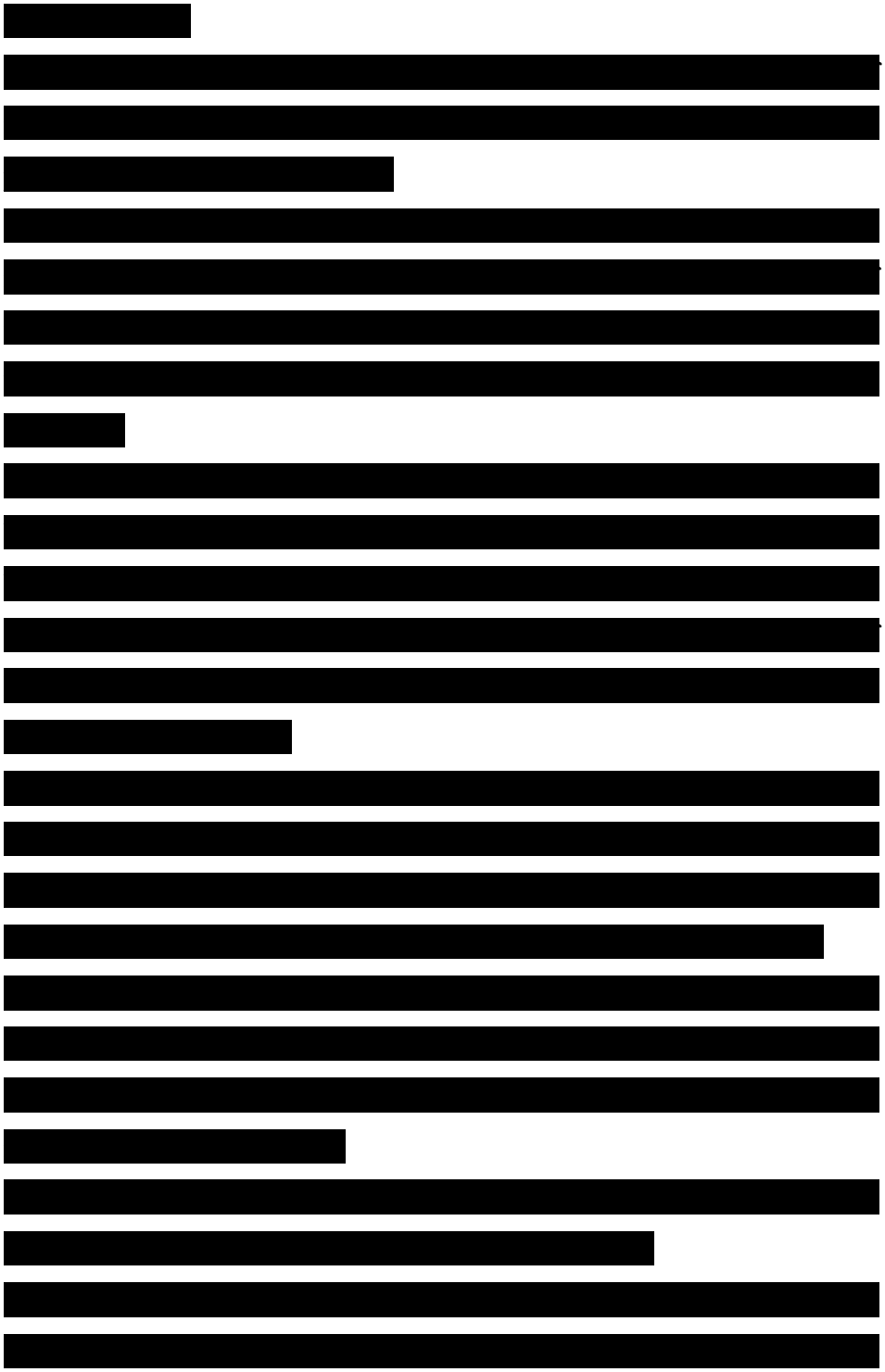

[redacted]

6. Bile acid derivatives as potent ACE2 activators

6.1 ACE2, the cell entry receptor for SARS-CoV-2

In the past decades, several waves of pandemics have hit humankind killing millions of people and exhausting the healthcare systems. Among all of these are severe acute respiratory syndrome (SARS), Middle East respiratory syndrome (MERS) and coronavirus disease 19 (COVID-19), the latest.

These outbreaks were all caused by viruses belonging to the same family of *Coronaviridae* (SARS-CoV, MERS-CoV and SARS-CoV-2).[172]

SARS-CoV-2 is a positive-sense single-stranded RNA virus, its exact origin is unclear, but the sequencing studies determined a zoonotic origin. In particular, the actual hypothesis is that a spillover event has happened at some point between a reservoir population, probably some species of bats, to a mammal carrier from which then the virus arrived in humans.

SARS-CoV-2 emerged with heavy contagiousness as its rapid spreading indeed caused the declaration of a global pandemic by the WHO on March 11th, 2020.

The total number of deaths nowadays is about 6 million people (https://github.com/CSSEGISandData/COVID-19). The lack of proper therapeutical strategies together with the initial inexperience with the disease outcomes strongly prompted the need to identify efficient remedies.

The SARS-CoV-2 virus has a typical Coronavirus structure composed of four structural proteins, called S (spike), E (envelope), M (membrane) and N (nucleocapsid). The first three (S, E, and M) form the external envelope of the virus while the N proteins bind the RNA holding it together.[173]

The Spike (S) proteins were proven essential to the transmission and replication of the virus. Each one forms homotrimers protruding from the

virus surface and presents two functional subunits, S1 and S2. The S1 subunit is responsible for the interaction with the angiotensin-converting enzyme 2 (ACE2) of the human host cell and is made from two subdomains, the N-terminal domain (NTD) and the C-terminal domain (CTD). Spike protein's CTD presents the receptor binding domain (RBD) responsible for binding ACE2.[174,175] On the other hand, S2 mediates the membrane fusion to allow the entrance of the viral RNA into the host cell. For these events to happen, the Spike protein needs to be activated by two proteolytic cleavages: the first between the two subunits, S1 and S2 and the second one on S2'.[176] Such cleavage events also called "priming" are due to the proteases expressed on the human cell surface, the main protease, responsible for the activation of S protein, is Transmembrane protease serine 2 (TMPRSS2); other proteases able to activate the Spike protein are the Cathepsins, included in the endolysosomes. The virus can enter the host cell directly by fusing into the membrane or indirectly, by being endocytosed and then fusing into the membrane of the endocytosome.

The importance of the interaction between Spike protein and ACE2 is glaring and targeting ACE2 with an agonist represents another possibility to displace the spike/ACE2 interaction and disrupt the virus attack.

The angiotensin-converting enzyme 2 (ACE2)[177,178] is a metallocarboxypeptidase, as such it can hydrolyse single amino acids from the C-terminus of the substrate[179] and exists in two forms: the membrane form (mACE2) is fixed on the surface of the cell and functions as the entry receptor for SARS-CoV-2 whereas the soluble form (sACE2) freely circulates into the organism. ACE2 is part of the renin-angiotensin-aldosterone (RAAS) system, the main blood pressure control axis. Any hypotensive stimulus induces the release of renin which converts

angiotensinogen into angiotensin I. Ang I is then hydrolysed by the angiotensin-converting enzyme (ACE) to produce angiotensin II.

Ang II binds to the Ang II type I receptor (AT_1) causing sodium and water retention, vasoconstriction, heart hypertrophy, inflammation, and cell proliferation. The role of ACE2 in RAAS is to counterbalance the effects of Ang II and ACE activity. Indeed, ACE2 converts Ang II into angiotensin-(1-7), therefore, lowering the pro-inflammatory and hypertensive effects of Ang II. Moreover, Ang-(1-7) binds *Mas* G protein-coupled receptor (*Mas*R) whose activation has the complete opposite effects of AT_1R, such as vasodilation, natriuresis, and anti-inflammatory effects.[180–183]

Due to the variety of different symptoms in COVID-19 patients, the expression of ACE2 in the different districts of the body has been the focus of life sciences research lately.[184,185] Even though the analysis of the transcriptome revealed a low expression of ACE2 in the lungs, the respiratory complications determined by COVID-19 infection are due to the massive induction of the production of pro-inflammatory cytokines which in turn could upregulate ACE2.[186,187] A large debate has been going on since the identification of the infection mechanism about the increased lethality of COVID-19 in patients suffering from hypertension, diabetes, cardiovascular diseases, or obesity.[188]

A proposal to justify the higher lethality of the infection in hypertensive patients was that hypertension treatment with ACE-inhibitors or Ang II type I receptor blockers (ARB) is somewhat linked to indirect upregulation of ACE2; even though the mechanism has not been yet understood, one could hypothesise that these drugs may induce accumulation of either Ang I or II which in turn stimulates the expression of ACE2 to rebalance the RAAS. *In vitro* models of infection have shown that ACE2 overexpression

can facilitate the entrance of the virus into the cells, thus increasing its infectivity. On the other hand, there are findings proposing that ACEi and ARBs use indeed determines an accumulation of Ang I and II which causes an increased production of Ang-(1-7) whose cardioprotective and anti-inflammatory activity have been demonstrated. What is undeniable, however, is that ACE2 is the key cell entry protein for SARS-CoV-2.[189] The conclusive speculation could be that once COVID-19 inflammation has established, a downregulation of ACE2 follows thus decreasing the protective and beneficial effect of the production of Ang-(1-7). In the end, the amount of scientific data regarding these correlations has not been considered enough to suggest the interruption of drug therapy in hypertensive patients.[190,191]

Furthermore, ACE2 can also withstand a proteolytic cleavage by a disintegrin and metalloproteinase (ADAM17 also known as TACE, tumour necrosis factor-α-converting enzyme) or TMPRSS2.[192,193]

The binding of Spike protein to mACE2 activates TACE which cleaves the enzyme into its soluble form, sACE2. The latter is still able to bind Spike protein and then convey the virus into the cells. This interaction is still under study and not much has been elucidated so far other than inspiring the possibility of administering an exogenous sACE2 to catch the Spike proteins and prevent the virus internalisation.

Another possible approach could be the identification of ACE2 activators which would potentially increase the beneficial effects of the ACE2/Ang-(1-7)/*Mas*R axis.[194]

It is of utter importance to highlight that identifying ACE2 activators would not only have a potential application in COVID-19 therapy but also in the large variety of cardiovascular diseases which are one of the most common conditions in the whole world.

6.2 Project presentation

Few attempts to identify ACE2 activators have been made so far and from these diminazene aceturate (DIZE) has been identified as an ACE2 activator.[194,195]

This compound is used as an anti-trypanosomiasis veterinary drug, but it proved to activate ACE2 in several animal models of hypertension, liver injury, kidney disease and myocardial infarction.[196–200]

DIZE was also able to revert inflammatory conditions in an NF-κB-dependent fashion. Even though it has been proposed as a beneficial agent for COVID-19 treatment, DIZE's cytotoxicity at the employed therapeutical doses hampered any further advance in the clinical studies.[201,202]

The increased availability of 3D structures of ACE2 in the Protein Data Bank (PDB) has made it possible to perform structure-based drug discovery (SDD) aiming at the identification of ACE2 activators.

Engaging SDD on the basis that some endogenous bile acids (BAs) may disrupt Spike protein/ACE2 interaction, an in-house library of compounds, all derivatives of ursodeoxycholic acid (UDCA), was analysed *in silico* and then *in vitro* to assess and better understand the structural characteristics that are needed to induce the activation of the enzyme.

6.3 Synthesis of UDCA derivatives

The in-house library was planned to include derivatives with the typical tetracyclic core of steroids which was differently substituted (Fig. 40). The varied positions in the steroidal core were:

1) The hydroxyl groups both at C-3 and C-7 with different configurations
2) The ethyl chain at C-6 with different configurations
3) The length and substituents of the side alkyl chain at C-17

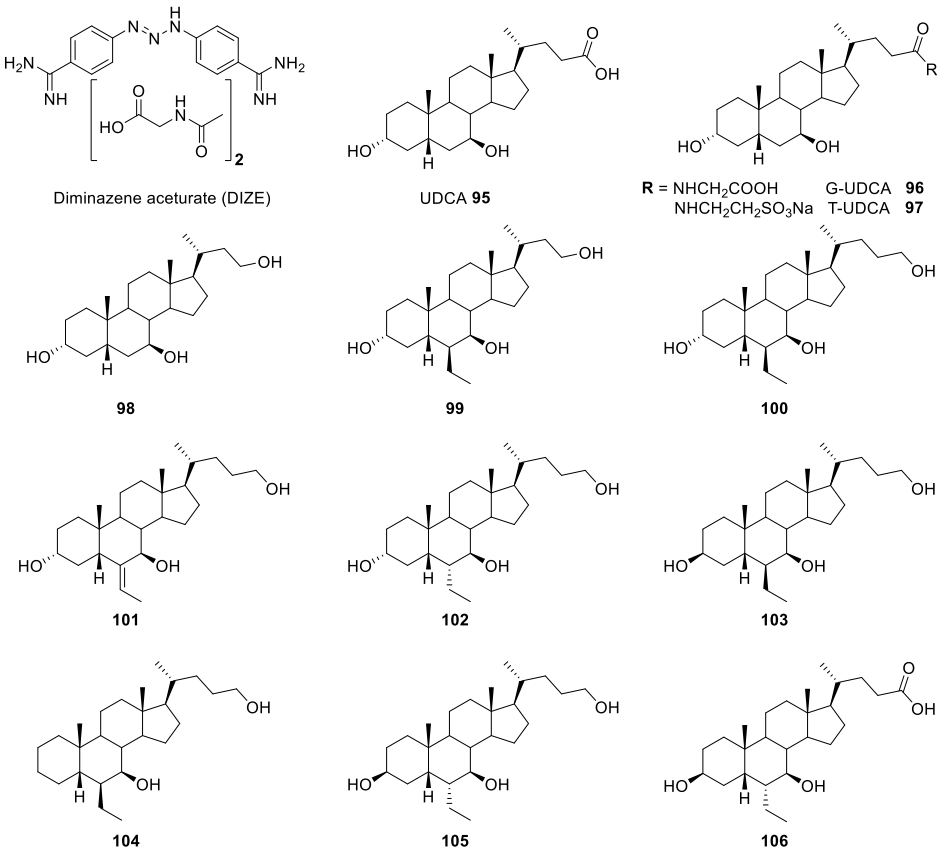

Figure 40.

Compounds **95** (ursodeoxycholic acid), **96** and **97** are secondary bile acids which are produced in the human organism and are commercially available and were used as purchased. All the others are semisynthetic derivatives of UDCA.

The synthesis of compound **98** started using the commercially available UDCA (Scheme 8).

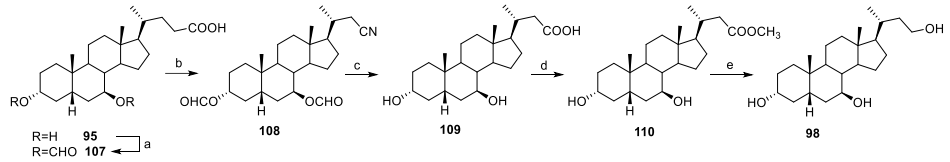

Scheme 8. *Reagents and Conditions:* a) HCOOH, $HClO_4$, quantitative yield; b) TFA, trifluoroacetic anhydride, $NaNO_2$, 97%; c) KOH 30% in MeOH/H_2O 1:1 v/v; d) p-TsOH, MeOH dry, 96% over two steps; e) $LiBH_4$, MeOH dry, THF, 0 °C, 94%

UDCA diformylation was followed by the Beckmann degradation performed by treating with $NaNO_2$ and trifluoroacetic anhydride in trifluoroacetic acid. The corresponding nitrile **108** was then heated with a 30% w/w KOH aqueous solution to remove the formyl groups and hydrolyse the nitrile into the carboxylic acid **109**. Then, a Fisher esterification followed by reduction with $LiBH_4$ afforded the final derivative **98**.

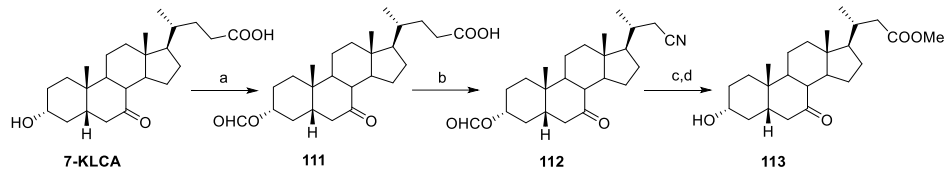

Scheme 9. *Reagents and conditions:* a) HCOOH, $HClO_4$; b) TFA, trifluoroacetic anhydride, $NaNO_2$; c) KOH 30% in MeOH/H_2O 1:1 v/v, 88% over three steps; d) p-TsOH, dry MeOH, 66%

Compound **99** was obtained with the same first 4 synthetic steps employed for compound **98** but starting from 7-ketolithocholic acid (7-KLCA), another commercially available secondary bile acid (Scheme 9). The final methyl ester **113** was then subjected to simultaneous trimethylsilyl (TMS) protection of the C-3 OH group and the formation of a silyl enol ether. The latter was used for an aldolic condensation with acetaldehyde and BF_3 diethyl etherate with the TMS deprotection at the same time to afford the intermediate **114** (Scheme 10).

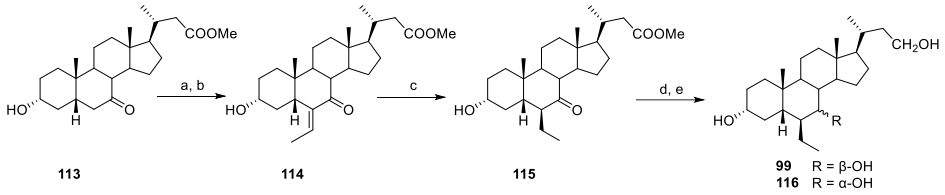

Scheme 10. *Reagents and conditions:* a) DIPA, n-BuLi, TMSCl, dry TEA, dry THF, -78 °C; b) acetaldehyde, $BF_3(OEt)_2$, CH_2Cl_2, -78 °C, 60% over two steps; c) H_2, $Pd(OH)_2/C$, THF/MeOH 1:1, quantitative yield; d) $NaBH_4$, dry MeOH, 0 °C; e) $LiBH_4$, dry MeOH, dry THF, 0 °C, 77% over two steps.

The heterogeneous catalytic hydrogenation of the double bond with palladium hydroxide on carbon afforded only the β-ethyl derivative **115**. Treating intermediate **115** with an excess of $NaBH_4$ in methanol and then performing a LiBH4 reduction on the crude reaction to secure the reduction of the methyl ester on the side chain, furnished the corresponding triol with both configurations at C-7 (compounds **99** and its C-7 epimer **116** as by-product).

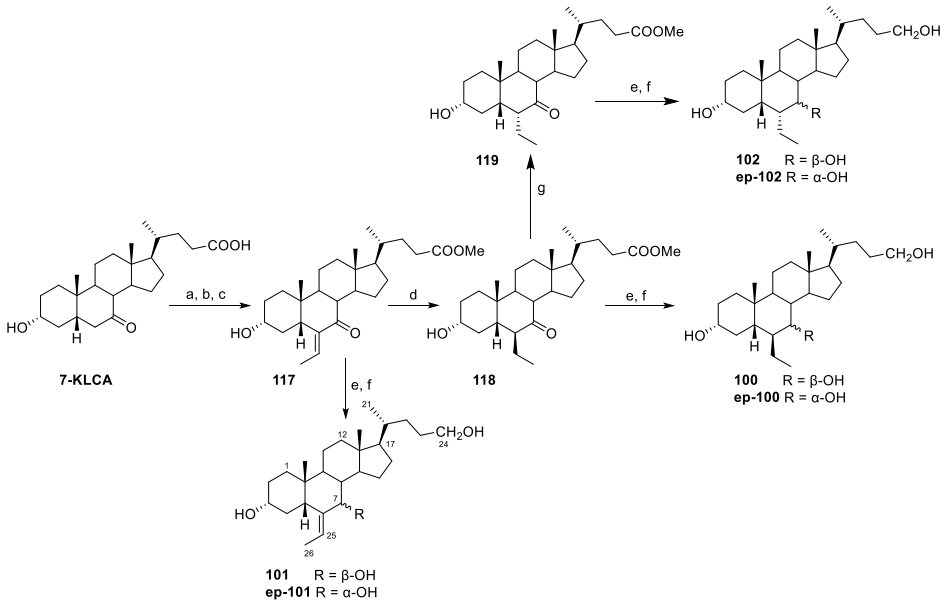

Scheme 11. *Reagents and conditions:* a) p-TsOH, dry MeOH, 99%; b) DIPA, n-BuLi, TMSCl, dry TEA, dry THF, -78 °C; c) acetaldehyde, $BF_3(OEt)_2$, CH_2Cl_2, -60 °C, 55% yield over two steps; d) H_2, $Pd(OH)_2$, THF/MeOH 1:1, quantitative yield; e) $NaBH_4$, dry MeOH, 0 °C; f) $LiBH_4$, MeOH, dry THF, 0 °C; g) MeONa in dry MeOH.

The synthesis of compounds **100**, **101** and **102** was also performed starting from 7-KLCA (Scheme 11). On this, a Fisher esterification was carried out followed by the formation of the silyl enol ether used afterwards in an aldolic condensation with acetaldehyde to afford **117**. Heterogeneous hydrogenation of **117** afforded the intermediate **118** whose $NaBH_4$ treatment in methanol afforded extensive C-7 epimerization and partial reduction at the C-24 methyl ester group. The latter was then completely reduced by $LiBH_4$ reduction. The resulting mixture contained 6β-ethyl derivatives **100** and its epimer at C-7 in a 7:3 ratio, separated by HPLC.

Intermediate **117** was also directly reduced first with $NaBH_4$ to afford the C-7 alcohol derivative and then with $LiBH_4$ to produce the final allyl alcohol **101** (85% yield over two steps).

On the other hand, intermediate **118** was epimerised at C-6 by treatment with a solution of sodium methoxide in methanol to give **119** with a quantitative conversion. Finally, derivative **102** was derived with two consecutive reduction steps on **119**, as described for **117**.

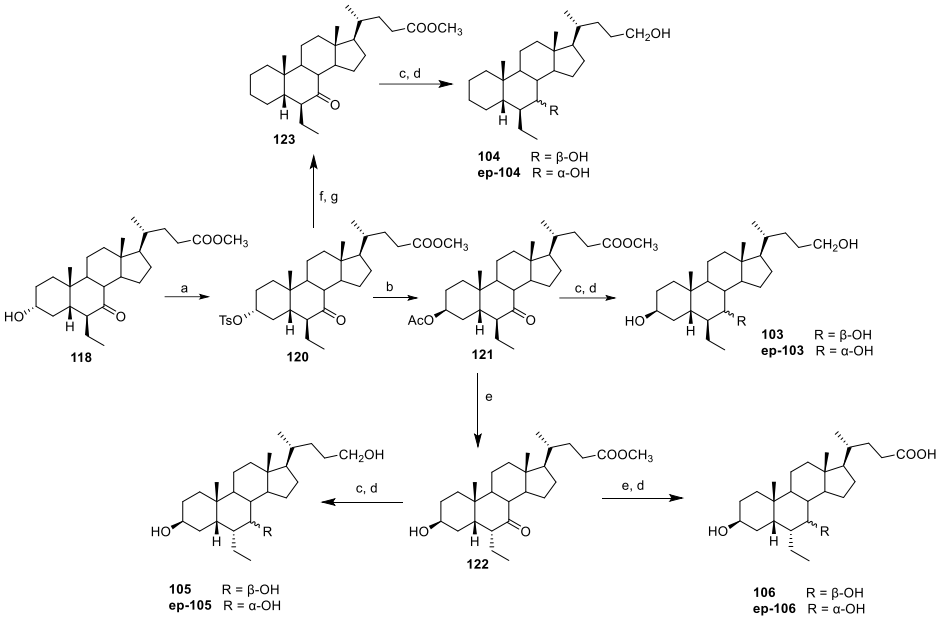

Scheme 12. *Reagents and conditions:* a) p-TsCl, dry pyridine; b) AcOK, DMF/H_2O 5:1, 74% yield over two steps; c) $NaBH_4$, dry MeOH, 0°C; d) $LiBH_4$, dry MeOH, dry THF, 0°C; e) NaOH, MeOH/H_2O 1:1; f) LiBr, Li_2CO_3, DMF; g) H_2, Pd/C, THF, 88% yield over two steps.

The synthesis of the last four derivatives (**103**, **104**, **105** and **106**) has a common intermediate, the ester **118**, whose synthesis has already been described above (Scheme 12). Apart from compound **104**, all derivatives feature a 3-β-OH configuration which was obtained by activating **118** with tosyl group at C-3 and then substituting it with potassium acetate. The resulting 3-O-acetyl derivative **121** was directly treated with prolonged excess of $NaBH_4$ to reduce the ketone at C-7 and then with $LiBH_4$ to afford the final triol **103** and its epimer. Compound **121** was also treated with a solution of sodium methoxide in methanol to induce quantitative epimerisation of the ethyl group at C-6. The 6-α-ethyl derivative **122** was equally treated with $NaBH_4$ and then with $LiBH_4$ to produce compound **105** together with its epimer.

On the other hand, to afford the corresponding carboxylic acid, compound **122** was first hydrolysed with sodium hydroxide and then a reduction with lithium borohydride was carried out to furnish **106**. The 3-O-tosyl

intermediate **120** was treated with LiBr and Li_2CO_3 in DMF to carry out an elimination. The following heterogeneous hydrogenation of the elimination products afforded the intermediate **123** which was turned into the final triol **104** with the same double reduction protocol already employed.

6.4 Virtual screening analyses

To assess the interaction of the putative ligands with ACE2, the docking simulations were performed using a 3D model of the X-ray structure of ACE2 in the open conformation (PDB ID 1R42).[203] The region of ACE2 that was selected to carry out the simulations was the hinge-bending region, already suggested as the binding site of ACE2 activators.[194,195] The structures of hydroxyzine, minithixen, DIZE and xanthenone, known ACE2 activators, were also included in the virtual screening. The results revealed that most of the steroidal derivatives have very promising docking scores, in some cases higher than the already known activators (Table 6).

Table 6. AutoDock4 Docking Scores (ADscore), Enzymatic Activity, and Inhibition of ACE2/Spike Interaction of the Tested Bile Acid Derivatives

Compound	ADscore (Kcal/mol)	ACE2 activity[a]	Spike/ACE2 binding inhibition (%)[b]
DIZE	-6.44	141.04 ± 2.73	n.a.
95	-8.37	102.23 ± 9.1	45.3 ± 2.23[c]
96	-8.58	108.34 ± 10.7	21.3 ± 0.63[c]
97	-8.11	105.77 ± 6.98	42.4 ± 3.83[c]
98	**-8.61**	**140.13 ± 6.94**	**10.8 ± 6.4**
99	**-8.25**	**114.24 ± 1.19**	**39.9 ± 7.25**
100	-9.34	109.83 ± 12.99	30.8 ± 1.98[c]
101	-9.42	105.01 ± 8.7	28.4 ± 8.02
102	**-9.08**	**114.33 ± 1.25**	**40.8 ± 5.84**
103	**-8.98**	**141.28 ± 7.3**	**3.8 ± 1.9**
104	-9.16	102.74 ± 7.7	28.2 ± 6.5
105	-9.07	98.82 ± 11.95	18.9 ± 7.46
106	-8.43	116.37 ± 3.75	32.9 ± 3.92

[a]Effect on ACE2 activity of compounds tested at 10 μM, referred to the activity in the absence of any compound (100). Results are expressed as mean ± standard error. *$p < 0.05$ vs Data are mean ± SE, n = 3. [b]Inhibition of Spike-RBD/ACE2 Binding for each compound tested at 10 μM, expressed as % ± SE. [c]Data was taken from ref.[204]

All compounds shared similar binding poses to the hinge-binding region of ACE2, reaching out to Lys94, Leu95, Glu98, and Glu102 residues from the helix α3 of subdomain I and to Tyr202, Asp206 residues from helix α7, to Val209, Asn210 residues from helix 3_{10} H3 and finally to Pro565 and Trp566 from Helix α19, all part of the subdomain II (Fig. 41).

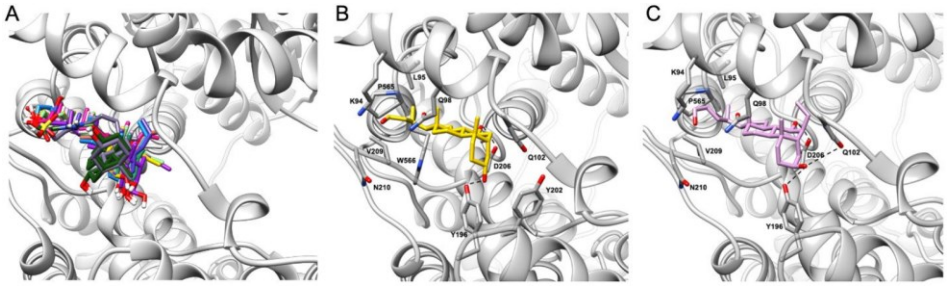

Figure 41. Graphical representation of the binding mode of the best docking poses. (A) Superimposition of the best docking pose for all the compounds in reported **Table 6**: (B) and (C) details of the best docking pose of **98** (gold sticks) and **103** (light-violet sticks), respectively. The interacting residues of the receptor are shown in grey sticks and labelled. Oxygen atoms are depicted in red and nitrogens in blue. Protein receptors are represented as grey cartoon. Hydrogens are omitted for the sake of clarity, while H-bonds are displayed as dashed black lines.

6.5 *In vitro* activity assays

To substantiate the promising results of the virtual screening, all compounds were tested to assess their activity on ACE2. The assay was carried out employing an ACE2 Inhibitor Screening Assay kit and the reference activator was DIZE. All the derivatives were able to activate ACE2 with compounds **98** and **103** being endowed with similar efficacy to DIZE (Table 6, Fig. 42).

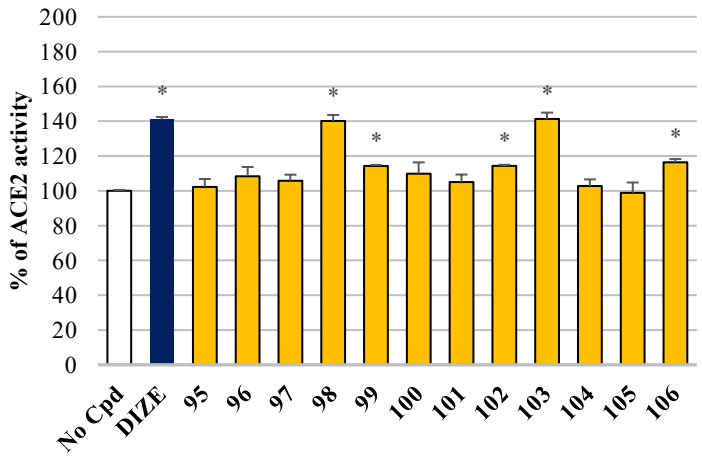

Figure 42. ACE2 activity assay. Compounds **95-106** were tested on a cell-free enzymatic assay to screen activators of ACE2 activity. Dize was used as positive control. The assay is designed to measure the exopeptidase activity of ACE2, it utilizes the ability of an active ACE2 to cleave a synthetic fluorogenic substrate to release a free fluorophore. The released fluorophore is quantified using a fluorescence microplate reader. Fluorescence values of activity in absence of any compound were arbitrarily set to 100%. Results are expressed as mean ± standard error. *$p < 0.05$ vs No Cpd.

The selected compounds were also tested in a Spike/ACE2 Inhibitor Screening Assay Kit to assess whether they could disrupt the interaction between the RBD of Spike protein and ACE2. Interestingly, compounds **99** and **102** were able to inhibit the Spike RBD/ACE2 interaction in a concentration-dependent fashion up to 40% (Table 6, Fig. 43).

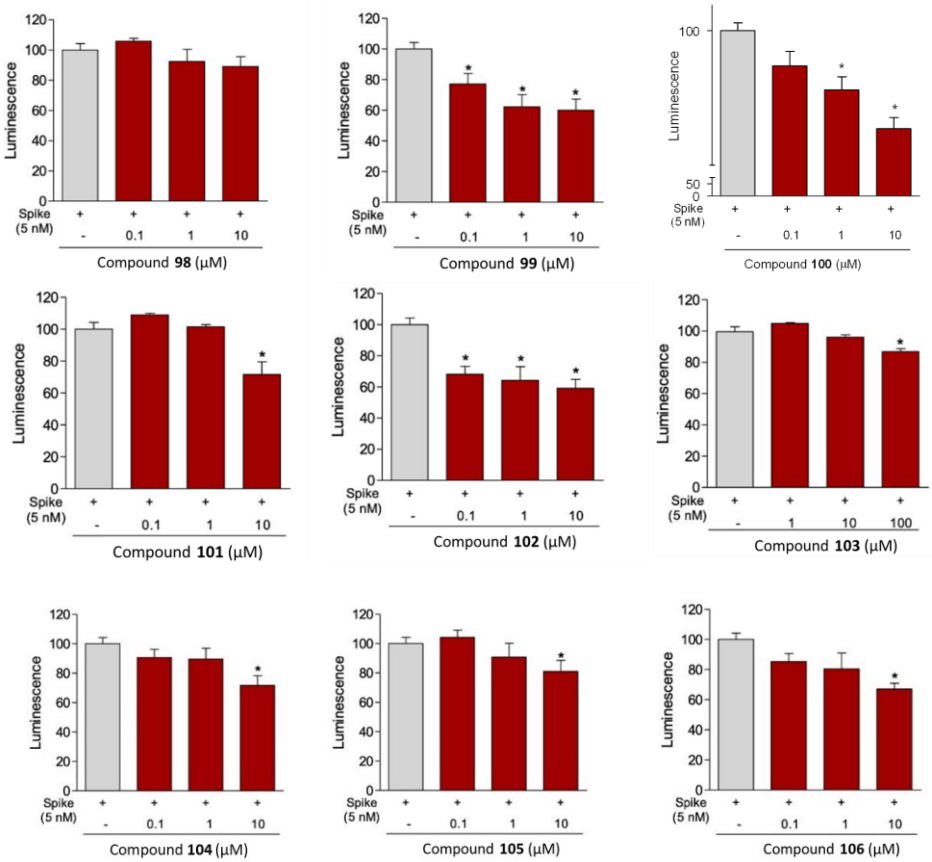

Figure 43. The ACE2/SARS-CoV-2 Spike Inhibitor Screening assay. Compounds **98-106** were tested at different concentrations (0.1, 1, and 10 μM; 1, 10, and 100 μM for cpd. **103**), to evaluate their ability to inhibit the binding of Spike protein (5 nM) to immobilized ACE2. Luminescence was measured using a Fluo-Star Omega fluorescent microplate reader. Luminescence values of Spike 5 nM were arbitrarily set to 100%. Results are expressed as mean ± standard error. *p < 0.05 vs Spike 5 nM.

6.6 Molecular dynamics on ACE2 and BAs derivatives

The project also included a detailed analysis of the *in-silico* MD simulations of two different 3D models of ACE2, the open form (native) and the closed one (bound to an inhibitor), PDB ID 1R42 and 1R4L, respectively. These two forms are two different conformational states between which ACE2 crisscrosses. The results of three MD simulations of 500 ns each on ACE2 apo-form showed the existence of two main conformations, one open and the other closed. The conformational equilibrium between these forms involves the movements of two subdomains (Sub I and Sub II) with the critical flexible area being located within the hinge-binding region, thus suggesting that our derivatives manage to bind the region involved in the shift from the active to the inactive form of ACE2 (Fig. 44, panel A).

The same type of MD simulations was also carried out on ACE2 with the most effective compounds **98** and **103**. Both derivatives when complexed with ACE2 were able to hamper the closure between Sub I and Sub II.

More specifically, compounds **98** and **103** occupy a pocket stacked between the helix α3, the loop between α7 and α8, and the loop connecting α18 and α19.

Compound **98** occupies an amphipathic pocket contacting with Val212, Leu 392, and Lys562. Both 3β and 7β-OH engage in an H-bond with Gln102 and Glu208, respectively. The terminal alkyl side chain contributes with additional hydrophobic interactions with Leu 395 and Pro565 and the hydroxyl group at C-24 H-bonds a Ser253.

As for compound **103**, two main binding clusters were identified. In the most populated one, the molecule enters the same amphipathic pocket as **98** but with a different orientation on its axis. The H-bonds with Gln102 and Pro565 are maintained (Fig. 44).

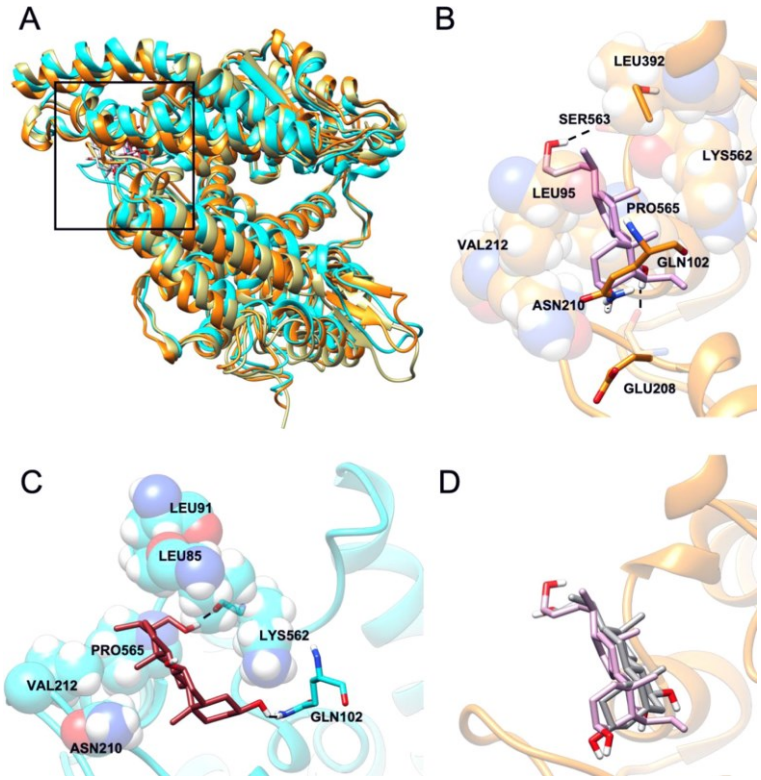

Figure 44. (A) Overall representation of the most populated MD-derived clusters of **103**/ACE2 complex (orange cartoon) and **98**/ACE2 complex (cyan cartoon). The black square indicates the hinge-bending region targeted as the agonist binding site. (B) Cluster0 (85%) binding mode of **103**/ACE2 complex (protein is represented in the orange cartoon, while ligand in the light-violet stick). (C) Cluster0 (76%) binding mode of **98**/ACE2 complex (protein is represented in the cyan cartoon, ligand in the brown stick). (D) Superimposition between the cluster1 of **98**/ACE2 complex and cluster0 **103**/ACE2 complex (protein represented in the orange cartoon, **103** in the light-violet stick, and **98** in the dark-grey stick).

6.7 Conclusions

This project led to the identification of a series of UDCA derivatives as promising ACE2 activators. Two compounds of the series, **98** and **103**, activated ACE2 with an efficacy comparable to that of DIZE, a well-known ACE2 activator. The MD simulations also disclosed an insight into the activation mechanism of the enzyme and the activation binding site.

The results of the binding modes suggest that the stereochemistry of the single substituents on the tetracyclic core does not play a key role in successful binding, and therefore the effects of chemical modifications to the steroidal scaffolds on the enzymatic activity must be analysed deeper.

The *in vitro* assay results sustained the conclusion reached by the analysis of the docking studies.

Interestingly, the results of the Spike RBD/ACE2 inhibition assay presented compounds **99** and **102** as the most effective compounds. These results finally suggested that the ability of binding and activating ACE2 does not disrupt the ability of Spike RBD to tightly bind to ACE2. Nonetheless, the identification of ACE2 activators is still desirable and beneficial in the treatment of hypertension, cardiovascular disease, and inflammation but also in supporting COVID-19 therapy.

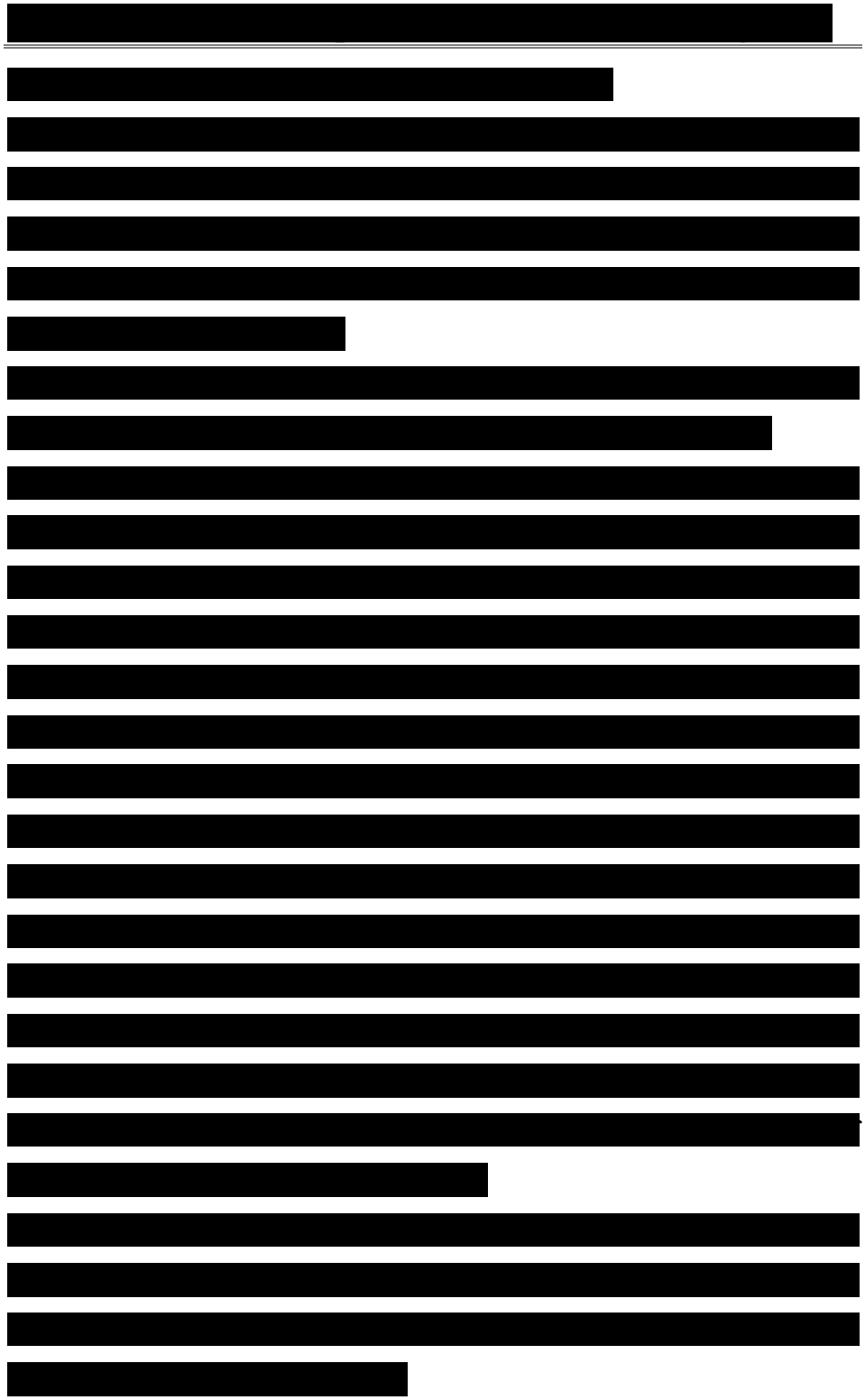

[redacted]

[redacted]

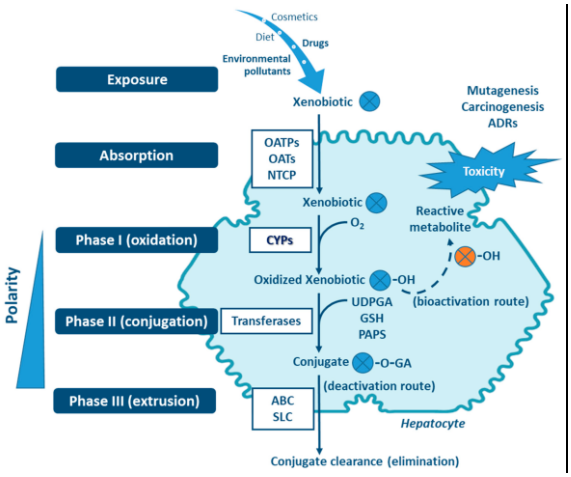
Cosmetics
Diet
Drugs
Environmental pollutants
Exposure
Xenobiotic
Mutagenesis
Carcinogenesis
ADRs
Absorption
OATPs
OATs
NTCP
Toxicity
Xenobiotic
Reactive metabolite
Phase I (oxidation)
CYPs
O_2
-OH
Oxidized Xenobiotic
-OH
(bioactivation route)
Polarity
Phase II (conjugation)
Transferases
UDPGA
GSH
PAPS
Conjugate
-O-GA
(deactivation route)
Phase III (extrusion)
ABC
SLC
Hepatocyte
Conjugate clearance (elimination)

[redacted]

[redacted]

[redacted]

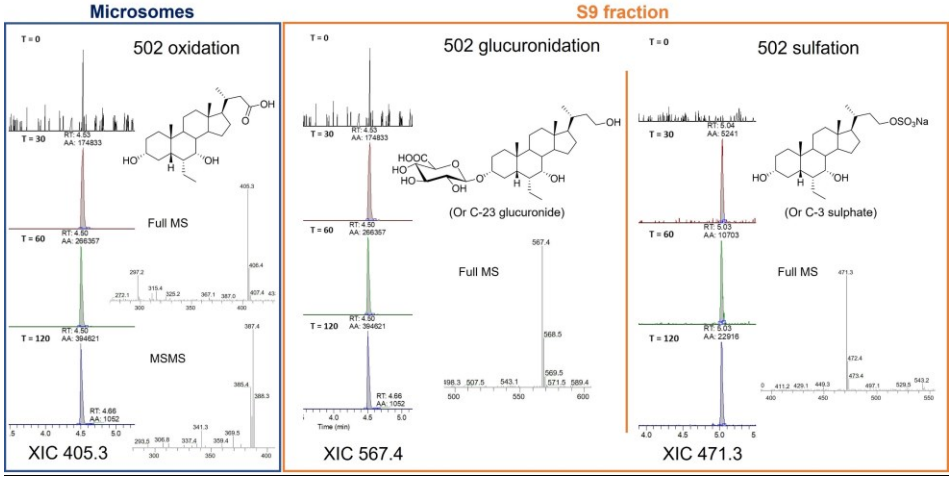

[redacted]

[redacted]

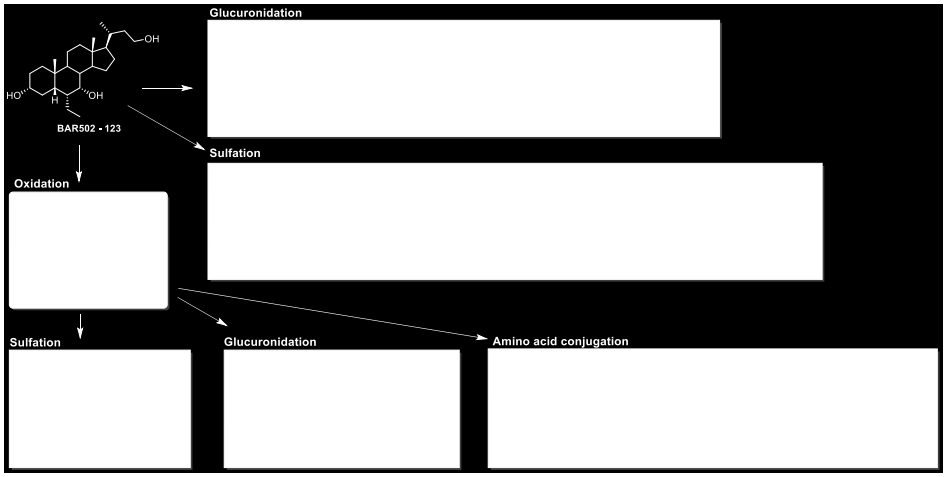

[redacted]

[redacted]

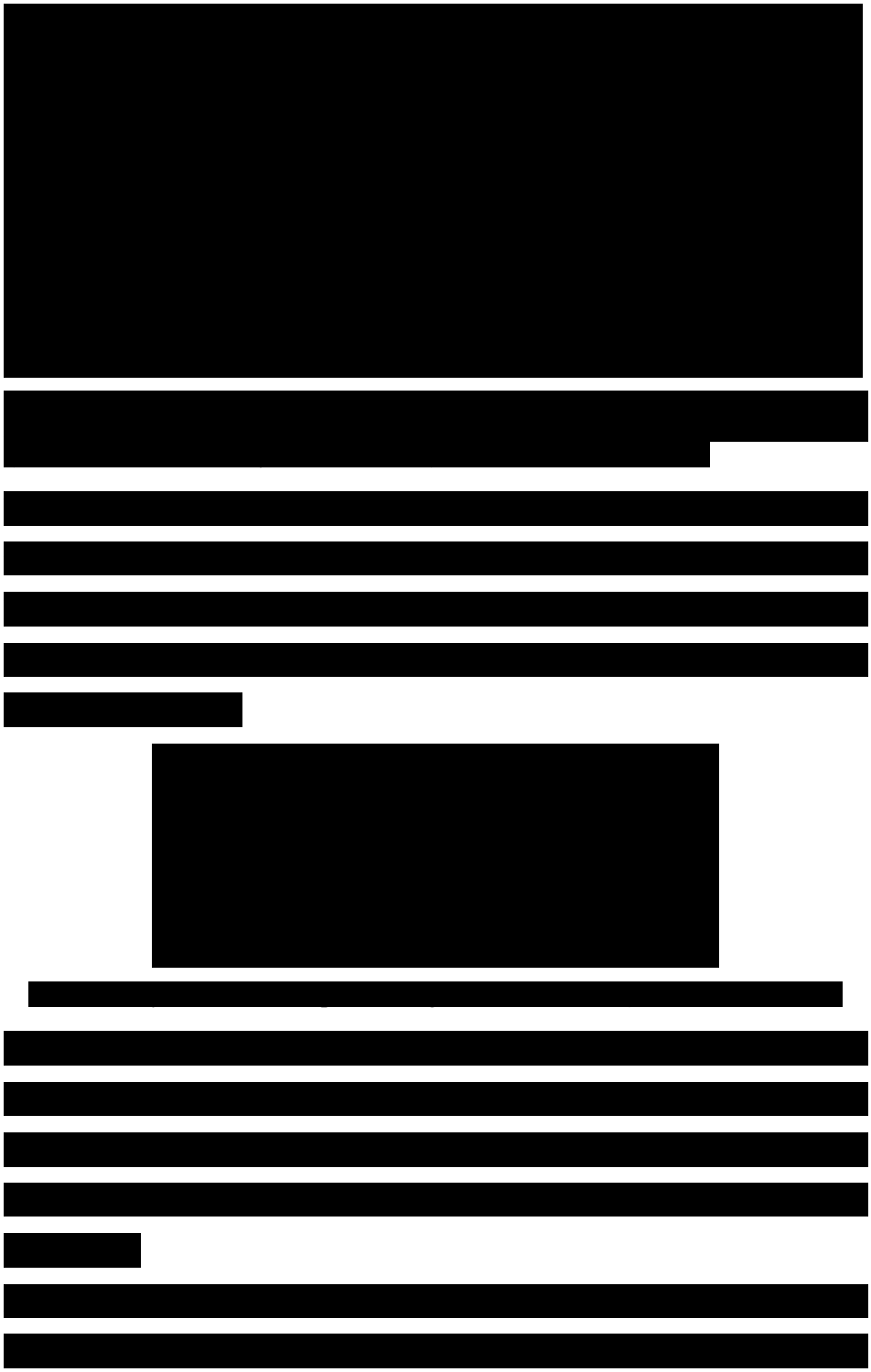

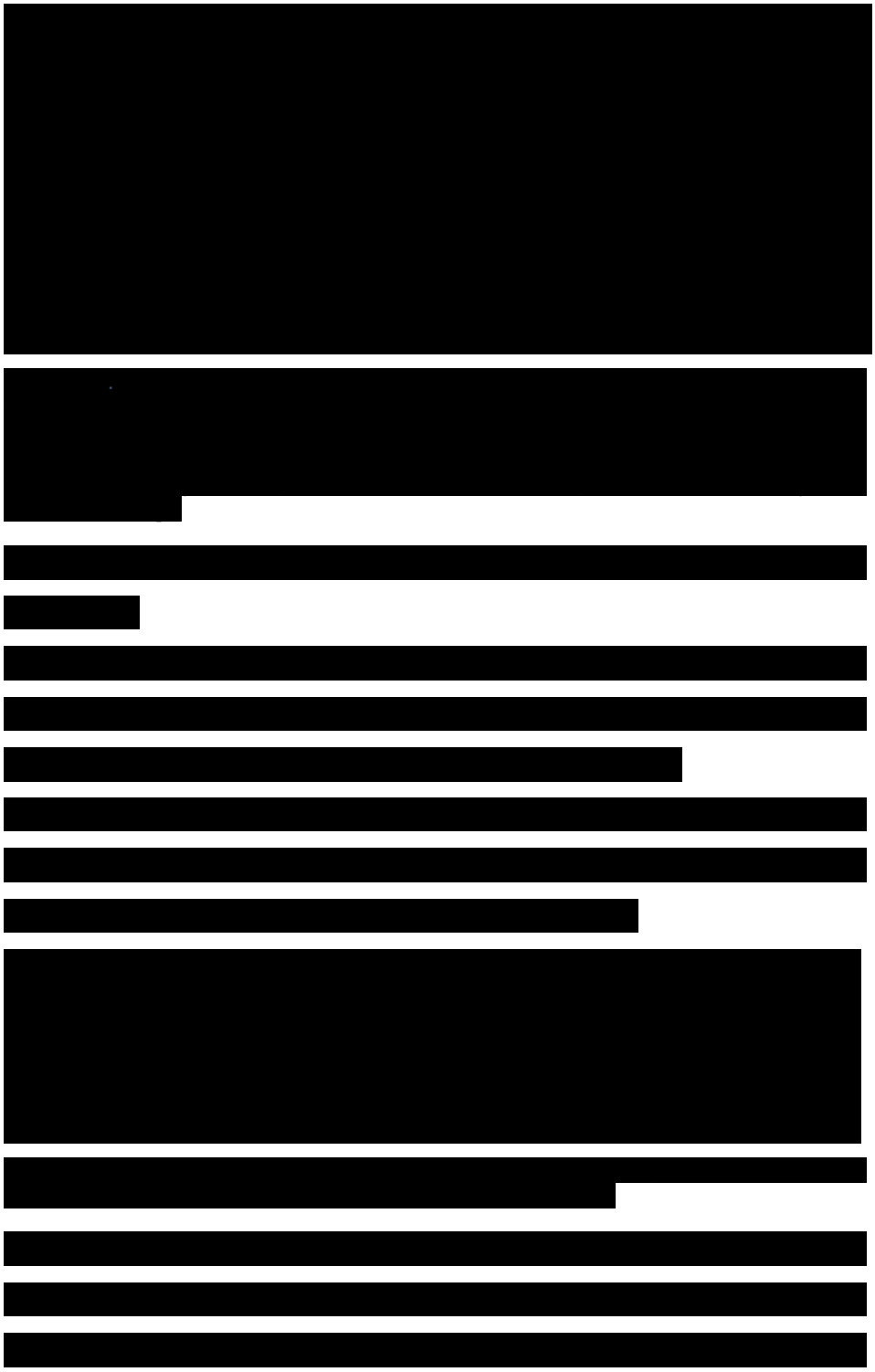

[redacted]

[redacted]

[redacted]

[redacted]

[redacted]

[redacted]

[redacted]

[redacted]

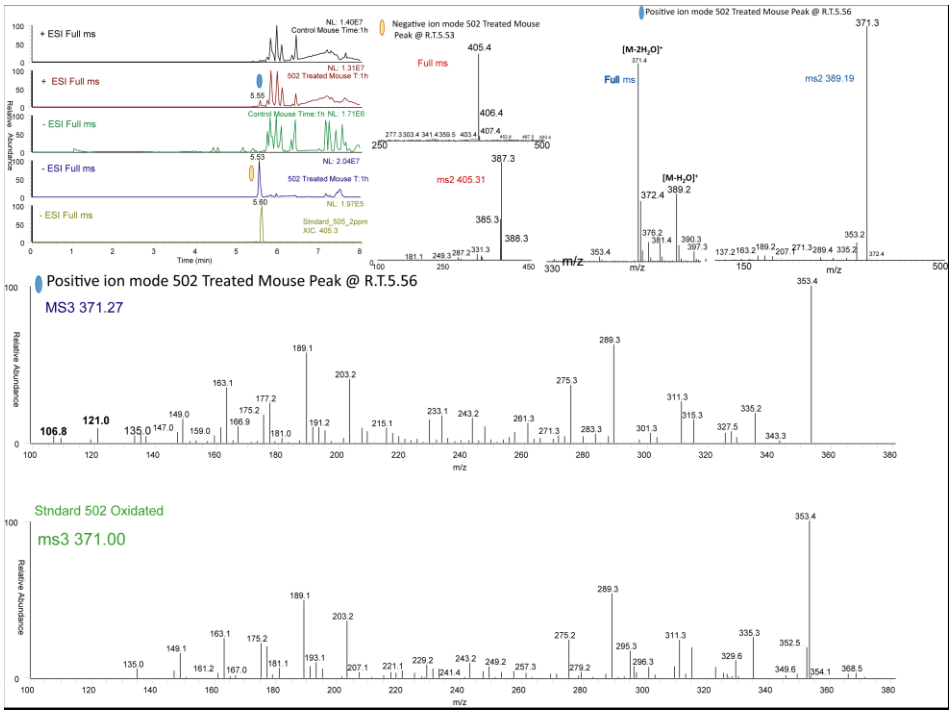

[redacted]

[redacted]

[redacted]

[redacted]

[redacted]

[redacted]

[redacted]

[redacted]

[redacted]

[redacted]

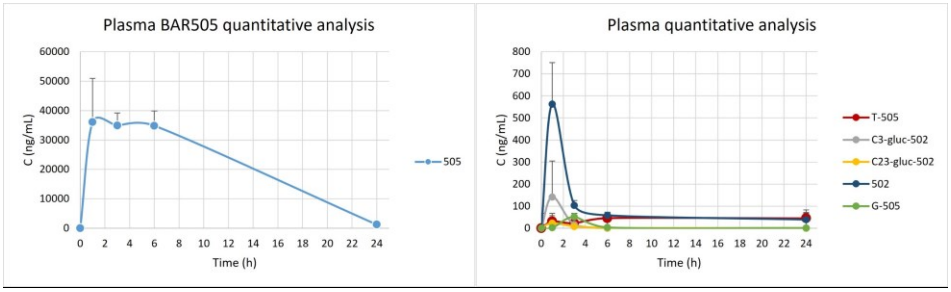
Plasma BAR505 quantitative analysis
C (ng/mL)
60000
50000
40000
30000
20000
10000
0
0 2 4 6 8 10 12 14 16 18 20 22 24
Time (h)
505
Plasma quantitative analysis
C (ng/mL)
800
700
600
500
400
300
200
100
0
0 2 4 6 8 10 12 14 16 18 20 22 24
Time (h)
T-505
C3-gluc-502
C23-gluc-502
502
G-505

[redacted]

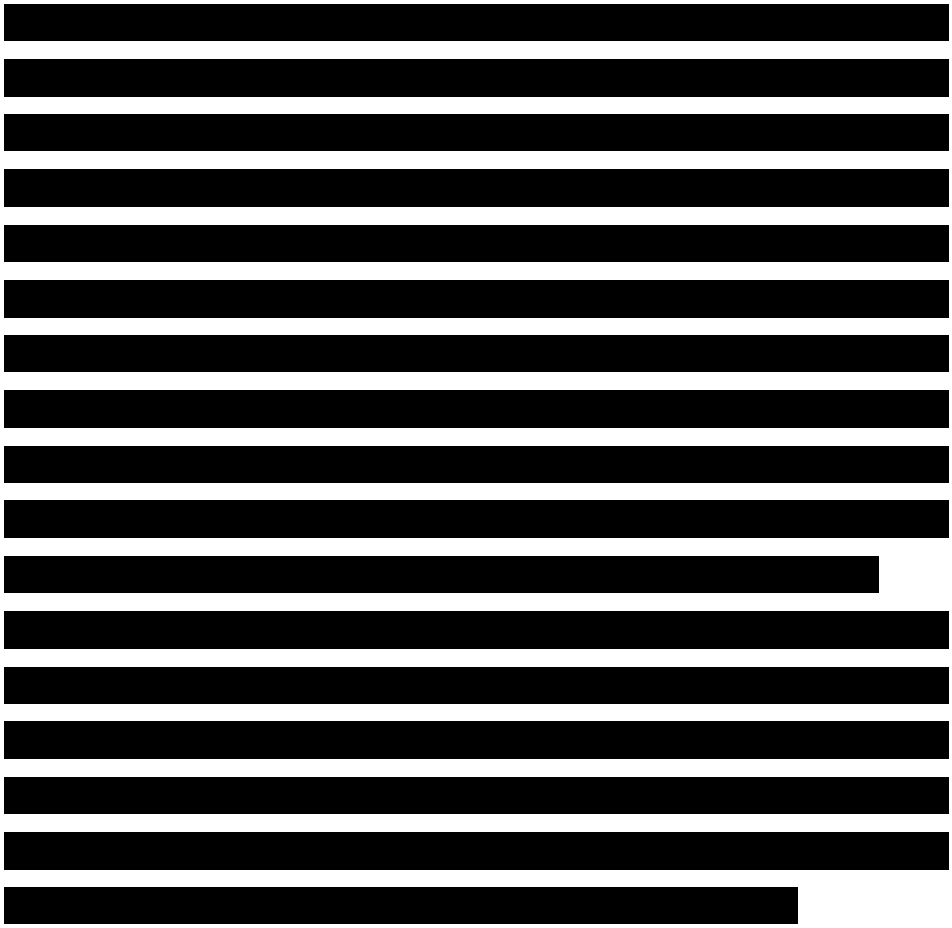

Experimental Section I

Chemistry. High-resolution electrospray ionization mass spectrometry (ESI-MS) spectra were performed with an LTQ-XL equipped with an Ultimate 3000 HPLC system (Thermo Fisher Scientific) mass spectrometer. NMR spectra were obtained on a Bruker 400 spectrometer (^{1}H at 400, ^{13}C at 100 MHz), recorded in $CDCl_3$ (δ_H = 7.26 and δ_C = 77.0 ppm) and CD_3OD (δ_H = 3.30 and δ_C = 49.0 ppm). Detected signals were in accordance with the proposed structures. Coupling constants (J values) are given in hertz (Hz), and chemical shifts (δ) are reported in ppm and referred to CHD_2OD and $CHCl_3$ as internal standards. Spin multiplicities are given as s (singlet), br s (broad singlet), d (doublet), t (triplet), or m (multiplet).

HPLC was performed with a Waters model 510 pump equipped with Waters® Rheodyne injector and a differential refractometer, model 401. Reaction progress was monitored via thin-layer chromatography (TLC) on Alugram silica gel G/UV254 plates. Silica gel MN Kieselgel 60 (70–230 mesh) from Macherey-Nagel Company was used for column chromatography. All chemicals were obtained from Zentek, Inc.

Silica gel (200–400 mesh) from Macherey-Nagel Company was used for flash chromatography. All chemicals were obtained from Sigma-Aldrich, Inc. Solvents and reagents were used as supplied from commercial sources with the following exceptions. Hexane, ethyl acetate, chloroform, dichloromethane, tetrahydrofuran, and triethylamine were distilled from calcium hydride immediately prior to use. Methanol was dried from magnesium methoxide as follows. Magnesium turnings (5 g) and iodine (0.5 g) were refluxed in a small (50–100 mL) quantity of methanol until all the magnesium has reacted. The mixture was diluted (up to 1 L) with reagent-grade methanol, refluxed for 2–3 h, and then distilled under

nitrogen. All reactions were carried out under argon atmosphere using flame-dried glassware.

The purity of all final compounds was determined to be greater than 95% by analytical HPLC analysis.

General procedures.

DIBAL-H reduction. At a solution of methyl quinoline-2-carboxylate in dry THF (25 mL) at 0 °C, a solution of DIBAL-H (2.0 eq, 1.0 M in THF) was added dropwise. The resulting mixture was stirred at room temperature for 8h at 0 °C. When the TLC shows the end of the substrate, the reaction was slowly added to a saturated solution of sodium potassium tartrate and stirred for 2h. The mixture was partitioned three times with CH_2Cl_2, and the combined organic extracts dried over Na_2SO_4. The solution was concentrated in vacuum and the residue was further purified on silica column using 6:4 v/v hexanes/ethyl acetate with 0.1% of TEA to give **52** in quantitative yield.

Mitsunobu reaction. At a solution of PPh_3 (3.5 eq) in dry THF a 0 °C, 3.5 eq of diisopropyl azodicarboxylate (DIAD) were added dropwise. After 10 minutes, a solution of alcohol **52** in dry THF was added and the mixture was stirred for 10 minutes more, before adding a solution of methyl 4-hydroxybenzoate or methyl 3-hydroxybenzoate (3.0 eq) in dry THF. The mixture was stirred vigorously for 12h, then diluted with water and extracted with EtOAc (3 x 50 mL). The organic layers were collected and washed twice with aqueous KOH 2.5 M solution, once with brine and then dried over Na_2SO_4, filtered, and concentrated under reduced pressure. The resulted residue was purified on silica column to give compounds **24** and **27**, respectively.

Methyl 4-(quinolin-2-ylmethoxy)benzoate (24). Crude purification by flash column chromatography (silica gel, hexanes/ethyl acetate 8:2 with

0.1% of TEA) furnished compound **24** (76% yield). An analytic sample was analysed by HPLC on a Nucleodur 100-5 C18 column (5 μm; 10 mm i.d. x 250 mm) with MeOH/H_2O 82:18 v/v as eluent (flow rate 3 mL/min, t_R = 13 min); ^{1}H NMR ($CDCl_3$, 400 MHz): δ 8.21 (1H, d, *J* = 8.5 Hz), 8.09 (1H, d, *J* = 8.3 Hz), 8.00 (2H, d, *J* = 9.0 Hz), 7.84 (1H, d, *J* = 8.3 Hz), 7.76 (1H, t, *J* = 8.3 Hz), 7.65 (1H, d, *J* = 8.5 Hz), 7.57 (1H, t, *J* = 8.3 Hz), 7.06 (2H, d, *J* = 9.0 Hz), 5.43 (2H, s), 3.88 (3H, s). ^{13}C NMR ($CDCl_3$, 100 MHz) δ 166.7, 162.0, 157.1, 147.4, 137.1, 131.5 (2C), 129.9, 128.9, 127.7, 127.6, 126.6, 123.0, 118.9, 114.6 (2C), 71.3, 51.7. HRMS-ESI *m/z* 294.1128 [M+H$^+$], $C_{18}H_{16}NO_3$ requires 294.1125.

Methyl 3-(quinolin-2-ylmethoxy)benzoate (27). Crude purification by flash column chromatography (silica gel, hexanes/ethyl acetate 9:1 v/v with 0.1% of TEA) gave compound **27** (78% yield). An analytic sample was analysed by HPLC on a Nucleodur 100-5 C18 column (5 μm; 10 mm i.d. x 250 mm) with MeOH/H_2O 82:18 v/v as eluent (flow rate 3 mL/min, tR = 14.8 min); ^{1}H NMR ($CDCl_3$, 400 MHz): δ 8.22 (1H, d, *J* = 8.4 Hz), 8.10 (1H, d, *J* = 8.0 Hz), 7.85 (1H, d, *J* = 8.0 Hz), 7.74 (2H, ovl), 7.68 (2H, ovl), 7.57 (1H, t, *J* = 8.0 Hz), 7.37 (1H, t, *J* = 7.7 Hz), 7.24 (1H, d, *J* = 7.7 Hz), 5.44 (2H, s), 3.91 (3H, s). ^{13}C NMR ($CDCl_3$, 100 MHz) δ 169.6, 158.4, 157.3, 147.5, 137.1, 131.6, 129.8, 129.5, 128.9, 127.7, 127.6, 126.6, 122.4, 119.7, 119.0, 115.6, 71.4, 52.1. HRMS-ESI *m/z* 294.1127 [M+H$^+$], $C_{18}H_{16}NO_3$ requires 294.1125.

Synthesis of (4-(quinolin-2-ylmethoxy)phenyl)methanol (25) and (3-(quinolin-2-ylmethoxy)phenyl)methanol (28). DIBAL-H reduction on esters **24** and **27** in the same experimental conditions previously reported for methyl quinoline-2-carboxylate, gave compounds **25** and **28**, respectively.

(4-(Quinolin-2-ylmethoxy)phenyl)methanol (25). Crude purification by flash column chromatography (silica gel, DCM/MeOH 99:1 v/v) gave compound **25** (68% yield). An analytic sample was analysed by HPLC on a Nucleodur 100-5 C18 column (5 μm; 10 mm i.d. x 250 mm) with MeOH/H_2O 40:60 v/v as eluent (flow rate 3 mL/min, t_R = 15.8 min); ^1H NMR ($CDCl_3$, 400 MHz): δ 8.21 (1H, d, *J* = 8.0 Hz), 8.12 (1H, d, *J* = 7.3 Hz), 7.84 (1H, d, *J* = 7.3 Hz), 7.76 (1H, t, *J* = 7.3 Hz), 7.68 (1H, d, *J* = 8.0 Hz), 7.57 (1H, t, *J* = 7.3 Hz), 7.30 (2H, d, *J* = 8.0 Hz), 7.02 (2H, d, *J* = 8.0 Hz), 5.41 (2H, s), 4.62 (2H, s). ^{13}C NMR ($CDCl_3$, 100 MHz) δ 157.9, 157.8, 147.4, 137.1, 133.8, 129.8, 128.8, 128.7 (2C), 127.6, 127.5, 126.5, 119.0, 114.9 (2C), 71.1, 64.7. HRMS-ESI *m/z* 266.1178 [$M+H^+$], $C_{17}H_{16}NO_2$ requires 266.1176.

(3-(Quinolin-2-ylmethoxy)phenyl)methanol (28). Crude purification by flash column chromatography (silica gel, DCM/MeOH 99:1 v/v) furnished compound **28** (60% yield). An analytic sample was analysed by HPLC on a Nucleodur 100-5 C18 column (5 μm; 10 mm i.d. x 250 mm) with MeOH/H_2O 75:15 v/v as eluent (flow rate 3 mL/min, t_R = 11 min); ^1H NMR ($CDCl_3$, 400 MHz): δ 8.20 (1H, d, *J* = 8.4 Hz), 8.10 (1H, d, *J* = 7.4 Hz), 7.84 (1H, d, *J* = 7.4 Hz), 7.75 (1H, t, *J* = 7.4 Hz), 7.68 (1H, d, *J* = 8.4 Hz), 7.56 (1H, t, *J* = 7.4 Hz), 7.28 (1H, dd, *J* = 7.3, 8.0 Hz), 7.08 (1H, s), 7.0 (1H, d, *J* = 8.4 Hz), 6.95 (1H, d, *J* = 7.3 Hz), 5.40 (2H, s), 4.68 (2H, s). ^{13}C NMR ($CDCl_3$, 100 MHz) δ 158.6, 157.8, 147.4, 142.8, 137.1, 129.8, 129.6, 128.7, 127.7, 127.6, 126.5, 119.6, 119.1, 113.9, 113.4, 71.1, 64.9. HRMS-ESI *m/z* 266.1179 [$M+H^+$], $C_{17}H_{16}NO_2$ requires 266.1176.

Basic hydrolysis. An aliquot of esters **24** and **27** was dissolved in MeOH/H_2O (1:1 v/v) and NaOH (5 mol eq.) was added. The resulting mixture was stirred under reflux for 8 h. The mixture was acidified with 6N HCl solution to pH 1-2, then was extracted three times with ethyl

acetate and the combined organic extracts were dried over Na_2SO_4. The solution was concentrated in vacuum. The residue was purified on a silica column to give carboxylic acids **25** and **28**, respectively.

4-(Quinolin-2-ylmethoxy)benzoic acid (26). Crude purification by flash column chromatography (silica gel, DCM/MeOH 99:1) furnished compound **25** (43% yield). An analytic sample was analysed by HPLC on a Phenomenex Luna C18 column (5 μm; 4.6 mm i.d. x 250 mm), with MeOH/H_2O 60:40 v/v and 0.1% of TFA as eluent (flow rate 1 mL/min, t_R = 7.2 min); ^{1}H NMR (CD_3OD, 400 MHz): δ 8.62 (1H, d, *J* = 8.5 Hz), 8.15 (1H, d, *J* = 8.0 Hz), 8.07 (1H, d, *J* = 8.0 Hz), 8.02 (2H, d, *J* = 8.6 Hz), 7.92 (1H, t, *J* = 8.0 Hz), 7.86 (1H, d, *J* = 8.5), 7.73 (1H, t, *J* = 8.0), 7.17 (2H, d, *J* = 8.6 Hz), 5.53 (2H, s). ^{13}C NMR (CD_3OD, 100 MHz) δ 169.4, 163.4, 158.1, 147.0, 140.6, 132.8 (2C), 132.3, 129.3 (2C), 128.6, 127.9, 124.9, 120.8, 115.6 (2C), 71.1. HRMS-ESI *m/z* 278.0825 [M-H$^-$], $C_{17}H_{12}NO_3$ requires 278.0823.

3-(Quinolin-2-ylmethoxy)benzoic acid (29). Purification of compound **29** (68% yield) was carried out on column chromatography by silica gel, using DCM/MeOH 99:1 v/v as eluent. An analytic sample was analysed by HPLC on a Nucleodur 100-5 column (5 μm; 10 mm i.d. x 250 mm), with n-hexane/ethyl acetate 40:60 v/v (flow rate 3 mL/min, t_R = 6.9 min). ^{1}H NMR (CD_3OD, 400 MHz): δ 8.40 (1H, d, *J* = 8.5 Hz), 8.06 (1H, d, *J* = 8.3 Hz), 7.95 (1H, d, *J* = 8.3 Hz), 7.80 (1H, t, *J* = 8.3 Hz), 7.74 (1H, d, *J* = 8.5 Hz), 7.70 (1H, s), 7.64 (1H, t, *J* = 8.3 Hz), 7.62 (1H, d ovl), 7.41 (1H, t), 7.30 (1H, dd, *J* = 1.5, 8.0 Hz), 5.42 (2H, s); ^{13}C NMR (CD_3OD, 100 MHz) δ 169.4, 159.9, 158.8, 148.4, 139.1, 133.5, 131.3, 130.7, 129.2, 129.1, 129.0, 128.0, 123.7, 120.8, 120.7, 116.6, 71.9. HRMS-ESI *m/z* 278.0827 [M-H$^-$], $C_{17}H_{12}NO_3$ requires 278.0823.

Synthetic procedures to prepare compounds 30-32.

TBS protection. Synthesis of compound **56.** To a solution of the methyl 3,5-dihydroxybenzoate (2.0 g, 12 mmol), imidazole (1.5 eq), and DMF (10 mL) was added portion-wise TBSCl (1.2 eq). The reaction mixture was stirred at rt for 1 h. The mixture was concentrated *in vacuo*, diluted with NH_4Cl saturated solution, and extracted with diethyl ether (3 x 50 mL). The combined organics were washed with brine, dried, and concentrated to provide the product as an oil which was purified on silica gel, using CH_2Cl_2:MeOH 95:5 as eluent (50 % yield).

Mesylation reaction. Synthesis of compound **53**. To a solution of **52** (1.6 g, 10 mmol) in diethyl ether (10 mL) at -20°C was added TEA (6.0 eq) followed by $MeSO_2Cl$ (5.0 eq). The reaction mixture was stirred at -20° C for 30 min and then allowed to warm to rt over 2 h. The mixture was quenched with saturated solution of aqueous $NaHCO_3$ (10 mL) and extracted with diethyl ether (3 x 30 mL). The combined organics were washed with H_2O (20 mL), brine (20 mL), dried (Na_2SO_4), and concentrated under vacuum to give crude **53** in quantitative yield.

Williamson reaction. The crude mesylate **53** (1.2 eq) was added to a stirred mixture of **56** (1.0 eq), K_2CO_3 (2.5 eq), and dry DMF. The reaction mixture was stirred at 100° C for 12 h and then diluted with H_2O and extracted with ethyl acetate (3 x 30 mL). The combined organics were washed with brine, dried (Na_2SO_4), concentrated, and purified by flash chromatography (hexanes/ethyl acetate 95:5 v/v) to provide compound **54** (87% yield).

TBS cleavage. A mixture of the compound **54** and TBAF (5.0 eq) in THF (3 mL) was stirred at rt overnight. Upon completion, the resulting solution was concentrated to give **30**.

Methyl 3-hydroxy-5-(quinolin-2-ylmethoxy)benzoate (30). Crude purification by flash column chromatography (silica gel, DCM/MeOH

998:2 v/v) furnished compound **30** (85% yield). An analytic sample was analysed by HPLC on a Nucleodur 100-5 column (5 μm; 10 mm i.d. x 250 mm) with n-hexane/ethyl acetate 7:3 v/v as eluent (flow rate 3 mL/min, t_R = 23.7 min); ^{1}H NMR (400 MHz, $CDCl_3$): δ 8.17 (1H, d, *J* = 8.5 Hz), 8.00 (1H, d, *J* = 8.0 Hz), 7.79 (1H, d, *J* = 8.0 Hz), 7.68 (1H, t, *J* = 8.0 Hz), 7.62 (1H, t, *J* = 8.5 Hz), 7.54 (1H, t, *J* = 8.0 Hz), 7.28 (1H, s), 7.21 (1H, s), 6.76 (1H, s), 5.38 (2H, s), 3.89 (3H, s). ^{13}C NMR (100 MHz, $CDCl_3$): δ 167.2, 159.1, 157.9, 157.3, 146.7, 137.8, 131.8, 130.2, 127.8, 127.7, 127.6, 126.8, 119.2, 109.8, 107.8, 106.8, 70.4, 52.1. HRMS-ESI *m/z* 310.1077 [$M+H^+$], $C_{18}H_{16}NO_4$ requires 310.1074.

3-Hydroxy-5-(quinolin-2-ylmethoxy)benzoic acid (31) and 3-(Hydroxymethyl)-5-(quinolin-2-ylmethoxy)phenol (32). DIBAL-H reduction and NaOH hydrolysis on **30**, in the same experimental conditions previously reported, gave compounds **31** and **32**, respectively.

3-Hydroxy-5-(quinolin-2-ylmethoxy)benzoic acid (31). Purification of compound **31** (quantitative yield) was carried out in column chromatography by silica gel, using DCM/MeOH 95:5 v/v as eluent. An analytic sample was analysed by HPLC on a PFP C18 (5 μm; 4.6 mm i.d. x 250 mm), with MeOH/H_2O 55:45 v/v and 0.1% TFA (flow rate 1 mL/min, t_R = 9.2 min). ^{1}H NMR (400 MHz, CD_3OD): δ 8.39 (1H, d, *J* = 8.4 Hz), 8.05 (1H, d, *J* = 8.0 Hz), 7.96 (1H, d, *J* = 8.0 Hz), 7.79 (1H, t, *J* = 8.0 Hz), 7.72 (1H, d, *J* = 8.4 Hz), 7.62 (1H, t, *J* = 8.0 Hz), 7.18 (1H, s), 7.08 (1H, s), 6.66 (1H, s), 5.37 (2H, s). ^{13}C NMR (100 MHz, CD_3OD): δ 160.7, 159.7, 158.2, 148.2, 139.1, 131.4, 131.3, 129.2, 129.1, 129.0, 128.9, 128.0, 120.6, 110.8, 107.8, 107.0, 71.8. HRMS-ESI *m/z* 294.0775 [$M-H^-$], $C_{17}H_{12}NO_4$ requires 294.0772.

3-(Hydroxymethyl)-5-(quinolin-2-ylmethoxy)phenol (32). Purification of **32** (92% yield) was carried out on silica gel, using DCM/MeOH 95:5

v/v as eluent. An analytic sample was purified by HPLC on a PFP C18 column (5 μm; 4.6 mm i.d. x 250 mm), with MeOH/H_2O 60:40 v/v and 0.1% TFA (flow rate 1 mL/min, t_R = 12.2 min). ^{1}H NMR (400 MHz, $CDCl_3$): δ 8.20 (1H, d, *J* = 8.5 Hz), 8.10 (1H, d, *J* = 8.0 Hz), 7.84 (1H, d, *J* = 8.0 Hz), 7.75 (1H, t, *J* = 8.0 Hz), 7.67 (1H, d, *J* = 8.5 Hz), 7.57 (1H, t, *J* = 8.0 Hz), 6.65 (1H, s), 6.49 (1H, s), 6.46 (1H, s), 5.40 (2H, s), 4.62 (2H, s). ^{13}C NMR (100 MHz, $CDCl_3$): δ 161.1, 159.8, 159.6, 148.3, 145.5, 139.0, 131.3, 129.1, 129.0, 128.9, 127.9, 120.6, 107.8, 105.5, 102.1, 71.6, 65.1. HRMS-ESI *m/z* 282.1127 [$M+H^+$], $C_{17}H_{16}NO_3$ requires 282.1125.

Synthetic procedures to prepare alkylaryl-ethers 33-38.

TBS protection on resorcinol (**57**) (47%) followed by Mitsunobu reaction with several different alcohols (propan-1-ol, propan-2-ol, butan-1-ol, butan-2-ol, 2-methylbutan-1-ol, and pentan-1-ol) and TBS cleavage in the same experimental conditions previously described furnished compounds **60a-f** in 47-84% yields.

Finally, Williamson ether synthesis between **60a-f** and quinolin-2-yl methyl methane sulfonate (**53**) with the same experimental procedures previously described gave compounds **33-38**.

2-((3-propoxyphenoxy)methyl)quinoline (33). Preparative HPLC purification on a Nucleodur 100-5 column (5 μm; 10 mm i.d. x 250 mm) eluting with n-hexane/ethyl acetate 9:1 v/v (flow rate 3 mL/min, t_R = 16.5 min) gave compound **33** in quantitative yield. ^{1}H NMR (400 MHz, $CDCl_3$): δ 8.20 (1H, d, *J* = 8.6 Hz), 8.09 (1H, d, *J* = 7.5 Hz), 7.84 (1H, d, *J* = 7.5 Hz), 7.74 (1H, t, *J* = 7.5 Hz), 7.68 (1H, d, *J* = 8.6 Hz), 7.56 (1H, t, *J* = 7.5 Hz), 7.17 (1H, t, *J* = 8.0 Hz), 6.63 (1H, s), 6.61 (1H, ovl), 6.54 (1H, dd, *J* = 8.0, 2.0 Hz), 5.38 (2H, s), 3.90 (2H, t, *J* = 7.0 Hz), 1.80 (2H, sextet, *J* = 7.0 Hz), 1.03 (3H, t, *J* = 7.0 Hz). ^{13}C NMR (100 MHz, $CDCl_3$): δ 160.4, 159.7, 157.9, 147.6, 137.0, 130.0, 129.7, 129.0, 127.7, 127.6, 126.5, 119.2,

107.6, 106.8, 101.8, 71.1, 69.7, 22.5, 10.5. HRMS-ESI *m/z* 294.1492 [M+H$^+$], $C_{19}H_{20}NO_2$ requires 294.1489.

2-((3-isopropoxyphenoxy)methyl)quinoline (34). Preparative HPLC purification on a Nucleodur 100-5 column (5 μm; 10 mm i.d. x 250 mm), eluting with n-hexane/ethyl acetate 95:5 v/v (flow rate 3 mL/min, t_R = 38 min) gave compound **34** in 61% yield. ^{1}H NMR (400 MHz, $CDCl_3$): δ 8.19 (1H, d, *J* = 8.6 Hz), 8.09 (1H, d, *J* = 7.5 Hz), 7.84 (1H, d, *J* = 7.5 Hz), 7.74 (1H, t, *J* = 7.5 Hz), 7.68 (1H, d, *J* = 8.6 Hz), 7.56 (1H, t, *J* = 7.5 Hz), 7.17 (1H, t, *J* = 8.0 Hz), 6.61 (1H, s), 6.60 (1H, ovl), 6.52 (1H, dd, *J* = 8.0, 2.0 Hz),5.38 (2H, s), 4.52 (1H, septet, *J* = 6.0 Hz), 1.32 (6H, d, *J* = 6.0 Hz). ^{13}C NMR (100 MHz, $CDCl_3$): δ 159.6, 159.2, 157.9, 147.5, 136.9, 129.9, 129.7, 128.9, 127.7, 127.6, 126.4, 119.1, 108.8, 106.8, 103.0, 71.3, 69.9, 22.0 (2C). HRMS-ESI *m/z* 294.1493 [M+H$^+$], $C_{19}H_{20}NO_2$ requires 294.1489.

2-((3-butoxyphenoxy)methyl)quinoline (35). Preparative HPLC purification on a Nucleodur 100-5 column (5 μm; 10 mm i.d. x 250 mm) eluting with n-hexane/ethyl acetate 9:1 v/v (flow rate 3 mL/min, t_R = 17.3 min) gave compound **35** in quantitative yield. ^{1}H NMR (400 MHz, $CDCl_3$): δ 8.19 (1H, d, *J* = 8.6 Hz), 8.09 (1H, d, *J* = 7.5 Hz), 7.84 (1H, d, *J* = 7.5 Hz), 7.74 (1H, t, *J* = 7.5 Hz), 7.68 (1H, d, *J* = 8.6 Hz), 7.56 (1H, t, *J* = 7.5 Hz), 7.17 (1H, t, *J* = 8.0 Hz), 6.61 (1H, s), 6.60 (1H, ovl), 6.52 (1H, dd, *J* = 8.0, 2.0 Hz), 5.38 (2H, s), 3.95 (2H, t, *J* = 7.0 Hz), 1.75 (2H, pentet, *J* = 7.0 Hz), 1.48 (2H, sextet, *J* = 7.4 Hz), 0.97 (3H, t, *J* = 7.4 Hz). ^{13}C NMR (100 MHz, $CDCl_3$): δ 160.5, 159.6, 158.0, 147.6, 137.0, 129.9, 129.7, 128.9, 127.7, 127.6, 126.5, 119.1, 107.6, 106.8, 101.7, 71.2, 67.7, 31.3, 19.2, 13.8. HRMS-ESI *m/z* 308.1648 [M+H$^+$], $C_{20}H_{22}NO_2$ requires 308.1645.

2-((3-(sec-butoxy)phenoxy)methyl)quinoline (36). Preparative HPLC purification on a Nucleodur 100-5 column (5 µm; 10 mm i.d. x 250 mm) eluting with n-hexane/ethyl acetate 9:1 v/v (flow rate 3 mL/min, t_R = 15 min) gave compound **36** in quantitative yield. ^{1}H NMR (400 MHz, $CDCl_3$): δ 8.19 (1H, d, *J* = 8.6 Hz), 8.09 (1H, d, *J* = 7.5 Hz), 7.84 (1H, d, *J* = 7.5 Hz), 7.74 (1H, t, *J* = 7.5 Hz), 7.68 (1H, d, *J* = 8.6 Hz), 7.56 (1H, t, *J* = 7.5 Hz), 7.17 (1H, t, *J* = 8.0 Hz), 6.61 (1H, s), 6.60 (1H, ovl), 6.52 (1H, dd, *J* = 8.0, 2.0 Hz), 5.37 (2H, s), 4.27 (2H, sextet, *J* = 6.1 Hz), 1.73 (1H, m), 1.60 (1H, m), 1.27 (2H, d, *J* = 6.1 Hz), 0.96 (3H, t, *J* = 7.4 Hz). ^{13}C NMR (100 MHz, $CDCl_3$): δ 159.7, 159.6, 158.0, 147.5, 136.9, 129.9, 129.7, 128.9, 127.7, 127.6, 126.4, 119.2, 108.9, 106.7, 103.1, 75.2, 71.1, 29.2, 19.2, 9.9. HRMS-ESI *m/z* 308.1647 [M+H$^+$], $C_{20}H_{22}NO_2$ requires 308.1645.

2-((3-(2-methylbutoxy)phenoxy)methyl)quinoline (37). Preparative HPLC purification on a Nucleodur 100-5 column (5 µm; 10 mm i.d. x 250 mm) eluting with n-hexane/ethyl acetate 9:1 v/v (flow rate 3 mL/min, t_R = 14.0 min) gave compound **37** in 90%. ^{1}H NMR (400 MHz, $CDCl_3$): δ 8.19 (1H, d, *J* = 8.6 Hz), 8.09 (1H, d, *J* = 7.5 Hz), 7.84 (1H, d, *J* = 7.5 Hz), 7.74 (1H, t, *J* = 7.5 Hz), 7.68 (1H, d, *J* = 8.6 Hz), 7.56 (1H, t, *J* = 7.5 Hz), 7.17 (1H, t, *J* = 8.0 Hz), 6.61 (1H, s), 6.60 (1H, ovl), 6.52 (1H, dd, *J* = 8.0, 2.0 Hz), 5.38 (2H, s), 3.80 (1H, dd, *J* = 9.0, 6.0 Hz), 3.71 (1H, dd, *J* = 9.0, 6.6 Hz), 1.85 (1H, septet, J = 6.6 Hz), 1.56 (1H, m), 1.25 (1H, m), 1.00 (3H, d, *J* = 6.6 Hz), 0.94 (3H, t, *J* = 7.3 Hz). ^{13}C NMR (100 MHz, $CDCl_3$): δ 160.6, 159.6, 158.0, 147.5, 136.9, 129.9, 129.8, 128.9, 127.8, 127.6, 126.5, 119.1, 107.7, 106.8, 101.8, 73.0, 71.2, 34.6, 26.1, 16.5, 11.3. HRMS-ESI *m/z* 322.1805 [M+H$^+$], $C_{21}H_{24}NO_2$ requires 322.1802.

2-((3-(pentyloxy)phenoxy)methyl)quinoline (38). Preparative HPLC purification on a Nucleodur 100-5 column (5 µm; 10 mm i.d. x 250 mm)

eluting with n-hexane/ethyl acetate 9:1 v/v (flow rate 3 mL/min, t_R = 13.8 min) gave compound **38** in 95% yield. ^{1}H NMR (400 MHz, $CDCl_3$): δ 8.19 (1H, d, *J* = 8.6 Hz), 8.09 (1H, d, *J* = 7.5 Hz), 7.84 (1H, d, *J* = 7.5 Hz), 7.74 (1H, t, *J* = 7.5 Hz), 7.68 (1H, d, *J* = 8.6 Hz), 7.56 (1H, t, *J* = 7.5 Hz), 7.17 (1H, t, *J* = 8.0 Hz), 6.61 (1H, s), 6.60 (1H, ovl), 6.52 (1H, dd, *J* = 8.0, 2.0 Hz), 5.38 (2H, s), 3.93 (2H, t, *J* = 7.0 Hz), 1.77 (2H, m), 1.40 (4H, m), 0.93 (3H, t, *J* = 7.0 Hz). ^{13}C NMR (100 MHz, $CDCl_3$): δ 160.4, 159.6, 157.9, 147.5, 136.9, 129.9, 129.7, 128.9, 127.7, 127.6, 126.4, 119.1, 107.6, 106.8, 101.8, 71.2, 68.0, 28.9, 28.2, 22.4, 13.9. HRMS-ESI *m/z* 322.1807 [$M+H^+$], $C_{21}H_{24}NO_2$ requires 322.1802.

Synthesis of ethers 39-44.

Synthesis of compounds 61a and 61b.

Williamson Reaction. To a solution of resorcinol (**57**) in dry DMF methyl 5-bromopentanoate (0.5 eq) or methyl 4-bromobutanoate (0.5 eq) and K_2CO_3 (1 eq) were added, and the reaction mixture was stirred at 100°C for about 12h. After reagent consumption, the reaction mixture was cooled at RT, acidified with HCl 6N and then diluted with water and extracted with ethyl acetate (3 x 50 mL). The organic phase was dried over Na_2SO_4, filtered, and evaporated yielding a crude product that was then purified through flash silica column chromatography.

Methyl 5-(3-hydroxyphenoxy)pentanoate (61a). Purification by flash silica column chromatography in hexanes/ethyl acetate 8:2 v/v afforded compound **61a** (64%).

Methyl 4-(3-hydroxyphenoxy)butanoate (61b). Purification by flash silica column chromatography in hexanes/ethyl acetate 8:2 v/v afforded compound **61b** (43%).

Williamson reaction. The 2-(cloromethyl)quinoline (**62**) was added to a stirred mixture of the phenol (1.0 eq), K_2CO_3 (2.5 eq), and dry DMF. The

reaction mixture was stirred at 100°C for 12h. The mixture was diluted with H_2O and extracted with EtOAc (3 x 30 mL). The combined organics were washed with brine, dried over Na_2SO_4, concentrated, and purified by flash chromatography.

Methyl 5-(3-quinolin-2-ylmethoxy)phenoxy)pentanoate (39). Purification by flash silica column chromatography in hexanes/ethyl acetate 9:1 v/v afforded compound **39** (75%). An analytic sample was analysed by HPLC on a Kinetex Biphenyl (5 μm; 250 mm x 4.6 mm) column in gradient (t_0= 20% ACN - t_{5min}= 20% ACN - t_{20min}= 95% ACN - t_{25min}= 95% ACN, flow rate 1 mL/min, t_R = 18.7 min). ^{1}H NMR (400 MHz, $CDCl_3$): δ 8.19 (1H, d, *J* = 8.5 Hz), 8.08 (1H, d, *J* = 8.5 Hz), 7.83 (1H, d, *J* = 8.2 Hz), 7.74 (1H, t, *J* = 8.5 Hz), 7.67 (1H, d, *J* = 8.5 Hz), 7.55 (1H, t, *J* = 8.1 Hz), 7.16 (1H, t, *J* = 8.1 Hz), 6.61 (2H, ovl), 6.51 (1H, dd, *J* = 8.1 Hz, 2.3 Hz), 5.37 (2H, s), 3.95 (2H, t, *J* = 7.5 Hz), 3.68 (3H, s), 2.39 (2H, t, *J* = 6.5 Hz), 1.80 (2H, t, *J* = 3.7 Hz). ^{13}C NMR (700 MHz, $CDCl_3$): δ 173.9, 160.3, 159.6, 158.0, 147.4, 137.2, 130.1, 129.9, 128.9, 127.8, 127.7, 126.6, 119.2, 107.6, 107.0, 101.9, 71.2, 67.3, 51.7, 33.7, 28.7, 21.7. HRMS-ESI *m/z* 365.1615 [$M+H^+$], $C_{22}H_{23}NO_4$ requires 342.1627.

Methyl 4-(3-(quinolin-2-ylmethoxy)phenoxy)butanoate (42). Purification by flash silica column chromatography in hexanes/ethyl acetate 9:1 v/v afforded compound **42** (72%). An analytic sample was analysed by HPLC on a Kinetex Biphenyl (5 μm; 250 mm x 4.6 mm) column in gradient (t_0= 20% ACN - t_{5min}= 20% ACN - t_{20min}= 95% ACN - t_{25min}= 95% ACN, flow rate 1 mL/min, t_R = 18.2 min). ^{1}H NMR (400 MHz, CDCl3): δ 8.20 (1H, d, J = 8.5 Hz), 8.10 (1H, d, J = 8.5 Hz), 7.83 (1H, d, J = 8.2 Hz), 7.74 (1H, t, J = 8.5 Hz), 7.68 (1H, d, J = 8.5 Hz), 7.56 (1H, t, J = 8.1 Hz), 7.16 (1H, t, J = 8.1 Hz), 6.61-6.60 (2H, ovl), 6.51 (1H, dd, J = 8.1 Hz, 2.3 Hz), 5.38 (2H, s), 3.98 (2H, t, J = 6.2 Hz), 3.68 (3H, s), 2.51

(2H, t, J = 7.0 Hz), 2.09 (2H, quint. J = 6.2 Hz, 7.0 Hz). 13C NMR (700 MHz, CDCl3): δ 173.7, 160.2, 159.6, 157.9, 147.4, 137.2, 130.1, 129.9, 128.9, 127.8, 127.6, 126.6, 119.2, 107.6, 107.1, 102.0, 71.2, 66.8, 51.7, 30.6, 24.7. HRMS-ESI m/z 352.1466 [$M+H^+$], $C_{21}H_{21}NO_4$ requires 352.1471.

NaOH hydrolysis of an aliquot of esters **39** and **42** in the same experimental condition mentioned above furnished carboxylic acids (compounds **40** and **43**, respectively).

5-(3-quinolin-2-ylmethoxy)phenoxy)pentanoic acid (40). Purification by flash column chromatography (silica gel, DCM/MeOH 9:1 v/v) furnished compound **40** (68%). An analytic sample was analysed by HPLC on a Kinetex Biphenyl (5 µm; 250 mm x 4.6 mm) column in gradient (t_0= 20% ACN - t_{5min}= 20% ACN - t_{20min}= 95% ACN - t_{25min}= 95% ACN, flow rate 1 mL/min, t_R = 16.3 min). ^{1}H NMR (400 MHz, CD_3OD): δ 9.15 (1H, d, *J* = 8.5 Hz), 8.37 (1H, d, *J* = 8.5 Hz), 8.31 (1H, d, *J* = 8.2 Hz), 8.18 (1H, t, *J* = 8.5 Hz), 8.15 (1H, d, *J* = 8.5 Hz), 7.97 (1H, t, *J*= 8.1 Hz), 7.23 (1H, t, *J* = 8.1 Hz), 6.70-6.72 (2H, ovl), 6.63 (1H, dd, *J* = 8.1 Hz, 2.3 Hz), 5.68 (2H, s), 3.99 (2H, t, *J* = 7.5 Hz), 2.36 (2H, t, *J* = 6.5 Hz), 1.78 (2H, t, *J* = 3.7 Hz). ^{13}C NMR (700 MHz, CD_3OD): δ 177.3, 161.8, 160.5, 158.4, 142.9, 133.4, 131.1 (2C), 129.6, 129.4, 129.3, 125.8, 121.1, 109.2, 108.0, 103.0, 70.1, 68.6, 34.5, 29.7, 22.7. HRMS-ESI m/z 350.1462 [$M-H^-$], $C_{21}H_{21}NO_4$ requires 350.1471.

4-(3-(quinolin-2-ylmethoxy)phenoxy)butanoic acid (43). Purification by flash column chromatography (silica gel, DCM/MeOH 9:1 v/v) furnished compound **43** (97%). An analytic sample was analysed by HPLC on a Kinetex Biphenyl (5 µm; 250 mm x 4.6 mm) column in gradient (t_0= 20% ACN - t_{5min}= 20% ACN - t_{20min}= 95% ACN - t_{25min}= 95% ACN, flow rate 1 mL/min, t_R = 15.7 min). ^{1}H NMR (400 MHz, CD_3OD): δ 9.14 (1H,

d, *J* = 8.5 Hz), 8.35 (1H, d, *J* = 8.5 Hz), 8.34 (1H, d, *J* = 8.2 Hz), 8.19 (1H, t, *J* = 8.5 Hz), 8.17 (1H, d, *J* = 8.5 Hz), 7.98 (1H, t, *J* = 8.1 Hz), 7.26 (1H, t, *J* = 8.7 Hz), 6.76-6.74 (2H, ovl), 6.66 (1H, d, *J* = 8.7 Hz), 5.68 (2H, s), 4.04 (2H, t, *J* = 6.2 Hz), 2.49 (2H, t, *J* = 7.0 Hz), 2.06 (2H, quint, *J* = 6.2 Hz, 7.0 Hz). ^{13}C NMR (700 MHz, CD_3OD): δ 175.4, 161.7, 160.3, 158.1, 144.8, 134.4, 131.1, 130.5, 130.3, 129.9, 129.3, 124.5, 120.8, 109.3, 108.1, 103.1, 69.2, 68.4, 31.3, 25.7. HRMS-ESI m/z 336,1309 [M-H$^-$], $C_{20}H_{19}NO_4$ requires 336,1314.

$LiBH_4$ reduction. A solution of $LiBH_4$ 2M (3 eq) in dry THF and dry MeOH (1 eq) were added to a solution of the esters **7** and **10** in dry THF at 0°C. The reaction was monitored *via* TLC and the substrate was fully converted after 5h. The reaction was cooled to 0°C, quenched by adding a solution of NaOH 1N (2 eq) and stirred for 1h. The mixture was then diluted with H_2O and extracted with ethyl acetate (3 x 50 mL). The organic phase was dried over Na_2SO_4, filtered, and evaporated yielding a crude product that was then purified by chromatography.

5-(3-(quinolin-2-ylmethoxy)phenoxy)pentan-1-ol (41). Purification by flash silica column chromatography in hexanes/ethyl acetate 1:1 v/v afforded compound **41** (80%). An analytic sample was analysed by HPLC on a Kinetex Biphenyl (5 μm; 250 mm x 4.6 mm) column in gradient (t_0= 20% ACN - t_{5min}= 20% ACN - t_{20min}= 95% ACN - t_{25min}= 95% ACN, flow rate 1 mL/min, t_R = 16.5 min). ^{1}H NMR (400 MHz, $CDCl_3$): δ 8.20 (1H, d, *J* = 8.5 Hz), 8.11 (1H, d, *J* = 8.5 Hz), 7.84 (1H, d, *J* = 8.2 Hz), 7.75 (1H, t, *J* = 8.5 Hz), 7.68 (1H, d, *J* = 8.5 Hz), 7.56 (1H, t, *J* = 8.1 Hz), 7.16 (1H, t, *J* = 8.1 Hz), 6.61-6.60 (2H, ovl), 6.52 (1H, dd, *J* = 8.1 Hz, 2.3 Hz), 5.38 (2H, s), 3.94 (2H, t, *J* = 7.5 Hz), 3.68 (2H, t, *J* = 6.5), 1.80 (2H, quint. *J* = 6.5 Hz, 7.5 Hz), 1.63-1.53 (4H, ovl). ^{13}C NMR (700 MHz, $CDCl_3$): δ 160.4, 159.7, 158.0, 147.5, 137.1, 130.1, 129.9, 129.0, 127.8, 127.7, 126.6,

119.2, 107.7, 107.0, 101.9, 71.3, 67.9, 62.9, 32.5, 29.0, 22.4. HRMS-ESI *m/z* 338,1671 [M+H$^+$], $C_{21}H_{23}NO_3$ requires 338.1678.

4-(3-(quinolin-2-ylmethoxy)phenoxy)butan-1-ol (44). Purification by flash silica column chromatography in hexanes/ethyl acetate 4:6 v/v afforded compound **44** (80%). An analytic sample was analysed by HPLC on a Kinetex Biphenyl (5 μm; 250 mm x 4.6 mm) column in gradient (t_0= 20% ACN - t_{5min}= 20% ACN - t_{20min}= 95% ACN - t_{25min}= 95% ACN, flow rate 1 mL/min, t_R = 18.9 min). ^{1}H NMR (400 MHz, $CDCl_3$): δ 8.20 (1H, d, *J* = 8.5 Hz), 8.09 (1H, d, *J* = 8.5 Hz), 7.83 (1H, d, *J* = 8.2 Hz), 7.74 (1H, t, *J* = 8.5 Hz), 7.67 (1H, d, *J* = 8.5 Hz), 7.55 (1H, t, *J* = 8.1 Hz), 7.16 (1H, t, *J* = 8.7 Hz), 6.61-6.62 (2H, ovl), 6.52 (1H, d, *J* = 8.7 Hz), 5.38 (2H, s), 3.98 (2H, t, *J* = 6.2 Hz), 3.71 (2H, t, *J* = 7.0 Hz), 1.86 (2H, m), 1.73 (2H, m). ^{13}C NMR (700 MHz, $CDCl_3$): δ 160.2, 159.6, 157.9, 147.5, 137.1, 130.1, 129.8, 128.9, 127.8, 127.6, 126.6, 119.2, 107.7, 107.0, 101.9, 71.2, 67.8, 62.4, 29.5, 25.7. HRMS-ESI m/z 324,1511 [M+H$^+$], $C_{20}H_{21}NO_3$ requires 324,1521.

Compounds **45** and **48** were synthesized, starting from 2-(chloromethyl)quinoline **62** by Williamson reaction, with analogous procedures to those detailed above for compounds **39** and **42**.

Synthesis of biphenylethers 45 and 48. Esters **45** and **48** were synthesized according to the general procedure of Williamson, starting from 2-(chloromethyl)quinoline and methyl 4'-hydroxy-[1,1'-biphenyl]-4-carboxylate (**63**) or methyl 4'-hydroxy-[1,1'-biphenyl]-3-carboxylate (**64**).

Methyl 4'-(quinolin-2-ylmethoxy)-[1,1'-biphenyl]-4-carboxylate (45). Purification by flash silica column chromatography in hexanes/ethyl acetate 9:1 v/v furnished compound **45** (87% yield). An analytic sample was analysed by HPLC on a Kinetex Biphenyl (5 μm; 250 mm x 4.6 mm) column in gradient (t_0= 20% ACN - t_{5min}= 20% ACN - t_{20min}= 95% ACN -

t_{25min}= 95% ACN, flow rate 1 mL/min, t_R = 19.7 min). ^{1}H NMR (400 MHz, $CDCl_3$): δ 8.22 (1H, d, *J* = 8.6 Hz), 8.11 (1H, d, *J* = 8.2 Hz), 8.08 (2H, d, *J* = 8.6 Hz), 7.85 (1H, d, *J* = 8.2 Hz), 7.76 (1H, t, *J* = 8.2 Hz), 7.70 (1H, d, *J* = 8.6 Hz), 7.61 (2H, d *J* = 8.6 Hz), 7.58 (2H, d, *J* = 8.9 Hz), 7.57 (1H, t, ovl), 7.13 (2H, d, *J* = 8.9 Hz), 5.46 (2H, s), 3.94 (3H, s). ^{13}C NMR (100 MHz, $CDCl_3$): δ 167.1, 158.6, 157.6, 147.5, 145.0, 137.1, 132.9, 130.1 (2C), 129.8, 128.9, 128.5 (2C), 128.3, 127.7, 127.6, 126.6 (2C), 126.5, 119.0, 115.3 (2C), 71.5, 52.1. HRMS-ESI *m/z* 370.1440 [M+H$^+$], $C_{24}H_{20}NO_3$ requires 370.1438.

Methyl 4'-(quinolin-2-ylmethoxy)-[1,1'-biphenyl]-3-carboxylate (48). Purification by flash silica column chromatography in hexanes/ethyl acetate 9:1 v/v furnished compound **48** (quantitative yield). An analytic sample was analysed by HPLC on a Kinetex Biphenyl column (5 µm; 250 mm x 4.6 mm) in gradient (t_0= 20% ACN - t_{5min}= 20% ACN - t_{20min}= 95% ACN - t_{25min}= 95% ACN, flow rate 1 mL/min, t_R = 19.8 min). ^{1}H NMR (400 MHz, $CDCl_3$): δ 8.23 (1H, t, *J* = 2.0 Hz), 8.21 (1H, d, *J* = 8.4 Hz), 8.11 (1H, d, *J* = 8.6 Hz), 7.98 (1H, d, *J* = 8.0 Hz), 7.84 (1H, d, *J* = 7.9 Hz), 7.77 (1H, t, *J* = 8.6 Hz), 7.73 (1H, d, *J* = 8.4 Hz), 7.71 (1H, d, *J* = 8.0 Hz), 7.57 (1H, t, ovl), 7.57 (2H, d, *J* = 8.7 Hz), 7.48 (1H, t, *J* = 8.0 Hz), 7.13 (2H, d, *J* = 8.7 Hz), 5.45 (2H, s), 3.94 (3H, s). ^{13}C NMR (100 MHz, $CDCl_3$): δ 167.0, 158.2, 157.7, 147.5, 140.8, 137.1, 133.1, 131.0, 130.6, 129.8, 128.9, 128.8, 128.3 (2C), 127.8 (2C), 127.7, 127.6, 126.5, 119.1, 115.3 (2C), 71.4, 52.1. HRMS-ESI *m/z* 370.1441 [M+H$^+$], $C_{24}H_{20}NO_3$ requires 370.1438.

4'-(quinolin-2-ylmethoxy)-[1,1'-biphenyl]-4-carboxylic acid (46) and 4'-(quinolin-2-ylmethoxy)-[1,1'-biphenyl]-3-carboxylic acid (49). Starting from esters **45** and **48**, NaOH hydrolysis was performed as mentioned before in order to obtain compounds **46** and **49**, respectively.

4'-(quinolin-2-ylmethoxy)-[1,1'-biphenyl]-4-carboxylic acid (46). Purification by flash column chromatography (silica gel, DCM/MeOH 95:5 v/v) furnished compound **46** (quantitative yield). An analytic sample was analysed by HPLC on a Kinetex Biphenyl (5 µm; 250 mm x 4.6 mm) column in gradient (t_0= 20% ACN - t_{5min}= 20% ACN - t_{20min}= 95% ACN - t_{25min}= 95% ACN, flow rate 1 mL/min, t_R = 16.9 min). ^{1}H NMR (400 MHz, CD_3OD+0.01% TFA): δ 9.23 (1H, d, *J* = 8.5 Hz), 8.42 (1H, d, *J* = 8.0 Hz), 8.39 (1H, d, *J* = 7.5 Hz), 8.24 (1H, t, *J* = 7.5 Hz), 8.23 (1H, d, *J* = 8.5 Hz), 8.10 (2H, d, *J* = 8.5 Hz), 8.03 (1H, t, *J* = 8.0 Hz), 7.76 (2H, d, *J* = 8.5 Hz), 7.73 (2H, d, *J* = 8.5 Hz), 7.32 (2H, d, *J* = 8.5 Hz), 5.80 (2H, s). ^{13}C NMR (100 MHz, $CDCl_3$): δ 168.7, 158.3, 157.3, 145.7, 145.0, 138.8, 133.2, 130.9, 130.4 (2C), 128.5 (2C), 128.4, 128.3, 127.8 (2C), 126.5 (3C), 119.2, 115.3 (2C), 69.8. HRMS-ESI m/z 354.1137 [M-H$^-$], $C_{23}H_{16}NO_3$ requires 354.1136.

4'-(quinolin-2-ylmethoxy)-[1,1'-biphenyl]-3-carboxylic acid (49). Purification by flash column chromatography (silica gel, DCM/MeOH 95:5 v/v) furnished compound **49** (quantitative yield). An analytic sample was analysed by HPLC on a Kinetex Biphenyl (5 µm; 250 mm x 4.6 mm) column in gradient (t_0= 20% ACN - t_{5min}= 20% ACN - t_{20min}= 95% ACN - t_{25min}= 95% ACN, flow rate 1 mL/min, t_R = 17.0 min). ^{1}H NMR (400 MHz, $CDCl_3$): δ 8.29 (1H, t, *J* = 1.6 Hz), 8.23 (1H, d, *J* = 8.5 Hz), 8.14 (1H, d, *J* = 8.4 Hz), 8.03 (1H, d, *J* = 7.8 Hz), 7.85 (1H, d, *J* = 8.0 Hz), 7.79 (1H, d, *J* = 7.8 Hz), 7.77 (1H, t, *J* = 8.4 Hz), 7.72 (1H, d, *J* = 8.5 Hz), 7.58 (2H, d, *J* = 8.4 Hz), 7.57 (1H, t, ovl), 7.52 (1H, t, *J* = 7.8 Hz), 7.14 (2H, d, *J* = 8.4 Hz), 5.47 (2H, s). ^{13}C NMR (100 MHz, DMSO-d6): 168.3, 159.0, 158.5, 147.9, 141.0, 138.2, 133.1, 132.4, 131.0, 130.3, 129.5, 129.0, 128.9, 128.6, 128.3, 127.8, 127.7, 127.6, 120.6, 116.5 (2C), 71.9. HRMS-ESI *m/z* 354.1137 [M-H$^-$], $C_{23}H_{16}NO_3$ requires 354.1136.

(4'-(quinolin-2-ylmethoxy)-[1,1'-biphenyl]-4-yl)methanol (47) and (4'-(quinolin-2-ylmethoxy)-[1,1'-biphenyl]-3-yl)methanol (50). Starting from ester **45** and **48**, $LiBH_4$ reduction was carried out in the same experimental conditions previously reported, to obtain compounds **47** and **50**, respectively.

(4'-(quinolin-2-ylmethoxy)-[1,1'-biphenyl]-4-yl)methanol (47). Purification by flash column chromatography (silica gel, hexanes/ethyl acetate 8:2 v/v) furnished compound **47** (92% yield). An analytic sample was analysed by HPLC on a Kinetex Biphenyl (5 μm; 250 mm x 4.6 mm) column in gradient (t_0= 20% ACN - t_{5min}= 20% ACN - t_{20min}= 95% ACN - t_{25min}= 95% ACN, flow rate 1 mL/min, t_R = 19.4 min). ^{1}H NMR (400 MHz, $CDCl_3$): δ 8.22 (1H, d, *J* = 8.4 Hz), 8.11 (1H, d, *J* = 8.5 Hz), 7.85 (1H, d, *J* = 8.0 Hz), 7.76 (1H, t, *J* = 8.5 Hz), 7.71 (1H, d, *J* = 8.4 Hz), 7.57 (1H, t, *J* = 8.0 Hz), 7.55 (2H, d, *J* = 8.6 Hz), 7.53 (2H, d, *J* = 8.6 Hz), 7.42 (2H, d, *J* = 8.6 Hz), 7.10 (2H, d, *J* = 8.6 Hz), 5.44 (2H, s), 4.74 (2H, s). ^{13}C NMR (100 MHz, $CDCl_3$): δ 157.9, 157.8, 157.3, 147.5, 140.1, 137.1, 133.9, 129.8, 128.9, 128.5, 128.4, 127.7, 127.6, 127.5 (2C), 126.8 (2C), 126.5, 119.1, 115.2 (2C), 71.3, 65.1. HRMS-ESI *m/z* 342.1491 [$M+H^+$], $C_{23}H_{20}NO_2$ requires 342.1489.

(4'-(quinolin-2-ylmethoxy)-[1,1'-biphenyl]-3-yl)methanol (50). Purification by HPLC on a Nucleodur 100-5 (5 μm; 10 mm i.d. x 250 mm) with n-hexane/ethyl acetate 1:1 v/v as eluent (flow rate 3 mL/min, t_R = 20 min) gave compound **50** (quantitative yield); An analytic sample was further analysed by HPLC on a Kinetex Biphenyl (5 μm; 250 mm x 4.6 mm) column in gradient (t_0= 20% ACN - t_{5min}= 20% ACN - t_{20min}= 95% ACN - t_{25min}= 95% ACN, flow rate 1 mL/min, t_R = 17.2 min). ^{1}H NMR (400 MHz, $CDCl_3$): δ 8.22 (1H, d, *J* = 8.6 Hz), 8.12 (1H, d, *J* = 7.8 Hz), 7.85 (1H, d, *J* = 7.8 Hz), 7.76 (1H, t, *J* = 7.8 Hz), 7.71 (1H, d, *J* = 8.6 Hz),

7.57 (1H, t, *J* = 7.7 Hz), 7.55 (1H, s), 7.52 (2H, d, *J* = 8.6 Hz), 7.47 (1H, d, *J* = 7.6 Hz), 7.40 (1H, t, *J* = 7.6 Hz), 7.31 (1H, d, *J* = 7.6 Hz), 7.09 (2H, d, *J* = 8.6 Hz), 5.42 (2H, s), 4.76 (2H, s). ^{13}C NMR (100 MHz, $CDCl_3$): δ 158.1, 157.8, 147.5, 141.4, 140.9, 137.1, 133.9, 129.8, 128.9, 128.8, 128.3 (2C), 127.7, 127.6, 126.6, 126.0, 125.3 (2C), 119.1, 115.1 (2C), 71.2, 65.4. HRMS-ESI *m/z* 342.1487 [$M+H^+$], $C_{23}H_{20}NO_2$ requires 342.1489.

***In vitro* assay.**

Transactivation assay. To evaluate GPBAR1-mediated transactivation, HEK-293T cells were transfected with 200 ng of human pGL4.29 (Promega), a reporter vector containing a cAMP response element (CRE) that drives the transcription of the luciferase reporter gene luc2P, with 100 ng of pCMVSPORT6-human GPBAR1, and with 100 ng of pGL4.70. At 24 h post-transfection, cells were stimulated 18 h with TLCA 10 μM or compounds **24-50** 10 μM**.** After treatments, cells were lysed in 100 μL of lysis buffer (25 mM TRIS-phosphate, pH 7.8; 2 mM DTT; 10% glycerol; 1% Triton X-100), and 10 μL of cellular lysate was assayed for luciferase activity using the luciferase assay system (Promega). Luminescence was measured using Glomax 20/20 luminometer (Promega). Luciferase activities were assayed and normalized with Renilla activities.

Human $CysLT_1$ (LTD4) (h) (antagonist effect) Cellular Functional Assay. These assays were performed at Eurofins Cerep-Panlabs (France). The cells are suspended in DMEM buffer (Invitrogen), and then distributed in microplates at a density of 3.104 cells/well. The fluorescent probe (Fluo4 Direct, Invitrogen) mixed with probenecid in Hank's balanced salt solution (BSS) buffer (Invitrogen) complemented with 20 mM Hepes (Invitrogen) (pH 7.4) is then added into each well and equilibrated with the cells for 60 min at 37 °C then 15 min at 22 °C. Thereafter, the assay plates are positioned in a microplate reader (CellLux, PerkinElmer) which is used

for the addition of the test compound or HBSS buffer then 5 min later 0.1 nM LTD4 or HBSS buffer (basal control), and the measurements of changes in fluorescence intensity which varies proportionally to the free cytosolic Ca^{2+} ion concentration. The results are expressed as a percent inhibition of the control response to 0.1 nM LTD4. The standard reference antagonist is MK 571.

Dose-Response Curve. To calculate the EC_{50} of GPBAR1, dose response curves were performed in HEK-293T cells transfected as described above and then treated with increasing concentrations of compounds **27-29**, **31-33**, **36-38** (from 0.1 to 50 μM), and compound **49** (from 0.1 to 100 μM). At 18 h post stimulations, cellular lysates were assayed for luciferase and Renilla activities using the Dual-Luciferase Reporter assay system (E1980, Promega). Luminescence was measured using Glomax 20/20 luminometer (Promega). Luciferase activities were normalized with Renilla activities. To calculate the IC50 of $CysLT_1R$, dose-response curves were performed at Eurofins Cerep-Panlabs (France).

Cell culture. RAW264.7 cells were grown at 37 °C in D-MEM containing 10% FBS, 1% L-glutamine and 1% penicillin/streptomycin. Cells were regularly passaged to maintain exponential growth. The cell line was classically activated with LPS (100 nM, L2880; Sigma-Aldrich, St. Louis, MO), and exposed or not to **28**, **29** and **37** at the concentration of 0.1, 1, 5 and 10 μM for 16 h.

Real-Time PCR. To analyze the gene expression, total RNA was isolated from RAW264.7 cells using the TRIzol reagent according to the manufacturer's specifications (Life Technologies, Carlsbad CA). Total RNA was further purified using Direct-zol™ RNA MiniPrep (Zymo Research, Irvine, CA), which includes an on-column DNase I treatment. The Zymo-Spin™ IIC Columns were included in the kit. After purification

from genomic DNA by DNase-I treatment (Thermo Fisher Scientific, Waltam, MA), 1 μg of RNA from each sample was reverse-transcribed using random hexamer primers with Superscript-II (Thermo Fisher Scientific, Waltam, MA) in a 20 μl reaction volume; 10 ng cDNA were amplified in a 20 μl solution containing 200 nM of each primer and 10 μl of SYBR Select Master Mix (Thermo Fisher Scientific, Waltam, MA). All reactions were performed in triplicate using a Step One Plus machine (Applied Biosystem, Foster City CA). Primers were designed using the software PRIMER3 (https://bioinfo.ut.ee/primer3-0.4.0/) using published data obtained from the NCBI database. The primer used were as following (forward and reverse): Tnf-α (for CCAC CACGCTCTTCTGTCTA; rev AGGGTCTGGGCCATAGAACT), Il-1β (for GCTGAAAGCTCTCCACCTCA; rev AGGCCACAGGTATTTTGTCG) and Il-10 (for CCCAGAAATCAAGGAGCATT; rev CTCTTCACCTGCT CCACTGC).

Statistical analysis. The ANOVA followed by the nonparametric Mann-Whitney U test was used for statistical comparisons (*$P < 0.05$) using the Prism 6.0 software (GraphPad).

Physiochemical properties and pharmacokinetic characterization.

Solubility and LogD Measurements. Each compound was dissolved in DMSO at a concentration of 10 mM. Then, ten microliters of the obtained solution were diluted either in 490 μL of PBS pH 7.4 or MeOH and maintained under agitation at 250 rpm for 24 h at rt. Tubes were subsequently centrifuged for 5 min at 4000 rpm and 10 μL of each sample were further diluted in 490 μL of MeOH and analyzed by LC-MS/MS. The ratio of mass-signal area obtained in PBS and in organic solvent was then calculated and used to determine the solubility of each compound.

LogD was estimated by dissolving 40 µL of selected compounds in 1960 µL of PBS pH 7.4/Octanol. After shaking the mix for 2 hours at rt, organic and aqueous phases were separated and 10 µl of each phase were withdrawn, diluted in 490 µL of MeOH and analyzed by LC-MSMS. Concentrations of products were determined by mass signal and LogD was calculated as the logarithm of the ratio of compounds concentrations in octanol and PBS.

Metabolic Stability. All incubations were performed under shaking at 37 °C in a final volume of 0.5 mL, containing 50 mM potassium phosphate buffer (pH 7.4), all compounds were tested at the final concentration of 1 µM and 1% DMSO was used as vehicle. For microsomes assay, the incubation mixtures contained 0.15 mg of Human liver microsomes (Sigma-Aldrich, St. Louis, MO, USA) 5 mM $MgCl_2$, 1 mM NADPH, 5 mM glucose 6-phosphate, 0.4 U·mL−1 glucose 6-phosphate dehydrogenase. Aliquots were removed at 0, 5, 10, 20, 30, 40, 50, 60 min after microsomes addition. For S9 fraction analysis, the buffer contained 0.15 mg of S9 proteins (Sigma-Aldrich, St. Louis, MO, USA), 0.3 mM NADPH, 5.6 mM glucose-6-phosphate, 0.6 units/ml glucose-6-phosphate dehydrogenase, 5.8 mM UDP-glucuronic acid, 0.05 mM acetyl-CoA, 0.5 mM dithiothreitol, 0.5 mM 3'-phosphoadenosine 5'-phosphosulfate, 1 mM glutathione, 0.2 mM acetyl carnitine, 4 units/mL carnitine acetyl transferase, 0.5 mM glycine, and 0.5 mM taurine and aliquots were removed at 0, 5, 15, 30, 45, 60, 90, 120, 150 min after S9 fraction addition. The reaction was stopped by adding 200 µL of ice-cold acetonitrile to withdrawn aliquots. After two hours, samples were centrifuged for 10 min at 10,000 rpm, and supernatants were subjected to LC-MS/MS analysis.

The slope of the linear regression of the curve obtained reporting the natural logarithm of compound area versus incubation time (−k) was used

in the conversion to in vitro $t_{1/2}$ values by $t_{1/2} = -\ln(2)/k$. *In vitro* intrinsic clearance (Cl_{int} expressed as µL/min/mg) was calculated and expressed as µL/min/mg. The percentage of unmodified compound has been calculated assuming the peak area of the compound at time 0 min as 100%. Testosterone was used as a positive control for microsome and phase I enzymes, and 7-hydroxycoumarin was used as positive control for phase II enzymes.

Computational studies.

$CysLT_1R$. The crystal structure of the Homo sapiens Cysteinyl leukotriene receptor 1 (PDB ID 6rz4) was downloaded from the Protein Data Bank website. The soluble cytochrome b562 fragment, the co-crystallized ligand and water molecules were removed and the residue Gln274 was reconstructed. The missing 2 residues of ECL3 and the missing transmembrane helix 8 (TM8) were modelled using the Modeller 9.2 software package. For TM8, the crystallographic structure of $CysLT_2R$ (PDB ID 6RZ6) was employed as a template and its secondary structure was confirmed using prediction tools PSIpred and Spider3. Residues protonation states were assigned in accordance with the most populated ones predicted by the H++ webserver at pH 7.4. The final model was validated via 1 µs long molecular dynamics simulation. The protein was put in a box of size 10x10x12 nm and embedded in a lipid bilayer composed of cholesterol (CHL) and 1-palmitoyl-2-oleoyl-sn-glycero-3-phosphocholine (POPC) with a 30:70 ratio using the CHARMM-GUI webserver. For solvation, TIP3P water molecules were employed and a 0.150 mM concentration of NaCl was added to reach electrostatic neutrality. The simulation was performed using the Amber ff14SB and Lipid 17 force fields with the GROMACS 2020.4 software package.

GPBAR1. GPBAR1 homology model reported in D'Amore et al.[136] was employed for docking calculations. The receptor was prepared as in Biagioli et al.[150]

Both the receptors were treated with the Protein Preparation Wizard tool implemented in Maestro ver. 11.8.

Ligands. 3D structures of **24-50** were built using the Graphical User Graphical User Interface (GUI) of Maestro ver. 11.8. The protonation state of **24-50** at pH 7.4 in water has been calculated using the Epik module. Finally, **24-50** were then minimized using the OPLS 2005 force field through 2500 iteration steps of the Polak-Ribiere Conjugate Gradient (PRCG) algorithm.

Docking calculations. Preliminary docking calculations were performed using Glide and Autodock 4.2 to reproduce the binding pose of the pranlukast ligand recently co-crystalized with $CysLT_1R$ (PDB ID 6rz4). This redocking step allowed us to identify the most suitable parameters and scoring function for docking of **24-50**. Considering the ability to reproduce the pranlukast crystallographic binding pose, Glide was finally employed for the docking calculations. The results were clustered and successively ranked according to the Glide Emodel and the Glide Score. Docking calculations of **24-50** on GPBAR1 were performed using the same approach described in Biagioli et al.[150]

To consider the ligand induced-fit effect on the receptors' binding sites – rearrangement of residue side chains to improve interaction with the ligand -, we performed docking calculations on **28** in both GPBAR1 and CysLT1R using as structure the centroid of the most populated protein conformation during the MD calculations on the **28**/GPBAR1 and **28**/$CysLT_1R$ complex, respectively.

In detail, the docking procedure was carried out with the Glide software package, using the Standard Precision (SP) algorithm of the GlideScore function and the OPLS 2005 force field. A grid box of 2.5 × 1.6 × 1.7 nm for GPBAR1 receptor and one of 1.6 × 2.0 × 1.8 nm for CysLT1R centred on the ligand binding cavity were created. A total amount of 100 poses was generated and the conformational sampling of the ligand was enhanced by two times, as reported by the default setting of Glide. Docking conformations of **24-50** were then clustered based on their atomic RMSD. Globally, seven clusters were obtained and, among them, only the conformation included in the most populated cluster with both the Glide Emodel and GlideScore lowest-energy value was considered.

MD calculations. MDs were performed with GROMACS suite ver. 2020.4, using the Amber ff14SB, Lipid 17 and the General Amber Force Field (GAFF) for the proteins, lipids and ligands, respectively. Protein/ligand complexes were prepared as previously reported for $CysLT_1R$ and GPBAR1 and embedded in a 30:70 CHL/POPC lipid bilayer of sizes 10x10nm. The resulting membrane was then solvated with TIP3P water and a 0.150 mM concentration of NaCl into a 10x10x12 nm box. The whole procedure was carried out using the CHARMM-GUI webserver.

The systems were minimized using the steepest descent algorithm in a two steps procedure. First, the protein and ligand heavy atoms were restrained, whereas water molecules and ions were left free and only the movement on the Z axis of hydroxyl group of CHL and the phosphate group of POPC was restrained. Afterward, the restraints were removed, and a second round of minimization was performed. The systems were then gradually heated from 50 to 300 K using a stepwise approach of NVT/NPT simulations at fixed temperature, before increasing it by 50 K. Each

NVT/NPT step lasted 1 ns. An initial restraint of 1000 kJ/mol at 50 K was applied on proteins, ligands and lipids as described for the minimization procedure. After each NVT/NPT cycle, the restraints were lowered by 160 kJ/mol. The Langevin dynamics integrator and the Berendsen barostat with semi-isotropic coupling at 1 atm were employed. After reaching 300 K, a preliminary production run of 10ns without restraints was performed using the Langevin dynamics integrator and the Parrinello-Rahman barostat with semi-isotropic coupling at 1 atm. The same parameters were employed for the following production runs of 1 μs. In all these simulations, a time step integration of 2 fs. For the computation of electrostatic and Van der Waals interactions, the Particle-Mesh Ewald (PME) and the cutoff algorithms were used, respectively, with a threshold of 1.2 nm. The cluster analysis trajectory was carried out using the GROMACS gmx cluster tools with the GROMOS method and a 0.2 nm cutoff.

Free-energy calculations. Well-tempered MetaD simulations were performed using the same protocol described for MD calculations. However, the GROMACS suite ver. 2020.4 was patched with the Plumed software package ver. 2.6.2 and the Cα atoms of the protein structured parts (i.e. alpha helices, beta strands) were restrained around the initial conformation using a RMSD-based harmonic potential with constant 10000 kJ/mol and threshold 0.1 nm. As collective variable, the distance between the heavy atoms of the quinoline moiety and the Cβ of CysLT1R Arg792.60 was chosen. This distance CV was allowed to explore the values from 0 to 3.0 nm to limit the sampling of the free-energy landscape to the interior of the binding pocket. To do so, an upper wall with constant 10000 kJ/mol was placed at 3.0 nm of the distance CV to prevent the ligand from exiting the CysLT1R cavity. A bias of 1 kJ/mol was deposited every

5 ps with a sigma of 0.05 nm and a bias factor of 15. The MetaD simulations were performed using 10 multiple walkers lasting 150 ns each, for a total of 1.5 μs of calculation.

MD trajectories were visualized using VMD software and all figures were rendered by UCSF Chimera.

***In vivo* stability of compound 49**

The amount of compound **49** in plasma samples of treated animals was evaluated by measuring the peak area of the compound at 1, 6 and 24 h after administration. 50 μL of plasma samples were mixed with 200 μL of acetonitrile, vortexed and incubated for 1 hour on ice. Samples were then centrifuged for 10 min at 10000 rpm and supernatants were evaporated to dryness. For LC/MS-MS analysis a QTRAP 6500 System (AB Sciex) equipped with Shimadzu LC-20A LC and AutoSampler was employed. Samples were dissolved in 100 μL of H2O, 30% MeOH, 0.2% FA and the chromatographic separation was performed using a Luna Omega 3 μm Polar C18 100x2.1 mm (Phenomenex) and the best chromatographic results were achieved using the following gradient: 20% B from 0 to 1 min, 20% to 80% B from 1 to 5.0 min, 80% to 95% B from 5.0 to 5.1 min, held at 95% B for 3 min and then to 20% B (Buffer A: H2O 0.2% FA; Buffer B: MeOH 0.1 % FA). The transition 356 →143 was employed for quantification. The following parameters were set: positive mode, DP 120 eV, EP 12 eV, CE 40 eV, CXP 23 V, CUR 30 psi, CAD Medium, IS 5500 V, TEM 350 °C, GS1 and GS2 50 psi.

GEO Data Sets

The GSE135251 series includes gene expression profiles (RNA-seq analysis, Illumina NextSeq 500 system) of 216 snap frozen liver biopsies, comprising 206 NAFLD cases with different fibrosis stages and 10 controls.

Animal model

C57BL/6J male mice were fed a high-fat diet (HFD) containing 59 KJ% fat plus 1% cholesterol, w/o sugar (ssniff ® EF R/M acc. D12330 mod. 22,7 ME/Kg) and fructose (HFD-F) in drinking water (42 g/l), or normal chow diet for 9 weeks. Food intake was estimated as the difference in weight between the offered and the remnant amount of food at 3-day intervals. The food was provided as pressed pellets and the residual spillage was not considered. After 10 days, HFD-F mice were randomized to receive HFD-F alone or in combination with compound **49** (30 mg/kg/day) by gavage for 8 weeks. Doses of each agent were chosen according to previously published data. Mice were housed under controlled temperature (22°C) and photoperiods (12:12-hour light/dark cycle), allowed unrestricted access to standard mouse chow and tap water. The experimental protocol was approved by the Animal Care and Use Committee of the University of Perugia and by the Italian Minister of Health and Istituto Superiore di Sanità (Italy) and were in agreement with the European guidelines for use of experimental animals (permission n. 583/2017-PR). The general health of the animals was monitored daily by the Veterinarian in the animal facility. At the day of sacrifice, fed mice were deeply anesthetized with a mixture of tiletamine hypochloride and zolazepam hypocloride/xylazine at a dose of 50/5 mg/Kg and sacrificed before 12 AM.

Anthropometrical determinations

Body weight and body length (nose-to-anus or nose–anus length), were measured in anesthetized mice at time of sacrifice and were used to calculate the Body mass index (BMI) (=body weight (g)/length2 (cm2)) and the Lee index (=cube root of body weight (g)/nose-to-anus length (cm)).

Biochemical analyses

AST, ALT, total- and HDL-cholesterol and triglycerides plasmatic levels were quantified using an automated clinical chemistry analyzer (Cobas, Roche).

OGTT and insulin levels

After 8 weeks of HFD-F mice were fasted overnight and orally administered glucose (1.5 g/kg body weight) for OGTT. The blood glucose concentrations were measured at 0, 15, 30, 60, 90, and 120 min after feeding or injection using a portable glucose meter (Accu-Check Go, Roche).

Thermal images

Temperature of brown adipose tissue (BAT) was recorded through the study using a non-invasive technology. Briefly, mice were maintained at 25 °C and the thermal images were taken by a FLIR E6 thermal imaging camera (FLIR System, Wilsonville, Oregon) and the surface temperature quantified by the FLIR Tools.

Histopathology

For histological examination, portions of the right and left liver lobes were fixed in 10% formalin, embedded in paraffin, sectioned and stained with Sirius red and/or Hematoxylin/Eosin (H&E), for morphometric analysis. NASH severity (steatosis, hepatocytes ballooning, lobular inflammation and portal inflammation) was scored in H&E-stained cross sections using an adapted grading system of human NASH as described previously.27 Hepatic fibrosis score was evaluated in Sirius red stained sections has described previously.

Quantitative Real-Time PCR analysis

RNA was extracted from eWAT with Direct-zol™ RNA MiniPrep w/ Zymo-Spin™ IIC Columns (Zymo Research, Irvine, CA) and it was

subjected to reverse transcription with FastGene Scriptase Basic Kit (Nippon Genetics Europe) in a 20 µL reaction volume.

For Real Time PCR, 50 ng cDNA were amplified in a 20 µL solution containing 200 nM of each primer and 10 µL of SYBR Select Master Mix (Thermo Fisher Scientific, Waltham, MA, USA). All reactions were performed in triplicate, and the thermal cycling conditions were as follows: 10 min at 95°C, followed by 40 cycles of 95°C for 10 sec and 60°C for 45 sec with QuantStudio™ 3 Real-Time PCR System (Applied Biosystems). The relative mRNA expression was calculated and expressed as $2^{-(\Delta\Delta Ct)}$. Expression of the respective gene was normalized against Gapdh mRNA as an internal control. The following primers for Real-Time PCR were used: mouse-Gapdh: ctgagtatgtcgtggagtctac and gttggtggtgcaggatgcattg; mouse-Srebf1: gatcaaagaggagccagtgc and tagatggtggctgctgagtg; mouse-Fasn: tcaagatgaaggtggcagaggtgct and ttgagcagtgccgggattcgg; mouse-Pgc1α: cttagcactcagaaccatgcag and aatgctcttcgctttattgctc; mouse-Fxr: actggaccacgaagatcagatt and gagcgtactcctcctgagtcat; mouse-adiponectin: tgacagatcagctcgagtgg and cagtgccgtcagttcttgtg; mouse-Tnf-α: ccaccacgctcttctgtcta and agggtctgggccatagaact; mouse-ucp2: ttgcccgtaatgccattgtc and gcaagggaggtcatctgtca; mouse- cd11b gtcagagtctgcctccgtgt and cagggtctaaagccaggtca; mouse-pparγ: gccagtttcgatccgtagaa and aatccttggccctctgagat.

AmpliSeq transcriptome

High-quality RNA was extracted from mice livers, using the Directzol™ RNA MiniPrep w/ Zymo-Spin™ IIC Columns (Zymo Research, Irvine, CA) according to the manufacturer's instructions. RNA quality and quantity were assessed with the Qubit® RNA HS Assay Kit and a Qubit 3.0 fluorometer (Invitrogen, Carlsbad, CA) followed by agarose gel

electrophoresis. Libraries were generated using the Ion AmpliSeq™ Transcriptome Mouse Gene Expression Core Panel and Chef-Ready Kit (Comprehensive evaluation of AmpliSeq transcriptome, a whole transcriptome RNA sequencing methodology) (Thermo Fisher Scientific, Waltham, MA). Briefly, 10 ng of RNA was reverse transcribed with SuperScript™ Vilo™ cDNA Synthesis Kit (Thermo Fisher Scientific, Waltham, MA) before library preparation on the Ion Chef™ instrument (Thermo Fisher Scientific, Waltham, MA). The resulting cDNA was amplified to prepare barcoded libraries using the Ion Code™ PCR Plate, and the Ion AmpliSeq™ Transcriptome Mouse Gene Expression Core Panel (Thermo Fisher Scientific, Waltham, MA), Chef-Ready Kit, according to the manufacturer's instructions. Barcoded libraries were combined to a final concentration of 100 pM and used to prepare Template-Positive Ion Sphere™ (Thermo Fisher Scientific, Waltham, MA) Particles to load on Ion 540™ Chips, using the Ion 540™ Kit-Chef (Thermo Fisher Scientific, Waltham, MA). Sequencing was performed on an Ion S5™ Sequencer with Torrent Suite™ Software v6 (Thermo Fisher Scientific, Waltham, MA). The analyses were performed with a range of fold <-2 and $>+2$ and a p value < 0.05, using Transcriptome Analysis Console Software (version 4.0.1), certified for AmpliSeq analysis (Thermo-Fisher). The transcriptomic data have been deposited as dataset on Mendeley data repository (reference number linking to the repository: Fiorucci, Stefano; Biagioli, Michele; Marchianò, Silvia; Di Giorgio, Cristina (2021), “Discovery of potent dual GPBAR1/CysLT1R modulator for the treatment of metabolic fatty liver disease”, Mendeley Data, V1, doi: 10.17632/6dnrk9fc72.1).

NMR spectra

^{1}H NMR (400 MHz, $CDCl_3$) of compound **24**

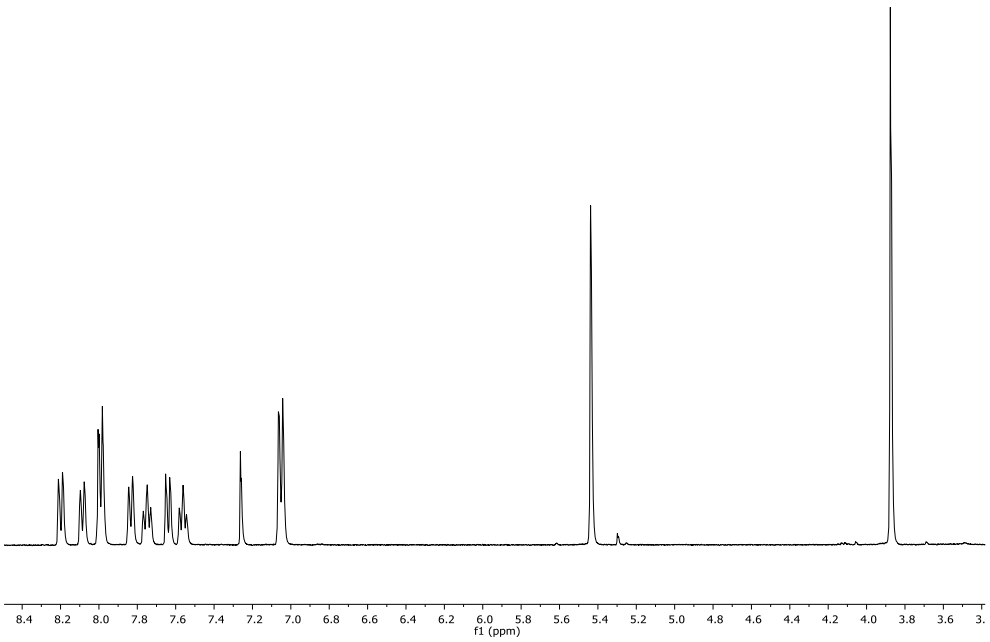

^{13}C NMR (100 MHz, $CDCl_3$) of compound **24**

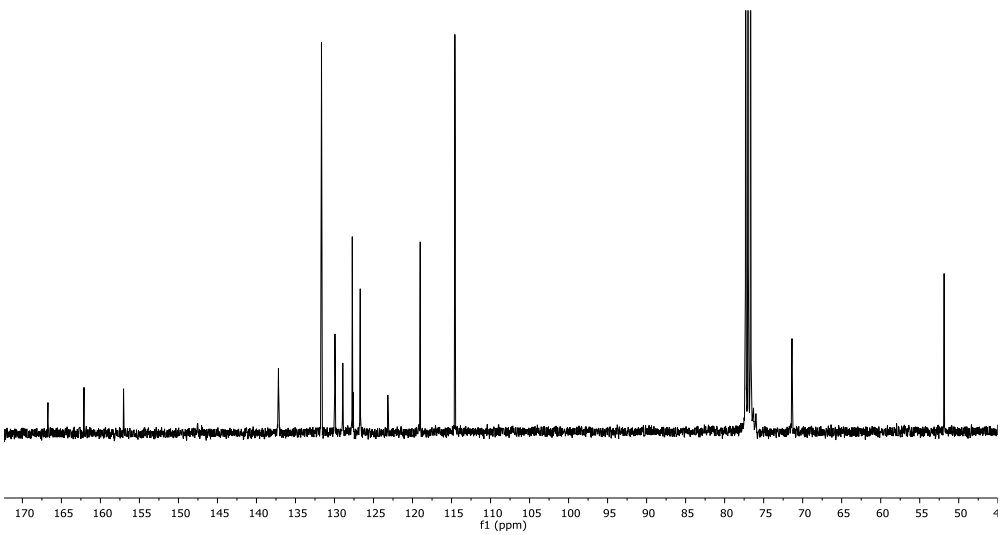

^{1}H NMR (400 MHz, $CDCl_3$) of compound **25**

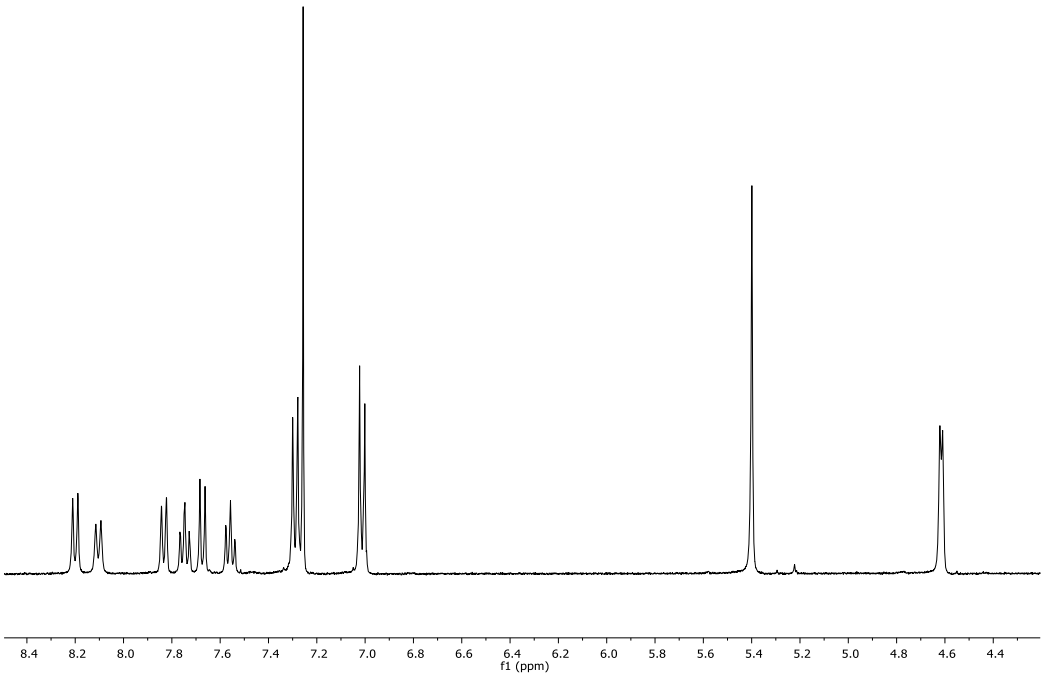

^{13}C NMR (100 MHz, $CDCl_3$) of compound **25**

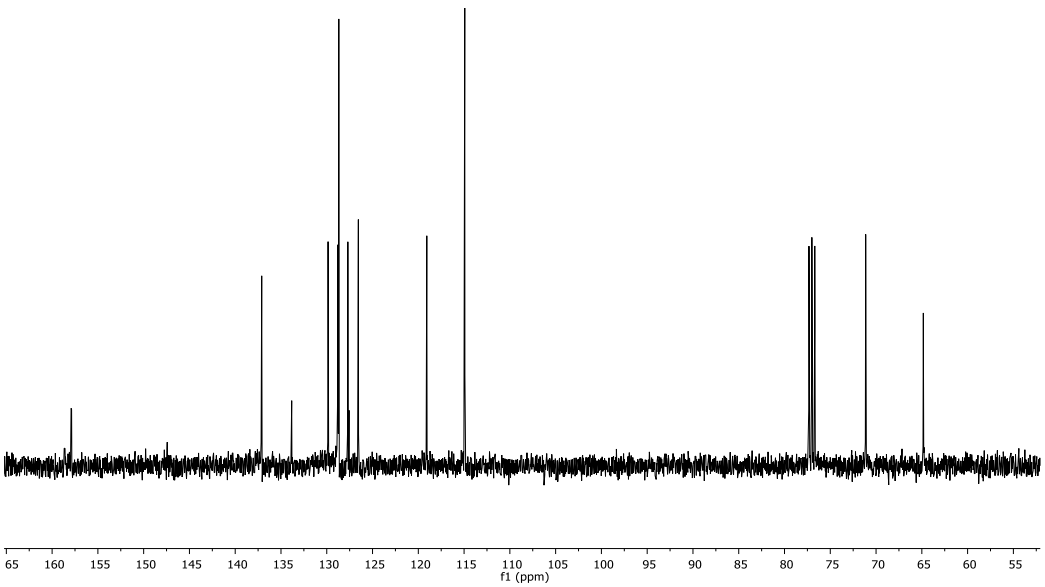

^{1}H NMR (400 MHz, CD_3OD) of compound **26**

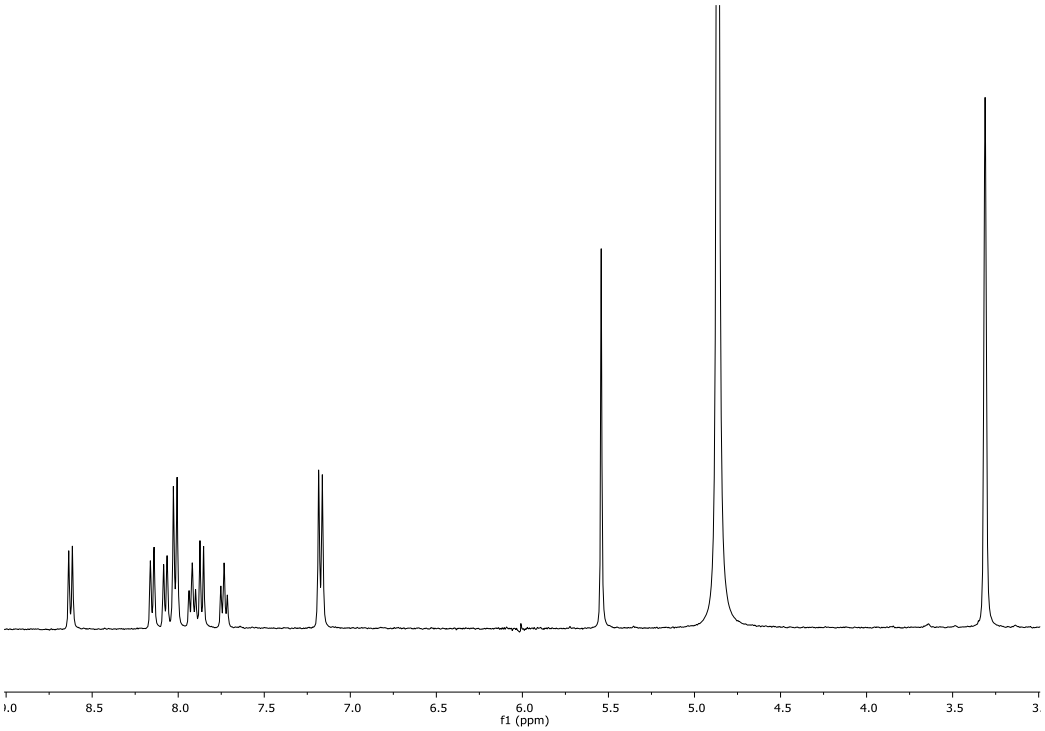

^{13}C NMR (100 MHz, CD_3OD) of compound **26**

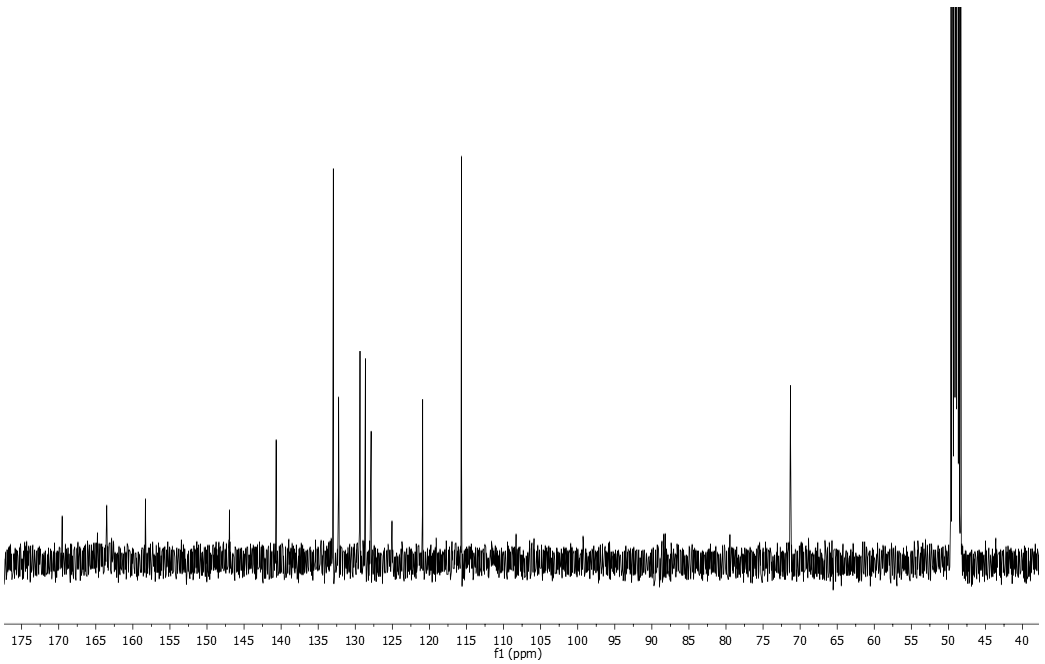

^{1}H NMR (400 MHz, $CDCl_3$) of compound **27**

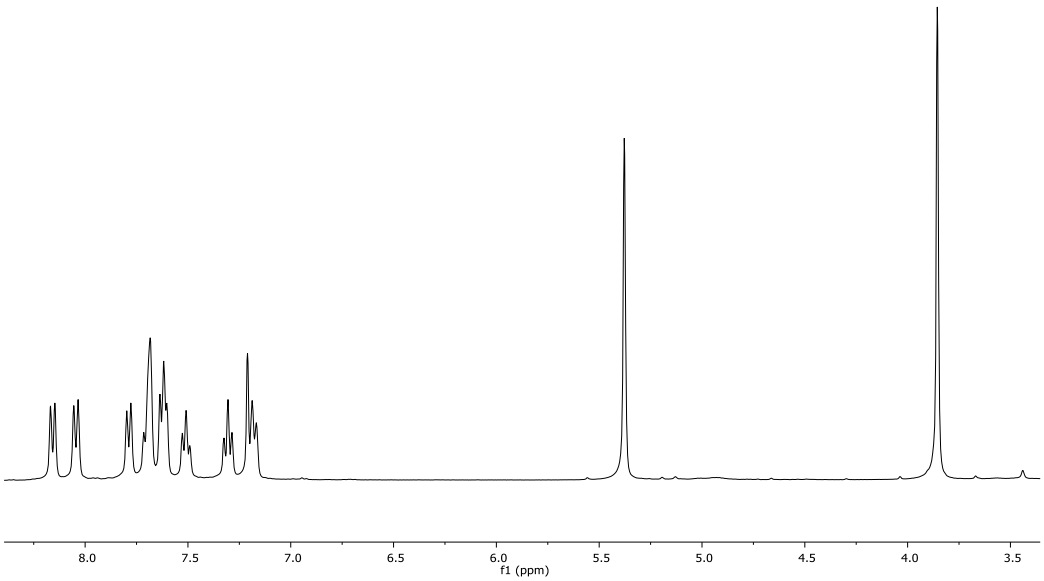

^{13}C NMR (100 MHz, $CDCl_3$) of compound **27**

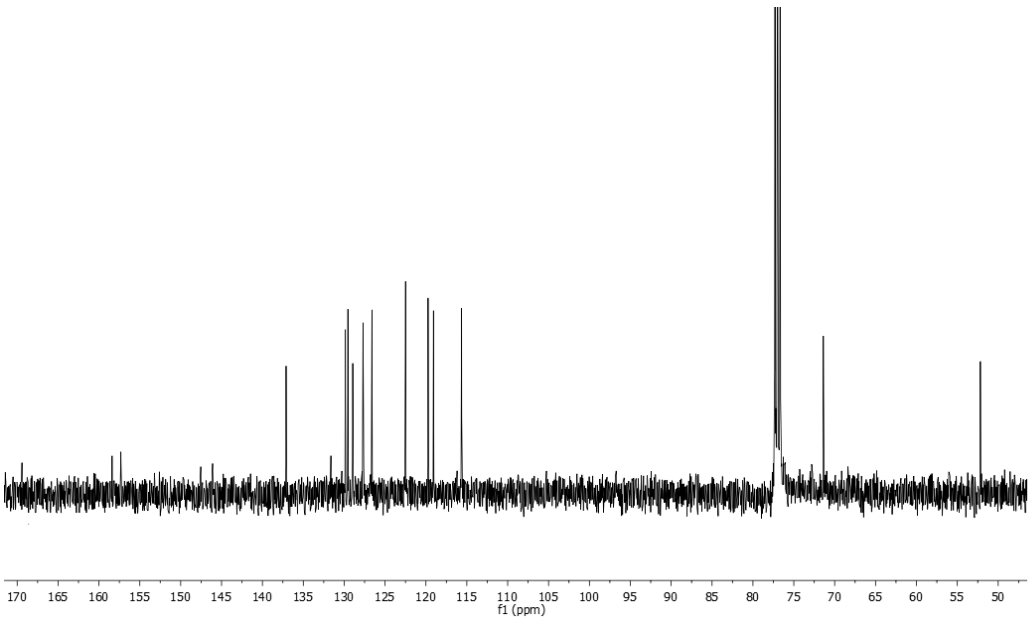

^{1}H NMR (400 MHz, $CDCl_3$) of compound **28**

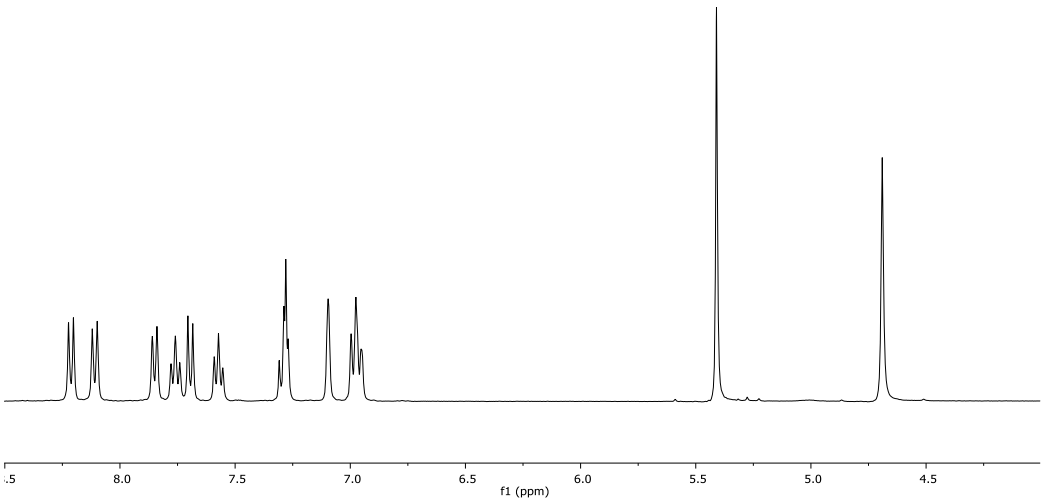

^{13}C NMR (100 MHz, $CDCl_3$) of compound **28**

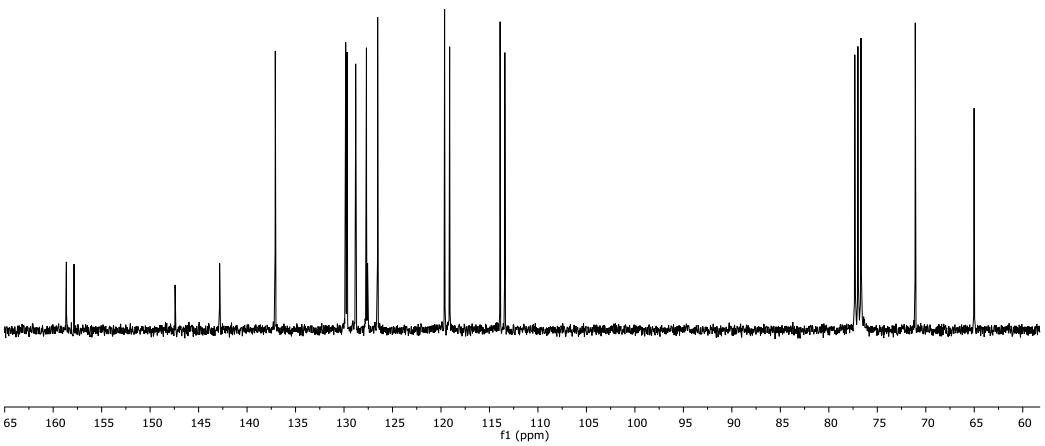

^{1}H NMR (400 MHz, CD_3OD) of compound **29**

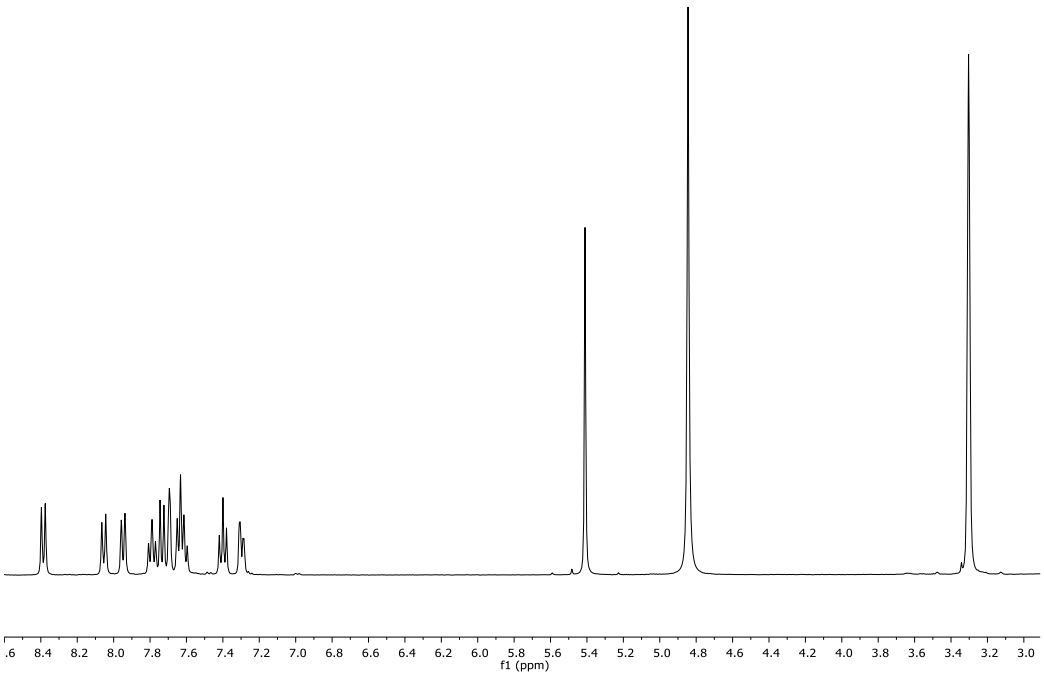

^{13}C NMR (100 MHz, CD_3OD) of compound **29**

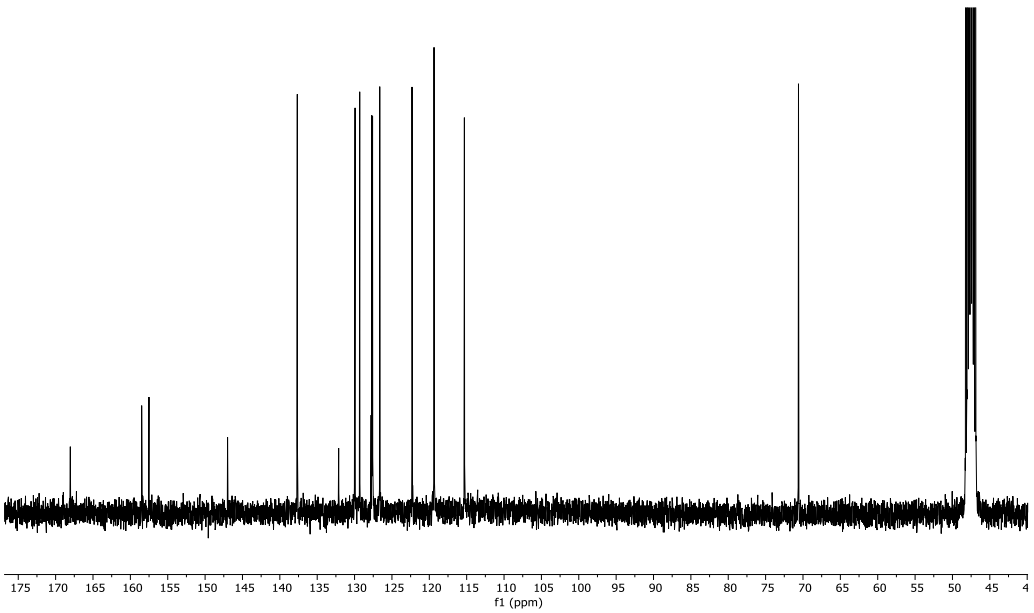

^{1}H NMR (400 MHz, $CDCl_3$) of compound **30**

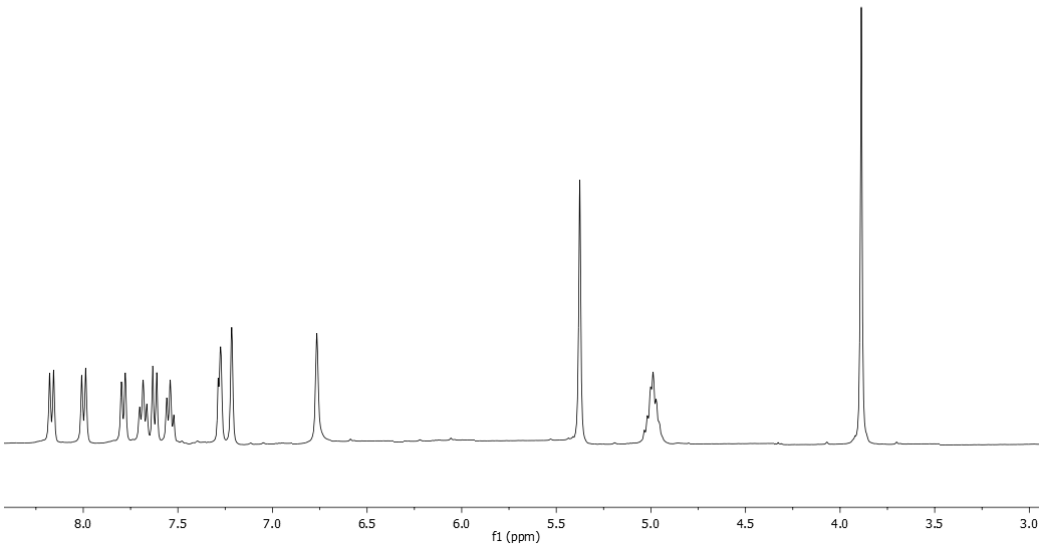

^{13}C NMR (100 MHz, $CDCl_3$) of compound **30**

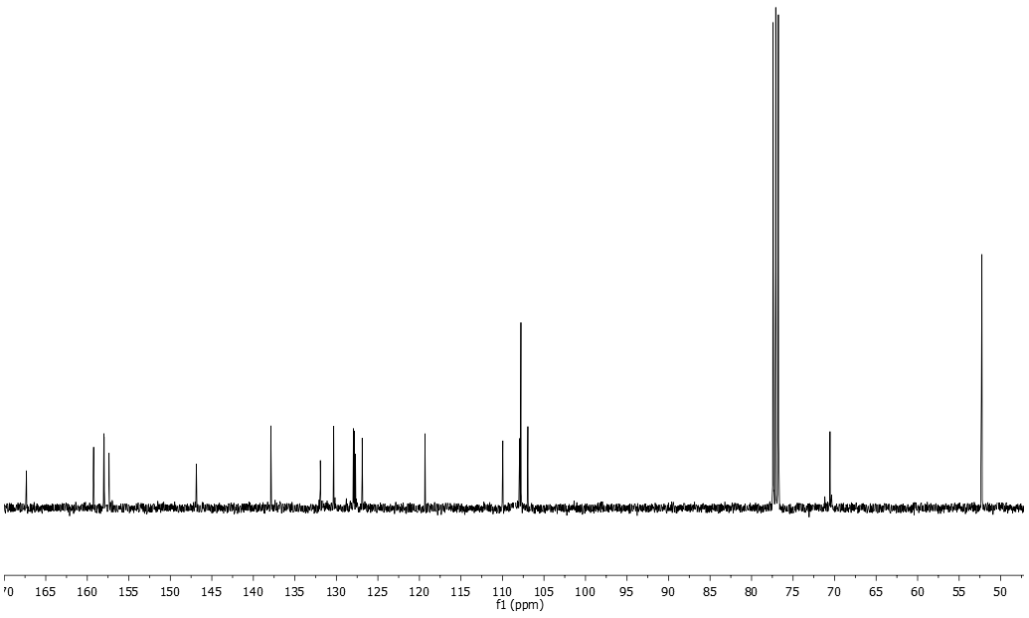

^{1}H NMR (400 MHz, CD_3OD) of compound **31**

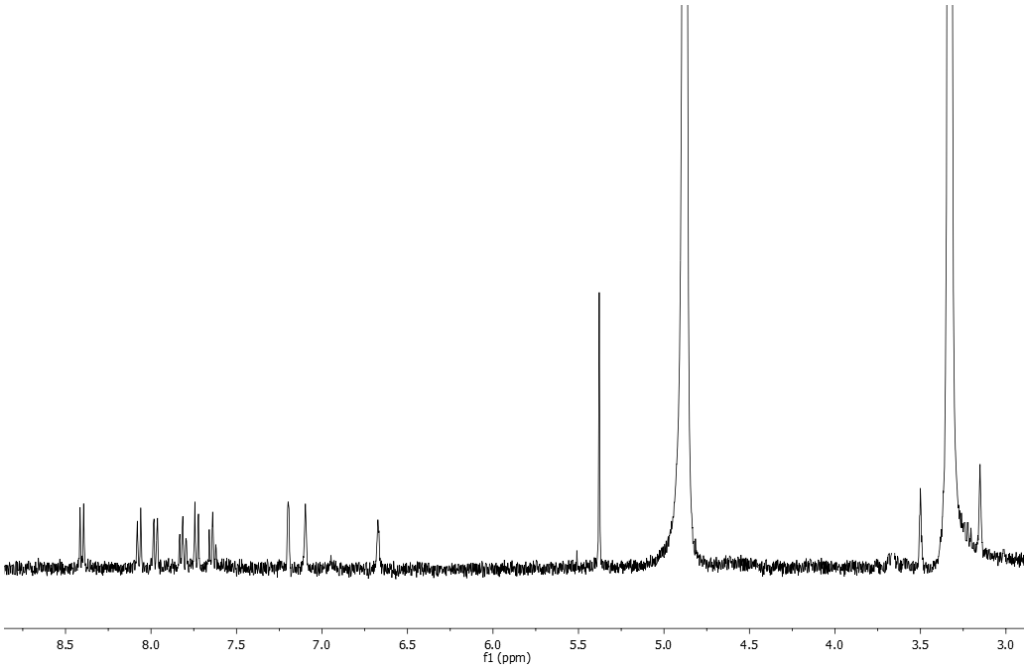

^{13}C NMR (100 MHz, CD_3OD) of compound **31**

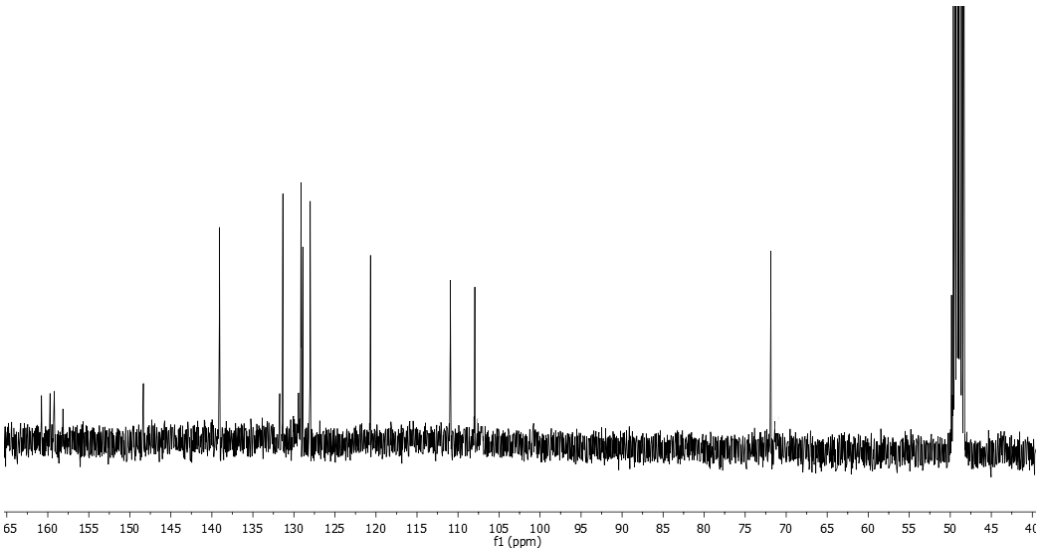

^{1}H NMR (400 MHz, CD_3OD) of compound **32**

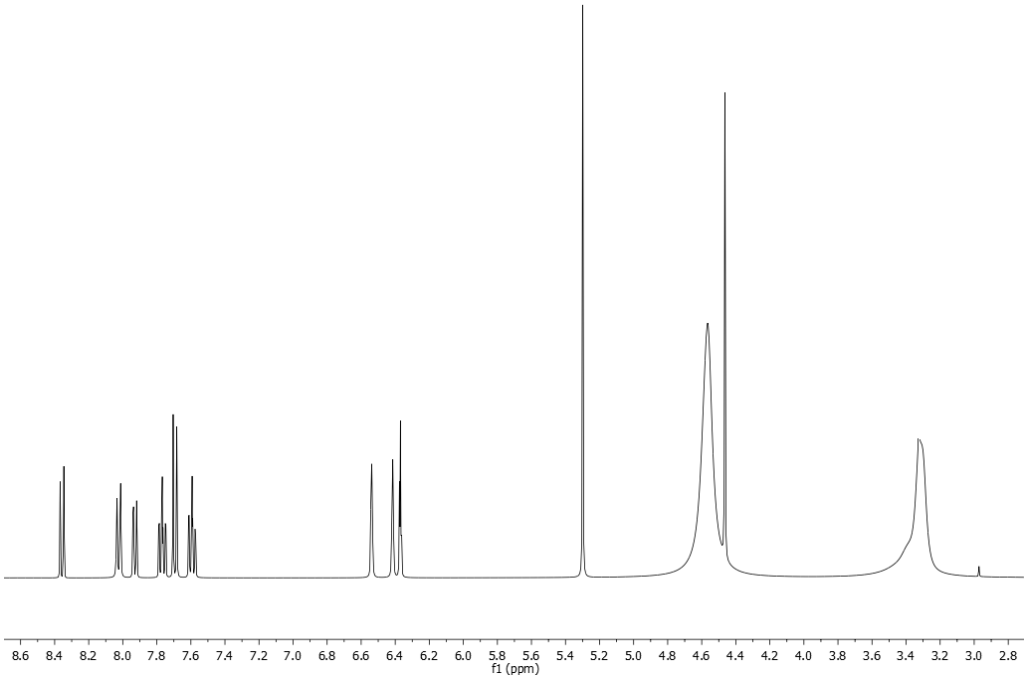

^{13}C NMR (100 MHz, CD_3OD) of compound **32**

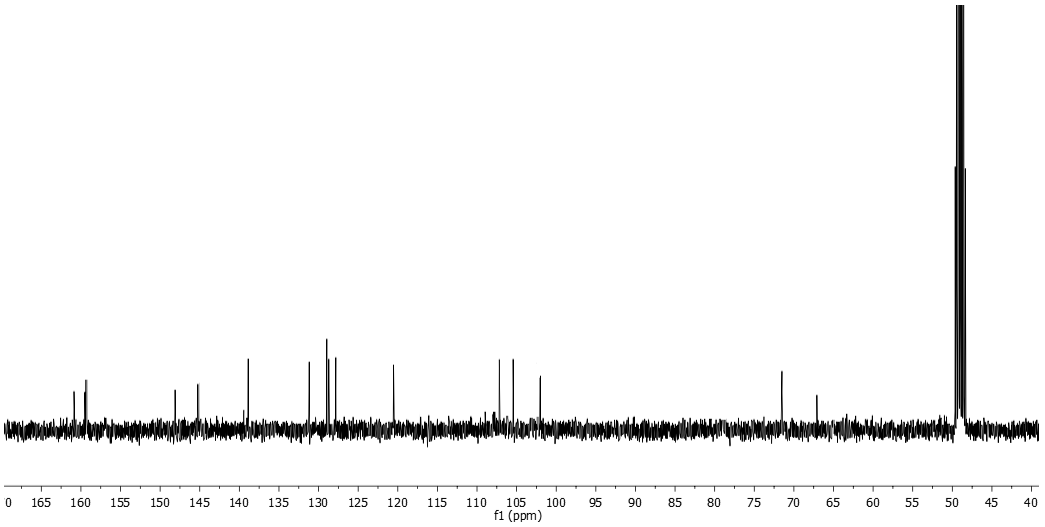

^{1}H NMR (400 MHz, $CDCl_3$) of compound **33**

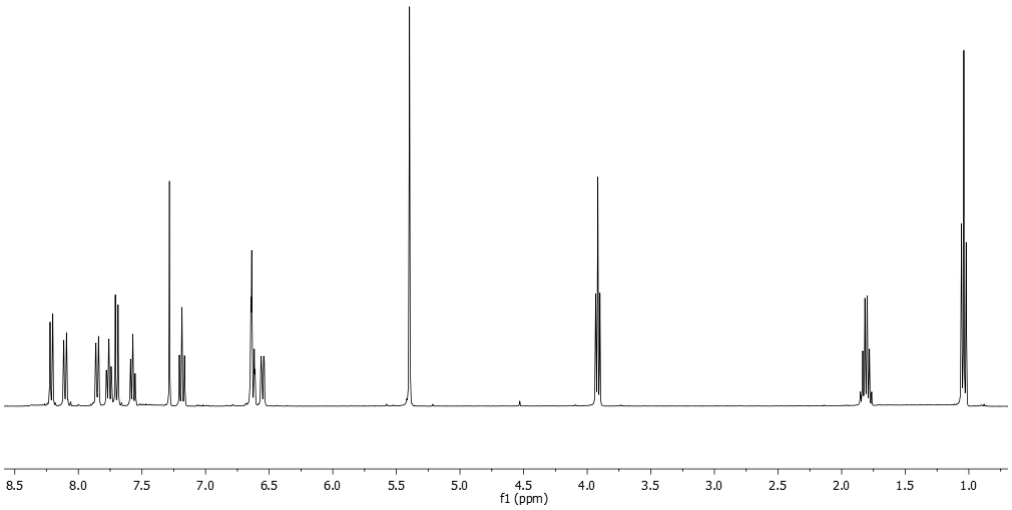

^{13}C NMR (100 MHz, $CDCl_3$) of compound **33**

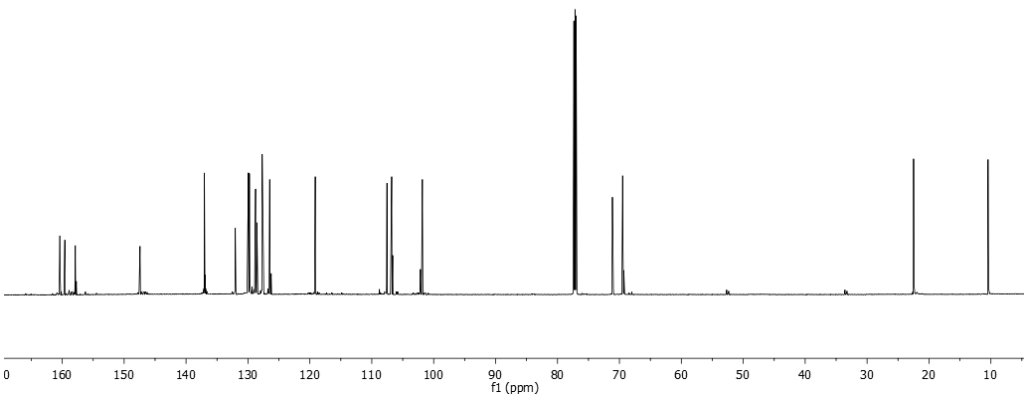

^{1}H NMR (400 MHz, $CDCl_3$) of compound **34**

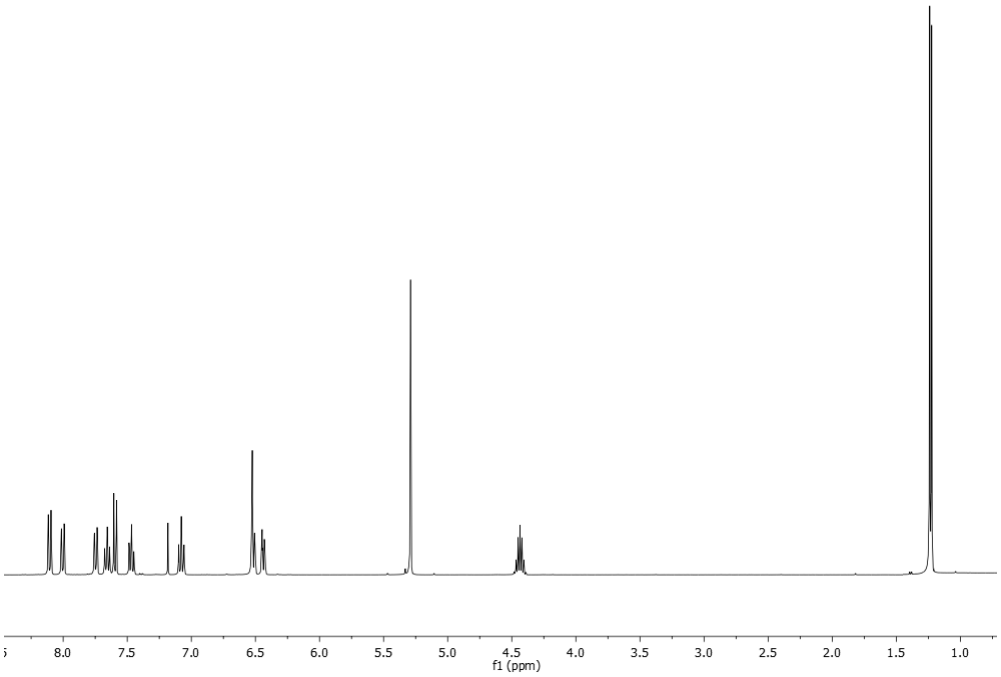

^{13}C NMR (100 MHz, $CDCl_3$) of compound **34**

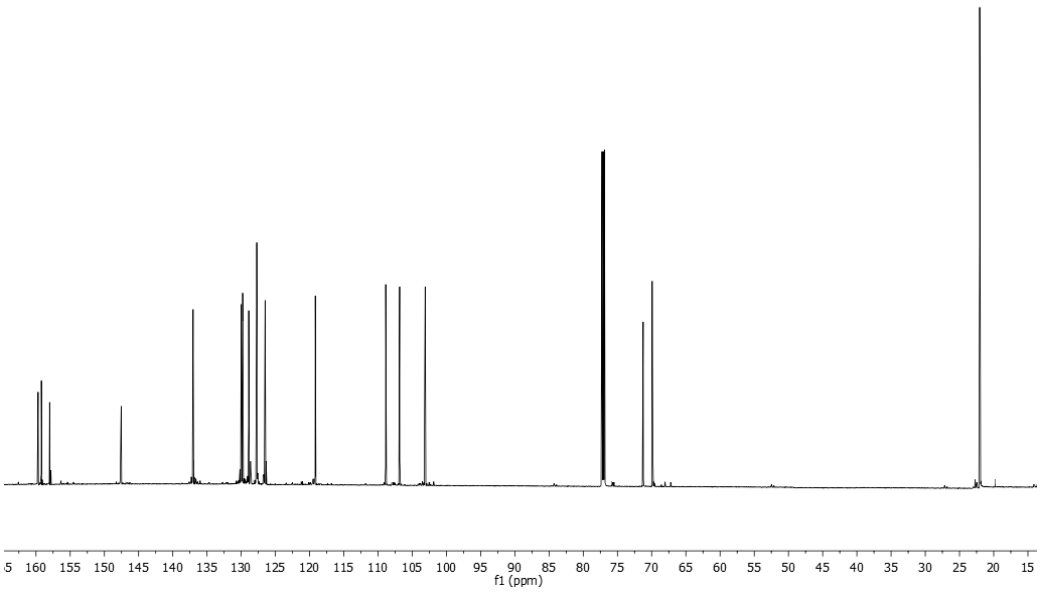

^{1}H NMR (400 MHz, $CDCl_3$) of compound **35**

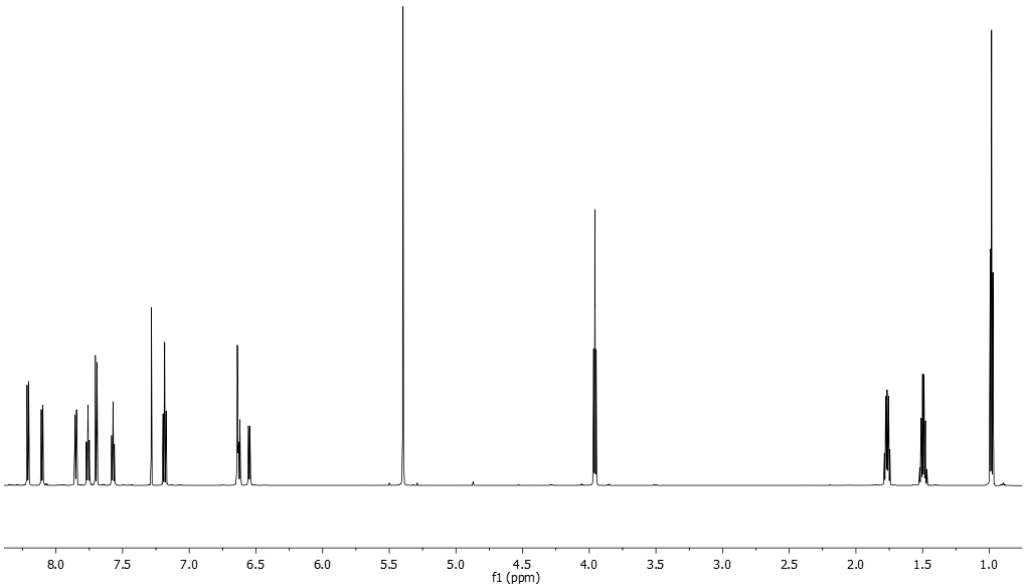

^{13}C NMR (100 MHz, $CDCl_3$) of compound **35**

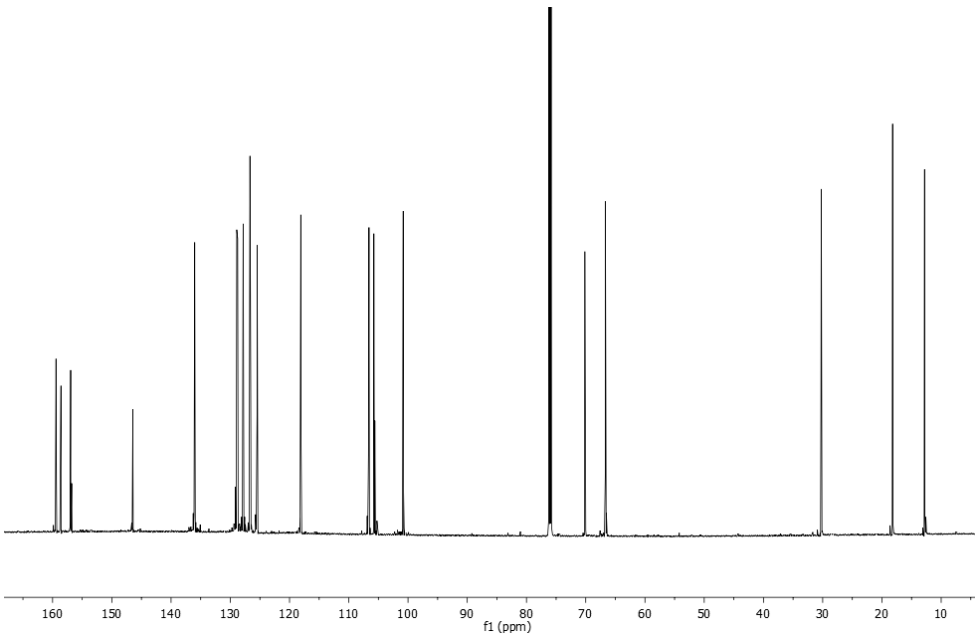

^{1}H NMR (400 MHz, $CDCl_3$) of compound **36**

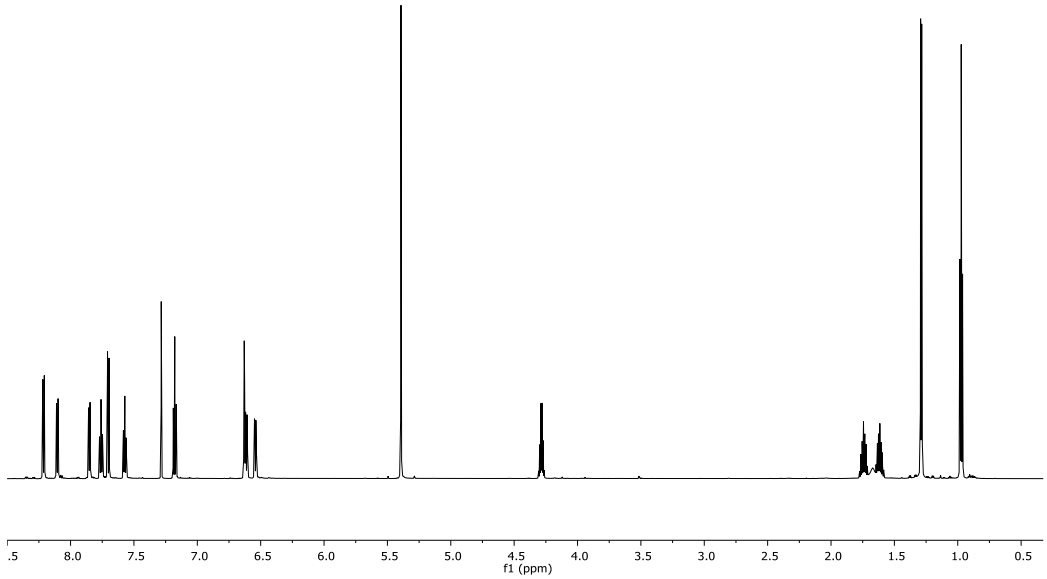

^{13}C NMR (100 MHz, $CDCl_3$) of compound **36**

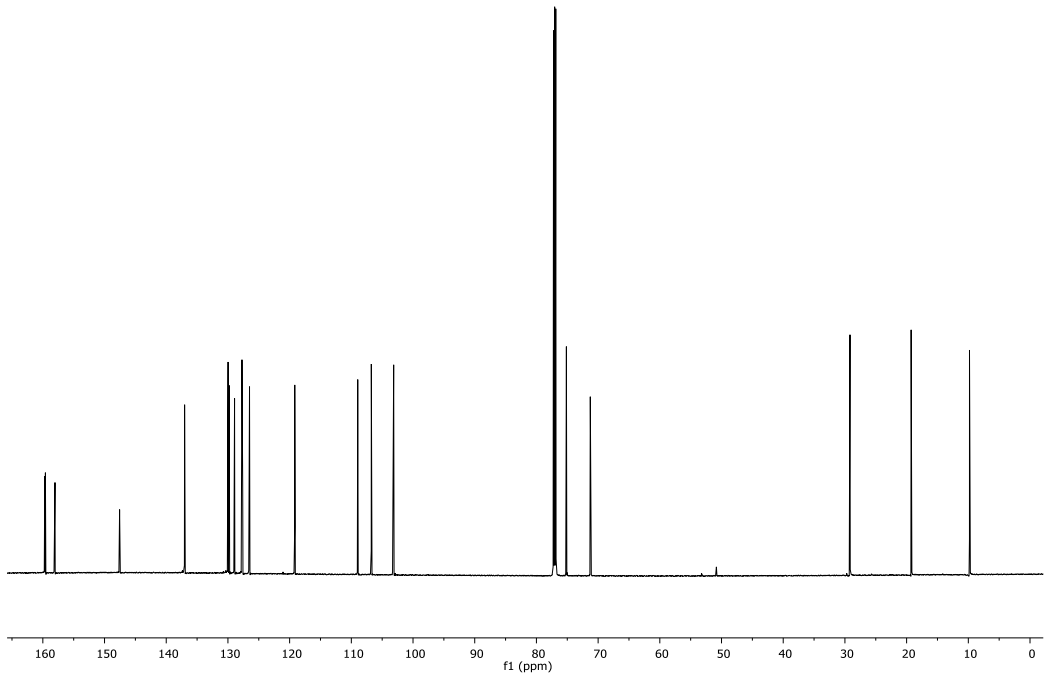

^{1}H NMR (400 MHz, $CDCl_3$) of compound **37**

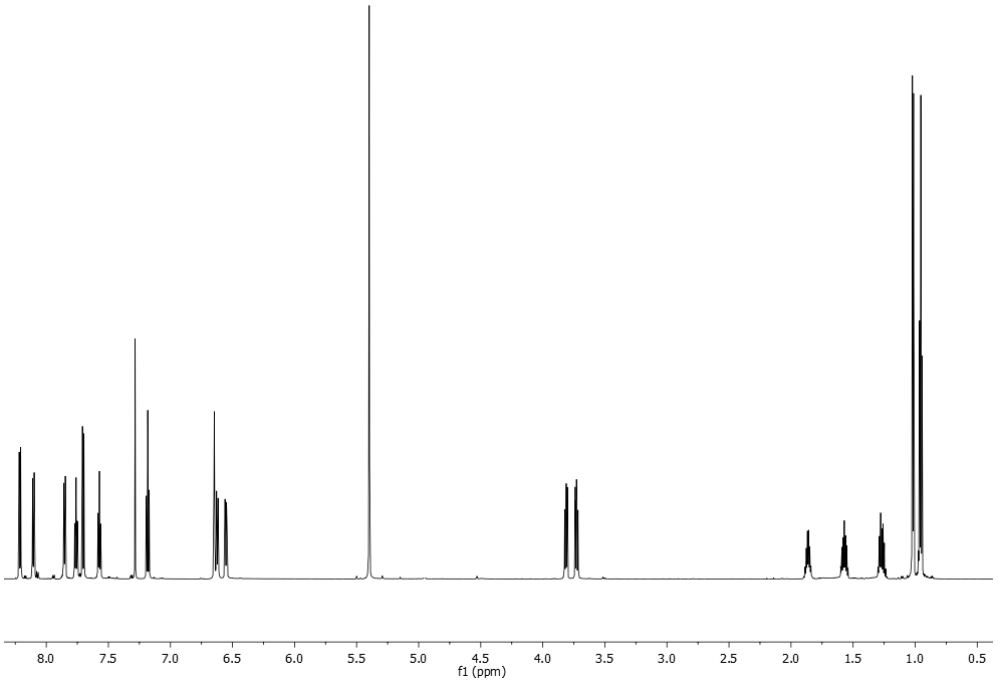

^{13}C NMR (100 MHz, $CDCl_3$) of compound **37**

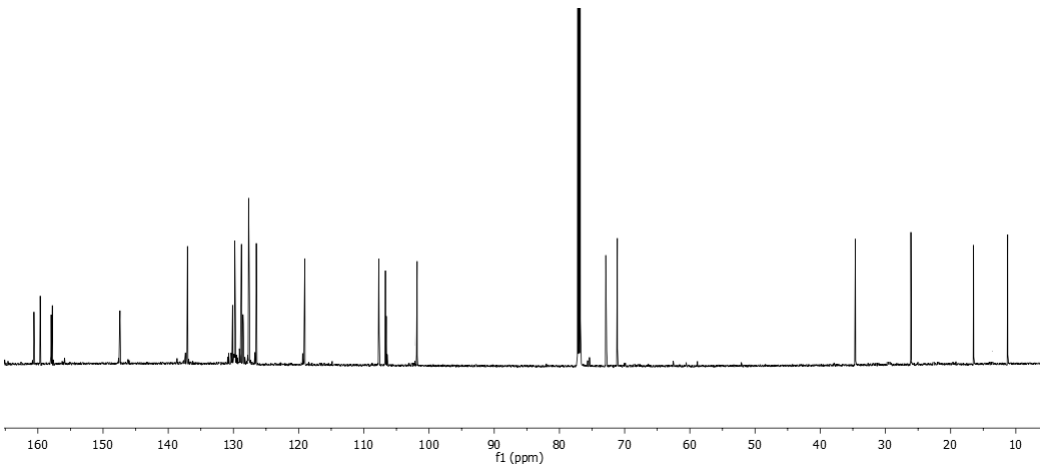

^{1}H NMR (400 MHz, $CDCl_3$) of compound **38**

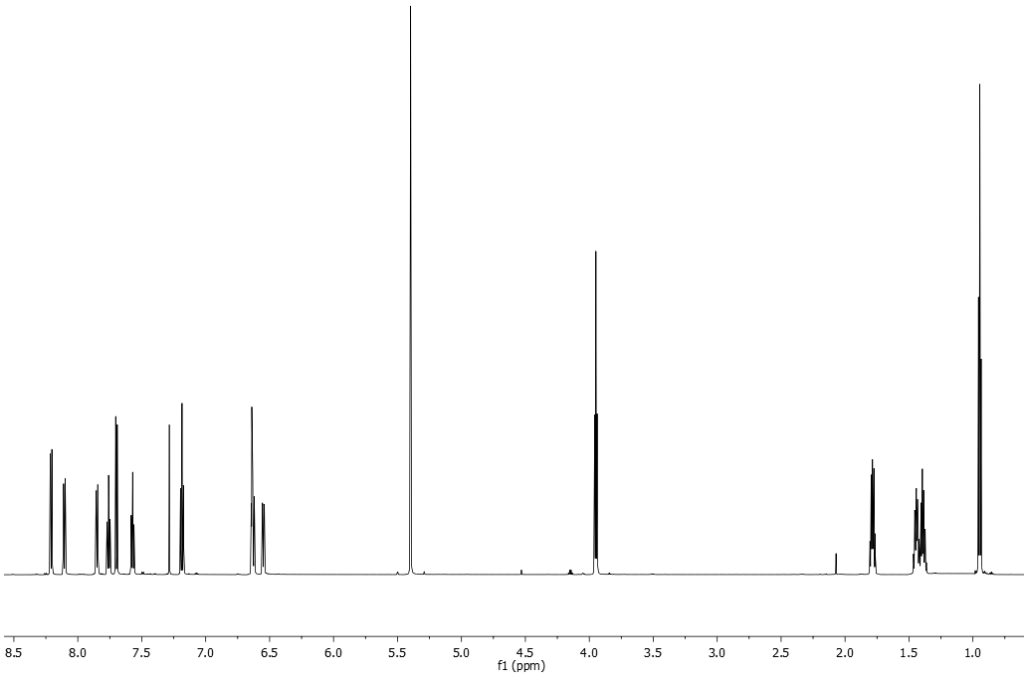

^{13}C NMR (100 MHz, $CDCl_3$) of compound **38**

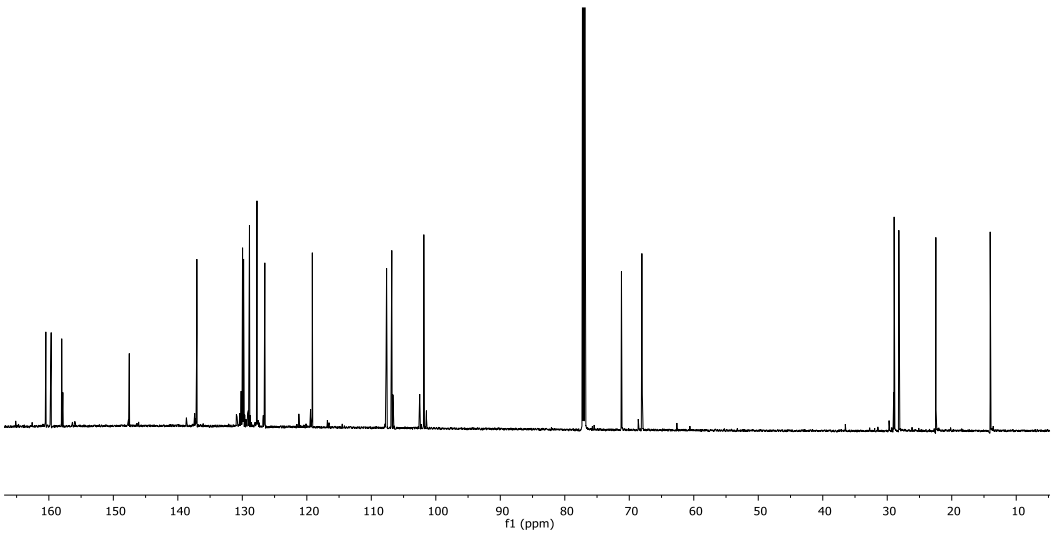

^{1}H NMR (400 MHz, $CDCl_3$) of compound **39**

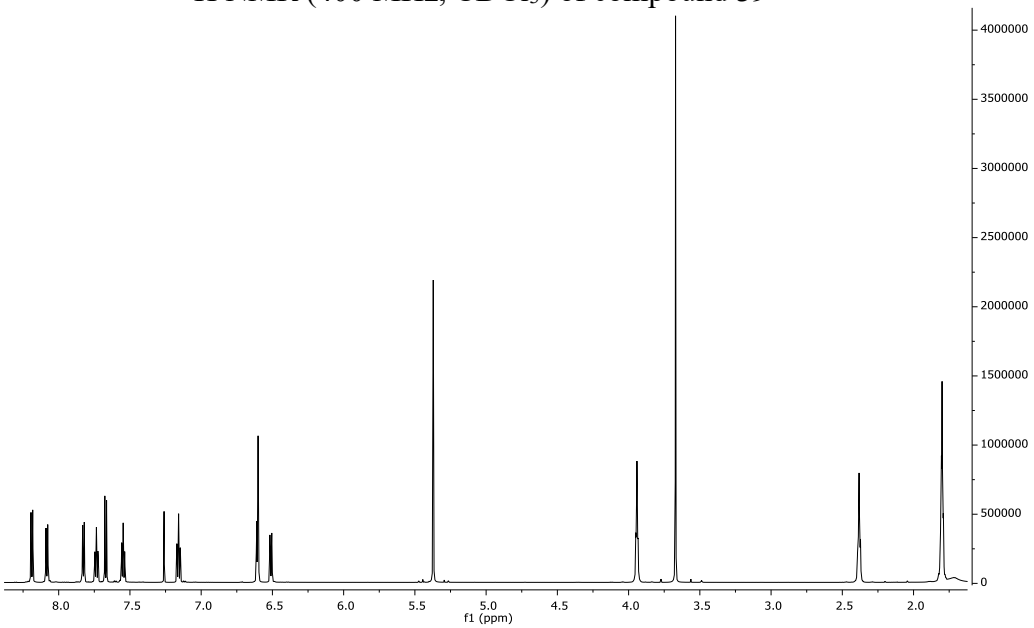

^{13}C NMR (400 MHz, $CDCl_3$) of compound **39**

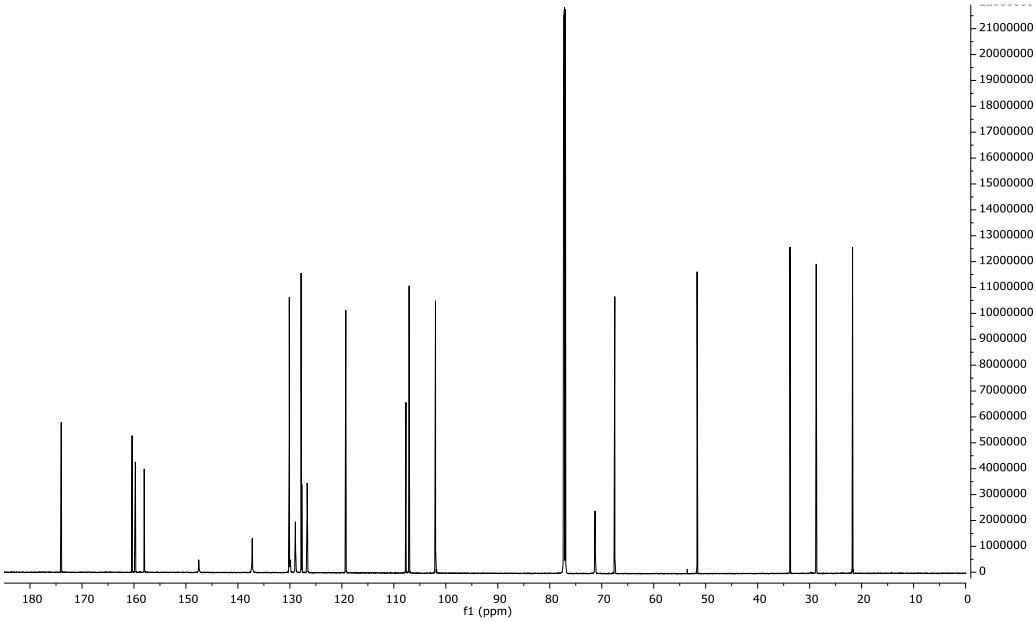

^{1}H NMR (400 MHz, CD_3OD) of compound **40**

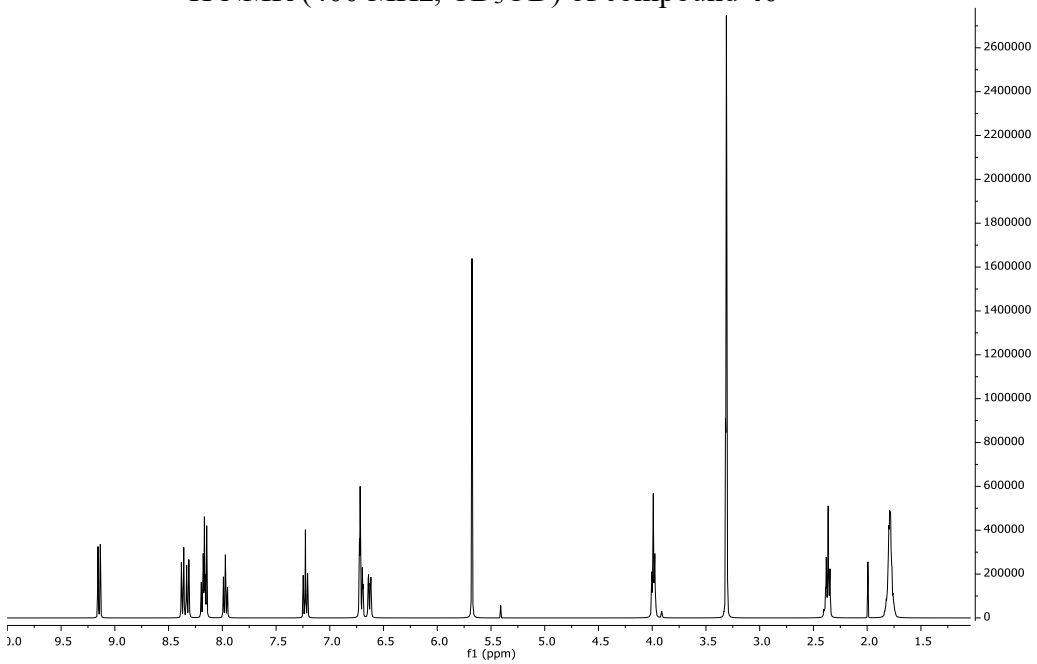

^{13}C NMR (400 MHz, CD_3OD) of compound **40**

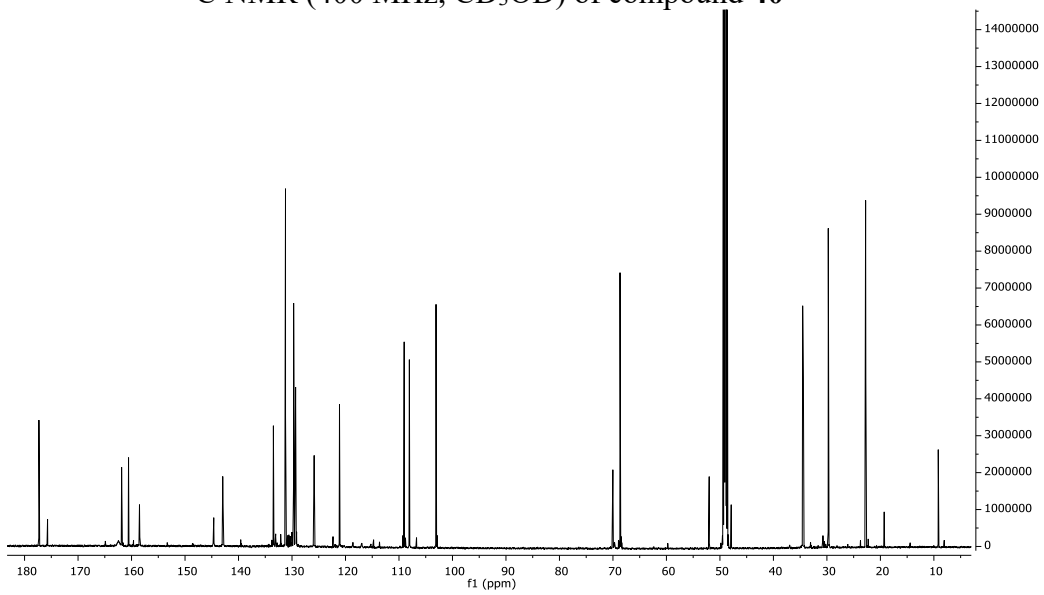

^{1}H NMR (400 MHz, $CDCl_3$) of compound **41**

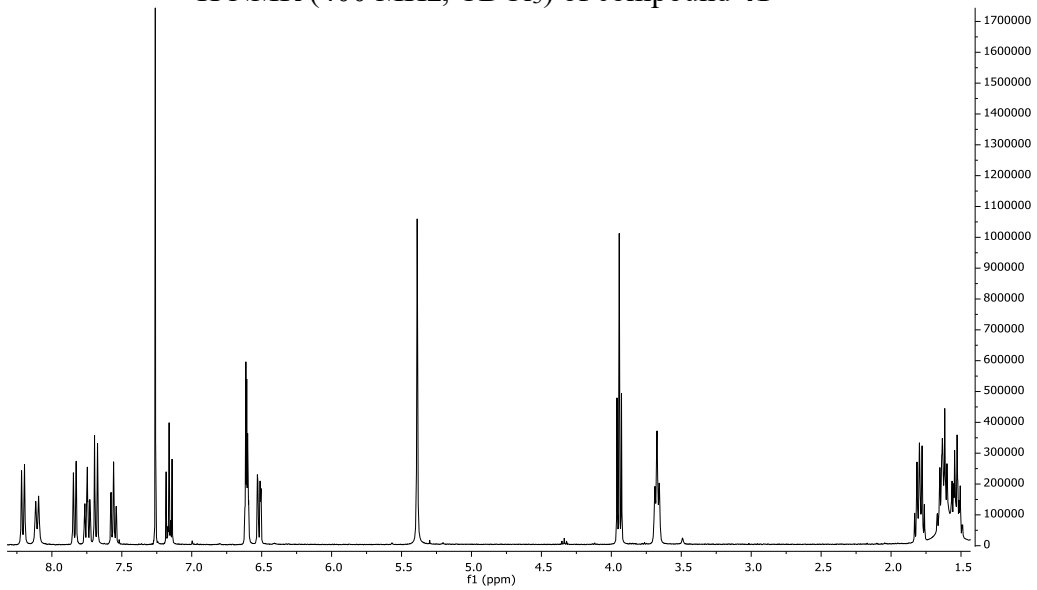

^{13}C NMR (400 MHz, $CDCl_3$) of compound **41**

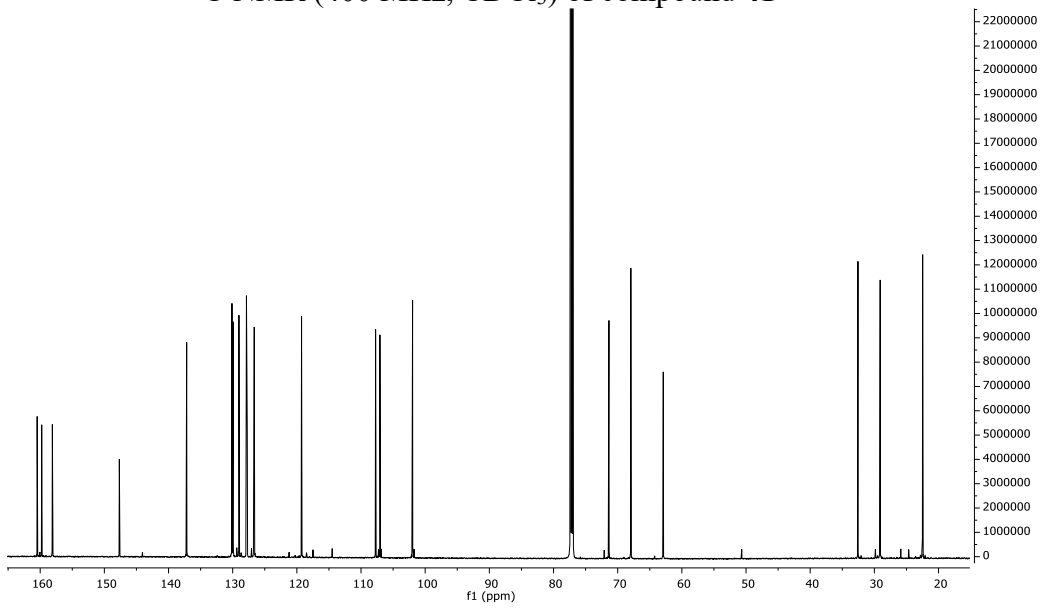

^{1}H NMR (400 MHz, $CDCl_3$) of compound **42**

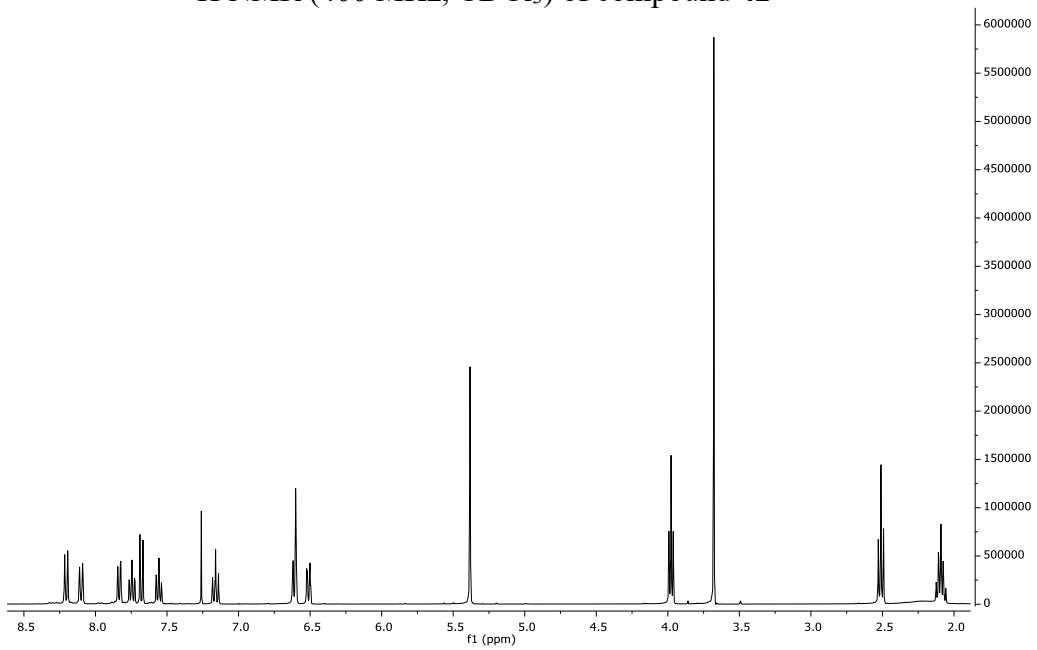

^{13}C NMR (400 MHz, $CDCl_3$) of compound **42**

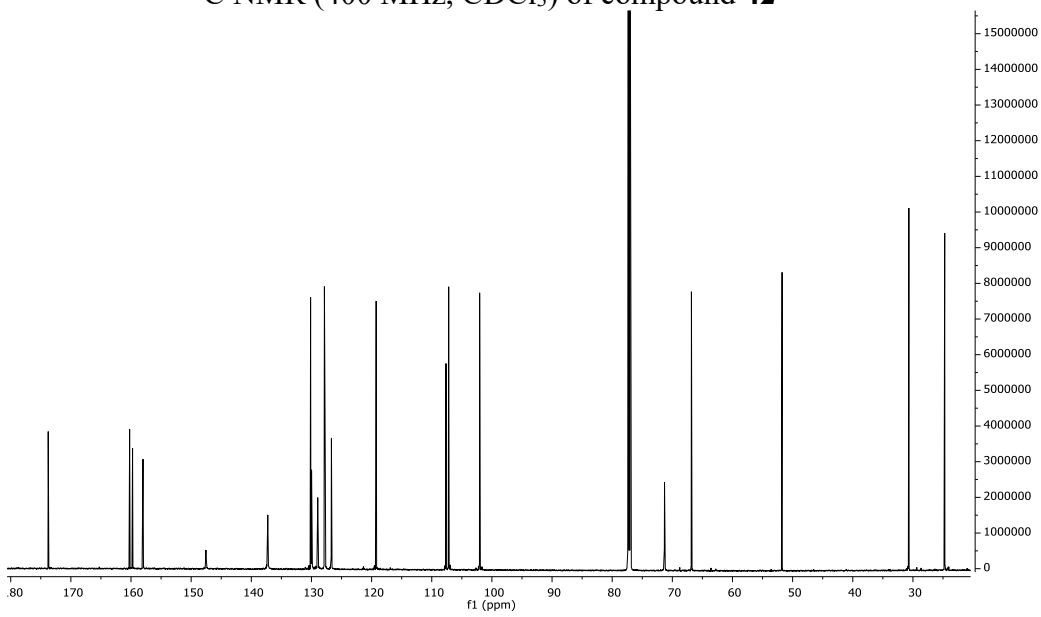

^{1}H NMR (400 MHz, CD_3OD) of compound **43**

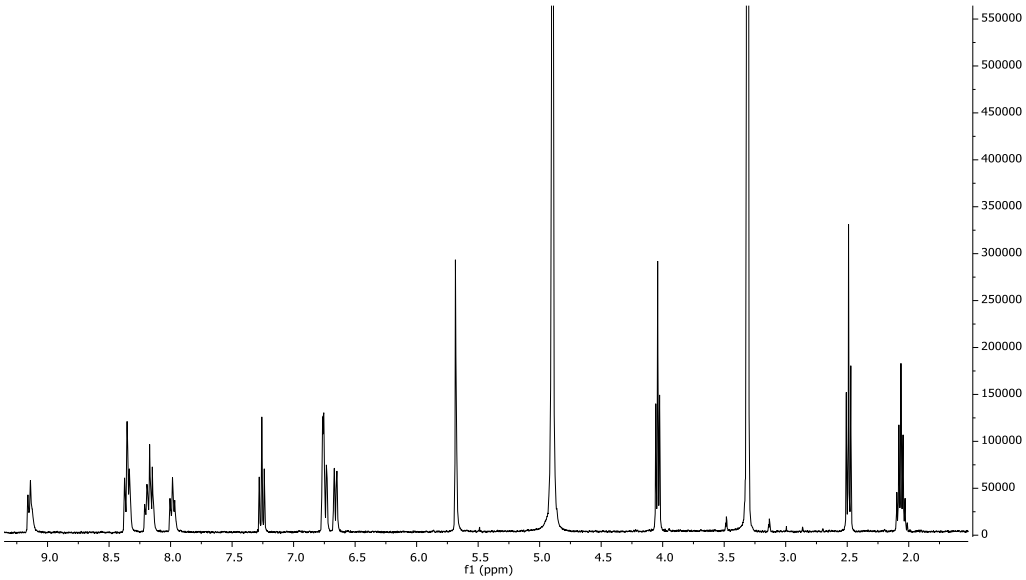

^{13}C NMR (400 MHz, CD_3OD) of compound **43**

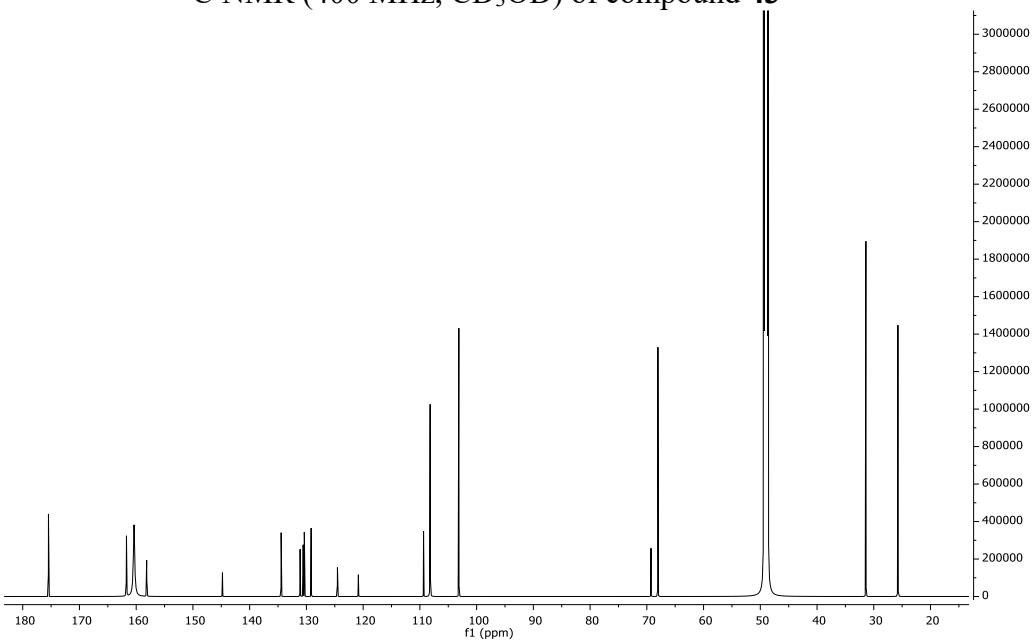

^{1}H NMR (400 MHz, $CDCl_3$) of compound **44**

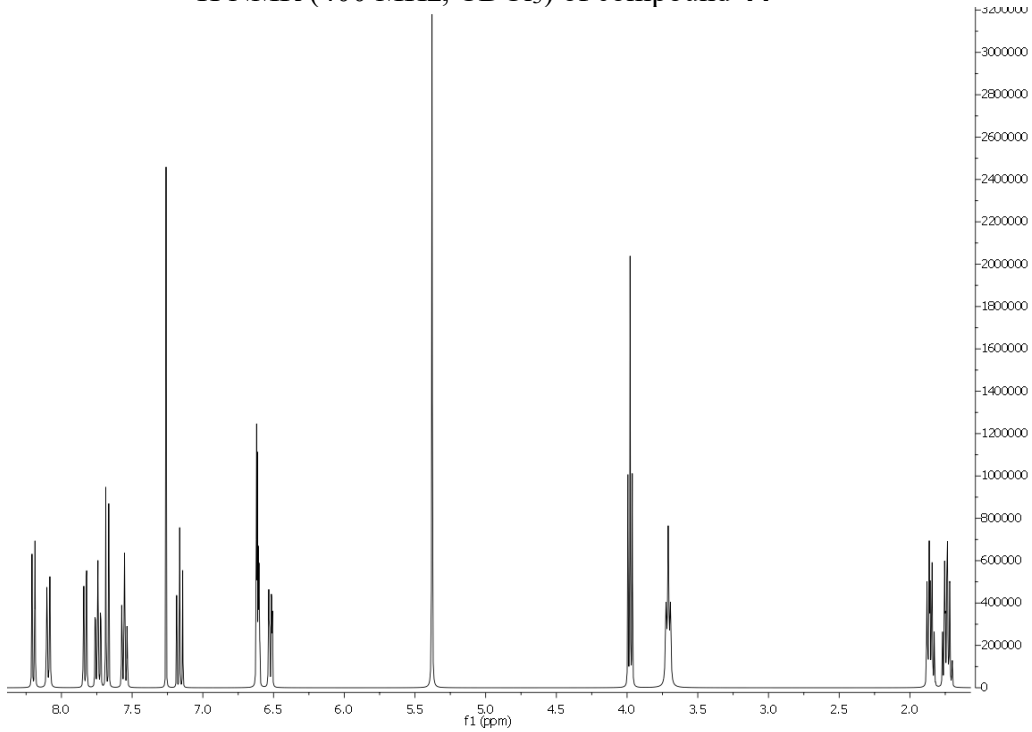

^{13}C NMR (400 MHz, $CDCl_3$) of compound **44**

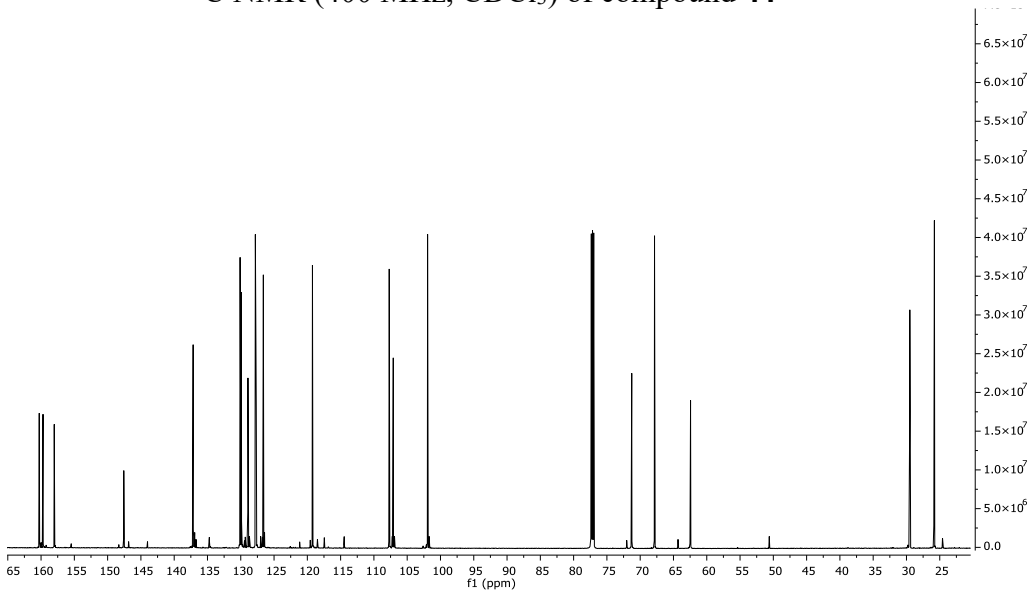

^{1}H NMR (400 MHz, $CDCl_3$) of compound **45**

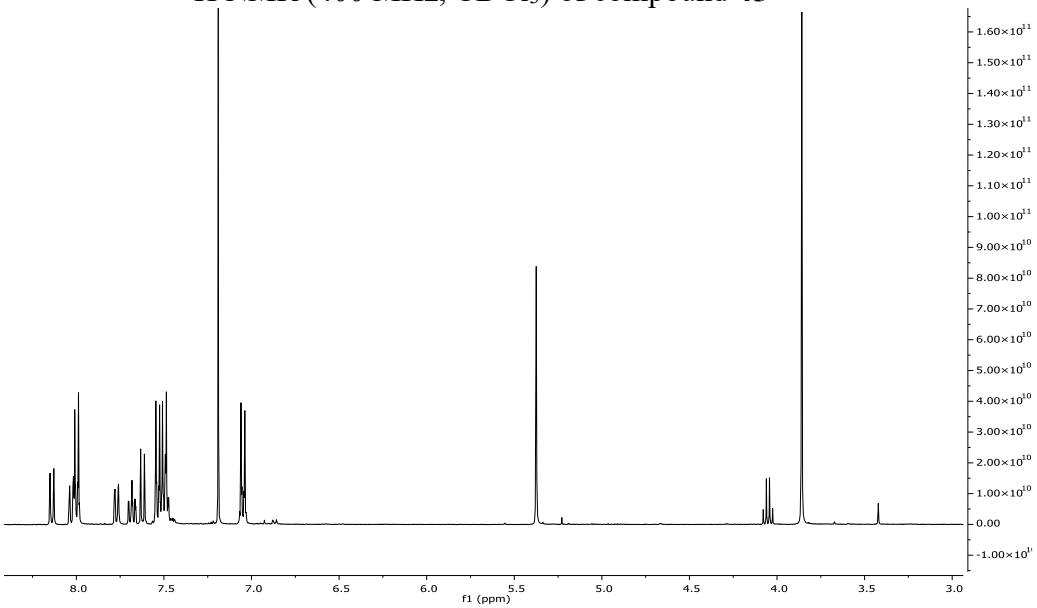

^{13}C NMR (400 MHz, $CDCl_3$) of compound **45**

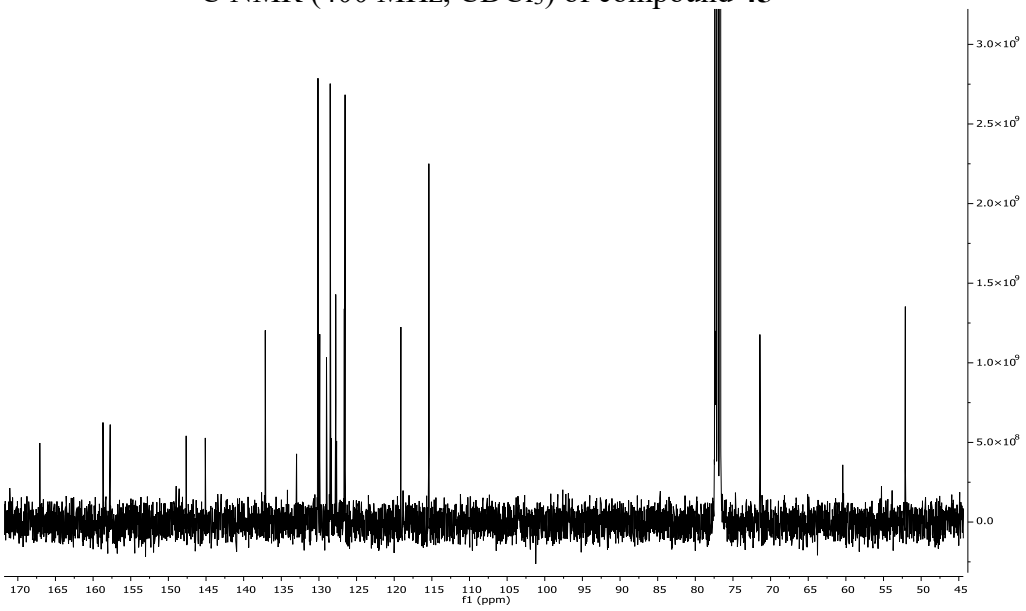

^{1}H NMR (400 MHz, $CDCl_3$) of compound **46**

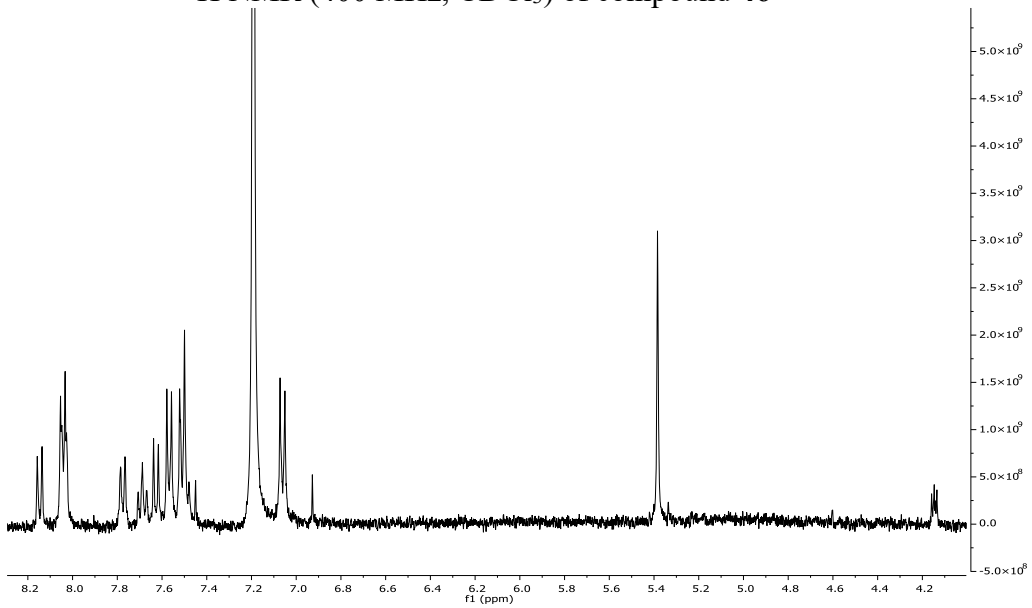

^{13}C NMR (400 MHz, $CDCl_3$) of compound **46**

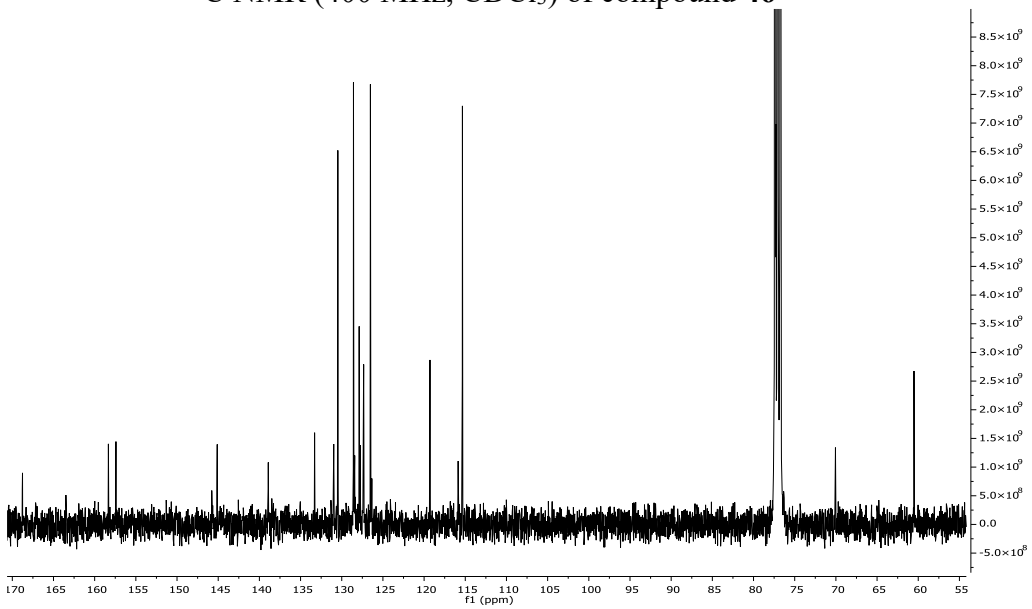

^{1}H NMR (400 MHz, $CDCl_3$) of compound **47**

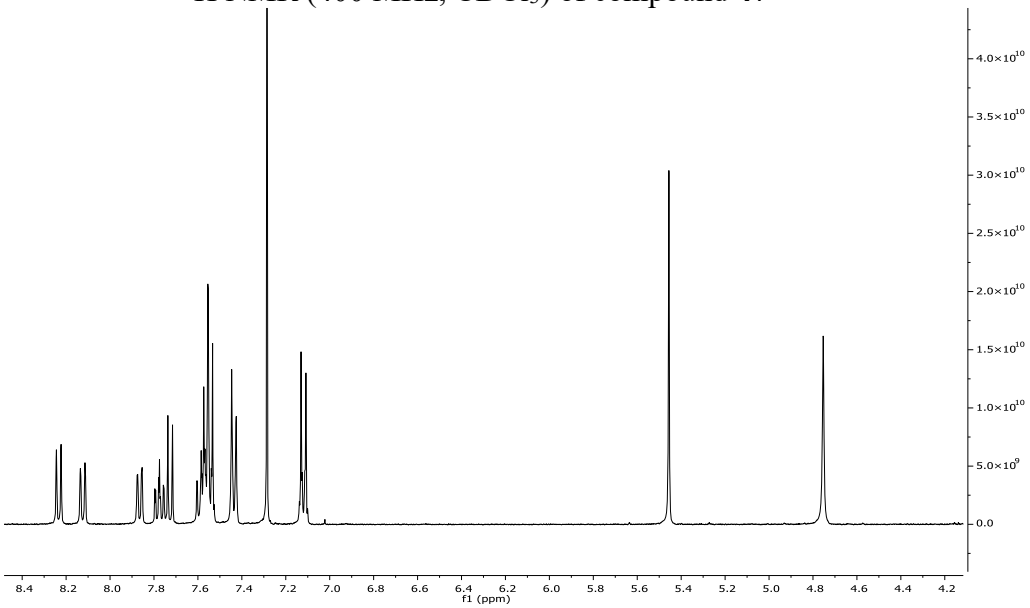

^{13}C NMR (400 MHz, $CDCl_3$) of compound **47**

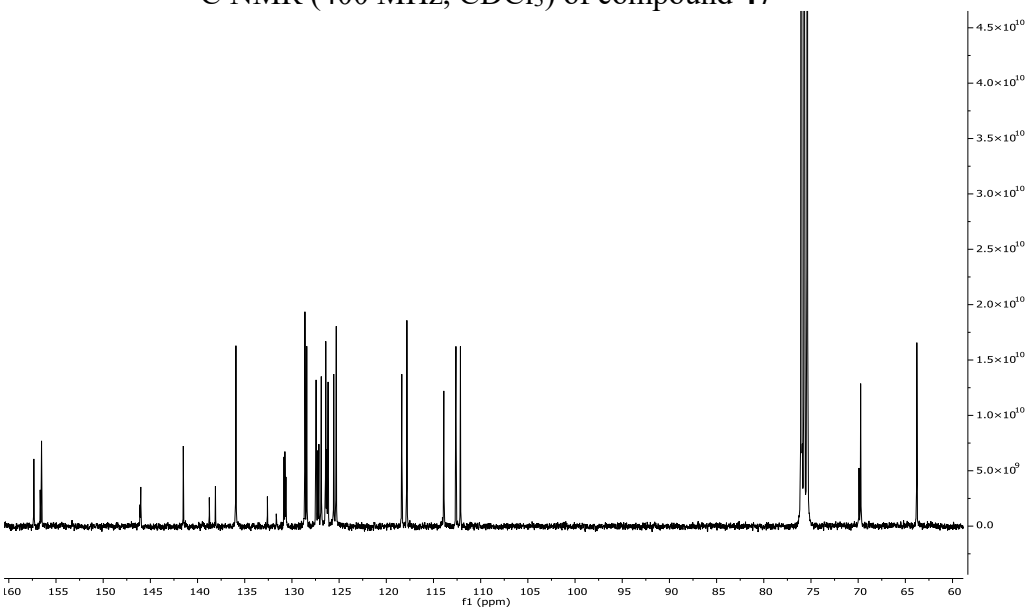

^{1}H NMR (400 MHz, $CDCl_3$) of compound **48**

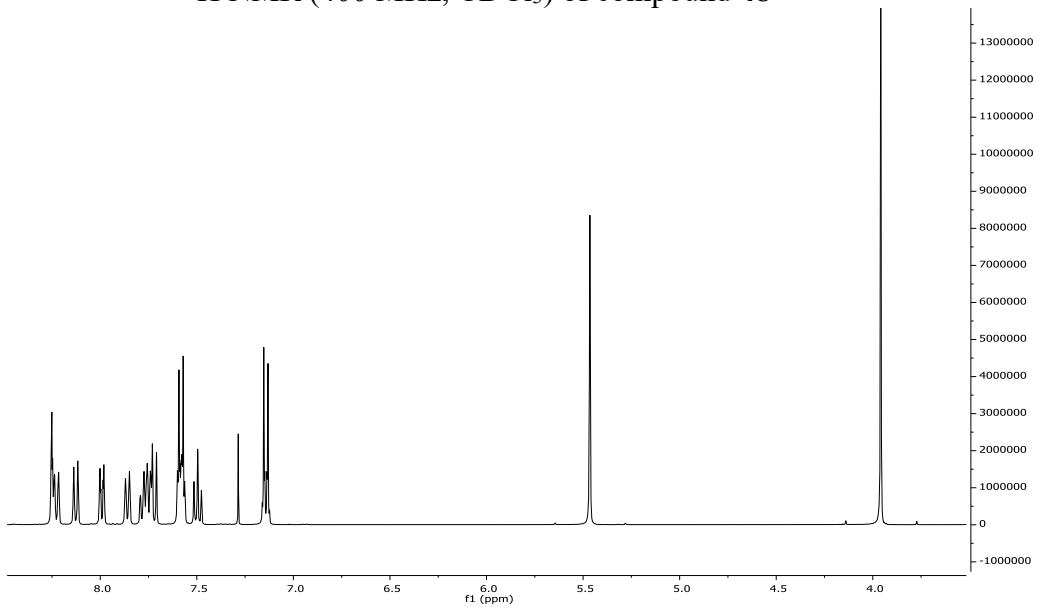

^{13}C NMR (400 MHz, $CDCl_3$) of compound **48**

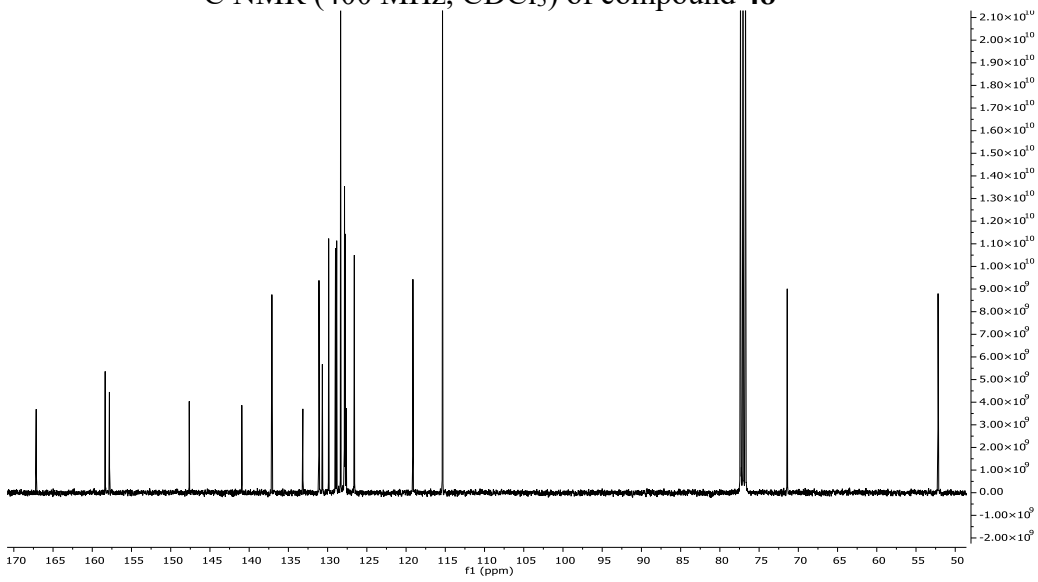

^{1}H NMR (400 MHz, DMSO) of compound **49**

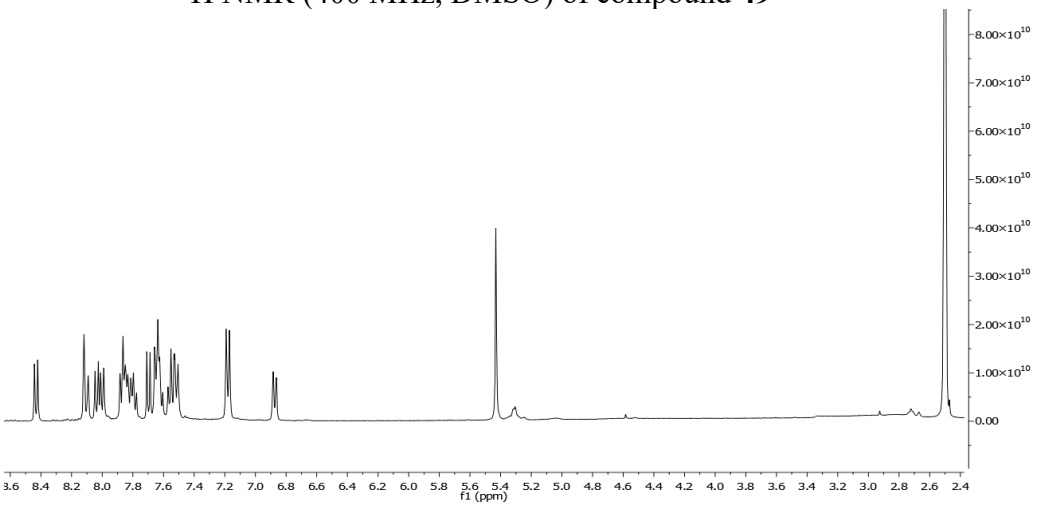

^{13}C NMR (400 MHz, DMSO) of compound **49**

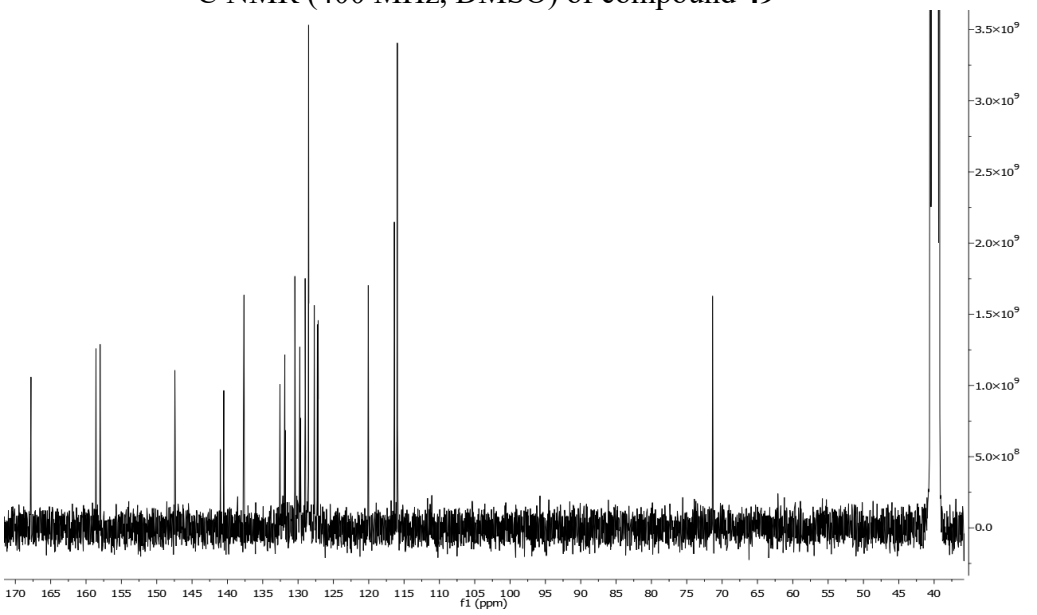

^{1}H NMR (400 MHz, $CDCl_3$) of compound **50**

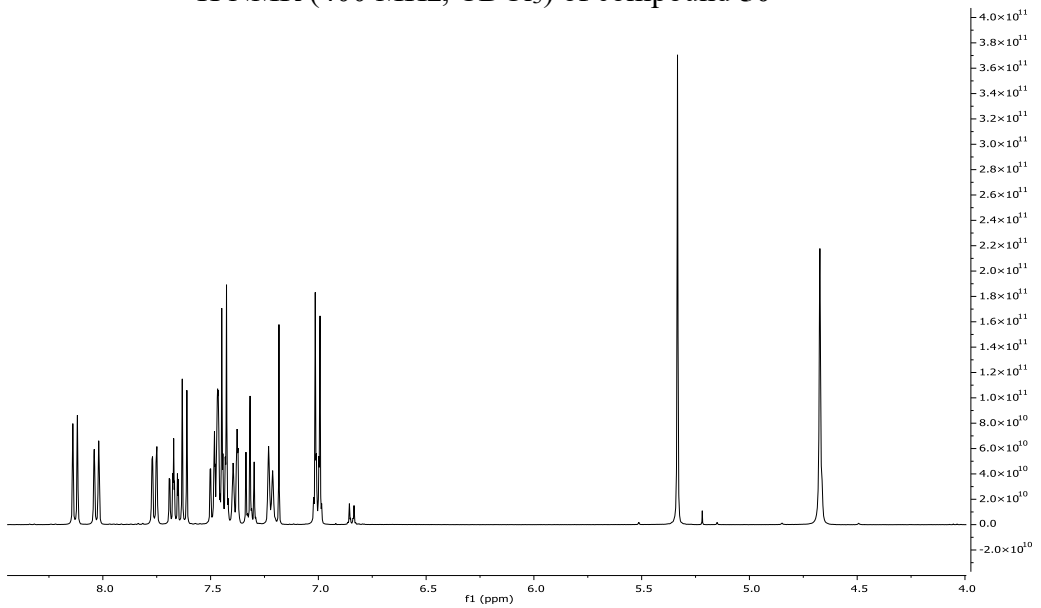

^{13}C NMR (400 MHz, $CDCl_3$) of compound **50**

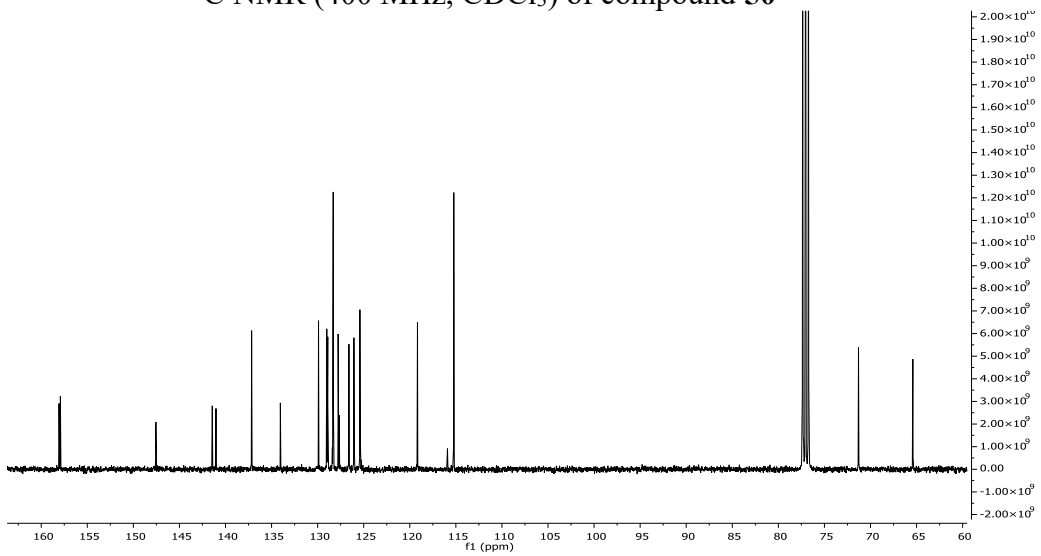

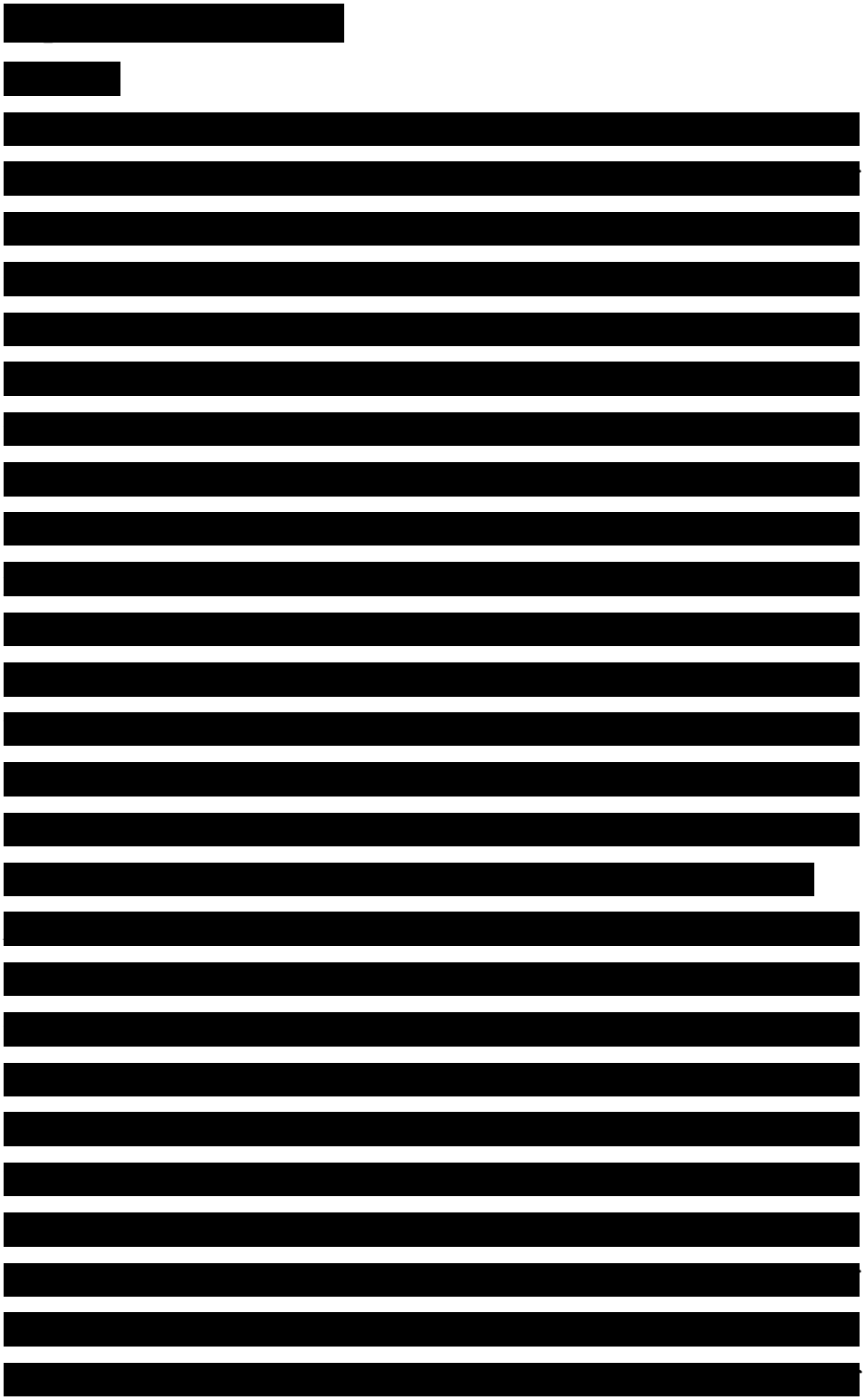

[redacted]

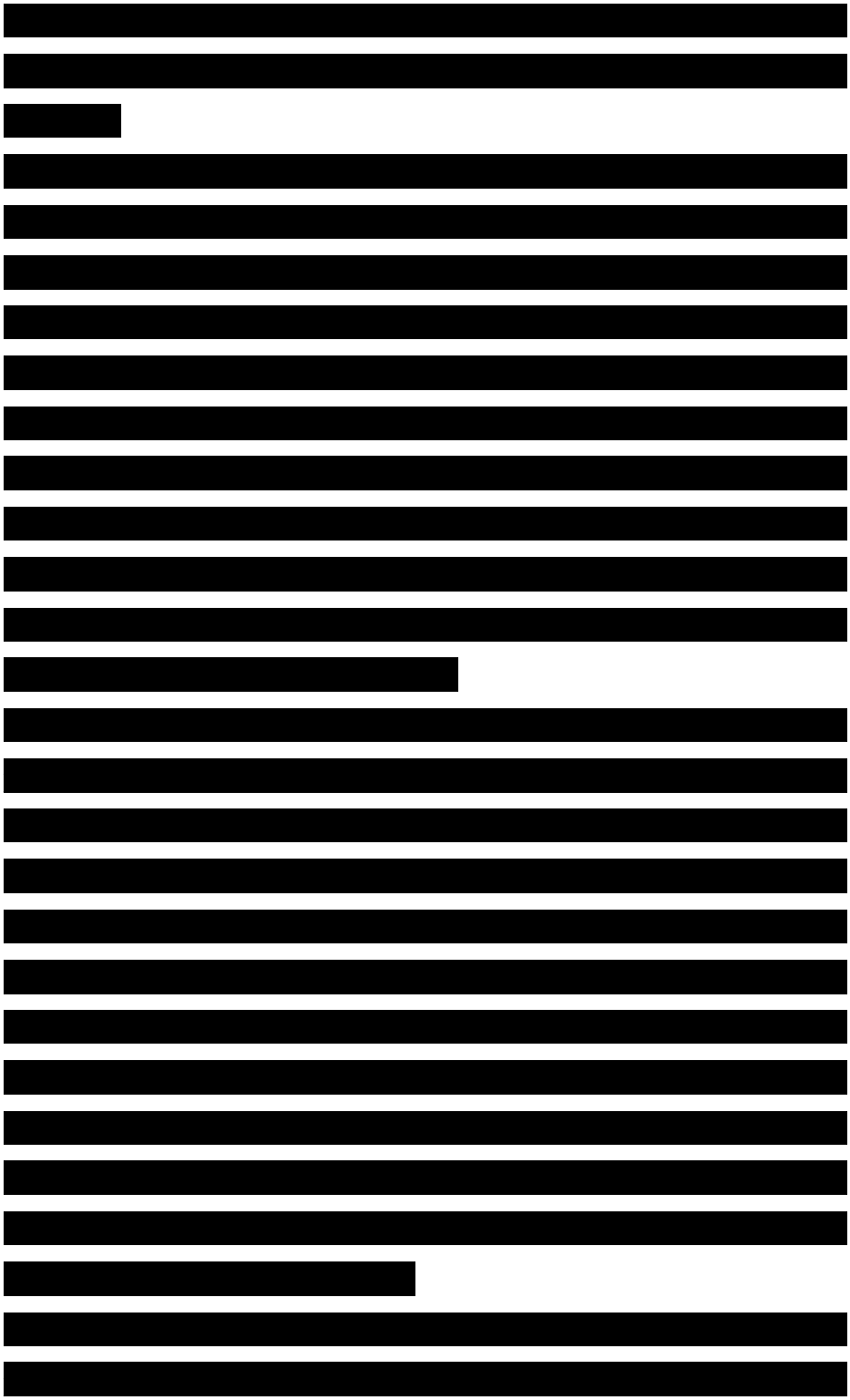

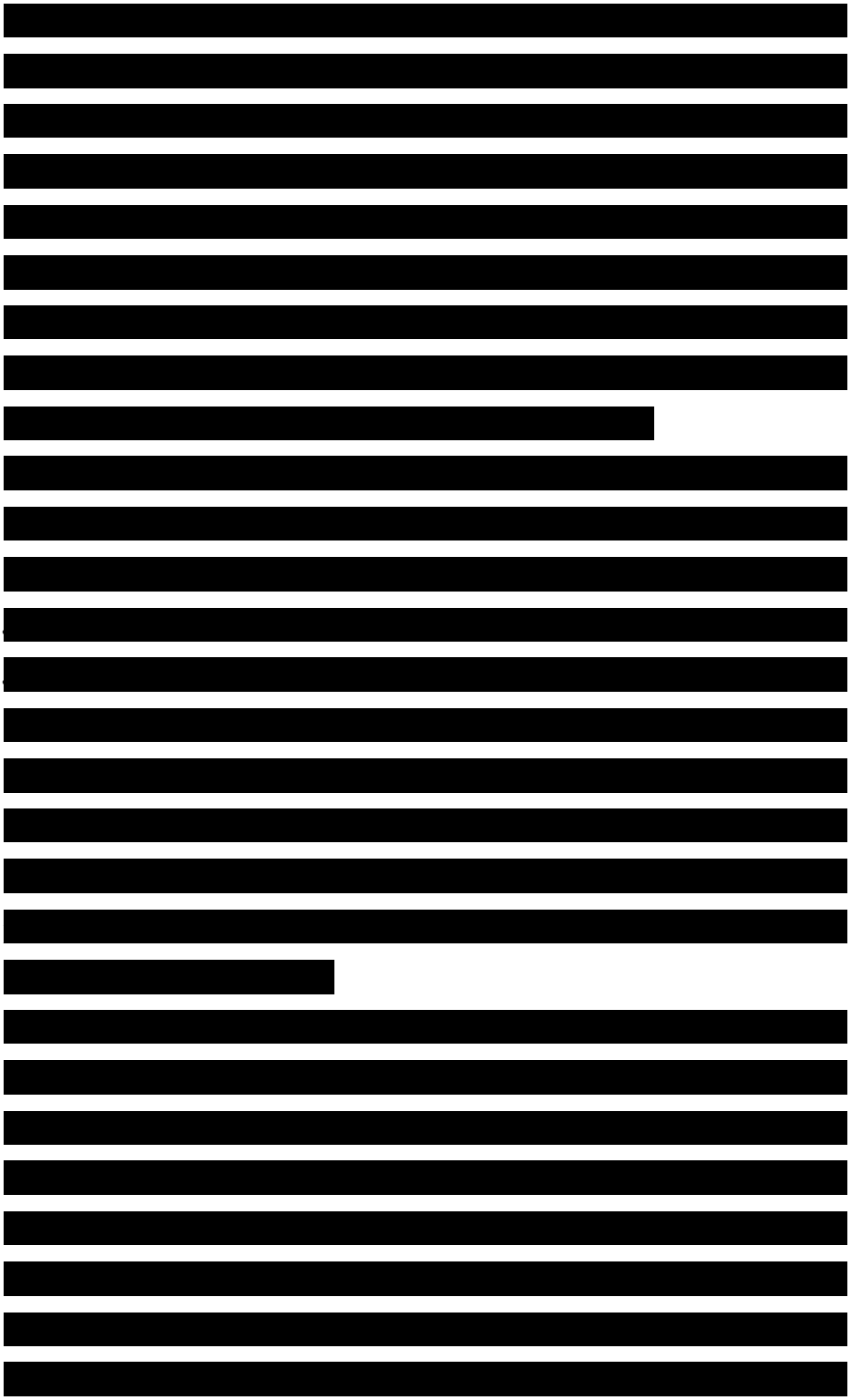

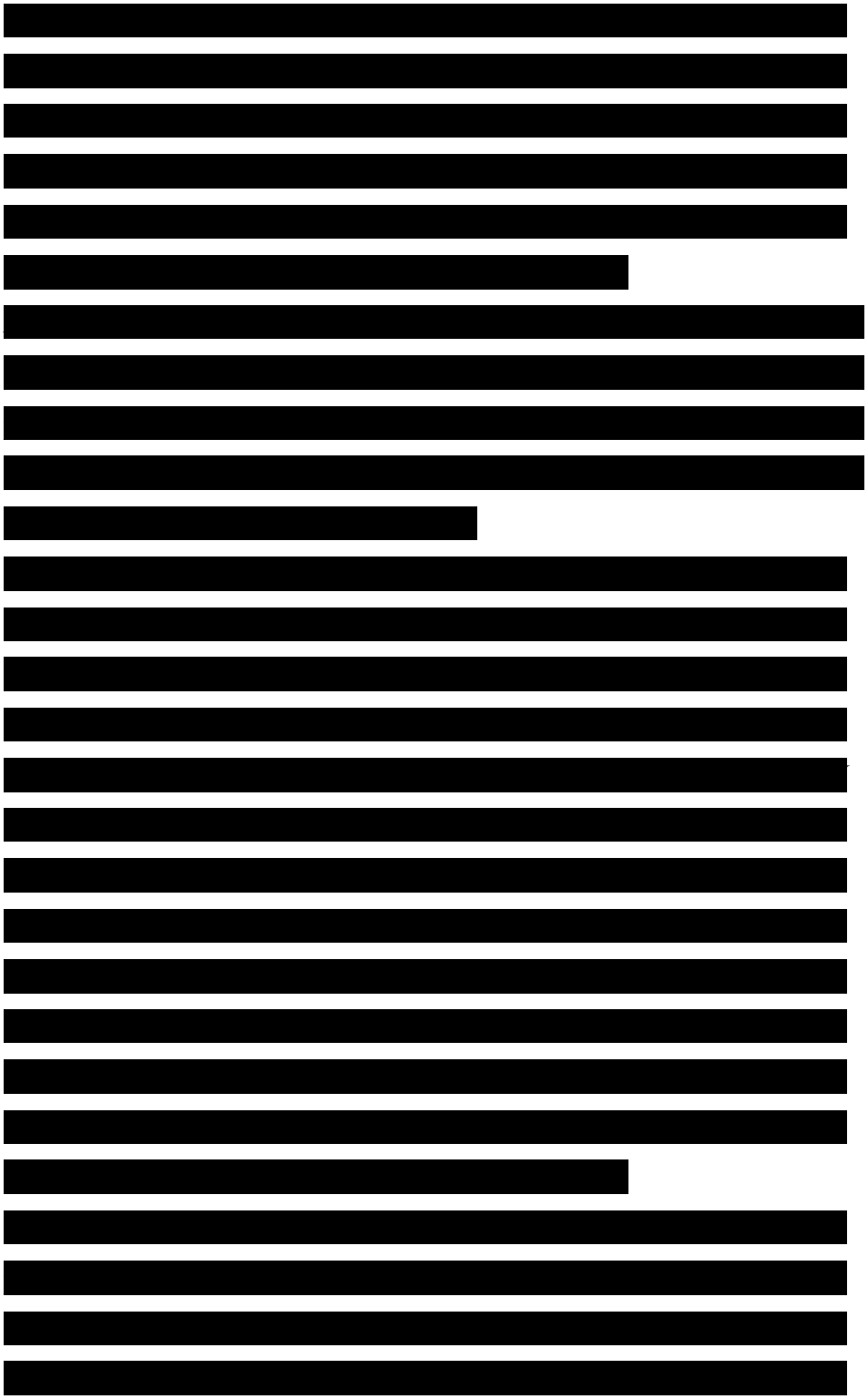

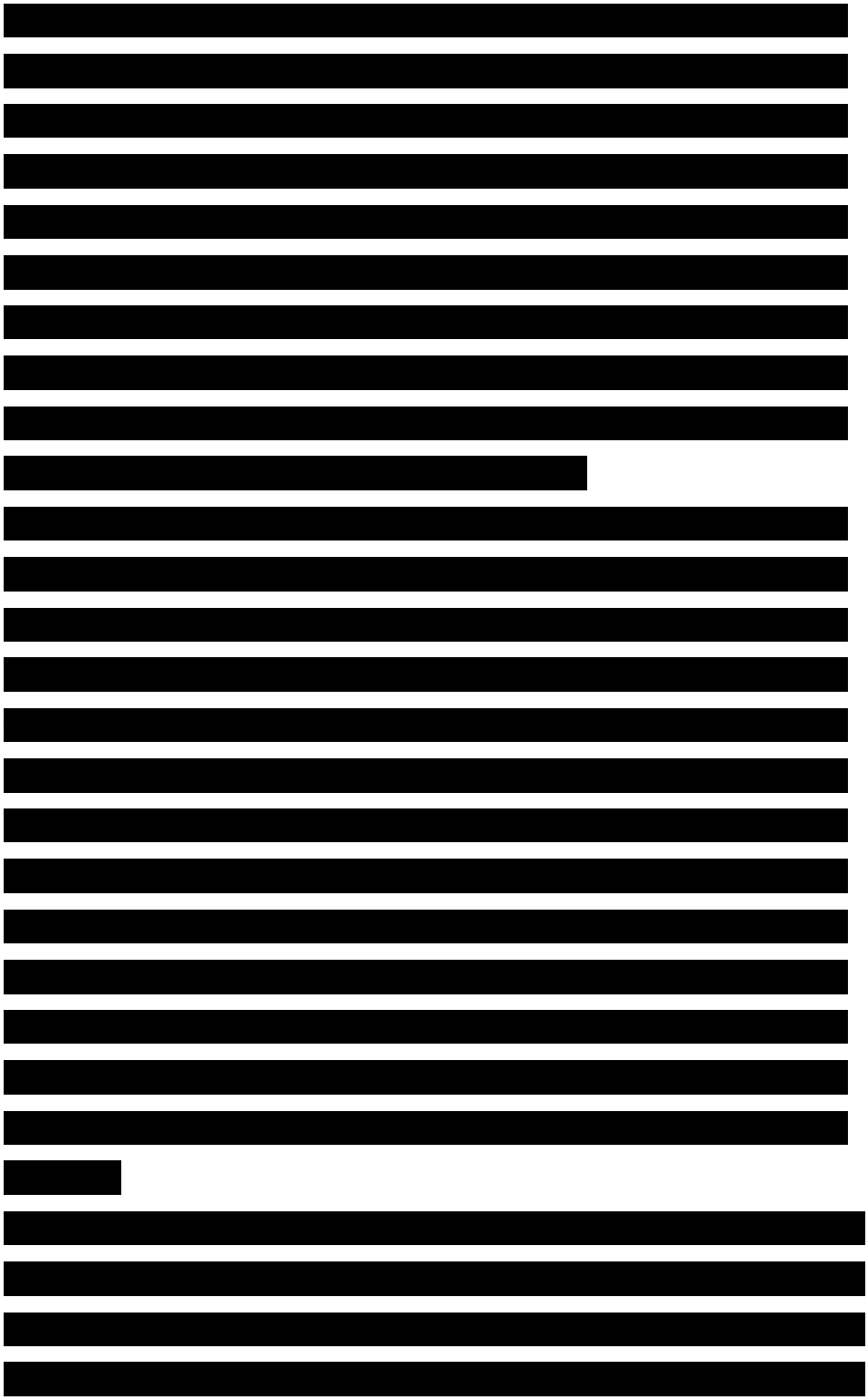

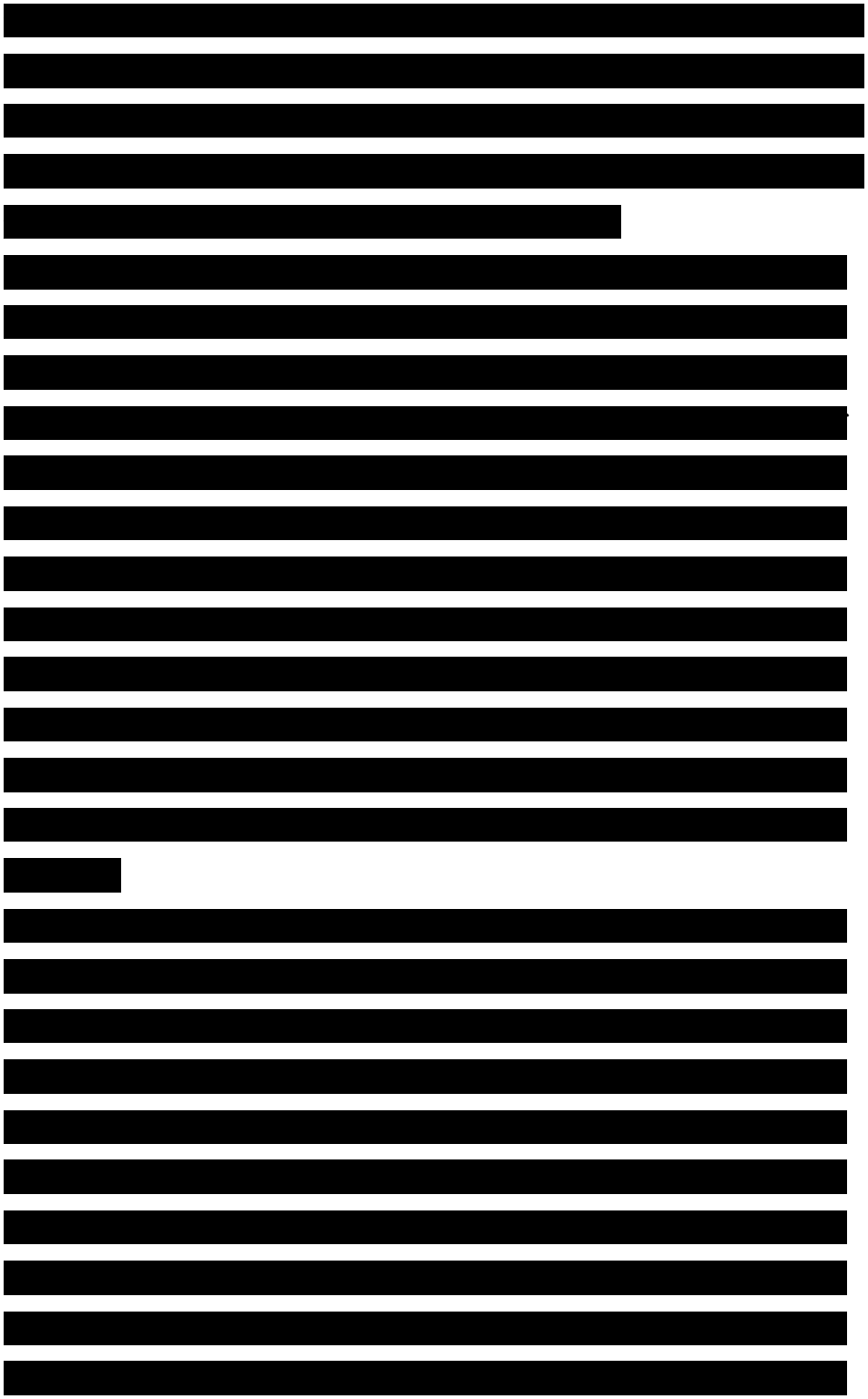

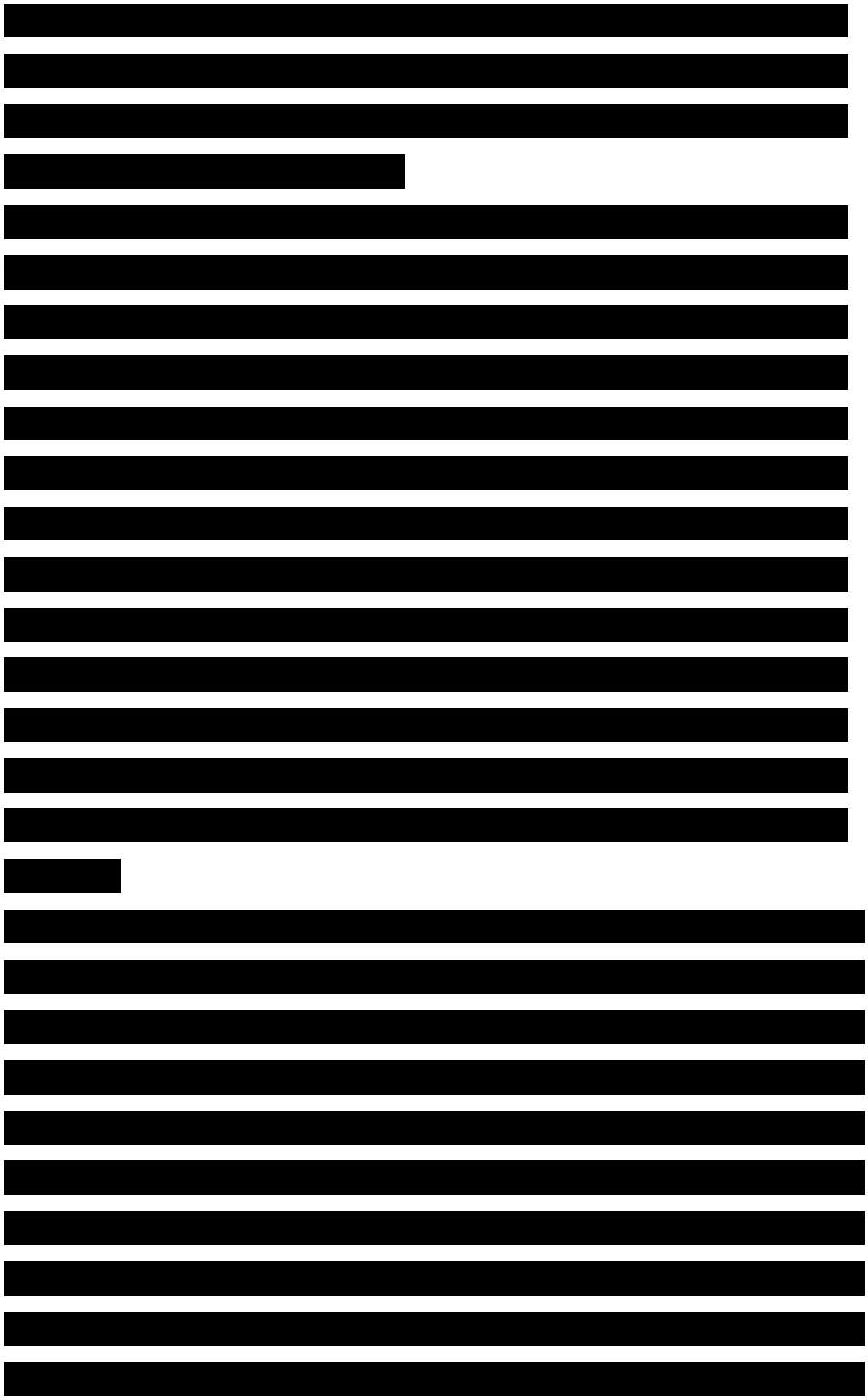

[redacted]

[redacted]

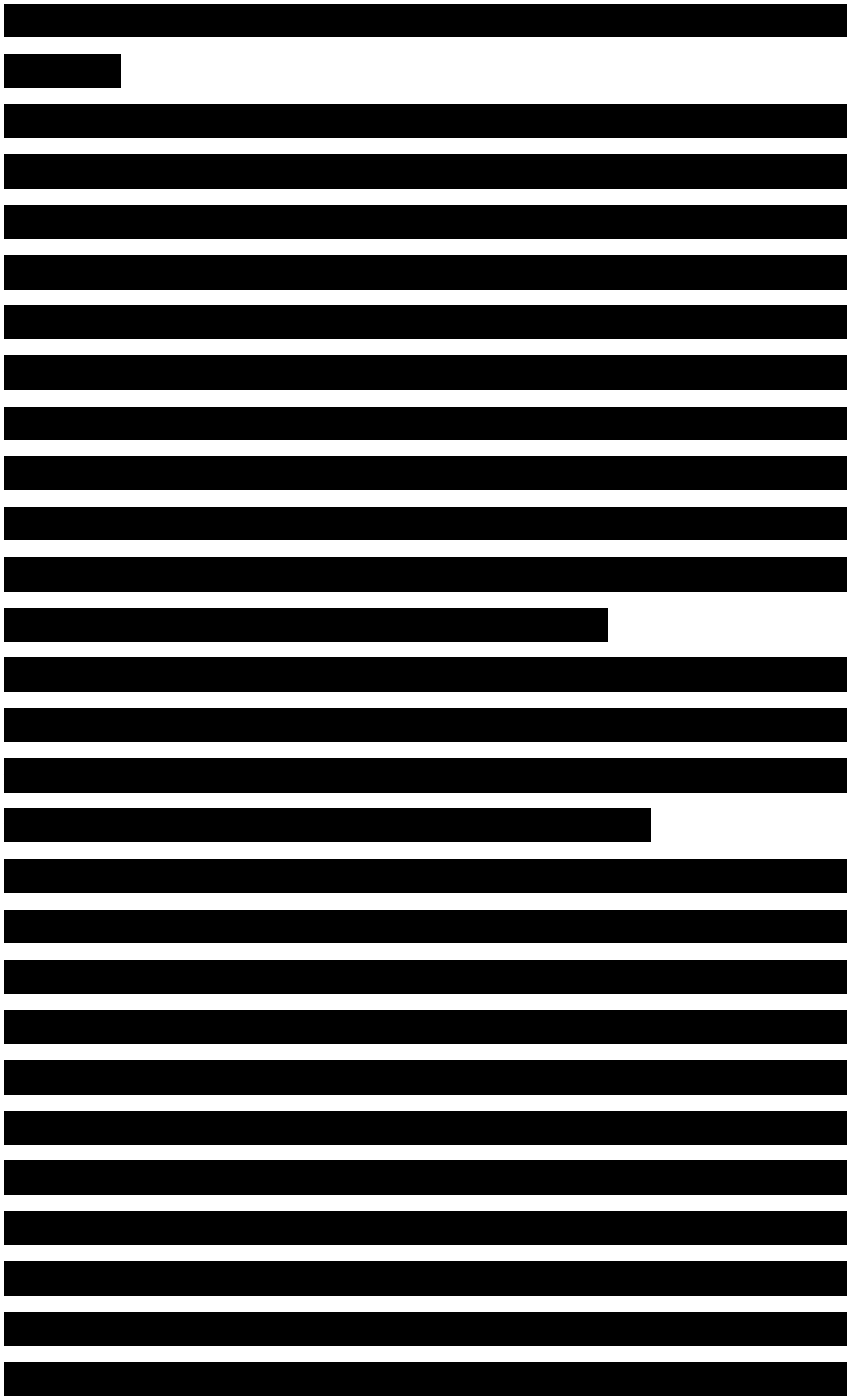

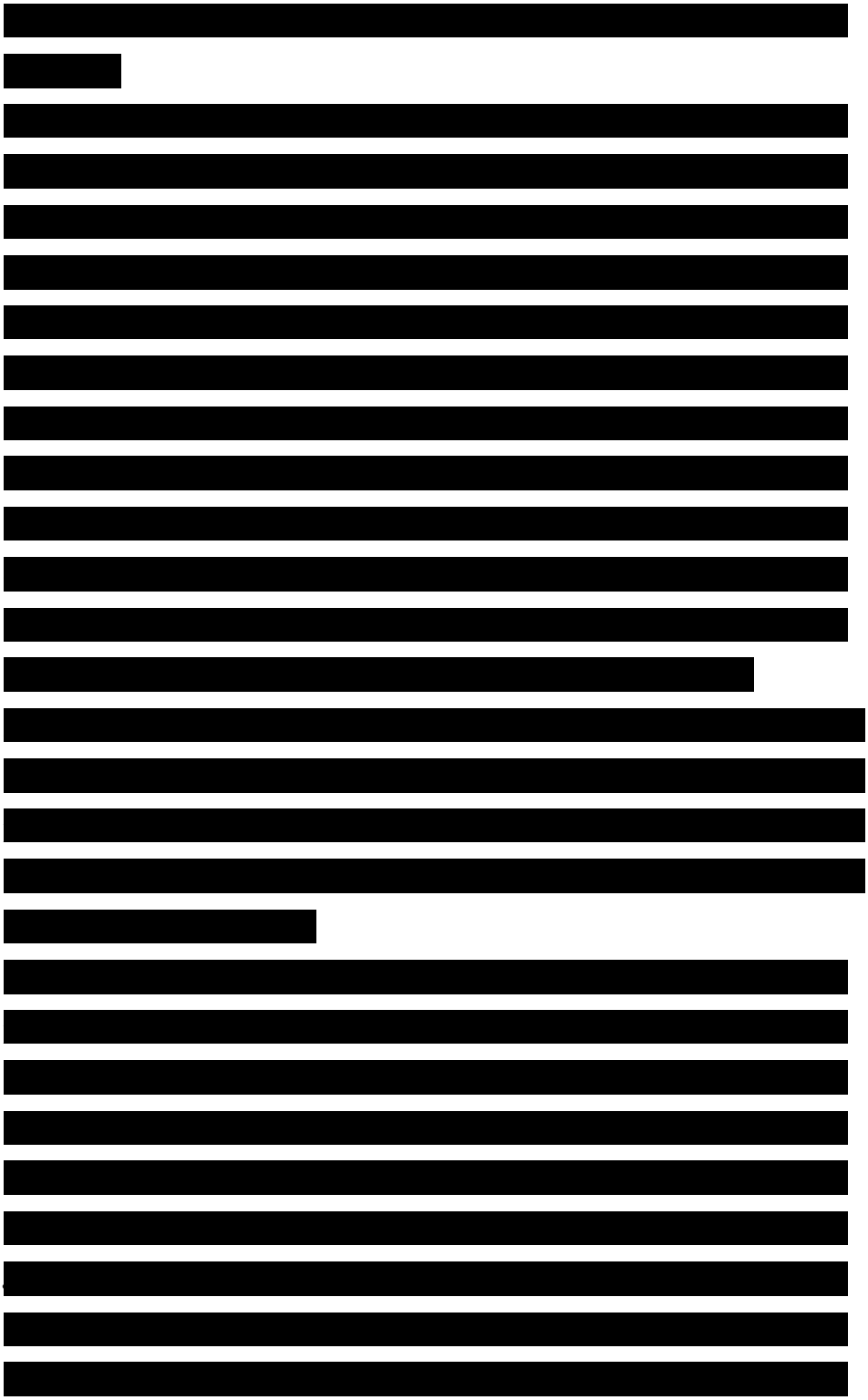

[redacted]

[redacted]

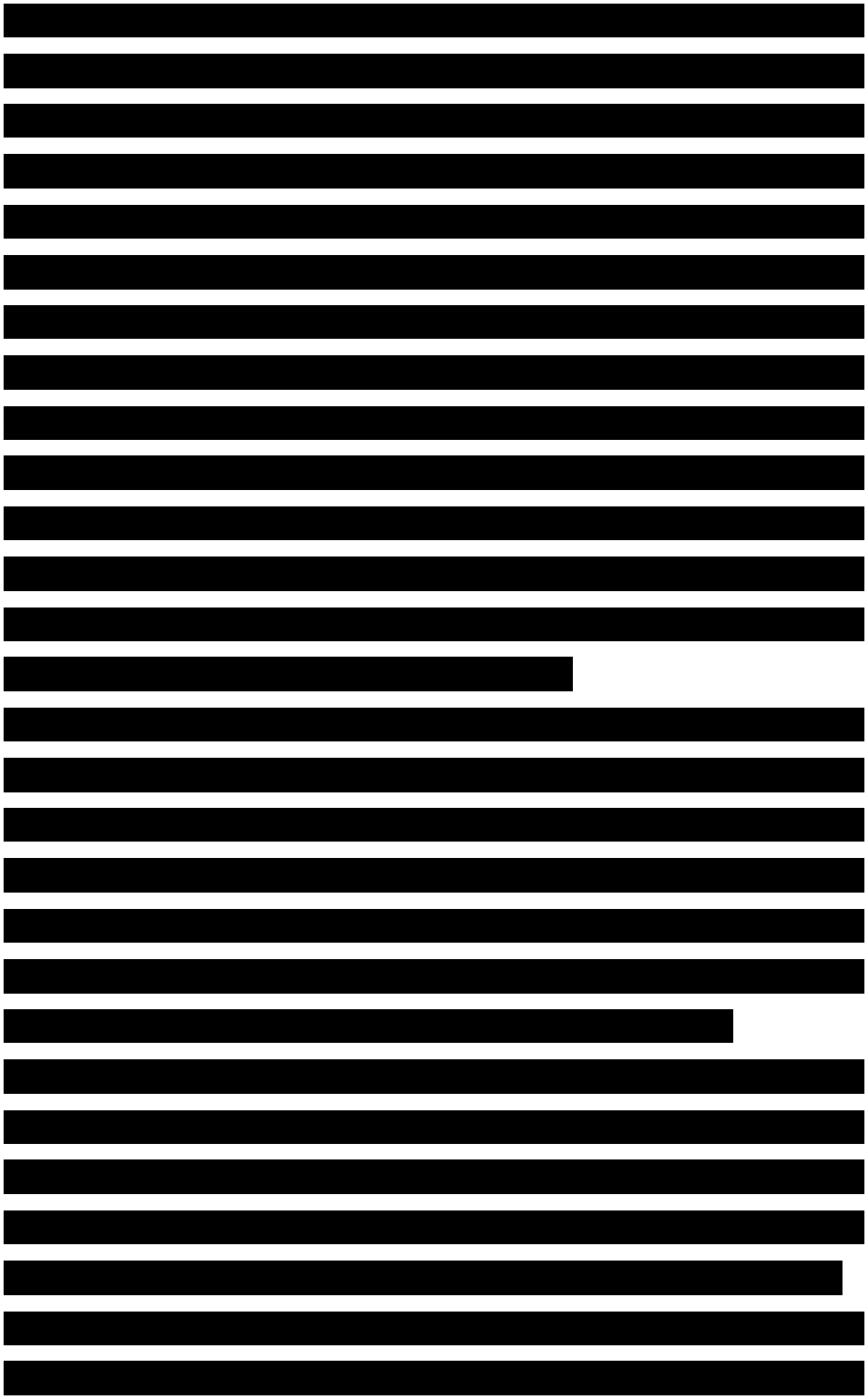

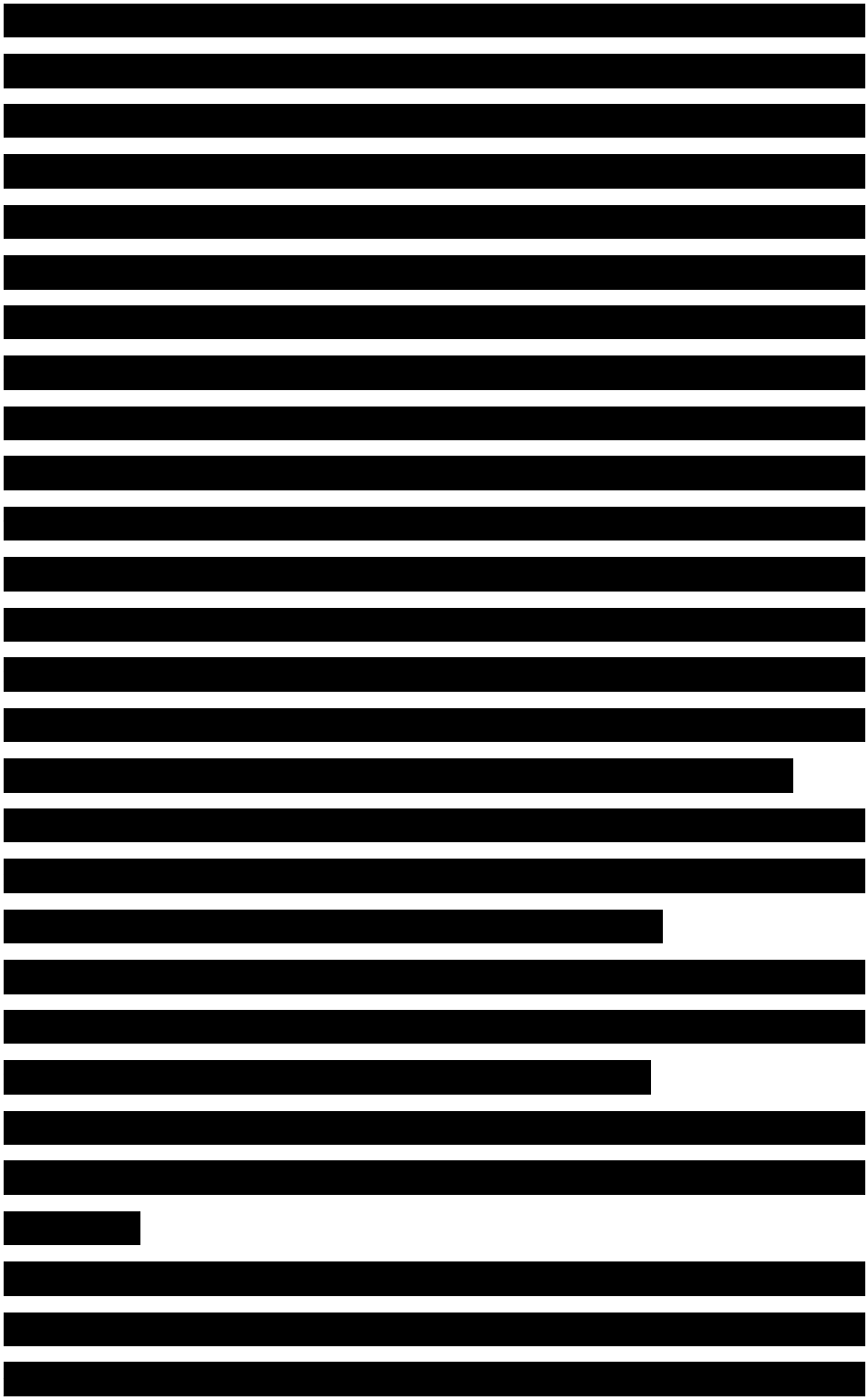

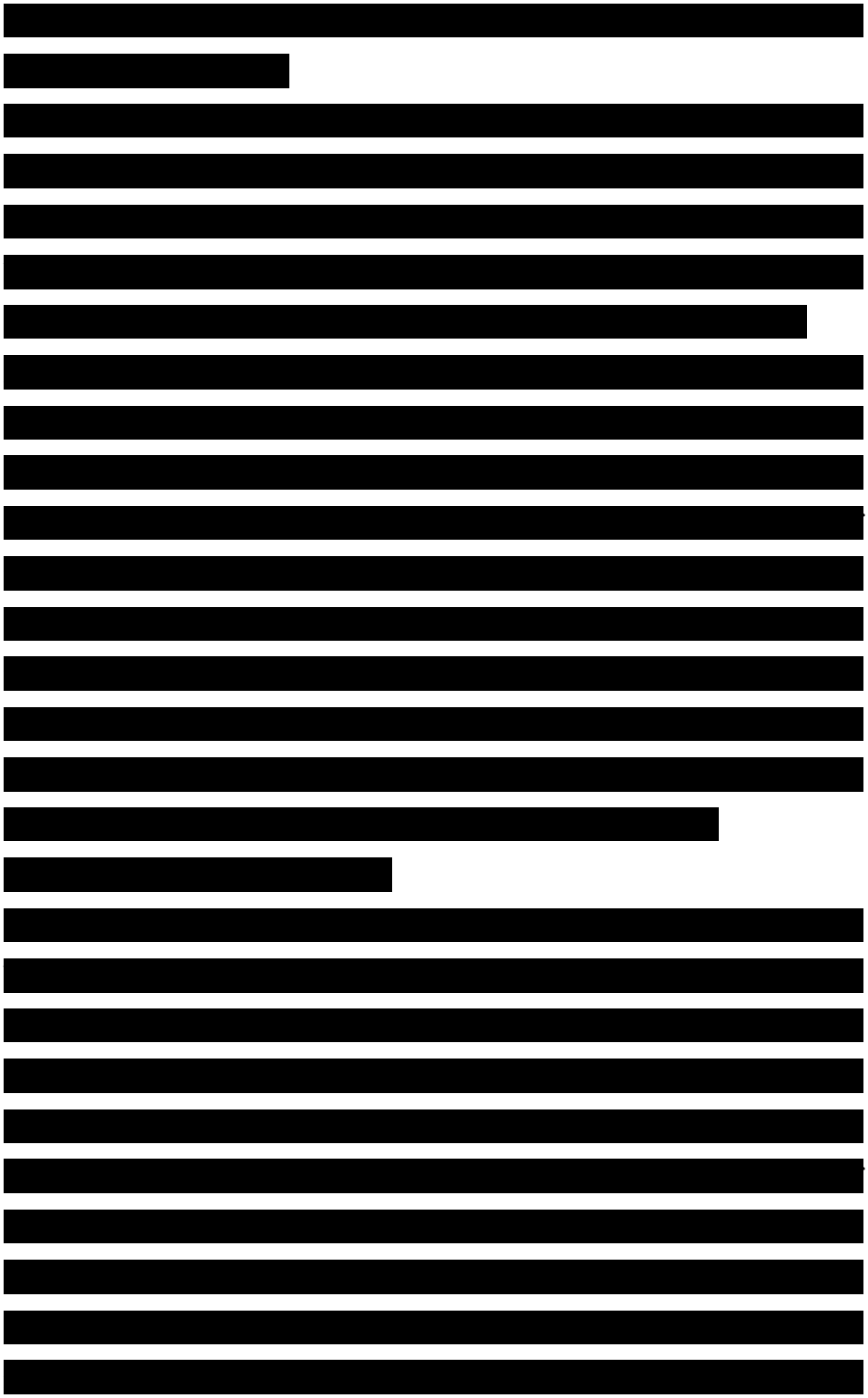

[redacted]

[redacted]

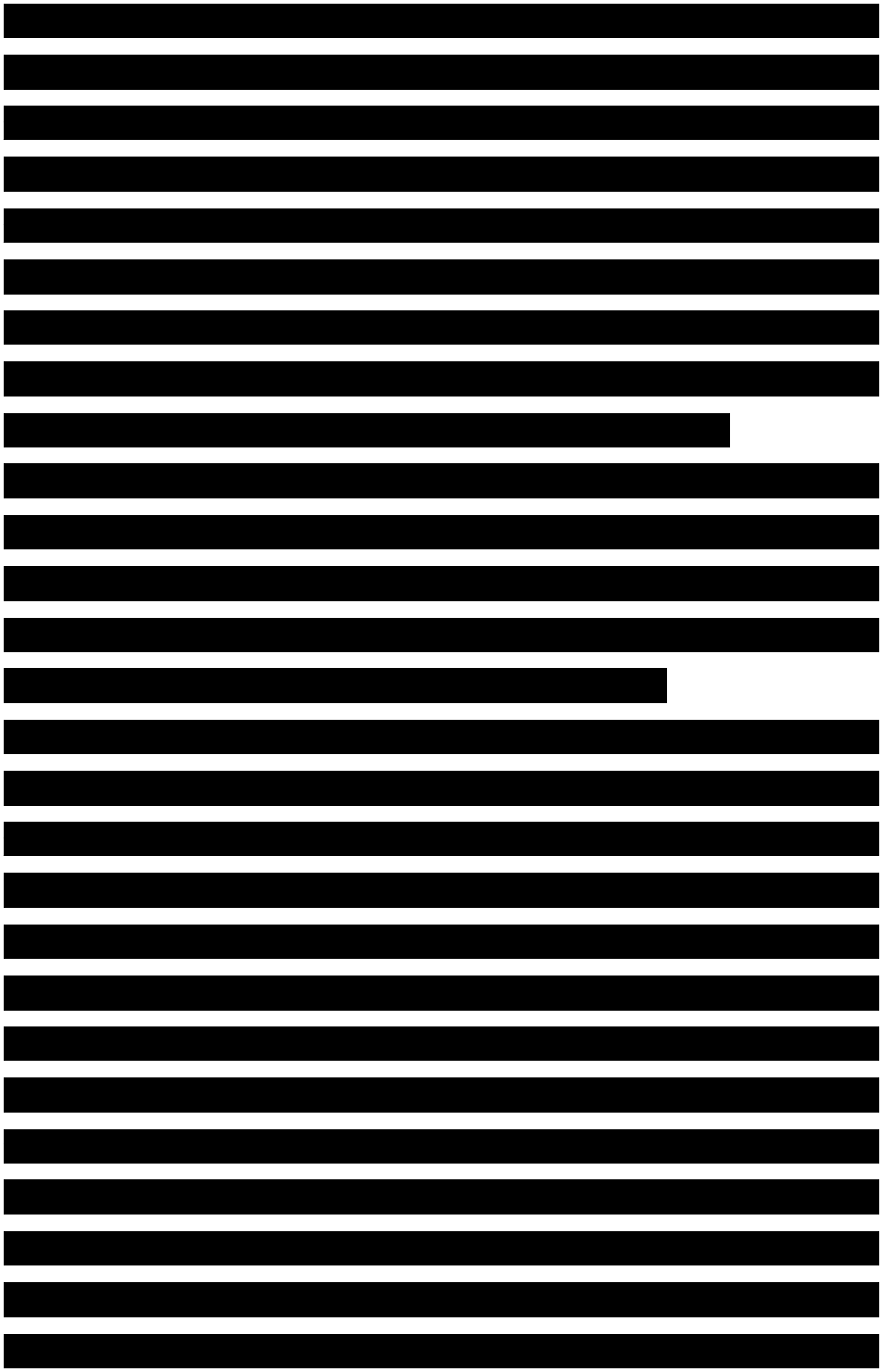

[redacted]

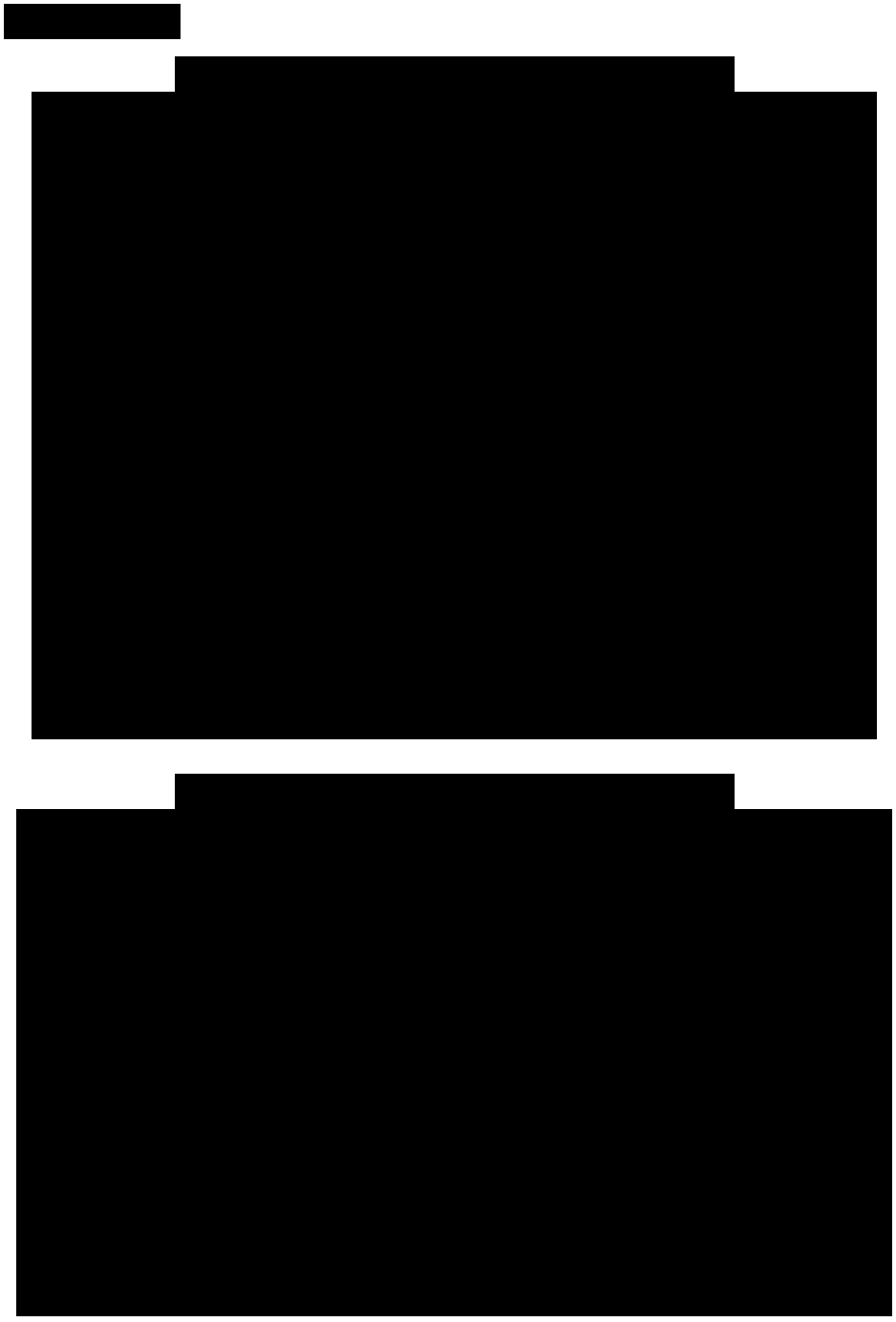

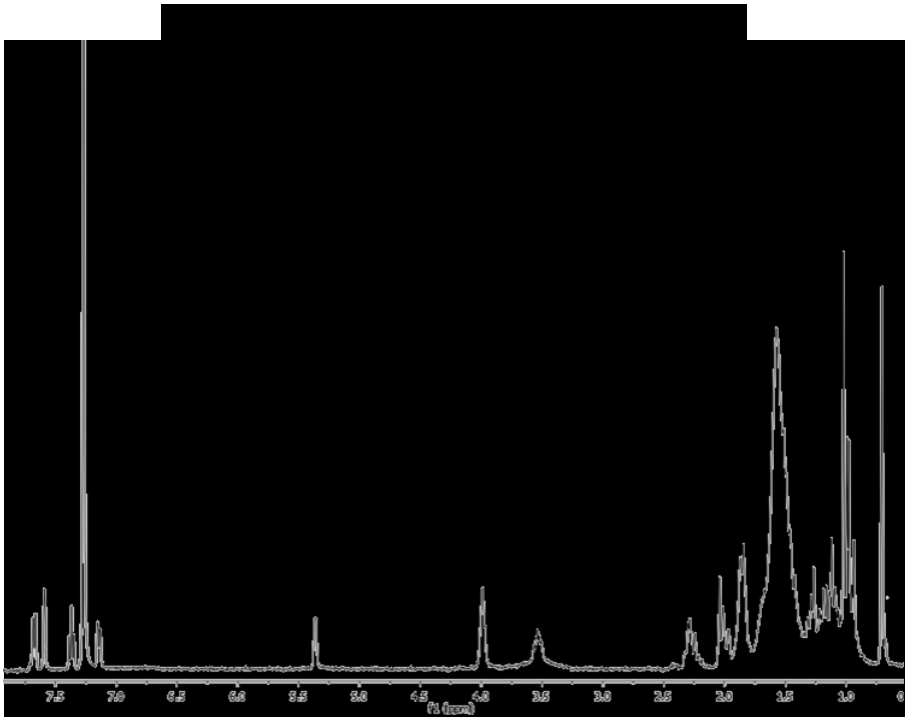
7.5
7.0
6.5
6.0
5.5
5.0
4.5
4.0
3.5
3.0
2.5
2.0
1.5
1.0

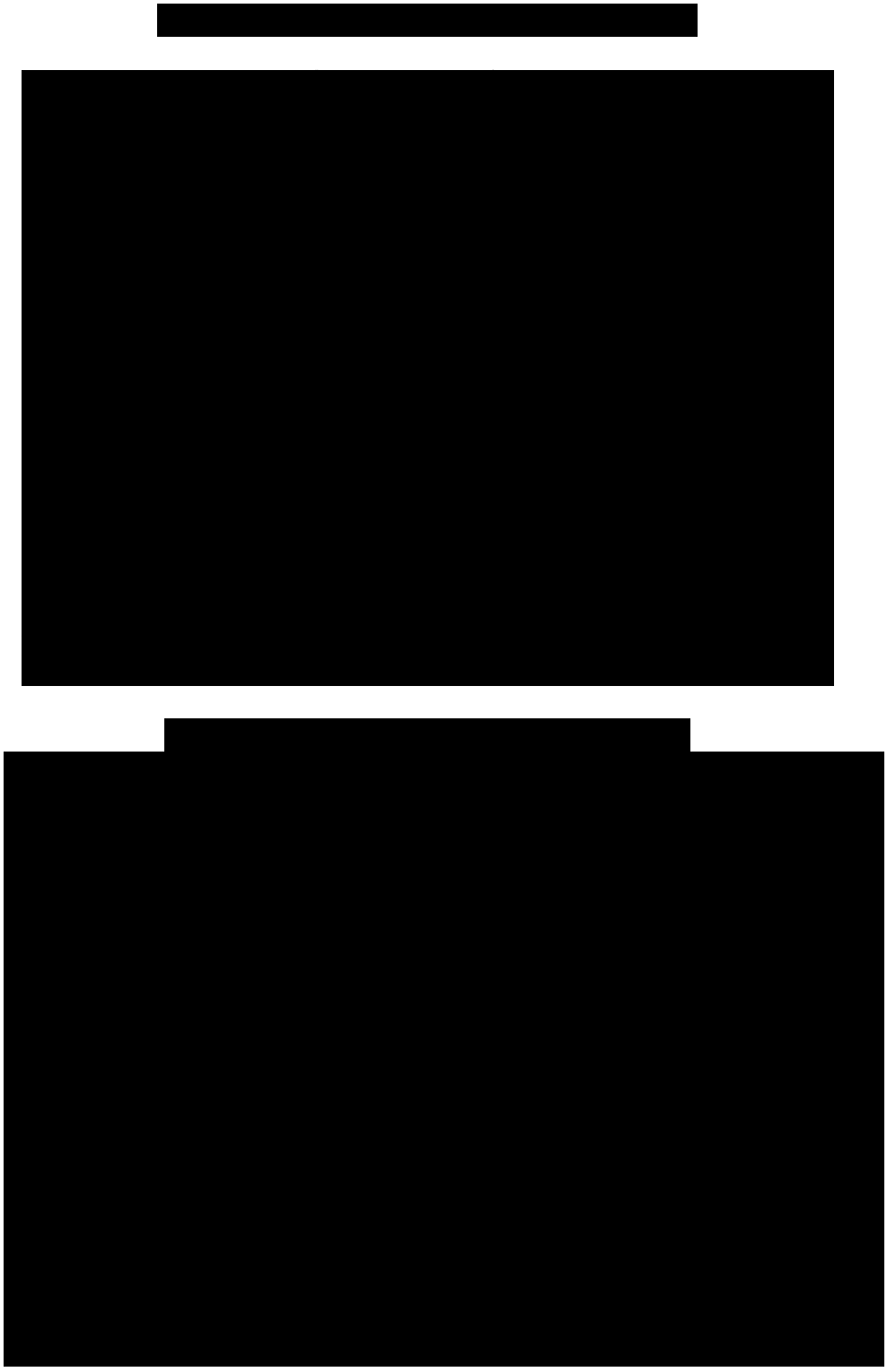

Experimental section III

Synthesis.

3α, 7β-diformyloxy-5β-cholan-24-oic acid (107). A solution of ursodeoxycholic acid **95** (1.3 mmol) in 10 mL of 90% formic acid containing 25μL of 70% perchloric acid was stirred at 47-50 °C for 12 h. The temperature of the heating bath was lowered to 40 °C, then 5 mL of acetic anhydride was added over 10 min and the mixture was stirred for 10 min more. The solution was cooled to room temperature, poured into 50 mL of water, and extracted with diethyl ether. The organic layers were washed with water to neutrality, dried over Na_2SO_4, and evaporated to give **107** (quantitative yield). An analytic sample was obtained by silica gel chromatography eluting with DCM/MeOH 9:1 v/v. Selected ^{1}H NMR (400 MHz CD_3OD): δ 8.03 (1H, s), 7.98 (1H, s), 4.89 (1H, m), 4.80 (1H, m), 0.98 (3H, s), 0.93 (3H, d, J = 6.5 Hz), 0.69 (3H, s); ^{13}C NMR (100 MHz CD_3OD): δ 178.1, 163.0, 162.5, 74.9, 74.8, 56.6, 56.4, 44.8, 43.5, 41.3, 41.2, 40.7, 36.6, 35.4 (2C), 35.1, 34.1, 34.0, 32.3, 32.0, 29.5, 27.6, 23.6, 22.3, 18.9, 12.5; HRMS-ESI *m/z* 449.2907 $[M+H]^+$, $C_{26}H_{41}O_6$ requires 449.2903.

3α, 7β-diformyloxy-24-*nor*-5β-cholan-23-nitrile (108). Crude **107** (1.1 mmol), 1.7 mL of cold trifluoroacetic acid, and 466 μL (3 eq) of trifluoroacetic anhydride were stirred at 0-5 °C until dissolution. Sodium nitrite (1.1 eq) was added in small portions. After the addition was completed, the reaction mixture was stirred first at 0-5 °C for 1 h, then at 38-40 °C for 8 h. On completion, the reaction was neutralized with NaOH 6 N, then the product was extracted with diethyl ether (3 x 50 mL), followed by washing with brine and dried over anhydrous Na_2SO_4. The ether was removed under reduced pressure to afford **108** (97%), which was subjected to the next step without any purification. An analytic sample was

obtained by silica gel chromatography eluting with hexanes/ethyl acetate 8:2 v/v. Selected ^{1}H NMR (400 MHz CD_3OD): δ 8.04 (1H, s), 7.99 (1H, s), 4.87 (1H, m), 4.73 (1H, m), 1.12 (3H, d, *J* = 6.5 Hz), 0.98 (3H, s), 0.71 (3H, s); ^{13}C NMR (100 MHz CD_3OD): δ 163.1, 162.6, 120.3, 74.8 (2C), 56.4, 55.5, 44.8, 43.2, 41.2, 40.9, 40.6, 35.4, 35.1, 34.6, 34.1, 34.0, 30.9, 29.3, 27.6, 25.1, 23.6, 22.3, 19.8, 12.5; HRMS-ESI *m/z* 416.2807 $[M+H]^+$, $C_{25}H_{38}NO_4$ requires 416.2801.

24-*nor*-ursodeoxycholic acid (109). Crude compound **108** (0.96 mmol) was refluxed in *ca*. 50 mL of methanol/water 1:1 v/v with 30% KOH w/w. After stirring for 48 h, the basic aqueous solution was neutralized with HCl 6 N. Then methanol was evaporated, and the residue was extracted with ethyl acetate (3 x 50mL). The combined organic layers were washed with brine, dried over anhydrous Na_2SO_4 and concentrated to give a white solid residue, that was purified by silica gel chromatography, eluting with DCM/MeOH 9:1 v/v (97%). An analytic sample was purified by HPLC on a Nucleodur 100-5 C18 (5 μm; 4.6 mm i.d. x 250 mm) with MeOH/H_2O (70:30) as eluent (flow rate 1 mL/min), to give compound **109** (t_R=20.7 min). $[\alpha]_{25}^{D}$=+11.0 (*c* 0.41, CH_3OH); selected ^{1}H NMR (400 MHz CD_3OD): δ 3.44 (2H, m), 0.98 (3H, d, *J* = 6.5 Hz), 0.93 (3H, s), 0.71 (3H, s). ^{13}C NMR (100 MHz CD_3OD): δ 177.3, 72.1, 71.9, 57.5, 56.6, 44.8, 44.5, 44.0, 42.5, 41.4, 40.7, 38.6, 38.0, 36.1, 35.2, 34.9, 31.0, 29.7, 27.9, 23.9, 22.4, 20.2, 12.7; HRMS-ESI *m/z* 379.2844 $[M+H]^+$, $C_{23}H_{39}O_4$ requires 379.2848.

Methyl 3α,7β-dihydroxy-24-*nor*-5β-cholan-23-oate (110). Compound **109** (0.26 mmol) was dissolved in 30 mL of dry methanol and *p*-toluenesulfonic acid (2 eq) was added. The solution was left to stir at room temperature for 5h. The mixture was neutralised by the addition of $NaHCO_3$ saturated solution. Most of the solvent was evaporated, and the

residue was extracted with ethyl acetate. The combined extract was washed with brine, dried over anhydrous Na_2SO_4, and evaporated to give **110** as an amorphous solid (97% yield). An analytic sample was purified by HPLC on a Nucleodur 100-5 C18 (5 μm; 4.6 mm i.d. x 250 mm) with MeOH/H_2O (9:1) as eluent (flow rate 1 mL/min), to give compound **110** (t_R=9.5 min). $[\alpha]_{25}^{D}$=+19.8 (*c* 0.22, $CHCl_3$); selected ^{1}H NMR (400 MHz $CDCl_3$): δ 3.60 (3H, s), 3.51 (2H, m), 0.92 (3H, d, *J* = 6.3 Hz), 0.88 (3H, s), 0.65 (3H, s). ^{13}C NMR (100 MHz $CDCl_3$): δ 173.8, 71.0, 70.9, 55.7, 54.9, 51.3, 43.6, 43.4, 42.4, 41.3, 39.9, 39.1, 37.1, 37.0, 34.8, 33.9, 33.6, 30.0, 28.6, 26.7, 23.3, 21.0, 19.5, 12.0; HRMS-ESI *m/z* 393.3009 $[M+H]^+$, $C_{24}H_{41}O_4$ requires 393.3005.

24-*nor*-5β-cholan-3α, 7β, 23-triol (98). To a solution of **110** (0.23 mmol) in dry THF (5 mL) at 0°C under argon were added $LiBH_4$ (5 eq) and dry methanol (5 eq) and the resulting mixture was stirred for 3 h at 0°C. The mixture was quenched by the addition of NaOH (1 M, 2 eq) and then allowed to warm to room temperature. Ethyl acetate was added, and the separated aqueous phase was extracted with ethyl acetate (3 × 30 mL). The combined organic phases were washed with water, dried over anhydrous Na_2SO_4 and concentrated. Purification by silica gel (DCM/MeOH 97:3 v/v) gave compound **98** as a colourless oil (85 mg, quantitative yield). An analytic sample was purified by HPLC on a Nucleodur 100-5 C18 (5 μm; 4.6 mm i.d. x 250 mm) with MeOH/H_2O (8:2) as eluent (flow rate 1 mL/min), to give compound **98** (t_R=17.8 min). $[\alpha]_{25}$ ^{D}=+23.7 (*c* 0.18, CH_3OH); ^{1}H NMR (400 MHz CD_3OD): δ 3.60 (1H, m ovl), 3.51 (1H, m), 3.50 (2H, m), 0.97 (3H, d, ovl), 0.96 (3H, s), 0.72 (3H, s). ^{13}C NMR (100 MHz CD_3OD): δ 72.1, 71.9, 60.8, 57.5, 57.1, 44.8, 44.5, 44.0, 41.6, 40.7, 39.9, 38.6, 38.0, 36.1, 35.2, 34.1, 31.0, 29.8, 27.9, 23.9, 22.4, 19.5, 12.6; HRMS-ESI *m/z* 365.3053 $[M+H]^+$, $C_{23}H_{41}O_3$ requires 365.3056.

Methyl 3α-hydroxy-7-oxo-24-*nor*-5β-cholan-23-oate (113). 7-KLCA (5.12 mmol) was formylated to afford **111** which was then subjected to Beckmann degradation at C24. The corresponding *nor*-nitrile **112** was then hydrolysed to the acid which was finally turned into the ester **113** in 66% yield. The formylation, Beckmann degradation and nitrile hydrolysis were previously described.

Methyl (*E*)-3α-acetoxy-6-ethylidene-7-oxo-24-*nor*-5β-cholan-23-oate (114). To a solution of diisopropylamine (7 eq) in dry THF (50 mL) was added dropwise a solution of *n*-butyllithium (2.5 M in hexane, 6 eq) at -78 °C. After 30 min, trimethylchlorosilane (7 eq) was added. After additional 30 min, a solution of **113** (1 eq) in dry THF (10 mL) was added. The reaction was stirred at -78 °C for 45 min and then triethylamine (7 eq) was added. After 1 h, the reaction mixture was allowed to warm to -20 °C, treated with an aqueous saturated solution of $NaHCO_3$ (100 mL) and brought up to room temperature for 2h. The aqueous phase was extracted with ethyl acetate (3 x 50 mL). The combined organic phases were washed then with a saturated solution of $NaHCO_3$, water and brine. After drying, the residue was evaporated under vacuum to give crude enol ether, which was dissolved in dry DCM (20 mL) and cooled at -78 °C. At this stirred solution acetaldehyde (5 eq) and $BF_3{\cdot}OEt_2$ (10 eq) were added dropwise. The reaction mixture was stirred for 1h at -78 °C and allowed to warm to room temperature. The mixture was quenched with a saturated aqueous solution of $NaHCO_3$ and extracted with DCM. The combined organic phases were washed with brine, dried over anhydrous Na_2SO_4, and concentrated under *vacuum*. Purification by silica gel (hexane/ethyl acetate 99:1 v/v with 0.5% TEA) gave compound **114** (60% over two steps).

NMR analysis demonstrated a diastereomeric ratio E/Z >95%. The *E* configuration of the exocyclic double bond was established by dipolar coupling H_3-25 (δ 1.67)/H-5 (δ 2.61) in the NOESY spectrum (400 MHz, mixing time 400 ms). $[\alpha]_D^{25}$= -3.31 (*c* 3.25, CH_3OH). Selected ^1H NMR (400 MHz, $CDCl_3$):δ 6.17 (1H, q, *J* = 7.2 Hz, H-24), 4.75 (1H, m, H-3), 3.64 (3H, s, $COOCH_3$), 2.61 (1H, dd, *J* = 13.1, 4.0 Hz, H-5), 1.98 (3H, s, $COCH_3$), 1.67 (3H, d, *J* = 7.2 Hz, H_3-25), 1.00 (3H, s, H_3-19), 0.97 (3H, d, *J* = 6.8 Hz, H_3-21), 0.67 (3H, s, H_3-18). ^{13}C NMR (100 MHz, $CDCl_3$): δ 204.5, 174.2, 170.5, 143.0, 130.6, 72.5, 54.7, 51.4, 50.7, 48.6, 45.3, 43.7, 41.5, 39.1, 38.8, 34.6, 34.2, 33.6, 33.4, 28.5, 25.9 (2C), 22.8, 21.3 (2C), 19.7, 12.7, 12.1. HR ESIMS *m/z* 459.3107 $[M+H]^+$, $C_{28}H_{43}O_5$ requires 459.3110.

Methyl 3α-acetoxy-6β-ethyl-7-oxo-24-*nor*-5β-cholan-23-oate (115). A solution of **114** (1.3 mmol) in dry THF/MeOH (100 mL, 1:1 v/v) was hydrogenated in presence of $Pd(OH)_2$ 20% wt on activated carbon (0.1 mol %) Degussa type. The mixture was transferred to a standard PARR apparatus and flushed first with nitrogen and then with hydrogen several times. The reaction was stirred under 50 psi of H_2 at room temperature for 12 h. The catalyst was filtered through Celite, and the recovered filtrate was concentrated under *vacuum* to give **115** (quantitative yield). The β configuration of the ethyl group at C-6 was determined by dipolar couplings H_3-25 (δ 0.83)/ H_3-19 (δ 1.22) in the NOESY spectrum (400 MHz, mixing time 400 ms). $[\alpha]_D^{25}$=+10.4 (*c* 0.39, CH_3OH). Selected^1H NMR (400 MHz, $CDCl_3$): δ 4.65 (1H, m, H-3), 3.67 (3H, s, $COOCH_3$), 2.60 (1H, t, *J* = 11.2 Hz, H-8), 2.43 (1H, dd, *J* = 14.2, 2.6 Hz, H-22a), 1.98 (3H, s, $COCH_3$), 1.88 (1H, m ovl, H-6), 1.22 (3H, s, H_3-19), 0.98 (3H, d, *J* = 6.4 Hz, H_3-21), 0.83 (3H, t, *J* = 7.0 Hz, H_3-25), 0.70 (3H, s, H_3-18).

^{13}C NMR (100 MHz, $CDCl_3$): δ 215.3, 174.0, 170.5, 72.8, 61.9, 55.0, 51.4, 49.2, 48.7, 45.5, 42.9, 42.6, 41.4, 38.7 (2C), 35.6, 35.3, 34.9, 28.3 (2C), 26.5, 25.9, 24.8, 21.4, 21.3, 19.6, 13.0, 12.1. HR ESIMS *m/z* 461.3265 $[M+H]^+$, $C_{28}H_{45}O_5$ requires 461.3267.

6β-ethyl-3α,7β-hydroxy-24-*nor*-5β-cholan-23-ol (99) and **6β-ethyl-3α,7α-hydroxy-24-*nor*-5β-cholan-23-ol (116).** To a methanol solution of compound **115** (0.22 mmol), a large excess of $NaBH_4$ was added at 0 °C. The mixture was left at room temperature for 10 h and then water and MeOH were added dropwise over a period of 15 min at 0 °C until effervescence stopped. Then after evaporation of the solvents, the residue was diluted with water and extracted with ethyl acetate (3 x 50 mL). The combined extract was washed with brine, dried over anhydrous Na_2SO_4, and evaporated to the crude residue that was subjected to the next step without further purification. To a solution of crude residue (0.214 mmol) in dry THF (15 mL), at 0 °C dry methanol (3 eq) and $LiBH_4$ (2 M in THF, 3 eq) were added. The resulting mixture was stirred for 2 h at 0 °C. The mixture was quenched by the addition of 1 M NaOH (2 eq) and then ethyl acetate. The organic phase was washed with water, dried over anhydrous Na_2SO_4 and concentrated. HPLC purification on a Nucleodur 100-5 C18 (5 μm; 10 mm i.d. x 250 mm) with MeOH/H_2O (86:14) as eluent (flow rate 3 mL/min), gave **99** (54%, t_R= 15 min) and **116** (23%, t_R= 11 min)**.**

6β-ethyl-3α,7β-hydroxy-24-*nor*-5β-cholan-23-ol (99). $[\alpha]_D^{25}$=+11.57 (*c* 0.14, CH_3OH). Selected ^{1}H NMR (400 MHz, $CDCl_3$): δ 3.80 (1H, dd, *J* = 10.5, 5.5 Hz, H-7), 3.71 (1H, m, H-23a), 3.61 (1H, m, ovl, H-23b), 3.61 (1H, m, ovl, H-3), 0.98 (3H, d, ovl, H_3-21), 0.97 (3H, s, H_3-19), 0.96 (3H, t, ovl, H_3-25), 0.70 (3H, s, H_3-18). ^{13}C NMR (100 MHz, CD_3OD): δ 75.2, 71.8, 60.8, 57.5, 56.6, 51.5, 45.5, 44.8, 42.0, 41.4, 40.7, 40.3, 39.9, 36.9,

36.0, 34.2, 30.5, 29.6, 28.3, 26.2, 23.4, 22.0, 19.4, 14.7, 12.9. HR ESIMS *m/z* 393.3365 $[M+H]^+$, $C_{25}H_{45}O_3$ requires 393.3369.

Methyl (*E*)-6-ethylidene-3α-hydroxy-7-oxo-5β-cholan-24-oate (117). 7-KLCA was subjected to a Fischer esterification as previously described. The resulting methyl ester (99% yield) was then converted into a silyl enol ether and then condensed with acetaldehyde to afford compound **117** in the same experimental conditions described for compound **114**. Purification by silica gel (hexane/ethyl acetate 99:1 v/v with 0.5% TEA) gave compound **117** (55% over two steps).

Methyl 6β-ethyl-3α-hydroxy-7-oxo-5β-cholan-24-oate (118). Compound **117** was reduced at the double bond in the same experimental conditions employed for compound **115** to afford compound **118** with a quantitative yield. The crude reaction was used for the next step without further purification.

6β-ethyl-3α,7β-dihydroxy-5β-cholan-24-ol (100) and 6β-ethyl-3α,7α-dihydroxy-5β-cholan-24-ol (ep-100). Compound **118** was treated first with $NaBH_4$ and then with $LiBH_4$ just as described for compound **115**. HPLC purification on a Nucleodur 100-5 C18 (5 μm; 10 mm i.d. x 250 mm) with MeOH/H_2O (88:12) as eluent (flow rate 3 mL/min), gave **100** (69%, t_R= 11 min) and **ep-100** (35%, t_R= 20.4 min).

6β-ethyl-3α,7β-dihydroxy-5β-cholan-24-ol (100). $[\alpha]_D^{25}$= +15.2 (*c* 1.21, CH_3OH). Selected ^1H NMR (400 MHz, CD_3OD): δ 3.74 (1H, dd, *J* = 10.3, 6.0 Hz, H-7), 3.51 (2H, ovl, H_2-24), 3.51 (1H, m, ovl, H-3), 1.00 (3H, s, H_3-19), 0.97 (3H, d, *J* = 6.5 Hz, H_3-21), 0.96 (3H, t, *J* = 7.6 Hz, H_3-26), 0.72 (3H, s, H_3-18). ^{13}C NMR (100 MHz, CD_3OD): δ 75.3, 71.9, 63.6, 57.5, 56.5, 51.6, 45.7, 44.9, 42.1, 41.5, 40.4, 40.3, 37.1, 35.8, 35.8, 32.4, 30.7, 29.7, 29.6, 28.3, 26.2, 23.4, 22.1, 19.4, 14.8, 12.7. HR ESIMS *m/z* 407.3529 $[M + H]^+$, $C_{26}H_{47}O_3$ requires 407.3525.

(*E*)-6-ethylidene-3α,7β-dihydroxy-5β-cholan-24-ol (101). Compound **117** was directly reduced in the same conditions described for compound **100**. HPLC purification on a Nucleodur 100-5 C18 (5 μm; 10 mm i.d. x 250 mm) with MeOH/H_2O (88:12) as eluent (flow rate 3 mL/min) gave compound **101** (85% over two steps, t_R= 9.2 min). $[\alpha]_D^{25}$= +18.1 (*c* 0.36, CH_3OH); Selected ^1H NMR (400 MHz, CD_3OD): δ 5.64 (1H, q, *J* = 6.9 Hz, H_2-25), 3.90 (1H, d, *J* = 9.8 Hz, H-7), 3.55 (2H, ovl, H_2-24), 3.55 (1H, m, ovl, H-3), 1.62 (3H, d, *J* = 6.9 Hz, H_3-26), 0.97 (3H, d, *J* = 6.8 Hz, H_3-21), 0.81 (3H, s, H_3-19), 0.70 (3H, s, H_3-18). ^{13}C NMR (100 MHz, CD_3OD): δ 142.7, 114.5, 63.6, 57.1, 56.1, 45.2, 44.9, 44.2, 40.7, 40.2, 36.3, 36.2, 35.9, 34.7, 32.4, 30.2, 29.5, 28.8, 27.4, 22.6, 21.5, 18.5, 11.8, 11.7. HR ESIMS *m/z* 405.3373 $[M + H]^+$, $C_{26}H_{45}O_3$ requires 405.3369.

6α-ethyl-3α,7β-dihydroxy-5β-cholan-24-ol (102) and 6α-ethyl-3α,7α-dihydroxy-5β-cholan-24-ol (ep-102). To a dry methanol solution of compound **118** sodium methoxide (2 eq) was added. The reaction was stirred at rt overnight. The mixture was quenched by adding water and then concentrated under *vacuum*. The residue was extracted with ethyl acetate (3 x 30 mL), and the organics were washed with brine, dried over anhydrous Na_2SO_4 and concentrated to afford compound **119** (quantitative yield). This was then reduced as described for the last derivatives.

Crude HPLC purification on a Nucleodur 100-5 C18 (5 μm; 10 mm i.d. x 250 mm) with MeOH/H_2O (80:20) as eluent (flow rate 3 mL/min) gave compound **102** (54% over two steps, t_R= 15 min) and **ep-102** (11% yield, over two steps, t_R= 17.4 min).

6β-ethyl-3β,7β-dihydroxy-5β-cholan-24-ol (103) and 6β-ethyl-3β,7α-dihydroxy-5β-cholan-24-ol (ep-103). To a pyridine solution of compound **118** p-tosyl chloride (2 eq) was added. The reaction was left

to stir for 4h. After starting material consumption, pyridine was distilled under *vacuum*. The dry residue was diluted with water and extracted with ethyl acetate (3 x 30 mL). The organics were dried over anhydrous Na_2SO_4 and concentrated. The 3-tosyloxy derivative **120** was subjected to the next step without further purification. A solution of compound **120** and potassium acetate (1.5 eq) in water/DMF 1:5 v/v was refluxed for 2h. The solution was then cooled to rt, diluted with water, and extracted with ethyl acetate (3 x 30 mL). The combined organics were washed with water, dried over anhydrous Na_2SO_4 and concentrated. Crude Purification by silica gel (hexane/ethyl acetate 7:3 v/v with 0.5% TEA) gave methyl 3β-acetoxy-6β-ethyl-7-oxo-5β-cholan-24-oate (**121**) with 74% yield over two steps. Compound **121** was reduced with $NaBH_4$/$LiBH_4$ procedure as already described to afford the two epimer triols **103** and **ep-103.** HPLC purification on a Nucleodur 100-5 C18 (5 μm; 10 mm i.d. x 250 mm) with MeOH/H_2O (88:12) as eluent (flow rate 3 mL/min) gave **103** (52 % over two steps, t_R= 11 min) and **ep-103** (22 % over two steps, t_R= 13 min).

6β-ethyl-3β,7β-dihydroxy-5β-cholan-24-ol (103). Selected ^{1}H NMR (700 MHz, CD_3OD): δ 3.59 (1H, brs, H-3), 3.57 (1H, dd, *J* = 12.6, 2.3Hz, H-7), 3.51 (2H, m, H_2-24), 0.98 (3H, s, H_3-19), 0.96 (3H, ovl, H_3-21), 0.96 (3H, t, ovl, H_3-26), 0.70 (3H, s, H_3-18). ^{13}C NMR (100 MHz, CD_3OD): δ 75.2, 68.3, 63.6, 58.3, 57.1, 45.7 (2C), 44.2, 41.8 (2C), 41.2, 40.0, 37.0, 35.9, 33.3, 31.1, 30.3, 29.4 (2C), 26.6 (2C), 23.2 (2C), 19.3, 13.0, 12.3. HR ESIMS m/z 407.3530 $[M+H]^+$, $C_{26}H_{47}O_3$ requires 407.3525.

Methyl 6β-ethyl-7-keto-5β-cholan-24-oate (123).

Lithium bromide (2 eq) and lithium carbonate (2 eq) were added to a solution of methyl 6β-ethyl-3α-tosyloxy-7-oxo-5β-cholan-24-oate **120**

(0.85 mmol) in dry DMF (30 mL), and the mixture was refluxed for 2 h. After cooling to room temperature, the mixture was slowly poured into 10% HCl solution (20 mL) and extracted with DCM (3 × 50 mL). The combined organic layer was washed successively with water, saturated $NaHCO_3$ solution and water, and then dried over anhydrous $MgSO_4$ and evaporated to dryness to give an oily residue (quantitative yield), which was subjected to the next step without any purification.

Hydrogenation on $Pd(OH)_2$ in the same operative condition previously described furnished **123** (88% over two steps). Selected ^{1}H NMR (400 MHz, CD_3OD): δ 3.63 (3H, s, $COOCH_3$), 2.53 (1H, t, *J* = 11.4 Hz, H-8), 2.33 (1H, m, H-23a), 2.19 (1H, m, H-23b), 1.18 (3H, s, H_3-19), 0.89 (3H, d, *J* = 6.2 Hz, H_3-21), 0.81 (3H, t, *J* = 7.4 Hz, H_3-26), 0.64 (3H, s, H_3-18); ^{13}C NMR (100 MHz, CD_3OD): δ 174.9, 62.4, 54.7, 51.5, 50.7, 48.7, 45.7, 43.2, 42.5, 38.8, 37.5, 36.3, 35.2, 31.0, 30.9, 30.3, 28.2, 26.7 (2C), 26.3, 24.9, 21.4, 20.4, 18.3, 13.0, 12.0; HR ESIMS *m/z* 417.3373 $[M+H]^+$, $C_{27}H_{43}O_3$ requires 417.3369.

6β-ethyl-7β-hydroxy-5β-cholan-24-ol (104) and 6β-ethyl-7α-hydroxy-5β-cholan-24-ol (ep-104). Reduction of compound **123** with $NaBH_4$/$LiBH_4$ in the same operative condition described for the synthesis of compounds **115**. HPLC purification on a Nucleodur 100-5 C18 (5 μm; 10 mm i.d. x 250 mm) with MeOH/H_2O (92:8) as eluent (flow rate 3 mL/min) furnished **104** (54%, t_R= 25 min) and **ep-104** (23%, t_R= 13 min).

6β-ethyl-7β-hydroxy-5β-cholan-24-ol (104). Selected ^{1}H NMR (700 MHz CD_3OD): δ 3.67 (1H, dd, *J* = 8.7, 4.7 Hz, H-7), 3.51 (2H, m, H_2-24), 0.98 (3H, s, H_3-19), 0.97 (3H, d, *J* = 6.6 Hz, H_3-21), 0.96 (3H, t, *J* = 7.4 Hz, H_3-26), 0.71 (3H, s, H_3-18). ^{13}C NMR (175 MHz CD_3OD): δ 75.5, 63.8, 57.6, 56.5, 44.2, 43.7, 42.8, 41.0, 40.9, 40.8, 38.2 (2C), 36.9,

34.4, 32.8, 29.7, 28.9, 27.0, 26.1, 24.7, 22.2, 22.0 (2C), 19.2, 13.9, 12.3. HR ESIMS *m/z* 391.3580 $[M+H]^+$, $C_{26}H_{47}O_2$ requires 391.3576.

Methyl 6α-ethyl-3β-hydroxy-7-oxo-5β-cholan-24-oate (122). Methyl 3β-acetoxy-6β-ethyl-7-oxo-5β-cholan-24-oate (**121**) was treated with sodium methoxide as described for compound **119** to afford C-6 epimerisation and deacetylation furnishing compound **122**. Selected ^{1}H NMR (400 MHz CD_3OD): δ 3.96 (1H, m, H-3), 3.64 (3H, s, $COOCH_3$), 2.85 (1H, dd, *J* = 5.6, 12.3 Hz, H-6), 2.50 (1H, t, *J* = 11.2 Hz, H-8), 2.33 (1H, m, H-23a), 2.20 (1H, m, H-23b), 1.27 (3H, s, H_3-19), 0.95 (3H, d, *J* = 6.4 Hz, H_3-21), 0.81 (3H, t, *J* = 7.2 Hz, H_3-26), 0.71 (3H, s, H_3-18); ^{13}C NMR (100 MHz CD_3OD): δ 213.4, 174.8, 65.9, 54.8, 51.8, 51.2, 50.0, 49.0, 45.7, 43.2, 42.7, 39.0, 36.2, 35.2, 31.0 (2C), 29.2, 29.0, 28.3, 27.2, 24.6, 24.0, 22.1, 18.7, 18.4, 12.0 (2C). HR ESIMS *m/z* 433.3322 $[M + H]^+$, $C_{27}H_{45}O_4$ requires 433.3318.

6α-ethyl-3β,7β-dihydroxy-5β-cholan-24-ol (105) and 6α-ethyl-3β,7α-dihydroxy-5β-cholan-24-ol (ep-105). Intermediate **122** was treated with $NaBH_4$/$LiBH_4$ as previously described. HPLC purification on a Nucleodur 100-5 C18 (5 μm; 10 mm i.d. x 250 mm) with MeOH/H_2O (88:12) as eluent (flow rate 3 mL/min), gave compound **105** as a white solid (53%, t_R= 8.2 min) and a small amount of compound **ep-105** (5%, t_R= 12.6 min).

6α-ethyl-3β,7β-dihydroxy-5β-cholan-24-ol (105). Selected ^{1}H NMR (500 MHz CD_3OD): δ 4.01 (1H, brs, H-3), 3.51 (2H, m, H_2-24), 3.05 (1H, t, *J* = 9.7 Hz, H-7), 0.97 (3H, s, H_3-19), 0.96 (3H, d, *J* = 6.4 Hz, H_3-21), 0.88 (3H, t, *J* = 7.6 Hz, H_3-26), 0.72 (3H, s, H_3-18). ^{13}C NMR (100 MHz CD_3OD): δ 76.3, 67.1, 63.6, 57.8, 56.8, 45.0, 44.8, 44.5, 41.7, 40.3, 39.1, 37.0, 35.9, 33.0, 31.2, 30.2, 29.8, 28.4, 28.0, 27.9, 24.8, 22.9, 21.8,

19.3, 12.8, 11.6. HR ESIMS *m/z*407.3529 $[M+H]^+$, $C_{26}H_{47}O_3$ requires 407.3525.

6α-ethyl-3β,7β-dihydroxy-5β-cholan-24-oic acid (106) and 6α-ethyl-3β,7α-dihydroxy-5β-cholan-24-oic acid (ep-106). Compound **106** (74% over two steps) was synthesized starting from compound **122**. This was first hydrolysed with NaOH (4 eq) in a mixture of MeOH/water 1:1 v/v overnight. After TLC monitoring, the mixture was acidified with HCl 6N solution and methanol was evaporated under *vacuum*. The water phase was extracted with ethyl acetate (3 x 25 mL), and the organic phase was then washed with brine, dried over anhydrous Na_2SO_4, and concentrated to give the carboxylic acid. This was then reduced with only $LiBH_4$ in the same operative condition described for the synthesis of compounds **115**. HPLC purification on a Nucleodur100-5 C18 (5 μm; 10 mm i.d. x 250 mm) with MeOH/H_2O (88:12) as eluent (flow rate 3 mL/min) afforded compound **106** (65%, t_R= 8 min) and **ep-106** (9%, t_R= 11 min).

6α-ethyl-3β,7β-dihydroxy-5β-cholan-24-oic acid (106). Selected ^1H NMR (500 MHz CD_3OD): δ 4.01 (1H, brs, H-3), 3.06 (1H, t, *J* = 9.7 Hz, H-7), 2.32 (1H, m, H-23a), 2.19 (1H, m, H-23b), 0.97 (3H, s, H_3-19), 0.96 (3H, d, ovl, H_3-21), 0.87 (3H, t, *J* = 7.7 Hz, H_3-26), 0.71 (3H, s, H_3-18). ^{13}C NMR (100 MHz CD_3OD): δ 178.3, 71.3, 67.5, 57.4, 51.7, 43.8, 42.8, 41.5, 41.2, 41.0, 37.0, 36.7, 33.8, 32.4, 32.0, 31.1 (2C), 29.3, 28.3, 24.6, 24.2, 23.3, 22.2, 18.8, 12.3, 12.2. HR ESIMS *m/z* 419.3169 $[M-H]^-$, $C_{26}H_{43}O_4$ requires 419.3167.

Computational Studies.

Virtual Screening. The crystal structure of the open apo form of homo sapiens ACE2 (PDB ID 1R42)31 was downloaded from the Protein Data Bank website. The disordered segment of the collectrin homology

domain and water molecules were removed. The receptor was treated with the Protein Preparation Wizard tool implemented in Maestro ver. 11.832 to assign bond orders, to add hydrogen atoms, adjust disulfide bonds, and assign residues protonation state at pH 7.4. Virtual screening (VS) was performed on an in-house library of 67 bile acids (BAs), 10 natural and 57 semisynthetic derivatives, enriched with previously identified ACE2 activators, hydroxyzine, minithixen, and DIZE. Chemical/physical properties of all compounds were calculated with QikProp tool ver. 5.832. Since even minor structural changes of steroids can produce potential biological activities, we build our in-house BAs library to include compounds sharing a 17-carbon-atom skeleton composed of four fused rings, which form the typical steroidal scaffold. They vary from one another in the position and name of the substituent groups. The steroidal carbons hydrogens that have been replaced in our in-house library are:

1) those in positions 3 and 7, which have been replaced with a hydroxyl group in both different configurations (α and β);
2) the hydrogen at C7, which has been replaced with an ethyl group in both configurations (α and β);
3) finally, the C24 has been substituted with different polar and apolar groups.

Docking calculations were performed in a box including the hinge bending region of ACE2 on the Protein Data Bank deposited structure of ACE2 in the open conformation (PDB ID 1R42), according to previous reports on the discovery of ACE2 activators. The VS procedure was carried out with the AutoDock4.2.6 suite and the Raccoon2 graphical interface using the Lamarckian genetic algorithm (LGA). The VS protocol adopted was the same described in our previous work. To further assess our docking

protocol, re-docking calculations were performed on the potent ACE2 inhibitor MLN-4760 in the ACE2 binding site (PDB ID 1R4L). Given the presence of a Zn^{2+} ion coordinating the ligand, the improved AutoDock4(Zn) force field was used for the calculation. AutoDock4(Zn) well reproduced the experimental binding pose. The receptor was submitted to the AutoGrid4 tool, which calculated interaction grids, considering the two ligands and receptor-atom types through the definition of a cubic box of 46 × 46 × 46 Å. Subsequently, for each grid, AutoDock4 calculated interaction energies (ADscore) that express the affinity of a given ligand for the receptor. All the images were rendered using UCSF Chimera.

Molecular Dynamics (MD). MD simulations of apo ACE2 and ACE2 in complex with 103 and 98 were performed with the CUDA version of the AMBER18 suite using the Amber f f14SB to treat the protein, while ligands charges were computed using the restrained electrostatic potential (RESP) fitting procedure. First, the ligand ESP was calculated through the Gaussian16 package using the 6-31G* asis set at the Hartree−Fock level of theory. Then, RESP charges and the ligand force field parameters were obtained from the two-stage fitting procedure using Antechamber and the general amber force field (GAFF2) parameters. The system was then immersed in a preequilibrated octahedral box of TIP3P water molecules, and the system was neutralized. The system was then minimized and successively equilibrated in a multistep procedure as previously described. Specifically, each system was minimized in four steps using the energy gradient convergence criterion set to 0.01 kcal/mol Å2 involving: (i) 5000 minimization steps (2500 with the steepest descent and 2500 with the conjugate gradient) of only hydrogen atoms; (ii) 20 000 minimization steps (10 000 with the steepest descent and 10 000 with the conjugate gradient)

of water and hydrogen atoms, keeping the solute restrained; (iii) 50 000 minimization steps (25 000 with the steepest descent and 25 000 with the conjugate gradient) of only the side chains of the protein, water, and hydrogen atoms; (iv) 100 000 (50 000 with the steepest descent and 50 000 with the conjugate gradient) of complete minimization. Successively, water molecules, ions, and protein side chains were thermally equilibrated in three steps: (i) 5 ns of NVT equilibration with the Langevin thermostat by gradually heating from 0 to 300 K, while gradually rescaling solute restraints from a force constant of 10 to 1 kcal/mol Å2; (ii) 5 ns of NPT equilibration at 1 atm with the Berendsen thermostat by gradually rescaling restraints from 1.0 to 0.1 kcal/mol Å2; and (iii) 5 ns of NPT equilibration with no restraints. Finally, three independent MD production runs of 500 ns each were performed for each system using a timestep of 2 fs. The SHAKE algorithm was used for those bonds containing hydrogen atoms in conjunction with periodic boundary conditions at constant pressure and temperature, particle mesh Ewald (PME) for the treatment of long-range electrostatic interactions and a cutoff of 10 Å for nonbonded interactions.

Principal Component Analysis. The principal component analysis (PCA) of apo ACE2 and ACE2 complexed with 98 and 103 was carried out using the CPPTRAJ Module of the AMBER18 Suite. First, the overall 1.5 μs of MD trajectories of each system were stripped of solvent and ions. Then, to consider the internal dynamics of ACE2, global rotational/translational motions of the protein were removed by fitting the stripped trajectories to the protein-heavy atoms of the first MD frame. This allowed us to generate the average structure of the protein of each system, which was used as the reference structure for the PCA analysis. Finally, we have generated the coordinate covariance matrix and diagonalized it,

thus obtaining the first four principal components (PCs) as eigenvectors and eigenvalues. The pseudotrajectory of the protein motion was then imported and visualized into the Normal Mode Wizard GUI (NMWiz) of VMD, to generate the porcupine plot of each motion, with the arrows representing the magnitude and direction of the eigenvectors. All the images were rendered using UCSF Chimera.

ACE2 Inhibitor Screening Assay Kit. The ACE2 Inhibitor Screening Assay Kit (BPS Bioscience Catalogue # 79923) measures the exopeptidase activity of ACE2. It utilizes the ability of an active ACE2 to cleave a Fluorogenic Substrate to release a free fluorophore that can be easily quantified using a fluorescence microplate reader. In the presence of an ACE2-specific inhibitor, the enzyme loses its peptidase activity, which results in a decrease in fluorescence intensity, whereas in the presence of an activator, an increase in fluorescence is observed. DIZE was used as a positive control of enzymatic activity. Briefly, the purified ACE2 is thawed and diluted in ACE2 buffer to the concentration of 0.5 ng/μL ACE2. This enzyme solution (20 μL) is added to each well of a 96-well plate, designated as “Positive Control” and “Test Inhibitor”. Conversely, the wells designated as “Blank” contain only the ACE2 buffer (20 μL). Next, 5 μL of Test Inhibitor solution are added to each well-designated Test Inhibitor. For the wells labelled Positive Control and Blank, add 5 μL of the Inhibitor buffer (10% DMSO in water). Finally, 25 μL of ACE2 Fluorogenic Substrate is added to all wells and the reaction is incubated at room temperature for 60 min, protected from direct light. After the incubation, the fluorescence intensity of the samples (λ excitation = 555 nm; λ emission = 585 nm) is measured in a FluoStar Omega microplate reader.

ACE2-SARS-CoV-2 Spike Inhibitor Screening Assay Kit. The ACE2-SARS-CoV-2 Spike Inhibitor Screening Assay Kit (BPS Bioscience Catalogue #79936) is designed for screening and profiling inhibitors of this interaction. This kit contains purified ACE2 and SARS-CoV-2 Spike (RBD)-Fc proteins, HRP-labeled anti-mouse-Fc region antibody, and assay buffers. The key to this kit is the high sensitivity of detection of Fc-tagged Spike protein by HRP-labeled Anti-Mouse-Fc.

Briefly, ACE2 protein is thawed, diluted 1 μg/mL in PBS, and attached to a nickel-coated 96-well plate at room temperature for 1 h with slow shaking. After the coating, the plate is washed and incubated with a Blocking Buffer for 10 min. Next, 10 μL of inhibitor solution containing the compounds to be tested is added to each well-designated Test Inhibitor and incubated at room temperature for 1 h with slow shaking. For the Positive Control and Blank, add 10 μL of inhibitor buffer (5% DMSO solution). Next, SARS-CoV-2 Spike (RBD)-Fc is thawed, diluted to 0.25 ng/μL (approximately 5 nM) in Assay Buffer 1 and added to all wells labelled Positive Control and Test Inhibitor. The reaction is incubated at room temperature for 1 h with slow shaking. After three washes and incubation with a Blocking Buffer (10 min), the plate is treated with an Anti-Mouse-Fc-HRP and incubated for 1 h at room temperature with slow shaking. Finally, an HRP substrate is added to the plate to produce chemiluminescence, which then can be measured using the FluoStar Omega microplate reader.

NMR spectra

^{1}H NMR (400 MHz, CD_3OD) of compound **98**

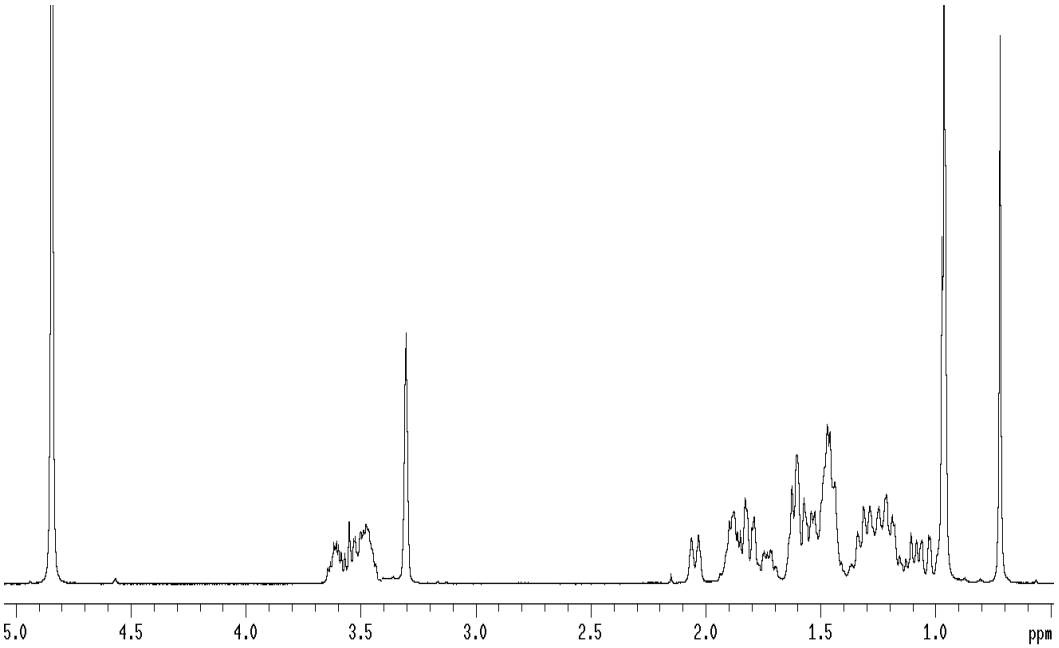

^{13}C NMR (100 MHz, CD_3OD) of compound **98**

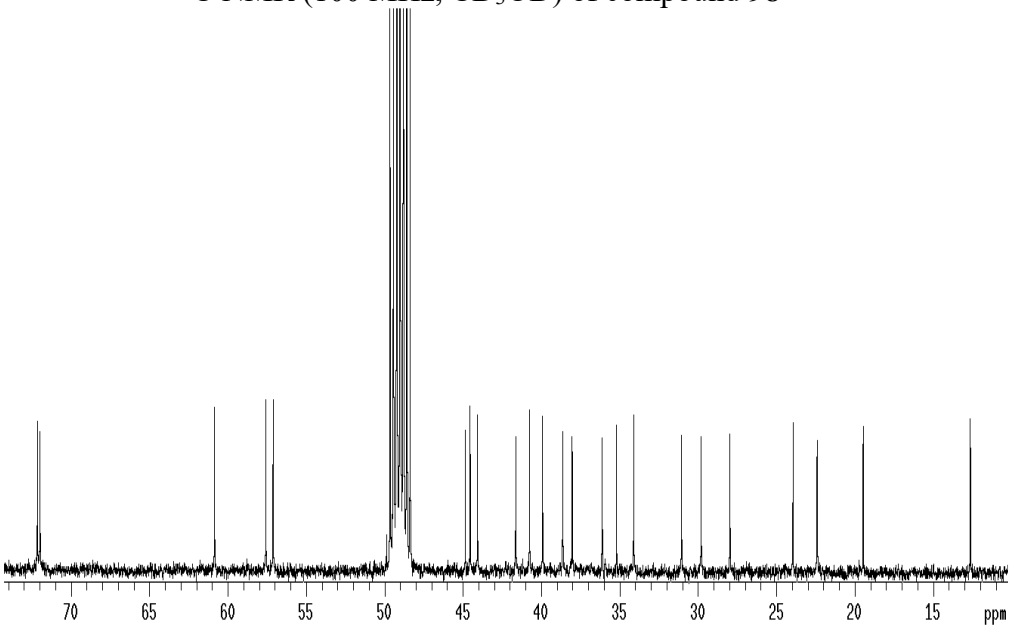

^{1}H NMR (400 MHz, $CDCl_3$) of compound **99**

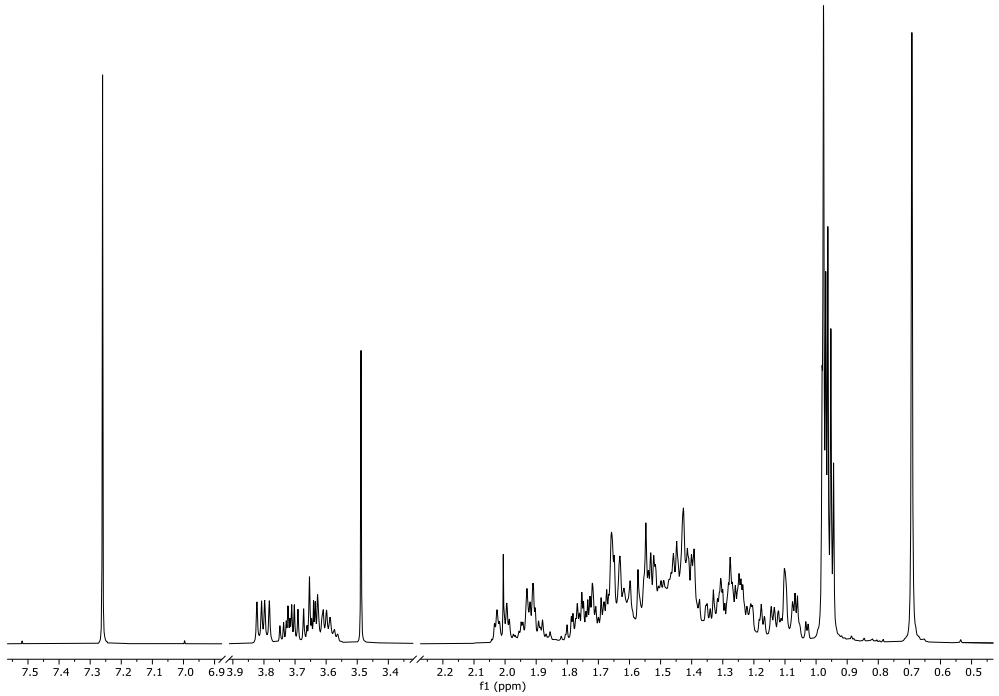

^{13}C NMR (100 MHz, $CDCl_3$) of compound **99**

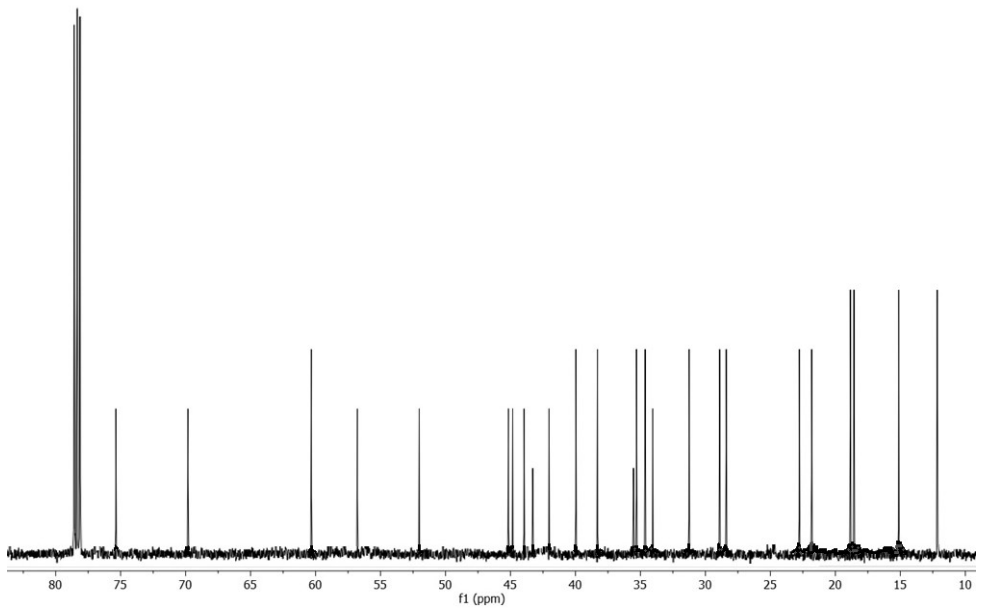

^{1}H NMR (400 MHz, CD_3OD) of compound **100**

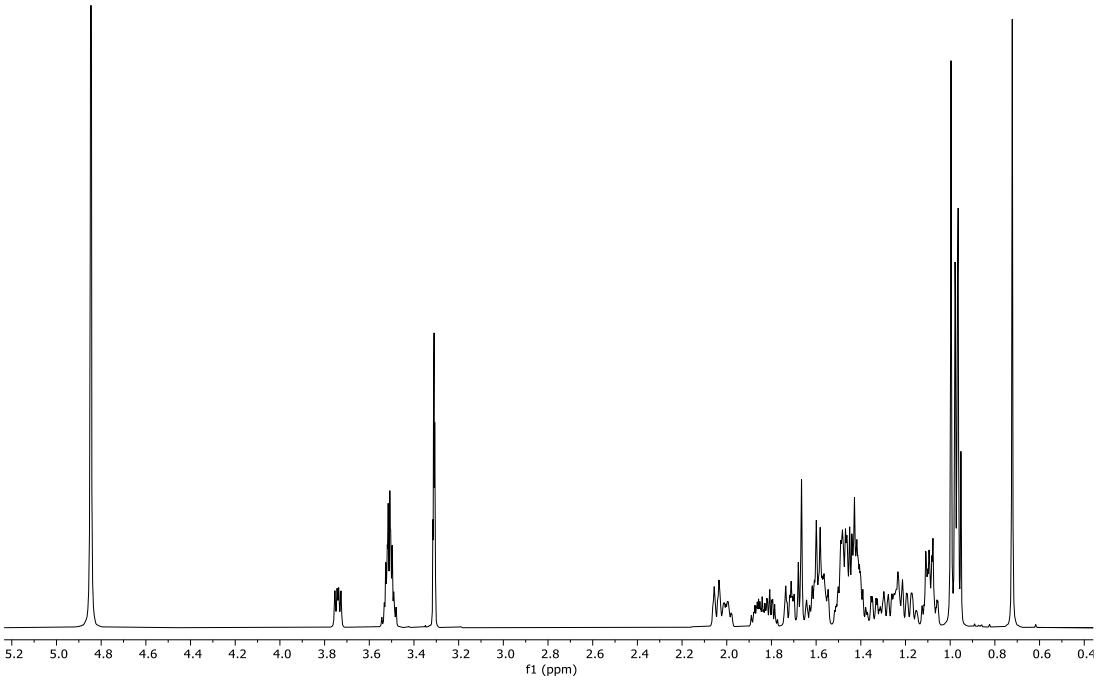

^{13}C NMR (100 MHz, CD_3OD) of compound **100**

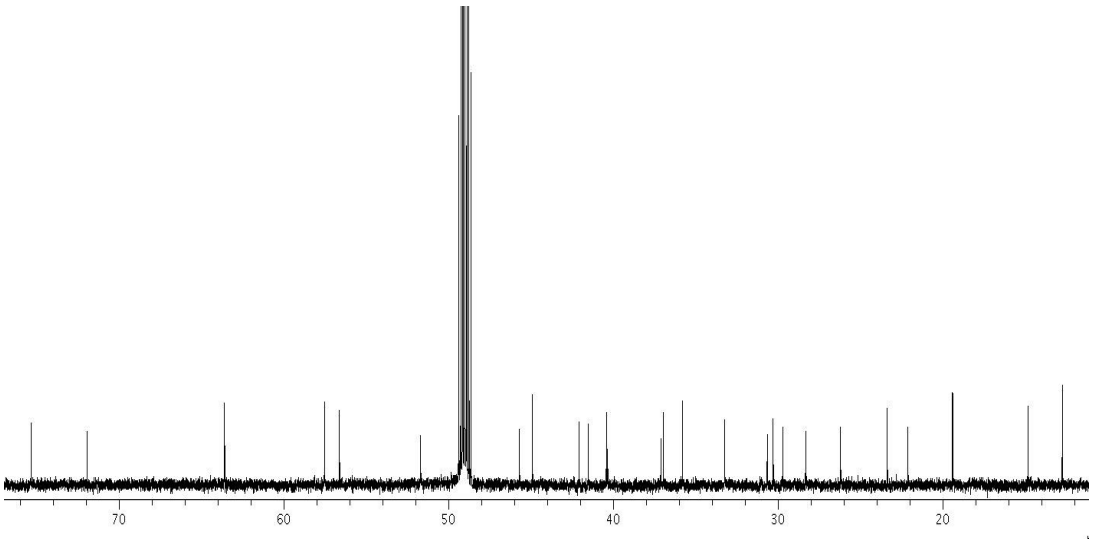

^{1}H NMR (400 MHz, CD_3OD) of compound **101**

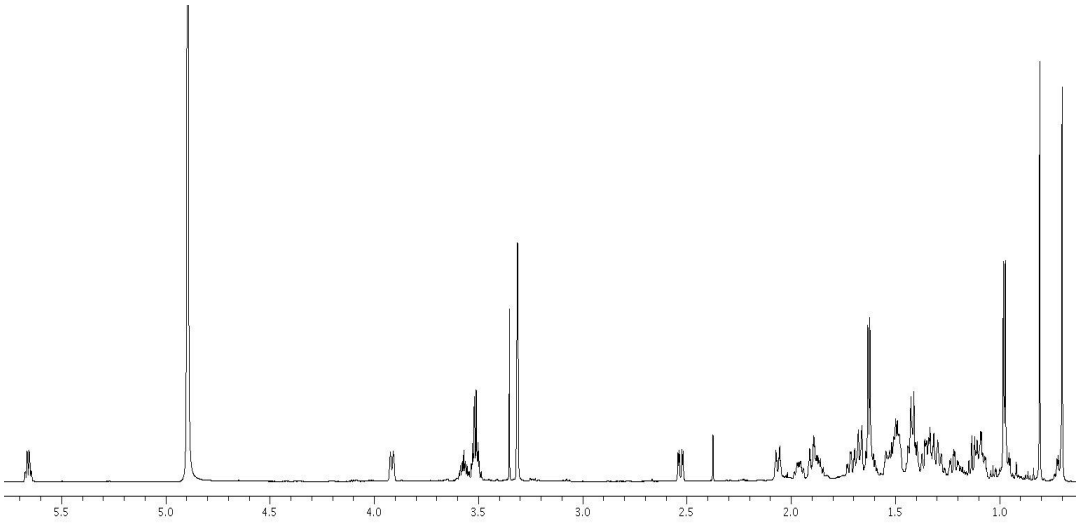

^{13}C NMR (100 MHz, $CDCl_3$) of compound **101**

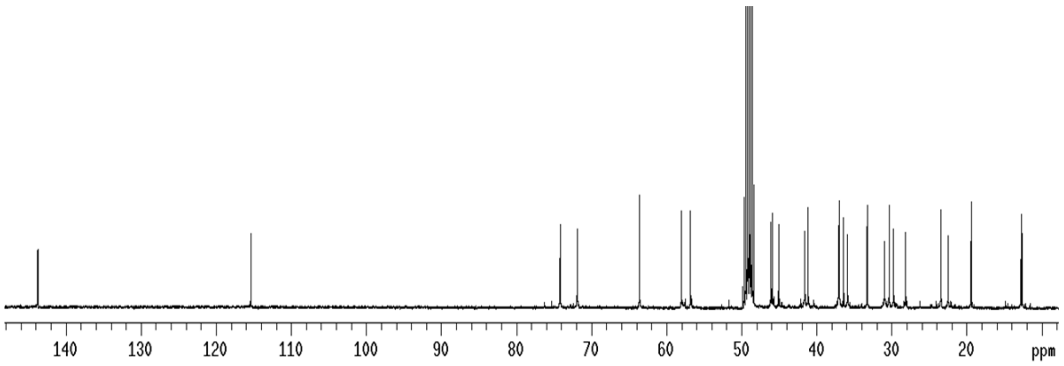

^{1}H NMR (400 MHz, CD_3OD) of compound **102**

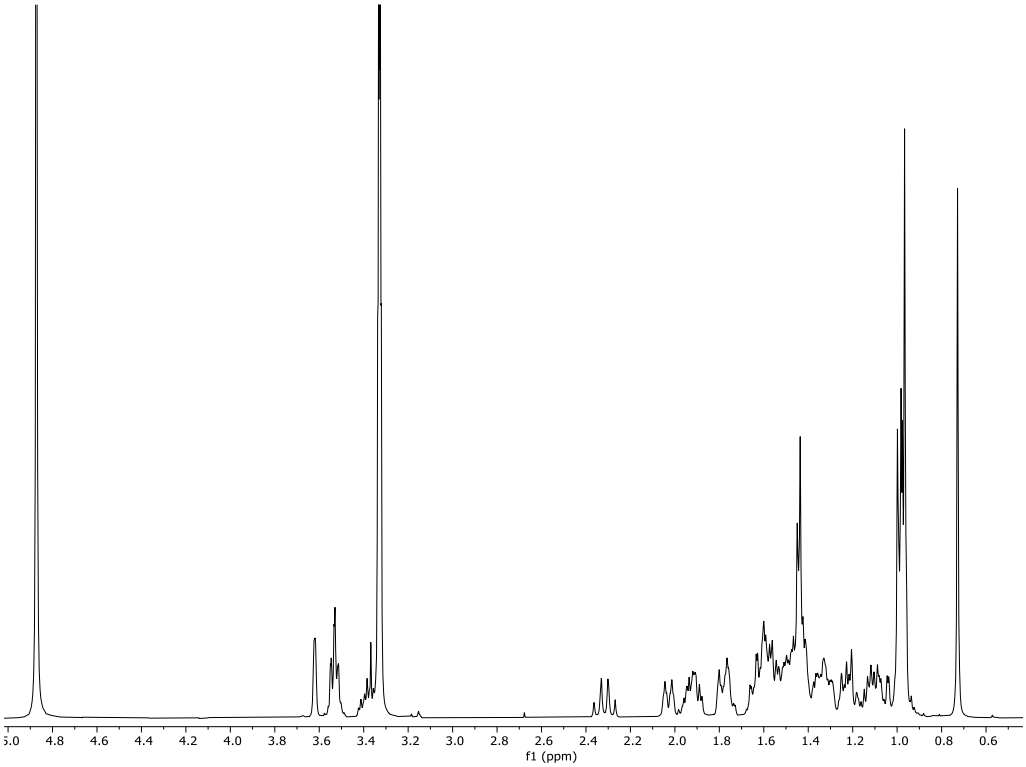

^{1}H NMR (500 MHz, CD_3OD) of compound **103**

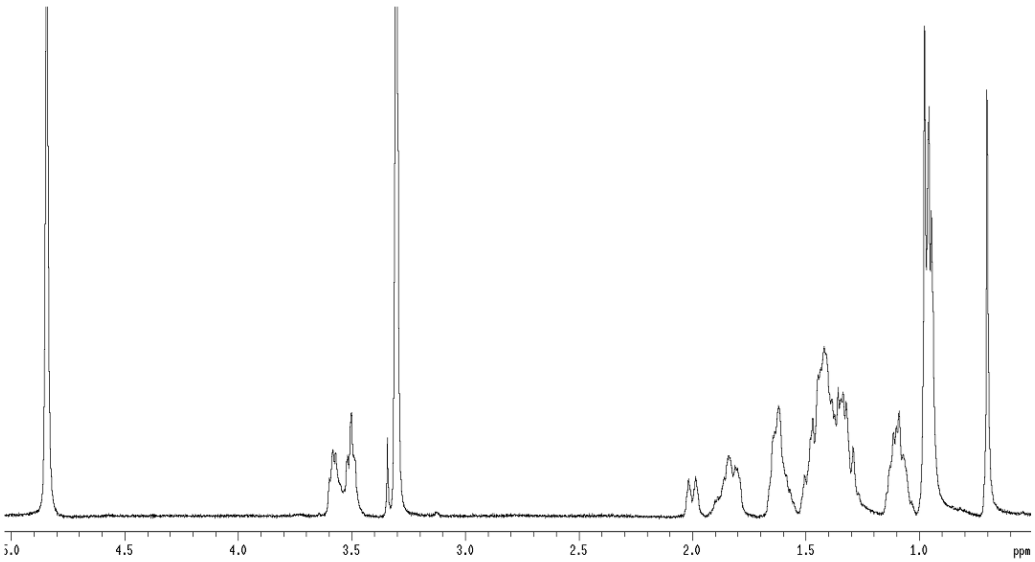

^{1}H NMR (700 MHz, CD_3OD) of compound **104**

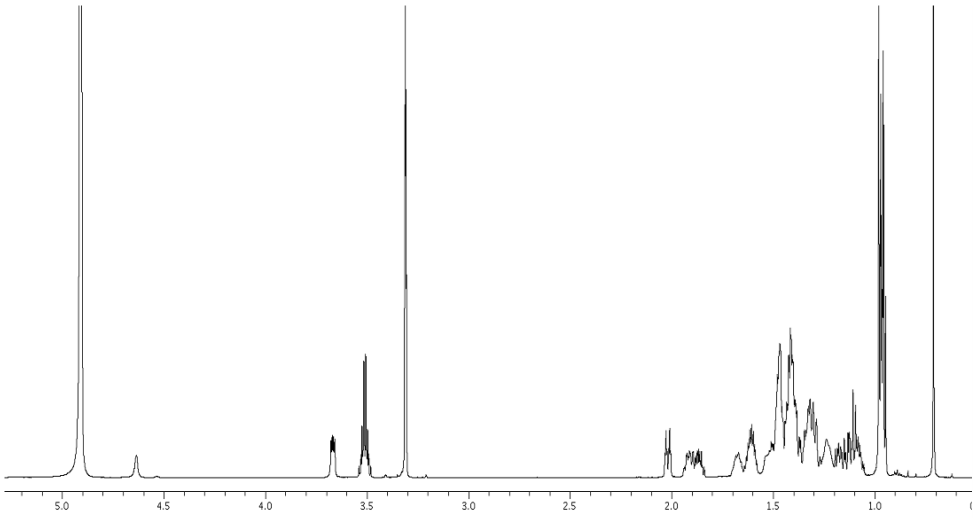

^{1}H NMR (500 MHz, CD_3OD) of compound **105**

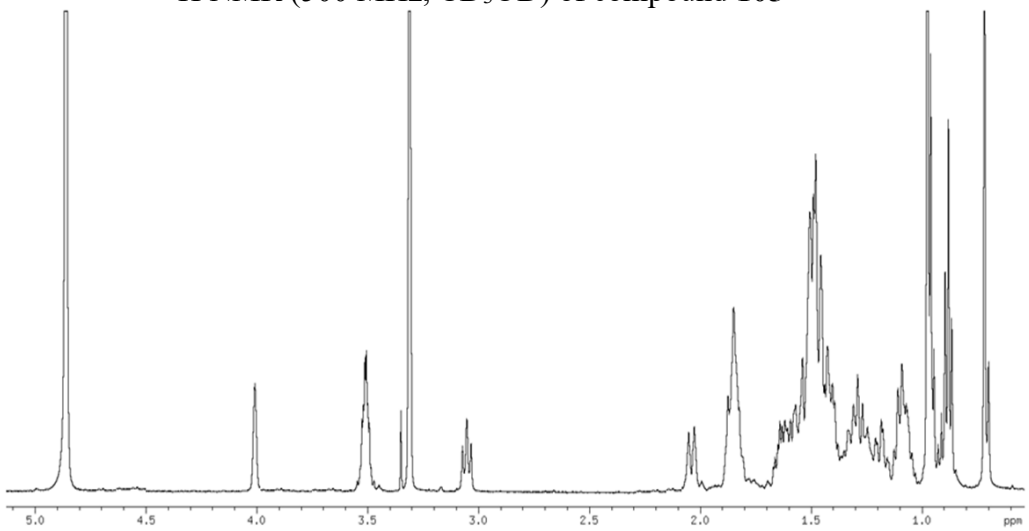

^{1}H NMR (500 MHz, CD_3OD) of compound **106**

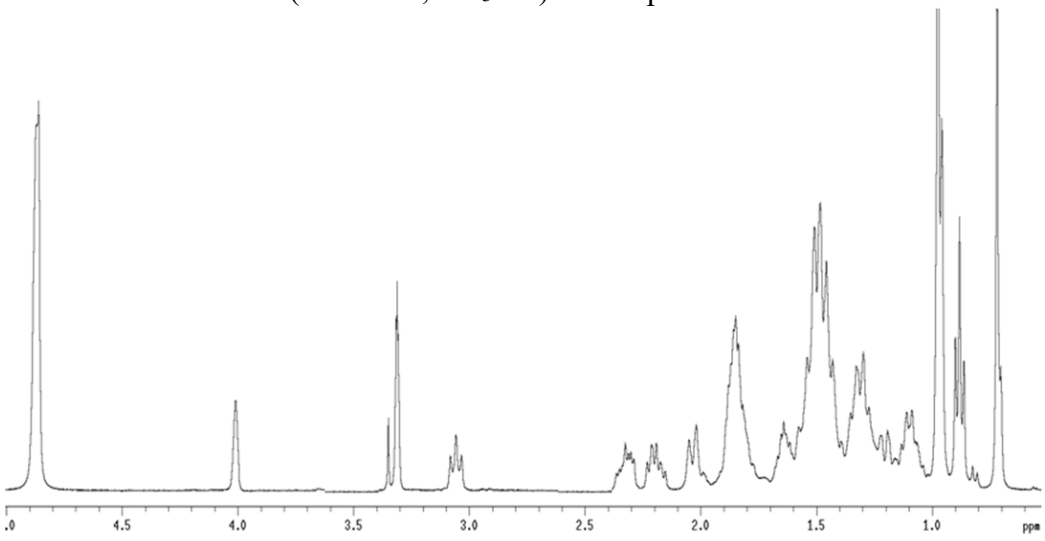

[redacted]

[redacted]

methyl 1,2,3,4-tetra-O-acetyl-β-D-glucuronate). The selective C-1 deacetylation of **134** was carried out as follows. Tributyltin methoxide (1.12 eq) was added to a DCM solution of compound **134**. The reaction was stirred and refluxed overnight. The mixture was washed twice with HCl 10% v/v and then with water. The organic phase was dried over anhydrous

[redacted]

-β-D-glucuronate (**135**). To a DCM solution of compound **135**, trichloroacetonitrile (5 eq) was added at 0°C. After 30 min, DBU (0.3 eq) was also added dropwise. Upon DBU addition, the reaction colour

darkened progressively. After 8h, the reaction was simply concentrated under *vacuum* and purified by flash silica column purification in hexanes/ethyl acetate 7:3 v/v to afford pure 2,3,4-tri-O-acetyl-α-D-glucopyranuronic acid methyl ester trichloroacetimidate (**136**) as a slightly yellow crystal (82% yield). δ 8.73 (s, 1H, NH), 6.64 (d, 1H, *J* = 3.6 Hz, H-1), 5.63 (t, 1H, *J* = 10 Hz, H-3), 5.27 (t, 1H, *J* =10 Hz, H-4), 5.16 (dd, 1H, *J* = 3.6 Hz, 10 Hz, H-2), 4.49 (d, 1H, *J* =10 Hz, H-5), 3.75 (s, 3H, CO_2Me), 2.05 (s, 3H, OAc), 2.04 (s, 3H, OAc), 2.02 (s, 3H, OAc). δ 169.78 (C═O), 169.72 (C═O), 169.47 (C═O), 167.14 (C═O), 160.58 (C═N), 92.64 (C-H), 70.49 (C-H), 69.47 (C-H), 69.10 (C-H), 68.96 (C-H), 53.04 (CO_2Me), 21.04, 20.66, 20.48, 20.39 (3 × OAc and 1 × CCl_3). HRMS-ESI 478.0075

anhydrous

[redacted]

δ 4.25 (d, 1H, *J* = 8.23 Hz, H-1'), 4.10 (m, 1H, H-3), 3.66 (s, 1H, H-7), 3.53 (ovl, 2H, H_2-23), 3.41 (m, 3H, H-5',4'and 3'), 3.21 (t, 1H, *J* =8.25 Hz, H-2'), 0.99 (d, 3H, *J* =6.68 Hz, H_3-21), 0.91 (s, 3H, H_3-19), 0.90 (ovl, 3H, H_3-25), 0.70 (s, 3H, H_3-18). HRMS-ESI 567.3611 [redacted]

δ 4.41 (d, 1H, *J* = 7.88 Hz, H-1'), 3.66 (s, 1H, H-7), 3.63 (ovl, 1H, H-3), 3.54 (ovl, 2H, H_2-23), 3.39 (m, 3H, H-5',4'and 3'), 3.18 (t, 1H, *J* =7.88 Hz, H-2'), 0.97 (d, 3H, *J* =6.27 Hz, H_3-21), 0.91 (s, 3H, H_3-19), 0.90 (ovl, 3H, H_3-25), 0.71 (s, 3H, H_3-18). HRMS-ESI 567.3611 [redacted]

[redacted]

δ 4.06 (ovl, 1H, H-3), 4.05 (ovl, 2H, H_2-23), 3.65 (s, 1H, H-7), 1.00 (d, 3H, J =6.65 Hz, H_3-21), 0.92 (s, 3H, H_3-19), 0.90 (ovl, 3H, H_3-25), 0.70 (s, 3H, H_3-18). HRMS-ESI 275.1102 [redacted]

δ 4.04 (m, 2H, H_2-23), 3.65 (s, 1H, H-7), 3.31 (ovl, 1H, H-3), 1.00 (d, 3H, J =7.47 Hz, H_3-21), 0.91 (s, 3H, H_3-19), 0.90 (ovl, 3H, H_3-25), 0.70 (s, 3H, H_3-18). HRMS-ESI 471.2654 [redacted]

δ 4.10 (m, 1H, H-3), 3.65 (s, 1H, H-7), 3.61 (ovl, 1H, H-23a), 3.55 (ovl, 1H, H-23b), 0.97 (d, 3H, J =6.58 Hz, H_3-21), 0.92 (s, 3H, H_3-19), 0.90 (ovl, 3H, H_3-25), 0.70 (s, 3H, H_3-18). HRMS-ESI 471.2634 [redacted]

anhydrous [redacted]

[redacted]

anhydrous [redacted]

[redacted] δ 3.65 (s, 1H, H-7), 3.31 (ovl, 1H, H-3), 2.42 (d, 1H, *J* =11.37 Hz, H-23a), 2.00 (d, 1H, *J* =12.7 Hz, H-23b), 1.02 (d, 3H, *J* =6.12 Hz, H_3-21), 0.92 (s, 3H, H_3-19), 0.90 (ovl, 3H, H_3-25), 0.73 (s, 3H, H_3-18). δ 177.65, 73.19, 71.14, 57.42, 51.71, 46.95, 43.79, 43.13, 41.55, 42.61, 40.93, 36.77, 36.63, 35.06, 34.51, 34.42, 31.24, 29.36, 24.53, 23.74, 23.50, 21.95, 20.01, 12.21, 12.02. HRMS-ESI 405.3083 [redacted] 405.3110

[redacted] δ 4.09 (m, 1H, H-3), 3.65 (s, 1H, H-7), 2.42 (d, 1H, *J* = 12.64, H-23a), 2.04 (ovl, 1H, H-23b), 1.02 (d, 3H, *J* =5.67 Hz, H_3-21), 0.92 (s, 3H, H_3-19), 0.90 (t, 3H, *J* = 7.04, H_3-25), 0.73 (s, 3H, H_3-18). HRMS-ESI 485.2364 [redacted] 485.2578

[redacted]

[redacted]

anhydrous

[redacted]

δ 4.41 (d, 1H, *J* = 8.02 Hz, H-1'), 3.66 (ovl, 1H, H-7), 3.65 (ovl, 1H, H-3), 3.51 (d, 1H, H-5'), 3.40 (m, 2H, H-4' and 3'), 3.18 (t, 1H, *J* =7.94 Hz, H-2'), 2.36 (dd, 1H, *J* =13.38, 2.98 Hz, H-23a), 2.01 (m, 1H, H-23b), 1.00 (d, 3H, *J* =6.42 Hz, H_3-21), 0.91 (s, 3H, H_3-19), 0.90 (ovl, 3H, H_3-25), 0.73 (s, 3H, H_3-18). HRMS-ESI [redacted] 582.3202 [redacted] 581.3404 [redacted]

6α-ethyl-3α,7α-dihydroxy-24-nor-5β-cholan-23-oyl glycine (132). To a solution of BAR505 in dry DMF, EDC·HCl (4 eq), HOBt (4 eq), and DIPEA (8 eq) were added in sequence. After 10 min, glycine methyl ester

(2 eq) was also added. The mixture was left stirring at rt for 6h and then diluted with water. The mixture was extracted with ethyl acetate (3 x 25 mL). The organics were dried over anhydrous

dried over anhydrous

δ 3.88 (s, 2H, CH_2-gly), 3.65 (s, 1H, H-7), 3.30 (ovl, 1H, H-3), 2.40 (d, 1H, *J* =12.9 Hz, H-23a), 2.01 (m, 1H, H-23b), 1.00 (d, 3H, *J* =6.23 Hz, H_3-21), 0.92 (s, 3H, H_3-19), 0.90 (ovl, 3H, H_3-25), 0.73 (s, 3H, H_3-18). HRMS-ESI 462.6590 462.3298

Sodium 6α-ethyl-3α,7α-dihydroxy-24-nor-5β-cholan-23-oyl taurine (133). To a solution of BAR505 in dry DMF, EDC·HCl (4 eq), HOBt (4 eq), and DIPEA (8 eq) were added in sequence. After 10 min, taurine (2 eq) was also added. The mixture was left stirring at rt for 6h and then concentrated.

δ 3.65 (s, 1H, H-7), 3.59 (t, 2H, *J* = 6.01, $NCH_2\mathbf{CH_2}S$), 3.32 (ovl, 1H, H-3), 2.97 (t, 2H, *J* = 6.01, $N\mathbf{CH_2}CH_2S$), 2.36 (dd, 1H, *J* =13.51, 3.38 Hz, H-23a), 1.99 (m, 1H, H-23b), 0.96 (d, 3H, *J* =6.02 Hz, H_3-21), 0.91 (s, 3H, H_3-19),

0.90 (ovl, 3H, H_3-25), 0.72 (s, 3H, H_3-18). HRMS-ESI 512.7265

512.3051

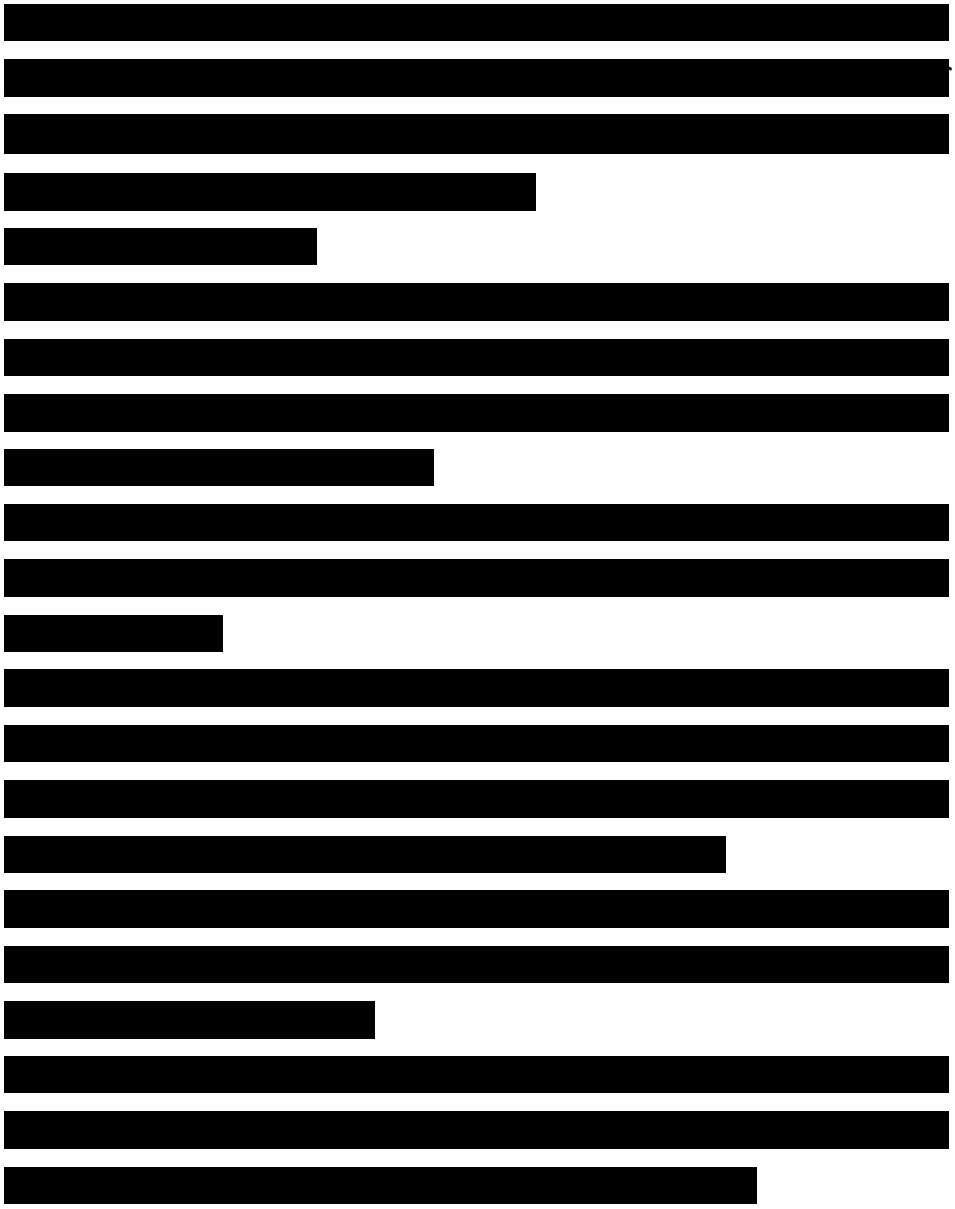

[redacted]

Compound Group	Compound Name	ISTD?	Precursor Ion	MS1 Res	Product Ion	MS2 Res	Dwell	Fragmentor	Collision Energy	Cell Accelerator Voltage	Polarity
	502_gluc	☐	567.3	Unit	567.3	Unit	150	250	0	7	Negative
	502_sulf	☐	471.3	Unit	96.8	Unit	150	250	54	7	Negative
	505	☐	405.1	Unit	405.1	Unit	150	200	0	7	Negative
	502_disulf	☐	275.1	Unit	96.8	Unit	150	150	30	7	Negative

Compound Group	Compound Name	ISTD?	Precursor Ion	MS1 Res	Product Ion	MS2 Res	Dwell	Fragmentor	Collision Energy	Cell Accelerator Voltage	Polarity
	502	☐	357.3	Unit	188.9	Unit	300	130	18	5	Positive
	502	☐	357.3	Unit	106.9	Unit	300	130	38	5	Positive

[redacted]

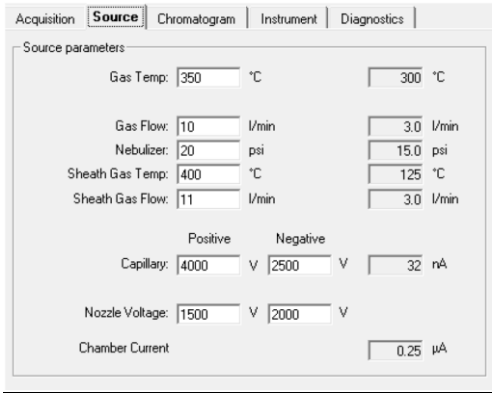

[redacted]

[redacted]

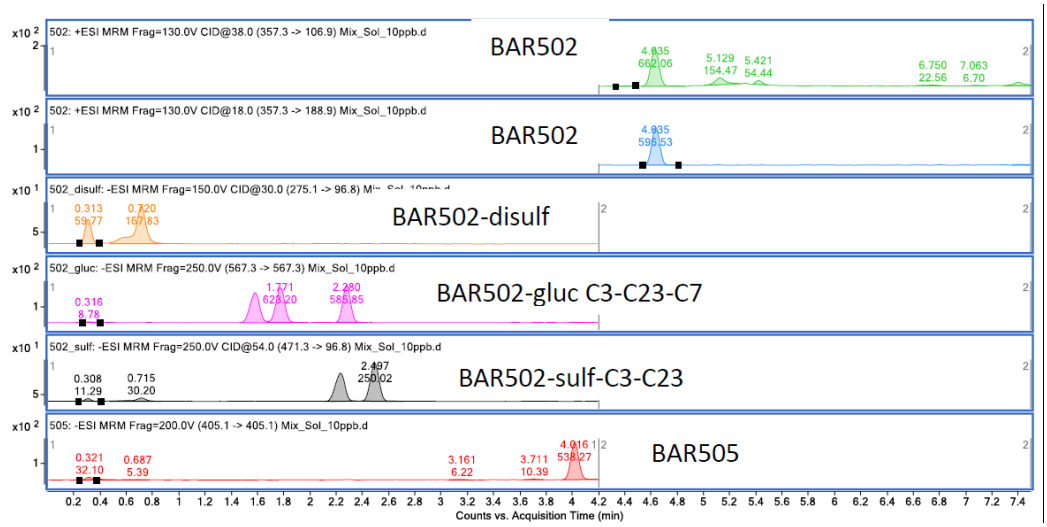
502: +ESI MRM Frag=130.0V CID@38.0 (357.3 -> 106.9) Mix_Sol_10ppb.d
BAR502
4.835
662.06
5.129
154.47
5.421
54.44
6.750
22.56
7.063
6.70
502: +ESI MRM Frag=130.0V CID@18.0 (357.3 -> 188.9) Mix_Sol_10ppb.d
BAR502
4.835
596.53
502_disulf: -ESI MRM Frag=150.0V CID@30.0 (275.1 -> 96.8)
0.313
59.77
0.720
167.83
BAR502-disulf
502_gluc: -ESI MRM Frag=250.0V (567.3 -> 567.3) Mix_Sol_10ppb.d
0.316
8.78
1.771
623.20
2.280
585.85
BAR502-gluc C3-C23-C7
502_sulf: -ESI MRM Frag=250.0V CID@54.0 (471.3 -> 96.8) Mix_Sol_10ppb.d
0.308
11.29
0.715
30.20
2.497
250.02
BAR502-sulf-C3-C23
505: -ESI MRM Frag=200.0V (405.1 -> 405.1) Mix_Sol_10ppb.d
0.321
32.10
0.687
5.39
3.161
6.22
3.711
10.39
4.016
538.27
BAR505
Counts vs. Acquisition Time (min)

[redacted]

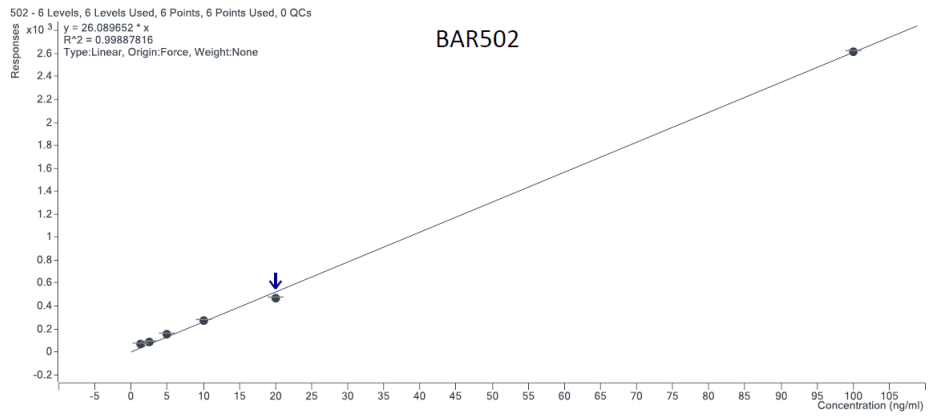
502 - 6 Levels, 6 Levels Used, 6 Points, 6 Points Used, 0 QCs
y = 26.089652 * x
R^2 = 0.99887816
Type:Linear, Origin:Force, Weight:None
x10 3
Responses
BAR502
Concentration (ng/ml)

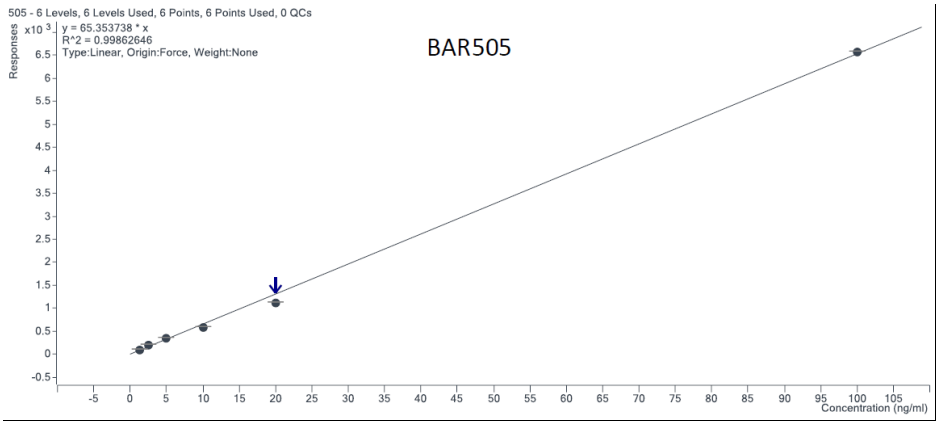
505 - 6 Levels, 6 Levels Used, 6 Points, 6 Points Used, 0 QCs
y = 65.353738 * x
R^2 = 0.99862646
Type:Linear, Origin:Force, Weight:None
BAR505
Responses
x10 3
Concentration (ng/ml)

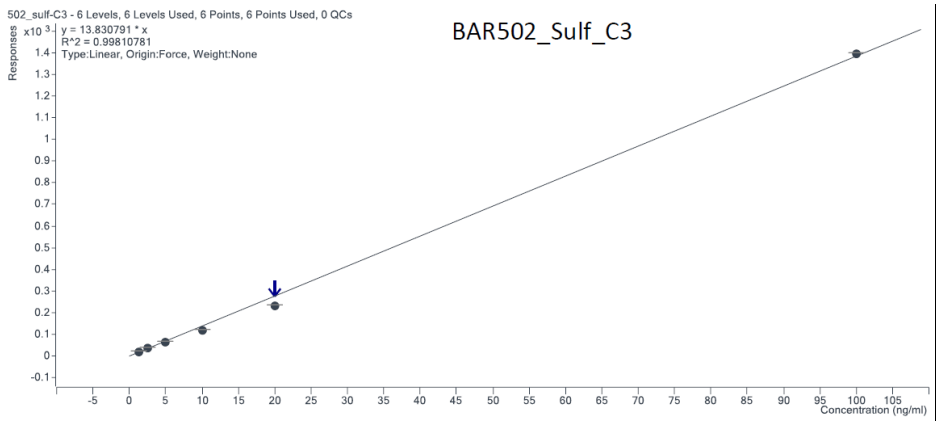
502_sulf-C3 - 6 Levels, 6 Levels Used, 6 Points, 6 Points Used, 0 QCs
y = 13.830791 * x
R^2 = 0.99810781
Type:Linear, Origin:Force, Weight:None
BAR502_Sulf_C3
Responses
x10 3
Concentration (ng/ml)

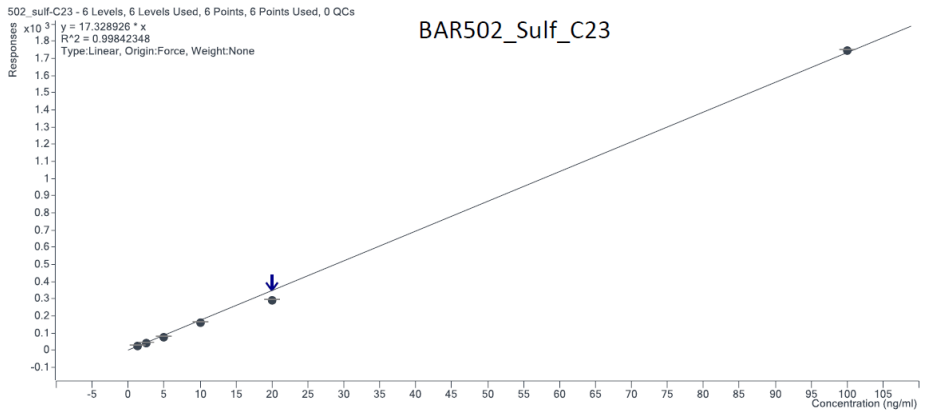
502_sulf-C23 - 6 Levels, 6 Levels Used, 6 Points, 6 Points Used, 0 QCs
y = 17.328926 * x
R^2 = 0.99842348
Type:Linear, Origin:Force, Weight:None
BAR502_Sulf_C23
Responses
x10 3
Concentration (ng/ml)

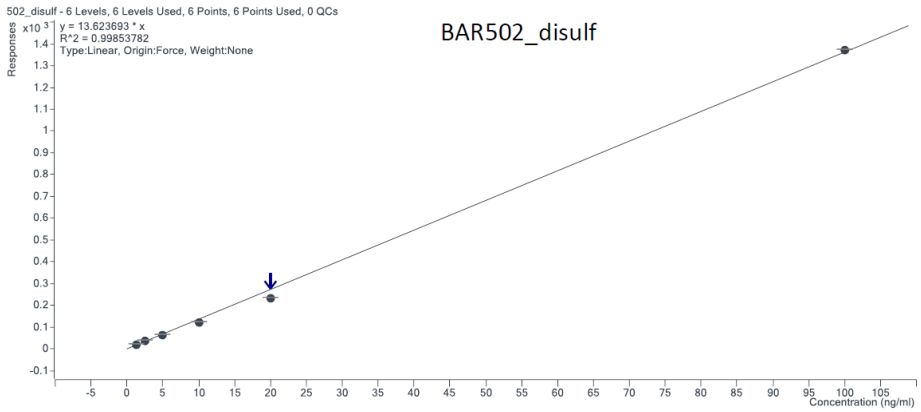

BAR502_disulf

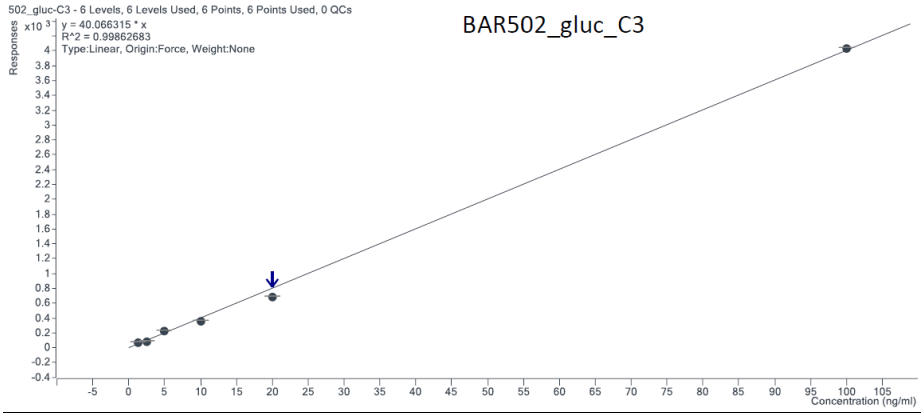

BAR502_gluc_C3

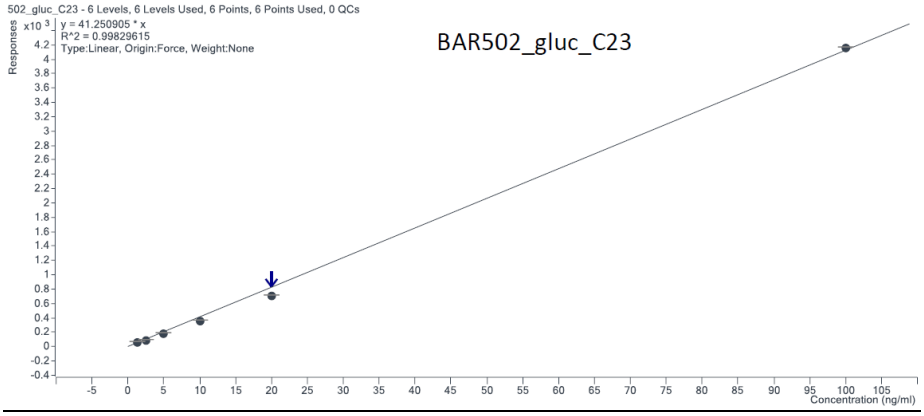

BAR502_gluc_C23

[redacted]

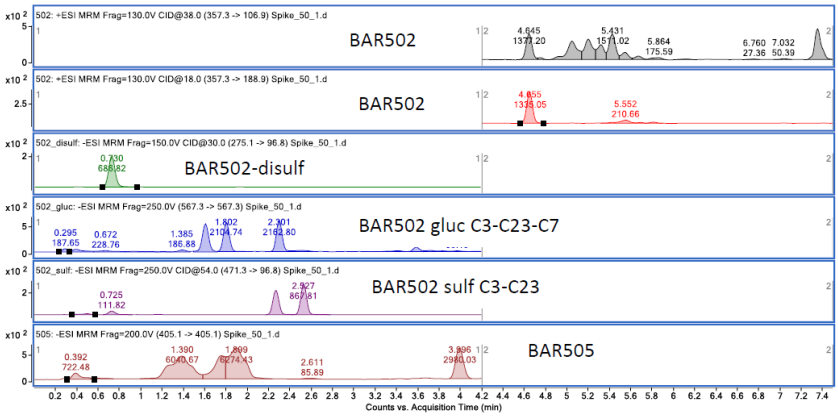

Spike	BAR_disulf	BAR502_gluc_C3	BAR502_gluc_C23	BAR502_gluc_C7	BAR502_sulf_C3	BAR502_Sulf_C23	BAR505	BAR502
I	572	1671	1743	1836	577	749	2569	1158
II	686	2168	2104	2162	706	867	2980	1335
III	506	1487	1496	1595	510	629	2340	991
Extraction Yield %	82	87	84	85	83	83	82	87

[redacted]

[redacted] sodium 6α-ethyl-3α,7α-dihydroxy-24-nor-5β-cholan-23-oyl taurine **133** [redacted]

Compound Group	Compound Name	ISTD?	Precursor Ion	MS1 Res	Product Ion	MS2 Res	Dwell	Fragmentor	Collision Energy	Cell Accelerator Voltage	Polarity
	C3-GLUC-505	☐	581.3	Unit	580.7	Unit	100	200	10	7	Negative
	C3-GLUC-505	☐	581.3	Unit	404.9	Unit	100	200	50	7	Negative
	502_gluc	☐	567.3	Unit	567.3	Unit	100	250	0	7	Negative
	505_T	☐	512	Unit	512	Unit	100	130	0	7	Negative
	505_T	☐	512	Unit	80	Unit	100	130	80	7	Negative
	505_C3_sulf	☐	485.4	Unit	96.8	Unit	100	204	44	7	Negative
	502_sulf	☐	471.3	Unit	96.8	Unit	100	250	54	7	Negative
	505_G	☐	462	Unit	462	Unit	100	190	0	7	Negative
	505_G	☐	462	Unit	74	Unit	100	190	38	7	Negative
	505	☐	405.1	Unit	405.1	Unit	100	200	0	7	Negative
▸	502_disulf	☐	275.1	Unit	96.8	Unit	100	150	35	7	Negative

Compound Group	Compound Name	ISTD?	Precursor Ion	MS1 Res	Product Ion	MS2 Res	Dwell	Fragmentor	Collision Energy	Cell Accelerator Voltage	Polarity
▸	502	☐	357.3	Unit	188.9	Unit	300	130	18	5	Positive
	502	☐	357.3	Unit	106.9	Unit	300	130	38	5	Positive

[redacted]

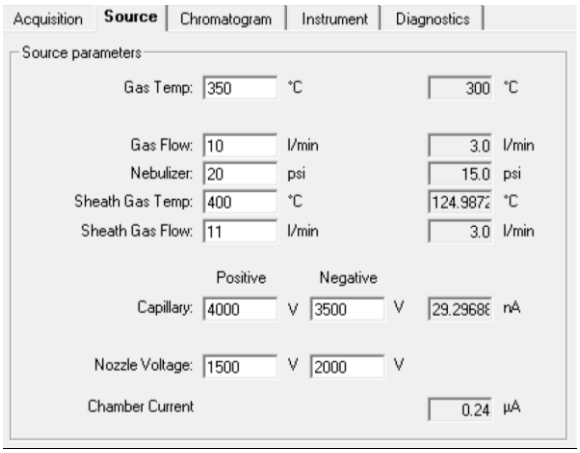

[redacted]

[redacted]

[redacted]

[redacted]

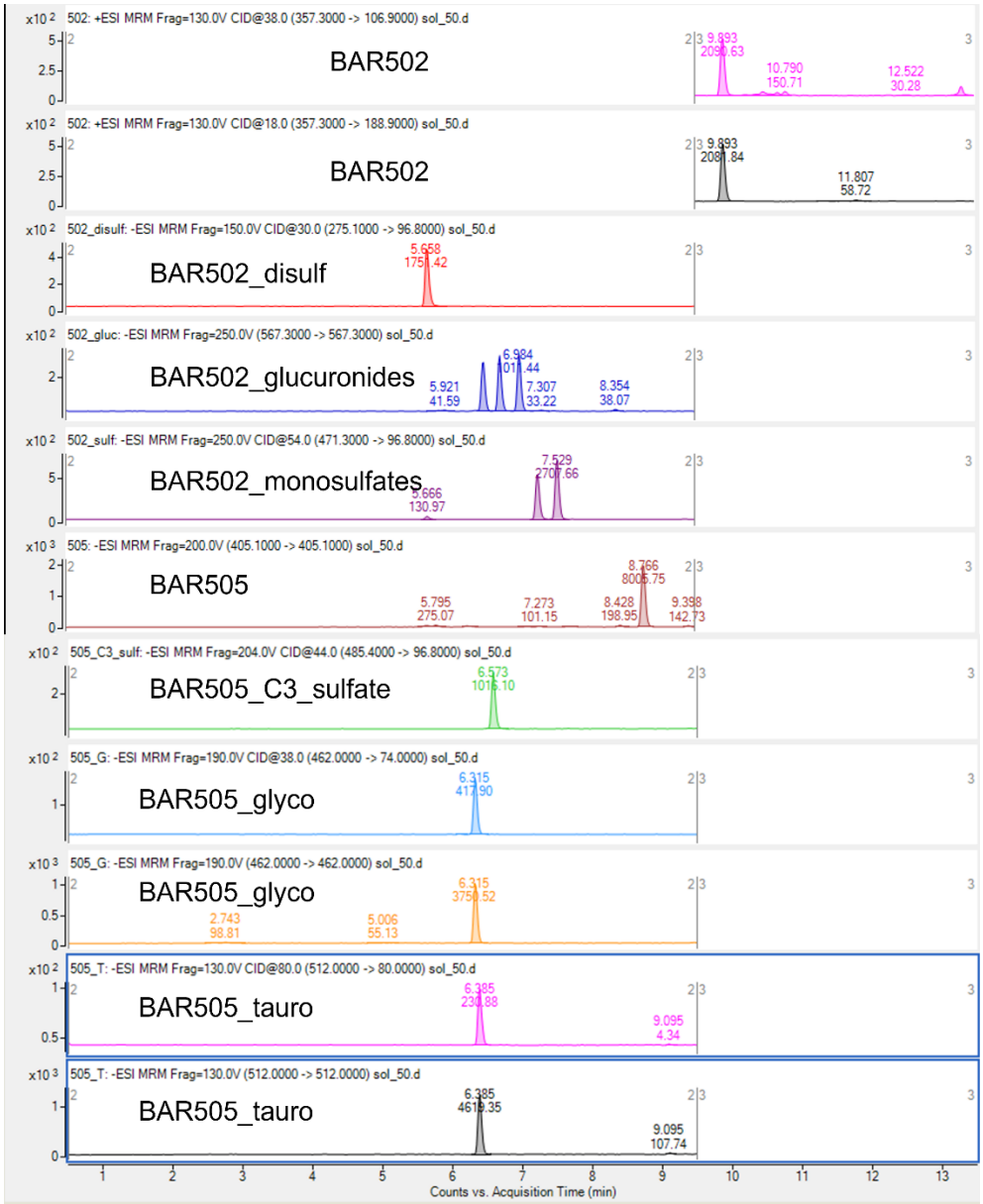

[redacted]

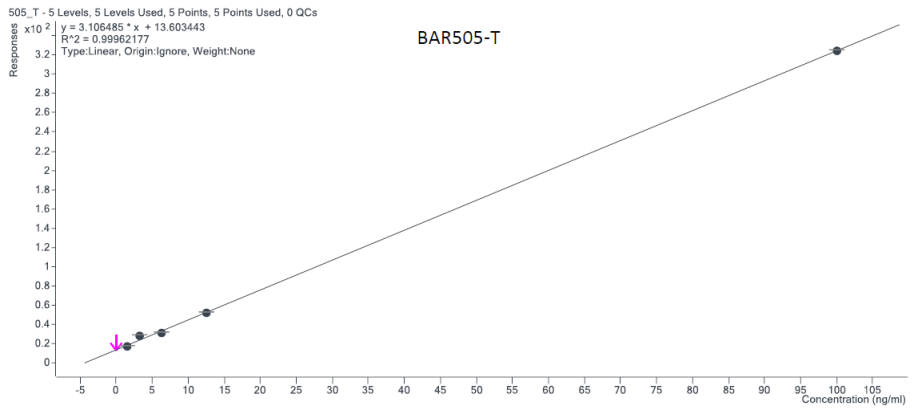
505_T - 5 Levels, 5 Levels Used, 5 Points, 5 Points Used, 0 QCs
y = 3.106485 * x + 13.603443
R^2 = 0.99962177
Type:Linear, Origin:Ignore, Weight:None
BAR505-T
Responses
x10 2
Concentration (ng/ml)

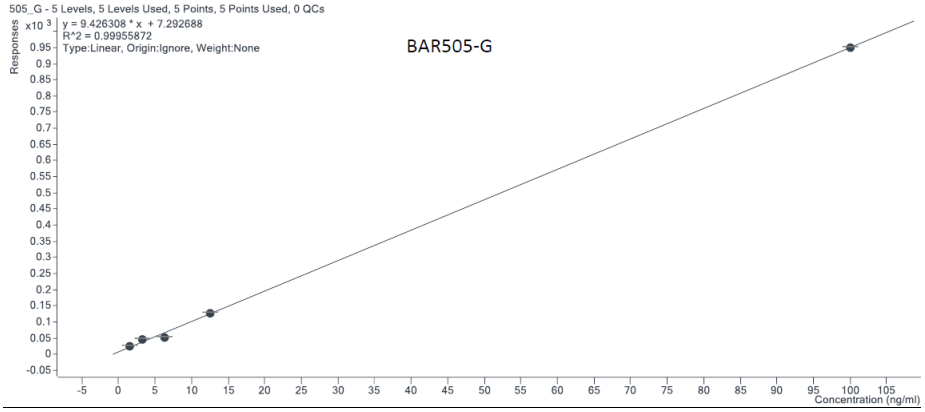
505_G - 5 Levels, 5 Levels Used, 5 Points, 5 Points Used, 0 QCs
y = 9.426308 * x + 7.292688
R^2 = 0.99955872
Type:Linear, Origin:Ignore, Weight:None
BAR505-G
Responses
x10 3
Concentration (ng/ml)

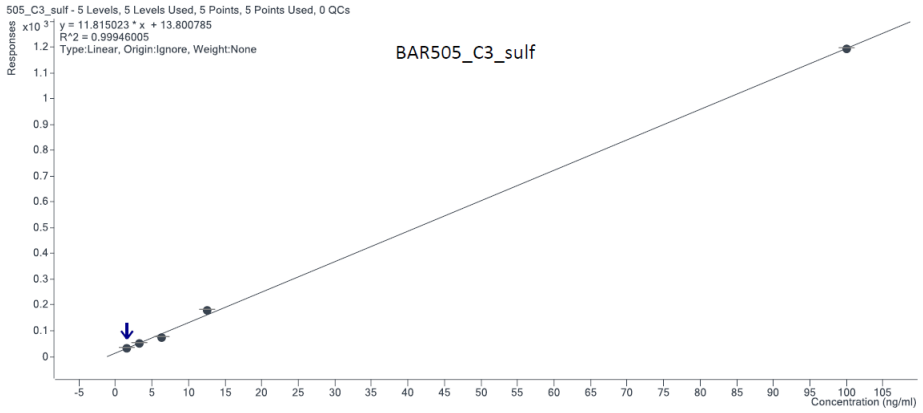
505_C3_sulf - 5 Levels, 5 Levels Used, 5 Points, 5 Points Used, 0 QCs
y = 11.815023 * x + 13.800785
R^2 = 0.99946005
Type:Linear, Origin:Ignore, Weight:None
BAR505_C3_sulf
Responses
x10 3
Concentration (ng/ml)

[redacted]

[redacted]

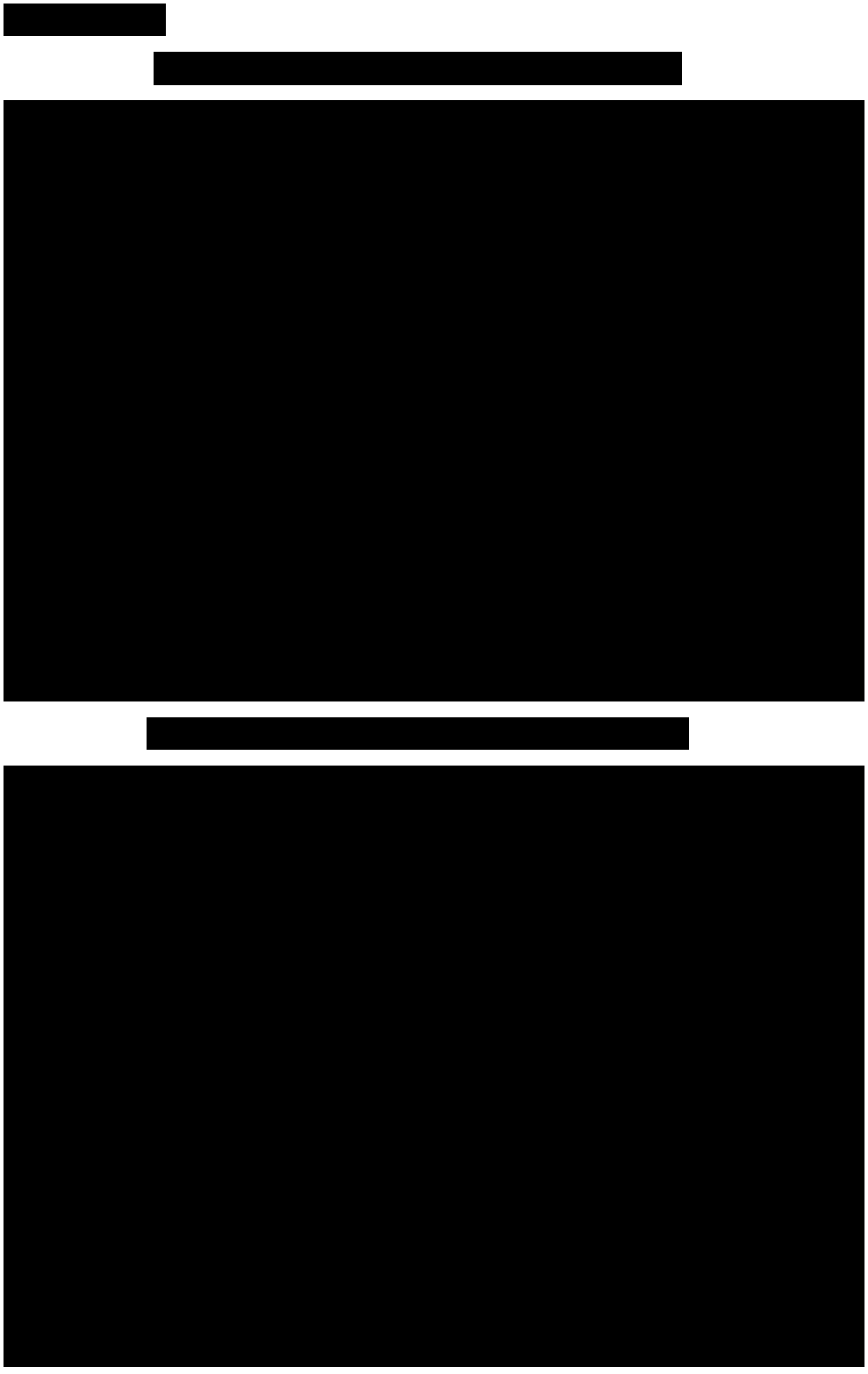

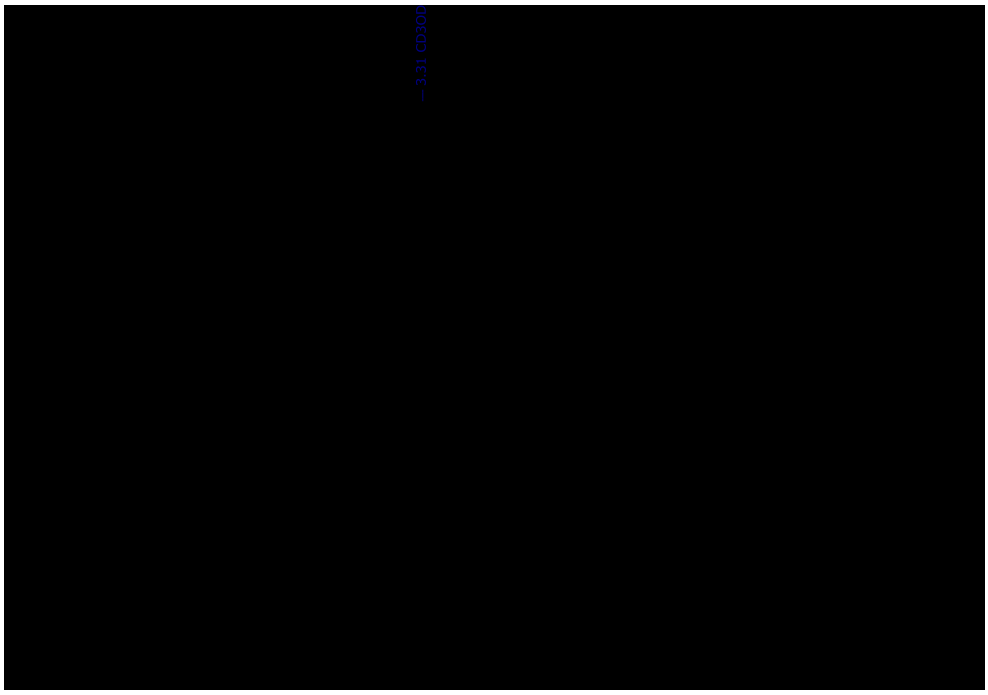
3.31 CD3OD

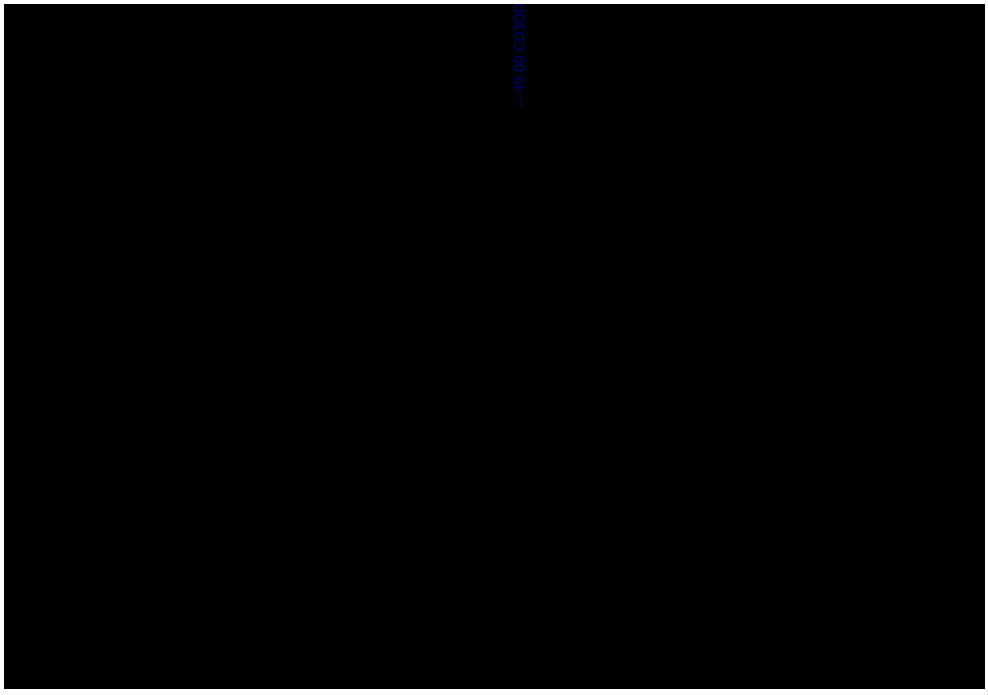
49.00 CD3OD

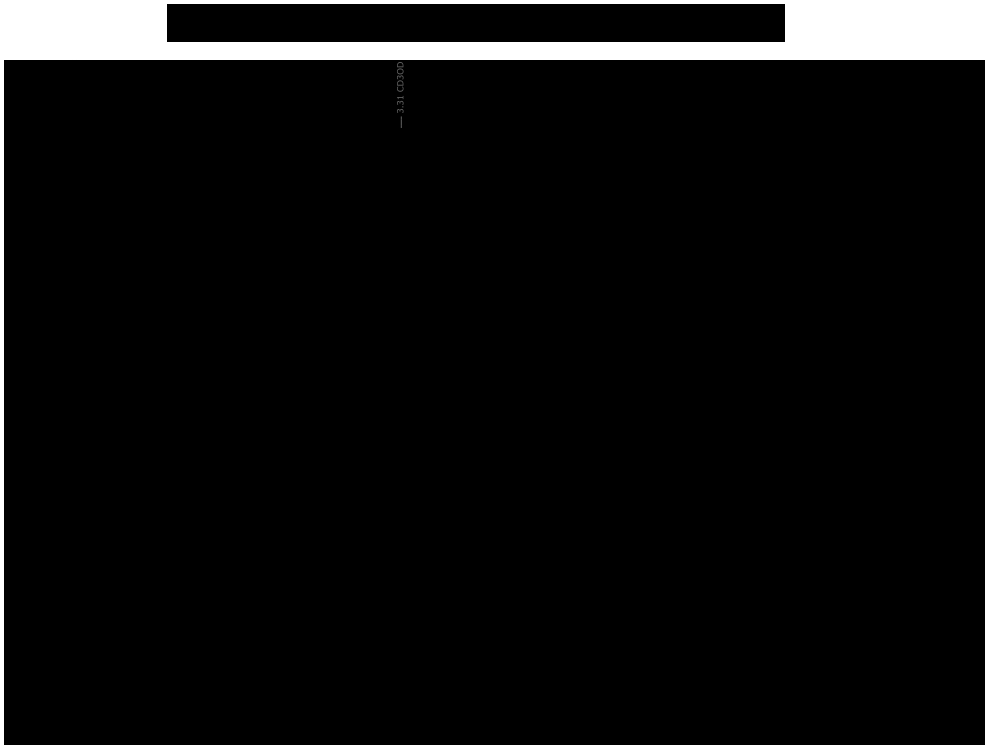

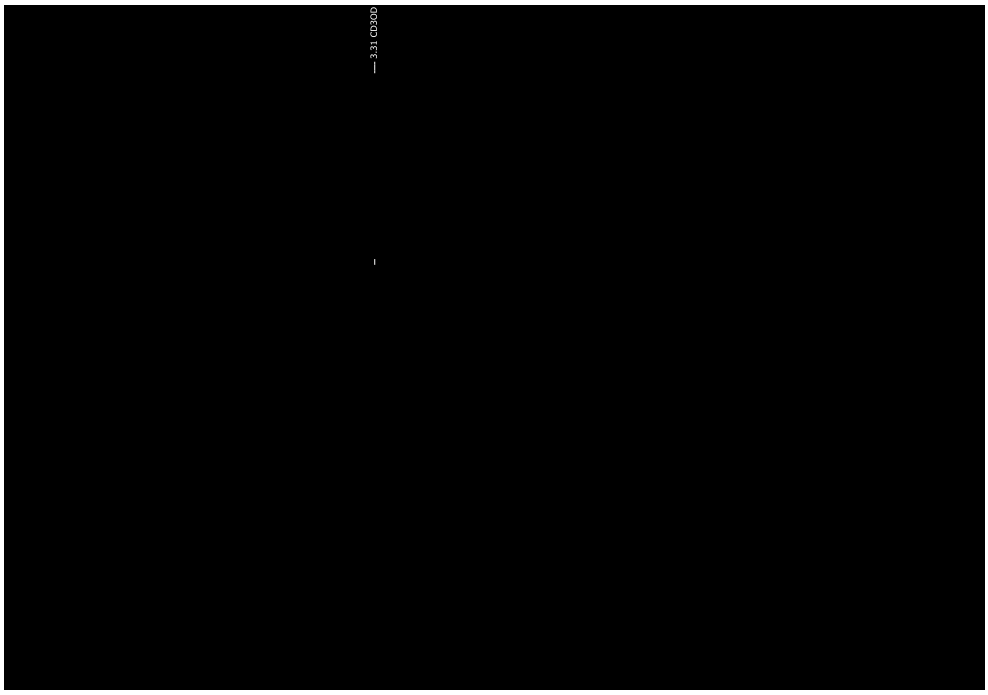
3.31 CD30D

Abbreviations

ACE2, angiotensin converting enzyme 2; ALOX5, Arachidonate 5-lipoxygenase; ALT, alanine transaminase; AST, aspartate transaminase; AUCs, areas under the curve; $CysLT_1R$, Cysteinyl Leukotriene Receptor 1; DIBAL-H, Diisobutylaluminium hydride; GPCRs, G-Protein Coupled Receptors; GPBAR1, G protein-coupled Bile Acid Receptor 1; Il-1β and Il-10, interleukin 1β and 10; LTRs, Leukotriene receptors; TLCA, taurolithocholic acid; Tnfα, Tumor necrosis factor alpha

BAT, brune adipose tissues; BMI, Body mass index; CRE, cAMP responsive element; CVD, cardiovascular disease; DD, drug discovery; DMF, N,N'-dimethylformamide; ESI-MS, electrospray ionization mass spectrometry; FLAP, 5-lipoxygenase-activating protein; GCKR, glucokinase regulatory protein; GPBAR1, G-Protein coupled Bile Acid Receptor 1; HCC, hepatocellular carcinoma; HFD-F, high fat diet and fructose; HSC, hepatic stellate cells; HTS, high-throughput screening, LC-MSMS, liquid chromatography-tandem mass spectrometry; LDD, ligand-based drug design, NAFLD, non-alcoholic fatty liver disease; NASH, non-alcoholic steatohepatitis; OGTT, oral glucose tolerance test; PGC-1α, peroxisome-proliferator-activated receptor-γ coactivator-1 alpha; PPARα, peroxisome proliferator-activated receptor alpha; SD, standard deviation; SEM, standard error of mean; TDD, target-based drug design, TLCA, taurolithocholic acid; Tnfα, Tumor necrosis factor alpha; UCP1, Uncoupling protein 1; WAT, white adipose tissue; cAMP, cyclic Adenosine MonoPhosphate; C_{int}, intrinsic clearance; DCM, Dichloromethane; EtOAc, ethyl acetate; HEK-293T, Human embryonic kidney 293 cells; IBD, Inflammatory bowel disease; IL-1α, IL-1β, IL-6 and IL-89, interleukins; LC-MS, Liquid chromatography–mass spectrometry; $LiBH_4$, Lithium borohydride; MD simulations, Molecular dynamics simulations; MeOH, Methanol; $NaBH_4$, sodium borohydride; PFP column, pentafluorophenylpropyl column; PPh_3, triphenylphosphine; RMSD, root-mean-square deviation; RORγt, retinoic acid receptor-related orphan receptor gamma t; RT-PCR, real-time polymerase chain reaction; SRC1, steroid receptor coactivator-1; RXR, retinoid X receptor; $t_{1/2}$, half-life; SNP, single nucleotide polymorphism; TBAF, tetra-n-butylammonium fluoride; TBP, TATA-Box Binding Protein; TM6SF2, transmembrane 6 superfamily member 2 TBS, tert-Butyldimethylsilyl; TEA, Triethylamine; THF, Tetrahydrofuran; TNBS, 2,4,6-trinitrobenzene sulfonic acid; TNF-α, Tumor necrosis factor; VLDL, very low density lipoprotein.

Bibliography

(1) Drews, J. Drug Discovery: A Historical Perspective. *Science (1979)* **2000**, *287* (5460), 1960–1964. https://doi.org/10.1126/science.287.5460.1960.

(2) Kiriiri, G. K.; Njogu, P. M.; Mwangi, A. N. Exploring Different Approaches to Improve the Success of Drug Discovery and Development Projects: A Review. *Futur J Pharm Sci* **2020**, *6* (1), 27. https://doi.org/10.1186/s43094-020-00047-9.

(3) Pammolli, F.; Magazzini, L.; Riccaboni, M. The Productivity Crisis in Pharmaceutical R&D. *Nat Rev Drug Discov* **2011**, *10* (6), 428–438. https://doi.org/10.1038/nrd3405.

(4) Naci, H.; Carter, A. W.; Mossialos, E. Why the Drug Development Pipeline Is Not Delivering Better Medicines. *BMJ* **2015**, h5542. https://doi.org/10.1136/bmj.h5542.

(5) Bleicher, K. H.; Böhm, H.-J.; Müller, K.; Alanine, A. I. Hit and Lead Generation: Beyond High-Throughput Screening. *Nat Rev Drug Discov* **2003**, *2* (5), 369–378. https://doi.org/10.1038/nrd1086.

(6) Croston, G. E. The Utility of Target-Based Discovery. *Expert Opin Drug Discov* **2017**, *12* (5), 427–429. https://doi.org/10.1080/17460441.2017.1308351.

(7) Pushpakom, S.; Iorio, F.; Eyers, P. A.; Escott, K. J.; Hopper, S.; Wells, A.; Doig, A.; Guilliams, T.; Latimer, J.; McNamee, C.; Norris, A.; Sanseau, P.; Cavalla, D.; Pirmohamed, M. Drug Repurposing: Progress, Challenges and Recommendations. *Nat Rev Drug Discov* **2019**, *18* (1), 41–58. https://doi.org/10.1038/nrd.2018.168.

(8) Blass, B. E. Drug Discovery and Development: An Overview of Modern Methods and Principles. In *Basic Principles of Drug Discovery and Development*; Elsevier, 2021; pp 1–41. https://doi.org/10.1016/B978-0-12-817214-8.00001-4.

(9) Netea, M. G.; Balkwill, F.; Chonchol, M.; Cominelli, F.; Donath, M. Y.; Giamarellos-Bourboulis, E. J.; Golenbock, D.; Gresnigt, M. S.; Heneka, M. T.; Hoffman, H. M.; Hotchkiss, R.; B Joosten, L. A.; Kastner, D. L.; Korte, M.; Latz, E.; Libby, P.; Mandrup-Poulsen, T.; Mantovani, A.; G Mills, K. H.; Nowak, K. L.; O, L. A.; Pickkers, P.; van der Poll, T.; Ridker, P. M.; Schalkwijk, J.; Schwartz, D. A.; Siegmund, B.; Steer, C. J.; Tilg, H.; M van der Meer, J. W.; van de Veerdonk, F. L.; Dinarello, C. A. *A Guiding Map for Inflammation*; 2017. https://doi.org/10.1038/ni.3790.

(10) Slavich, G. M. Understanding Inflammation, Its Regulation, and Relevance for Health: A Top Scientific and Public Priority. *Brain Behav Immun* **2015**, *45*, 13–14. https://doi.org/10.1016/j.bbi.2014.10.012.

(11) Hotamisligil, G. S. Inflammation, Metaflammation and Immunometabolic Disorders. *Nature* **2017**, *542* (7640), 177–185. https://doi.org/10.1038/nature21363.

(12) Bennett, J. M.; Reeves, G.; Billman, G. E.; Sturmberg, J. P. Inflammation–Nature's Way to Efficiently Respond to All Types of Challenges: Implications for Understanding and Managing "the Epidemic" of Chronic Diseases. *Front Med (Lausanne)* **2018**, *5*. https://doi.org/10.3389/fmed.2018.00316.

(13) Furman, D.; Campisi, J.; Verdin, E.; Carrera-Bastos, P.; Targ, S.; Franceschi, C.; Ferrucci, L.; Gilroy, D. W.; Fasano, A.; Miller, G. W.; Miller, A. H.; Mantovani, A.; Weyand, C. M.; Barzilai, N.; Goronzy, J. J.; Rando, T. A.; Effros, R. B.; Lucia, A.; Kleinstreuer, N.; Slavich, G. M. Chronic Inflammation in the Etiology of Disease across the Life Span. https://doi.org/10.1038/s41591-019-0675-0.

(14) Zhang, C.; Yang, M. Current Options and Future Directions for NAFLD and NASH Treatment. *Int J Mol Sci* **2021**, *22* (14), 7571. https://doi.org/10.3390/ijms22147571.

(15) Younossi, Z.; Anstee, Q. M.; Marietti, M.; Hardy, T.; Henry, L.; Eslam, M.; George, J.; Bugianesi, E. Global Burden of NAFLD and NASH: Trends, Predictions, Risk Factors and Prevention. *Nat Rev Gastroenterol Hepatol* **2018**, *15* (1), 11–20. https://doi.org/10.1038/nrgastro.2017.109.

(16) Le, M. H.; Yeo, Y. H.; Li, X.; Li, J.; Zou, B.; Wu, Y.; Ye, Q.; Huang, D. Q.; Zhao, C.; Zhang, J.; Liu, C.; Chang, N.; Xing, F.; Yan, S.; Wan, Z. H.; Tang, N. S. Y.; Mayumi, M.; Liu, X.; Liu, C.; Rui, F.; Yang, H.; Yang, Y.; Jin, R.; Le, R. H. X.; Xu, Y.; Le, D. M.; Barnett, S.; Stave, C. D.; Cheung, R.; Zhu, Q.; Nguyen, M. H. 2019 Global NAFLD Prevalence: A Systematic Review and Meta-Analysis. *Clinical Gastroenterology and Hepatology* **2021**. https://doi.org/10.1016/j.cgh.2021.12.002.

(17) Riazi, K.; Azhari, H.; Charette, J. H.; Underwood, F. E.; King, J. A.; Afshar, E. E.; Swain, M. G.; Congly, S. E.; Kaplan, G. G.; Shaheen, A.-A. The Prevalence and Incidence of NAFLD Worldwide: A Systematic Review and Meta-Analysis. *Lancet Gastroenterol Hepatol* **2022**, *7* (9), 851–861. https://doi.org/10.1016/S2468-1253(22)00165-0.

(18) Schwimmer, J. B.; McGreal, N.; Deutsch, R.; Finegold, M. J.; Lavine, J. E. Influence of Gender, Race, and Ethnicity on Suspected Fatty Liver in Obese Adolescents. *Pediatrics* **2005**, *115* (5), e561–e565. https://doi.org/10.1542/peds.2004-1832.

(19) Mazzolini, G.; Sowa, J.-P.; Atorrasagasti, C.; Kücükoglu, Ö.; Syn, W.-K.; Canbay, A. Significance of Simple Steatosis: An Update on the Clinical and Molecular Evidence. *Cells* **2020**, *9* (11), 2458. https://doi.org/10.3390/cells9112458.

(20) Pais, R.; Pascale, A.; Fedchuck, L.; Charlotte, F.; Poynard, T.; Ratziu, V. Progression from Isolated Steatosis to Steatohepatitis and Fibrosis in Nonalcoholic Fatty Liver Disease. *Clin Res Hepatol Gastroenterol* **2011**, *35* (1), 23–28. https://doi.org/10.1016/j.gcb.2010.06.004.

(21) Bettermann, K.; Hohensee, T.; Haybaeck, J. Steatosis and Steatohepatitis: Complex Disorders. *Int J Mol Sci* **2014**, *15* (6), 9924–9944. https://doi.org/10.3390/ijms15069924.

(22) Friedman, S. L.; Neuschwander-Tetri, B. A.; Rinella, M.; Sanyal, A. J. Mechanisms of NAFLD Development and Therapeutic Strategies. *Nat Med* **2018**, *24* (7), 908–922. https://doi.org/10.1038/s41591-018-0104-9.

(23) Siddiqui, M. S.; Harrison, S. A.; Abdelmalek, M. F.; Anstee, Q. M.; Bedossa, P.; Castera, L.; Dimick-Santos, L.; Friedman, S. L.; Greene, K.; Kleiner, D. E.; Megnien, S.; Neuschwander-Tetri, B. A.; Ratziu, V.; Schabel, E.; Miller, V.; Sanyal, A. J. Case Definitions for Inclusion and Analysis of Endpoints in Clinical Trials for Nonalcoholic Steatohepatitis through the Lens of Regulatory Science. *Hepatology* **2018**, *67* (5), 2001–2012. https://doi.org/10.1002/hep.29607.

(24) Drew, L. Fighting the Fatty Liver. *Nature* **2017**, *550* (7675), S102–S103. https://doi.org/10.1038/550S102a.

(25) Schwabe, R. F.; Tabas, I.; Pajvani, U. B. Mechanisms of Fibrosis Development in Nonalcoholic Steatohepatitis. *Gastroenterology* **2020**, *158* (7), 1913–1928. https://doi.org/10.1053/j.gastro.2019.11.311.

(26) Raza, S. Current Treatment Paradigms and Emerging Therapies for NAFLD/NASH. *Frontiers in Bioscience* **2021**, *26* (2), 4892. https://doi.org/10.2741/4892.
(27) Younossi, Z.; Stepanova, M.; Ong, J. P.; Jacobson, I. M.; Bugianesi, E.; Duseja, A.; Eguchi, Y.; Wong, V. W.; Negro, F.; Yilmaz, Y.; Romero-Gomez, M.; George, J.; Ahmed, A.; Wong, R.; Younossi, I.; Ziayee, M.; Afendy, A. Nonalcoholic Steatohepatitis Is the Fastest Growing Cause of Hepatocellular Carcinoma in Liver Transplant Candidates. *Clinical Gastroenterology and Hepatology* **2019**, *17* (4), 748-755.e3. https://doi.org/10.1016/j.cgh.2018.05.057.
(28) Palmer, N. D.; Musani, S. K.; Yerges-Armstrong, L. M.; Feitosa, M. F.; Bielak, L. F.; Hernaez, R.; Kahali, B.; Carr, J. J.; Harris, T. B.; Jhun, M. A.; Kardia, S. L. R.; Langefeld, C. D.; Mosley, T. H.; Norris, J. M.; Smith, A. v.; Taylor, H. A.; Wagenknecht, L. E.; Liu, J.; Borecki, I. B.; Peyser, P. A.; Speliotes, E. K. Characterization of European Ancestry Nonalcoholic Fatty Liver Disease-Associated Variants in Individuals of African and Hispanic Descent. *Hepatology* **2013**, *58* (3), 966–975. https://doi.org/10.1002/hep.26440.
(29) Schwimmer, J. B.; Celedon, M. A.; Lavine, J. E.; Salem, R.; Campbell, N.; Schork, N. J.; Shiehmorteza, M.; Yokoo, T.; Chavez, A.; Middleton, M. S.; Sirlin, C. B. Heritability of Nonalcoholic Fatty Liver Disease. *Gastroenterology* **2009**, *136* (5), 1585–1592. https://doi.org/10.1053/j.gastro.2009.01.050.
(30) Wagenknecht, L. E.; Scherzinger, A. L.; Stamm, E. R.; Hanley, A. J. G.; Norris, J. M.; Chen, Y.-D. I.; Bryer-Ash, M.; Haffner, S. M.; Rotter, J. I. Correlates and Heritability of Nonalcoholic Fatty Liver Disease in a Minority Cohort. *Obesity* **2009**, *17* (6), 1240–1246. https://doi.org/10.1038/oby.2009.4.
(31) Loomba, R.; Schork, N.; Chen, C.-H.; Bettencourt, R.; Bhatt, A.; Ang, B.; Nguyen, P.; Hernandez, C.; Richards, L.; Salotti, J.; Lin, S.; Seki, E.; Nelson, K. E.; Sirlin, C. B.; Brenner, D. Heritability of Hepatic Fibrosis and Steatosis Based on a Prospective Twin Study. *Gastroenterology* **2015**, *149* (7), 1784–1793. https://doi.org/10.1053/j.gastro.2015.08.011.
(32) Dongiovanni, P.; Romeo, S.; Valenti, L. Genetic Factors in the Pathogenesis of Nonalcoholic Fatty Liver and Steatohepatitis. *Biomed Res Int* **2015**, *2015*, 1–10. https://doi.org/10.1155/2015/460190.
(33) Romeo, S.; Kozlitina, J.; Xing, C.; Pertsemlidis, A.; Cox, D.; Pennacchio, L. A.; Boerwinkle, E.; Cohen, J. C.; Hobbs, H. H. Genetic Variation in PNPLA3 Confers Susceptibility to Nonalcoholic Fatty Liver Disease. *Nat Genet* **2008**, *40* (12), 1461–1465. https://doi.org/10.1038/ng.257.
(34) Singal, A. G.; Manjunath, H.; Yopp, A. C.; Beg, M. S.; Marrero, J. A.; Gopal, P.; Waljee, A. K. The Effect of PNPLA3 on Fibrosis Progression and Development of Hepatocellular Carcinoma: A Meta-Analysis. *American Journal of Gastroenterology* **2014**, *109* (3), 325–334. https://doi.org/10.1038/ajg.2013.476.
(35) Mancina, R. M.; Dongiovanni, P.; Petta, S.; Pingitore, P.; Meroni, M.; Rametta, R.; Borén, J.; Montalcini, T.; Pujia, A.; Wiklund, O.; Hindy, G.; Spagnuolo, R.; Motta, B. M.; Pipitone, R. M.; Craxì, A.; Fargion, S.; Nobili, V.; Käkelä, P.; Kärjä, V.; Männistö, V.; Pihlajamäki, J.; Reilly, D. F.; Castro-Perez, J.; Kozlitina, J.; Valenti, L.; Romeo, S. The MBOAT7-TMC4 Variant Rs641738 Increases Risk of Nonalcoholic Fatty Liver Disease in Individuals of European Descent. *Gastroenterology* **2016**, *150* (5), 1219-1230.e6. https://doi.org/10.1053/j.gastro.2016.01.032.
(36) Petta, S.; Miele, L.; Bugianesi, E.; Cammà, C.; Rosso, C.; Boccia, S.; Cabibi, D.; di Marco, V.; Grimaudo, S.; Grieco, A.; Pipitone, R. M.; Marchesini, G.; Craxì,

A. Glucokinase Regulatory Protein Gene Polymorphism Affects Liver Fibrosis in Non-Alcoholic Fatty Liver Disease. *PLoS One* **2014**, *9* (2), e87523. https://doi.org/10.1371/journal.pone.0087523.

(37) Bruce, K. D.; Cagampang, F. R.; Argenton, M.; Zhang, J.; Ethirajan, P. L.; Burdge, G. C.; Bateman, A. C.; Clough, G. F.; Poston, L.; Hanson, M. A.; McConnell, J. M.; Byrne, C. D. Maternal High-Fat Feeding Primes Steatohepatitis in Adult Mice Offspring, Involving Mitochondrial Dysfunction and Altered Lipogenesis Gene Expression. *Hepatology* **2009**, *50* (6), 1796–1808. https://doi.org/10.1002/hep.23205.

(38) Vilar-Gomez, E.; Martinez-Perez, Y.; Calzadilla-Bertot, L.; Torres-Gonzalez, A.; Gra-Oramas, B.; Gonzalez-Fabian, L.; Friedman, S. L.; Diago, M.; Romero-Gomez, M. Weight Loss Through Lifestyle Modification Significantly Reduces Features of Nonalcoholic Steatohepatitis. *Gastroenterology* **2015**, *149* (2), 367-378.e5. https://doi.org/10.1053/j.gastro.2015.04.005.

(39) Atrice, B. É.; And, D.; Wahli, W. *Peroxisome Proliferator-Activated Receptors: Nuclear Control of Metabolism**; 1999. https://academic.oup.com/edrv/article/20/5/649/2530847.

(40) Zhu, Y.; Qi, C.; Korenberg, J. R.; Chen, X. N.; Noya, D.; Rao, M. S.; Reddy, J. K. Structural Organization of Mouse Peroxisome Proliferator-Activated Receptor Gamma (MPPAR Gamma) Gene: Alternative Promoter Use and Different Splicing Yield Two MPPAR Gamma Isoforms. *Proceedings of the National Academy of Sciences* **1995**, *92* (17), 7921–7925. https://doi.org/10.1073/pnas.92.17.7921.

(41) Willson, T. M.; Cobb, J. E.; Cowan, D. J.; Wiethe, R. W.; Correa, I. D.; Prakash, S. R.; Beck, K. D.; Moore, L. B.; Kliewer, S. A.; Lehmann, J. M. The Structure−Activity Relationship between Peroxisome Proliferator-Activated Receptor γ Agonism and the Antihyperglycemic Activity of Thiazolidinediones. *J Med Chem* **1996**, *39* (3), 665–668. https://doi.org/10.1021/jm950395a.

(42) Brown, P. J.; Winegar, D. A.; Plunket, K. D.; Moore, L. B.; Lewis, M. C.; Wilson, J. G.; Sundseth, S. S.; Koble, C. S.; Wu, Z.; Chapman, J. M.; Lehmann, J. M.; Kliewer, S. A.; Willson, T. M. A Ureido-Thioisobutyric Acid (GW9578) Is a Subtype-Selective PPARα Agonist with Potent Lipid-Lowering Activity. *J Med Chem* **1999**, *42* (19), 3785–3788. https://doi.org/10.1021/jm9903601.

(43) Campos, R. v; Lee, Y. C.; Drucker, D. J. Divergent Tissue-Specific and Developmental Expression of Receptors for Glucagon and Glucagon-like Peptide-1 in the Mouse. *Endocrinology* **1994**, *134* (5), 2156–2164. https://doi.org/10.1210/endo.134.5.8156917.

(44) Tornehave, D.; Kristensen, P.; Rømer, J.; Knudsen, L. B.; Heller, R. S. Expression of the GLP-1 Receptor in Mouse, Rat, and Human Pancreas. *Journal of Histochemistry & Cytochemistry* **2008**, *56* (9), 841–851. https://doi.org/10.1369/jhc.2008.951319.

(45) Lyseng-Williamson, K. A. Glucagon-Like Peptide-1 Receptor Agonists in Type 2 Diabetes: Their Use and Differential Features. *Clin Drug Investig* **2019**, *39* (8), 805–819. https://doi.org/10.1007/s40261-019-00826-0.

(46) Bunkoczi, G.; Salah, E.; Filippakopoulos, P.; Fedorov, O.; Müller, S.; Sobott, F.; Parker, S. A.; Zhang, H.; Min, W.; Turk, B. E.; Knapp, S. Structural and Functional Characterization of the Human Protein Kinase ASK1. *Structure* **2007**, *15* (10), 1215–1226. https://doi.org/10.1016/j.str.2007.08.011.

(47) Fujino, G.; Noguchi, T.; Matsuzawa, A.; Yamauchi, S.; Saitoh, M.; Takeda, K.; Ichijo, H. Thioredoxin and TRAF Family Proteins Regulate Reactive Oxygen

Species-Dependent Activation of ASK1 through Reciprocal Modulation of the N-Terminal Homophilic Interaction of ASK1. *Mol Cell Biol* **2007**, *27* (23), 8152–8163. https://doi.org/10.1128/MCB.00227-07.

(48) Sturchler, E.; Feurstein, D.; McDonald, P.; Duckett, D. Mechanism of Oxidative Stress-Induced ASK1-Catalyzed MKK6 Phosphorylation. *Biochemistry* **2010**, *49* (19), 4094–4102. https://doi.org/10.1021/bi100010j.

(49) Weijman, J. F.; Kumar, A.; Jamieson, S. A.; King, C. M.; Caradoc-Davies, T. T.; Ledgerwood, E. C.; Murphy, J. M.; Mace, P. D. Structural Basis of Autoregulatory Scaffolding by Apoptosis Signal-Regulating Kinase 1. *Proceedings of the National Academy of Sciences* **2017**, *114* (11). https://doi.org/10.1073/pnas.1620813114.

(50) Volynets, G. P.; Chekanov, M. O.; Synyugin, A. R.; Golub, A. G.; Kukharenko, O. P.; Bdzhola, V. G.; Yarmoluk, S. M. Identification of 3 *H* -Naphtho[1,2,3- *de*]Quinoline-2,7-Diones as Inhibitors of Apoptosis Signal-Regulating Kinase 1 (ASK1). *J Med Chem* **2011**, *54* (8), 2680–2686. https://doi.org/10.1021/jm200117h.

(51) Terao, Y.; Suzuki, H.; Yoshikawa, M.; Yashiro, H.; Takekawa, S.; Fujitani, Y.; Okada, K.; Inoue, Y.; Yamamoto, Y.; Nakagawa, H.; Yao, S.; Kawamoto, T.; Uchikawa, O. Design and Biological Evaluation of Imidazo[1,2-a]Pyridines as Novel and Potent ASK1 Inhibitors. *Bioorg Med Chem Lett* **2012**, *22* (24), 7326–7329. https://doi.org/10.1016/j.bmcl.2012.10.084.

(52) Loomba, R.; Lawitz, E.; Mantry, P. S.; Jayakumar, S.; Caldwell, S. H.; Arnold, H.; Diehl, A. M.; Djedjos, C. S.; Han, L.; Myers, R. P.; Subramanian, G. M.; McHutchison, J. G.; Goodman, Z. D.; Afdhal, N. H.; Charlton, M. R. The ASK1 Inhibitor Selonsertib in Patients with Nonalcoholic Steatohepatitis: A Randomized, Phase 2 Trial. *Hepatology* **2018**, *67* (2), 549–559. https://doi.org/10.1002/hep.29514.

(53) Romero, F. A.; Jones, C. T.; Xu, Y.; Fenaux, M.; Halcomb, R. L. The Race to Bash NASH: Emerging Targets and Drug Development in a Complex Liver Disease. *Cite This: J. Med. Chem* **2020**, *63*, 5031–5073. https://doi.org/10.1021/acs.jmedchem.9b01701.

(54) Arab, J. P.; Karpen, S. J.; Dawson, P. A.; Arrese, M.; Trauner, M. Bile Acids and Nonalcoholic Fatty Liver Disease: Molecular Insights and Therapeutic Perspectives. *Hepatology* **2017**, *65* (1), 350–362. https://doi.org/10.1002/hep.28709.

(55) Hofmann, A. F.; Roda, A. Physicochemical Properties of Bile Acids and Their Relationship to Biological Properties: An Overview of the Problem. *J Lipid Res* **1984**, *25* (13), 1477–1489. https://doi.org/10.1016/S0022-2275(20)34421-7.

(56) Chiang, J. Y. L. Bile Acid Metabolism and Signaling. In *Comprehensive Physiology*; Wiley, 2013; pp 1191–1212. https://doi.org/10.1002/cphy.c120023.

(57) Jansen, P. L. M.; Schaap, F. G.; Trauner, M.; Jansen, P. L. M. Bile Acid Receptors as Targets for Drug Development. *Nat Rev Gastroenterol Hepatol* **2014**, *11*, 55–67. https://doi.org/10.1038/nrgastro.2013.151.

(58) Sairenji, T.; Collins, K. L.; Evans, D. v. An Update on Inflammatory Bowel Disease. *Primary Care: Clinics in Office Practice* **2017**, *44* (4), 673–692. https://doi.org/10.1016/j.pop.2017.07.010.

(59) Zhang, Y.-Z. Inflammatory Bowel Disease: Pathogenesis. *World J Gastroenterol* **2014**, *20* (1), 91. https://doi.org/10.3748/wjg.v20.i1.91.

(60) Xavier, R. J.; Podolsky, D. K. Unravelling the Pathogenesis of Inflammatory Bowel Disease. *Nature* **2007**, *448* (7152), 427–434. https://doi.org/10.1038/nature06005.
(61) Abraham, C.; Cho, J. H. Inflammatory Bowel Disease. *New England Journal of Medicine* **2009**, *361* (21), 2066–2078. https://doi.org/10.1056/NEJMra0804647.
(62) Ogura, Y.; Bonen, D. K.; Inohara, N.; Nicolae, D. L.; Chen, F. F.; Ramos, R.; Britton, H.; Moran, T.; Karaliuskas, R.; Duerr, R. H.; Achkar, J.-P.; Brant, S. R.; Bayless, T. M.; Kirschner, B. S.; Hanauer, S. B.; Nuñez, G.; Cho, J. H. A Frameshift Mutation in NOD2 Associated with Susceptibility to Crohn's Disease. *Nature* **2001**, *411* (6837), 603–606. https://doi.org/10.1038/35079114.
(63) Inohara, N.; Ogura, Y.; Fontalba, A.; Gutierrez, O.; Pons, F.; Crespo, J.; Fukase, K.; Inamura, S.; Kusumoto, S.; Hashimoto, M.; Foster, S. J.; Moran, A. P.; Fernandez-Luna, J. L.; Nuñez, G. Host Recognition of Bacterial Muramyl Dipeptide Mediated through NOD2. *Journal of Biological Chemistry* **2003**, *278* (8), 5509–5512. https://doi.org/10.1074/jbc.C200673200.
(64) Cooney, R.; Baker, J.; Brain, O.; Danis, B.; Pichulik, T.; Allan, P.; Ferguson, D. J. P.; Campbell, B. J.; Jewell, D.; Simmons, A. NOD2 Stimulation Induces Autophagy in Dendritic Cells Influencing Bacterial Handling and Antigen Presentation. *Nat Med* **2010**, *16* (1), 90–97. https://doi.org/10.1038/nm.2069.
(65) Shaw, M. H.; Kamada, N.; Warner, N.; Kim, Y.-G.; Nuñez, G. The Ever-Expanding Function of NOD2: Autophagy, Viral Recognition, and T Cell Activation. *Trends Immunol* **2011**, *32* (2), 73–79. https://doi.org/10.1016/j.it.2010.12.007.
(66) Sabbah, A.; Chang, T. H.; Harnack, R.; Frohlich, V.; Tominaga, K.; Dube, P. H.; Xiang, Y.; Bose, S. Activation of Innate Immune Antiviral Responses by Nod2. *Nat Immunol* **2009**, *10* (10), 1073–1080. https://doi.org/10.1038/ni.1782.
(67) Rioux, J. D.; Xavier, R. J.; Taylor, K. D.; Silverberg, M. S.; Goyette, P.; Huett, A.; Green, T.; Kuballa, P.; Barmada, M. M.; Datta, L. W.; Shugart, Y. Y.; Griffiths, A. M.; Targan, S. R.; Ippoliti, A. F.; Bernard, E.-J.; Mei, L.; Nicolae, D. L.; Regueiro, M.; Schumm, L. P.; Steinhart, A. H.; Rotter, J. I.; Duerr, R. H.; Cho, J. H.; Daly, M. J.; Brant, S. R. Genome-Wide Association Study Identifies New Susceptibility Loci for Crohn Disease and Implicates Autophagy in Disease Pathogenesis. *Nat Genet* **2007**, *39* (5), 596–604. https://doi.org/10.1038/ng2032.
(68) McCarroll, S. A.; Huett, A.; Kuballa, P.; Chilewski, S. D.; Landry, A.; Goyette, P.; Zody, M. C.; Hall, J. L.; Brant, S. R.; Cho, J. H.; Duerr, R. H.; Silverberg, M. S.; Taylor, K. D.; Rioux, J. D.; Altshuler, D.; Daly, M. J.; Xavier, R. J. Deletion Polymorphism Upstream of IRGM Associated with Altered IRGM Expression and Crohn's Disease. *Nat Genet* **2008**, *40* (9), 1107–1112. https://doi.org/10.1038/ng.215.
(69) Cosnes, J. Tobacco and IBD: Relevance in the Understanding of Disease Mechanisms and Clinical Practice. *Best Pract Res Clin Gastroenterol* **2004**, *18* (3), 481–496. https://doi.org/10.1016/j.bpg.2003.12.003.
(70) Lakatos, P. L.; Szamosi, T.; Lakatos, L. Smoking in Inflammatory Bowel Diseases: Good, Bad or Ugly? *World J Gastroenterol* **2007**, *13* (46), 6134. https://doi.org/10.3748/wjg.v13.i46.6134.
(71) Birrenbach, T.; Böcker, U. Inflammatory Bowel Disease and Smoking. *Inflamm Bowel Dis* **2004**, *10* (6), 848–859. https://doi.org/10.1097/00054725-200411000-00019.
(72) Leslie, W. D.; Miller, N.; Rogala, L.; Bernstein, C. N. Vitamin D Status and Bone Density in Recently Diagnosed Inflammatory Bowel Disease: The Manitoba IBD

Cohort Study. *Am J Gastroenterol* **2008**, *103* (6), 1451–1459. https://doi.org/10.1111/j.1572-0241.2007.01753.x.

(73) Shaw, S. Y.; Blanchard, J. F.; Bernstein, C. N. Association Between the Use of Antibiotics in the First Year of Life and Pediatric Inflammatory Bowel Disease. *American Journal of Gastroenterology* **2010**, *105* (12), 2687–2692. https://doi.org/10.1038/ajg.2010.398.

(74) Mawdsley, J. E.; Rampton, D. S. The Role of Psychological Stress in Inflammatory Bowel Disease. *Neuroimmunomodulation* **2006**, *13* (5–6), 327–336. https://doi.org/10.1159/000104861.

(75) Joossens, M.; Huys, G.; Cnockaert, M.; de Preter, V.; Verbeke, K.; Rutgeerts, P.; Vandamme, P.; Vermeire, S. Dysbiosis of the Faecal Microbiota in Patients with Crohn's Disease and Their Unaffected Relatives. *Gut* **2011**, *60* (5), 631–637. https://doi.org/10.1136/gut.2010.223263.

(76) Andoh, A.; Imaeda, H.; Aomatsu, T.; Inatomi, O.; Bamba, S.; Sasaki, M.; Saito, Y.; Tsujikawa, T.; Fujiyama, Y. Comparison of the Fecal Microbiota Profiles between Ulcerative Colitis and Crohn's Disease Using Terminal Restriction Fragment Length Polymorphism Analysis. *J Gastroenterol* **2011**, *46* (4), 479–486. https://doi.org/10.1007/s00535-010-0368-4.

(77) Breese, E.; Braegger, C. P.; Corrigan, C. J.; Walker-Smith, J. A.; Macdonald, T. T. *Interleukin-2-and Interferon-y-Secreting T Cells in Normal and Diseased Human Intestinal Mucosa*; 1993; Vol. 78.

(78) Fuss, I. J.; Heller, F.; Boirivant, M.; Leon, F.; Yoshida, M.; Fichtner-Feigl, S.; Yang, Z.; Exley, M.; Kitani, A.; Blumberg, R. S.; Mannon, P.; Strober, W. Nonclassical CD1d-Restricted NK T Cells That Produce IL-13 Characterize an Atypical Th2 Response in Ulcerative Colitis. *Journal of Clinical Investigation* **2004**, *113* (10), 1490–1497. https://doi.org/10.1172/JCI19836.

(79) HELLER, F.; FLORIAN, P.; BOJARSKI, C.; RICHTER, J.; CHRIST, M.; HILLENBRAND, B.; MANKERTZ, J.; GITTER, A.; BURGEL, N.; FROMM, M. Interleukin-13 Is the Key Effector Th2 Cytokine in Ulcerative Colitis That Affects Epithelial Tight Junctions, Apoptosis, and Cell Restitution. *Gastroenterology* **2005**, *129* (2), 550–564. https://doi.org/10.1016/j.gastro.2005.05.002.

(80) Sabatino, A. di; Biancheri, P.; Rovedatti, L.; Macdonald, T. T.; Corazza, G. R. New Pathogenic Paradigms in Inflammatory Bowel Disease. **2011**. https://doi.org/10.1002/ibd.21735.

(81) Veldhoen, M.; Hocking, R. J.; Flavell, R. A.; Stockinger, B. Signals Mediated by Transforming Growth Factor-β Initiate Autoimmune Encephalomyelitis, but Chronic Inflammation Is Needed to Sustain Disease. *Nat Immunol* **2006**, *7* (11), 1151–1156. https://doi.org/10.1038/ni1391.

(82) Zhou, L.; Ivanov, I. I.; Spolski, R.; Min, R.; Shenderov, K.; Egawa, T.; Levy, D. E.; Leonard, W. J.; Littman, D. R. IL-6 Programs TH-17 Cell Differentiation by Promoting Sequential Engagement of the IL-21 and IL-23 Pathways. *Nat Immunol* **2007**, *8* (9), 967–974. https://doi.org/10.1038/ni1488.

(83) Barnes, P. J.; Karin, M. Nuclear Factor-KB — A Pivotal Transcription Factor in Chronic Inflammatory Diseases. *New England Journal of Medicine* **1997**, *336* (15), 1066–1071. https://doi.org/10.1056/NEJM199704103361506.

(84) Camma, C.; Giunta, M.; Rosselli, M.; Cottone, M. Mesalamine in the Maintenance Treatment of Crohn's Disease: A Meta-Analysis Adjusted for Confounding Variables. *Gastroenterology* **1997**, *113* (5), 1465–1473. https://doi.org/10.1053/gast.1997.v113.pm9352848.

(85) Bello, C.; Goldstein, F.; Thornton, J. J. Alternate-Day Prednisone Treatment and Treatment Maintenance in Crohn's Disease. *Am J Gastroenterol* **1991**, *86* (4), 460–466.

(86) Steinhart, A. H.; Ewe, K.; Griffiths, A. M.; Modigliani, R.; Thomsen, O. O. Corticosteroids for Maintenance of Remission in Crohn's Disease. *Cochrane Database of Systematic Reviews* **2003**. https://doi.org/10.1002/14651858.CD000301.

(87) Korelitz, B. I.; Adler, D. J.; Mendelsohn, R. A.; Sacknoff, A. L. Long-Term Experience with 6-Mercaptopurine in the Treatment of Crohn's Disease. *Am J Gastroenterol* **1993**, *88* (8), 1198–1205.

(88) Hedin, C. R. H.; Vavricka, S. R.; Stagg, A. J.; Schoepfer, A.; Raine, T.; Puig, L.; Pleyer, U.; Navarini, A.; van der Meulen-de Jong, A. E.; Maul, J.; Katsanos, K.; Kagramanova, A.; Greuter, T.; González-Lama, Y.; van Gaalen, F.; Ellul, P.; Burisch, J.; Bettenworth, D.; Becker, M. D.; Bamias, G.; Rieder, F. The Pathogenesis of Extraintestinal Manifestations: Implications for IBD Research, Diagnosis, and Therapy. *J Crohns Colitis* **2019**, *13* (5), 541–554. https://doi.org/10.1093/ecco-jcc/jjy191.

(89) Regueiro, M.; Feagan, B. G.; Zou, B.; Johanns, J.; Blank, M. A.; Chevrier, M.; Plevy, S.; Popp, J.; Cornillie, F. J.; Lukas, M.; Danese, S.; Gionchetti, P.; Hanauer, S. B.; Reinisch, W.; Sandborn, W. J.; Sorrentino, D.; Rutgeerts, P.; Debinski, H.; Florin, T.; Hetzel, D.; Lawrance, I.; Radford-Smith, G.; Sloss, A.; Sorrentino, D.; Gassner, S.; Haas, T.; Reicht, G.; Reinisch, W.; Strasser, M.; Vogelsang, H.; Bossuyt, P.; DeWit, O.; D'Haens, G.; Franchimont, D.; Louis, E.; Vermeire, S.; Bernstein, C. N.; Bourdages, R.; Chiba, N.; Dhalla, S. S.; Feagan, B. G.; Fedorak, R. N.; Lachance, J. R.; Panaccione, R.; Ropeleski, M.; Singh Salh, B.; Lukas, M.; Colombel, J.-F.; Allez, M.; Desreumaux, P.; Dupas, J. L.; Grimaud, J.-C.; Hebuterne, X.; Laharie, D.; Lerebours, E.; Peyrin-Biroulet, L.; Reimund, J.-M.; Viennot, S.; Zerbib, F.; Antoni, C.; Atreya, R.; Baumgart, D. C.; Berg, C.; Boecker, U.; Bramkamp, G.; Bünning, C.; Ehehalt, R.; Howaldt, S.; Kucharzik, T.; Lamprecht, H. G.; Mudter, J.; Preiss, J. C.; Schreiber, S.; Seidler, U.; Altorjay, I.; Banai, J.; Lakatos, P. L.; Varga, M.; Vincze, A.; Avni-Biron, I.; Fishman, S.; Fraser, G. M.; Goldin, E.; Rachmilewitz, D.; Annese, V.; Ardizzone, S.; Biancone, L.; Bossa, F.; Danese, S.; Fries, W.; Gionchetti, P.; Maconi, G.; Terrosu, G.; Usai, P.; D'Haens, G. R.; Gearry, R. B.; Hill, J.; Rowbotham, D. S.; Schultz, M.; Stubbs, R. S.; Wallace, D.; Walmsley, R. S.; Wyeth, J.; Malecka-Panas, E.; Paradowski, L.; Regula, J.; Beales, I. P.; Campbell, S.; Hawthorne, A. B.; Parkes, M.; Travis, S. P.; Achkar, J. P.; Behm, B. W.; Bickston, S. J.; Brown, K. J.; Chiorean, M. V.; DeVilliers, W. J. S.; Elliott, D. E.; Grunkmeier, D.; Hamilton, J. W.; Hanauer, S. B.; Hanson, J. S.; Hardi, R.; Helper, D. J.; Herfarth, H.; Higgins, P. D. R.; Holderman, W. H.; Kottoor, R.; Kreines, M. D.; Leman, B. I.; Li, X.; Loftus, E. V.; Noar, M.; Oikonomou, I.; Onken, J.; Peterson, K. A.; Phillips, R. P.; Randall, C. W.; Ricci, M.; Ritter, T.; Rubin, D. T.; Safdi, M.; Sandborn, W. J.; Sauberman, L.; Scherl, E.; Schwarz, R. P.; Sedghi, S.; Shafran, I.; Sninsky, C. A.; Stein, I.; Swoger, J.; Vecchio, J.; Weinberg, D. I.; Wruble, L. D.; Yajnik, V.; Younes, Z. Infliximab Reduces Endoscopic, but Not Clinical, Recurrence of Crohn's Disease After Ileocolonic Resection. *Gastroenterology* **2016**, *150* (7), 1568–1578. https://doi.org/10.1053/j.gastro.2016.02.072.

(90) de Cruz, P.; Kamm, M. A.; Hamilton, A. L.; Ritchie, K. J.; Krejany, E. O.; Gorelik, A.; Liew, D.; Prideaux, L.; Lawrance, I. C.; Andrews, J. M.; Bampton, P. A.; Jakobovits, S.; Florin, T. H.; Gibson, P. R.; Debinski, H.; Gearry, R. B.;

Macrae, F. A.; Leong, R. W.; Kronborg, I.; Radford-Smith, G.; Selby, W.; Johnston, M. J.; Woods, R.; Elliott, P. R.; Bell, S. J.; Brown, S. J.; Connell, W. R.; Desmond, P. v. Efficacy of Thiopurines and Adalimumab in Preventing Crohn's Disease Recurrence in High-Risk Patients - a POCER Study Analysis. *Aliment Pharmacol Ther* **2015**, *42* (7), 867–879. https://doi.org/10.1111/apt.13353.

(91) Huh, J. R.; Littman, D. R. Th17 Review Series Small Molecule Inhibitors of RORγt: Targeting Th17 Cells and Other Applications. *Eur. J. Immunol* **2012**, *42*, 2232–2237. https://doi.org/10.1002/eji.201242740.

(92) Maruyama, T.; Miyamoto, Y.; Nakamura, T.; Tamai, Y.; Okada, H.; Sugiyama, E.; Nakamura, T.; Itadani, H.; Tanaka, K. Identification of Membrane-Type Receptor for Bile Acids (M-BAR). *Biochem Biophys Res Commun* **2002**, *298* (5), 714–719. https://doi.org/10.1016/S0006-291X(02)02550-0.

(93) Maruyama, T.; Tanaka, K.; Suzuki, J.; Miyoshi, H.; Harada, N.; Nakamura, T.; Miyamoto, Y.; Kanatani, A.; Tamai, Y. Targeted Disruption of G Protein-Coupled Bile Acid Receptor 1 (Gpbar1/M-Bar) in Mice. *Journal of Endocrinology* **2006**, *191* (1), 197–205. https://doi.org/10.1677/joe.1.06546.

(94) Keitel, V.; Häussinger, D. Perspective: TGR5 (Gpbar-1) in Liver Physiology and Disease. *Clin Res Hepatol Gastroenterol* **2012**, *36* (5), 412–419. https://doi.org/10.1016/j.clinre.2012.03.008.

(95) Keitel, V.; Häussinger, D. Role of TGR5 (GPBAR1) in Liver Disease. *Semin Liver Dis* **2018**, *38* (04), 333–339. https://doi.org/10.1055/s-0038-1669940.

(96) Keitel, V.; Reinehr, R.; Gatsios, P.; Rupprecht, C.; Görg, B.; Selbach, O.; Häussinger, D.; Kubitz, R. The G-Protein Coupled Bile Salt Receptor TGR5 Is Expressed in Liver Sinusoidal Endothelial Cells. *Hepatology* **2007**, *45* (3), 695–704. https://doi.org/10.1002/hep.21458.

(97) Keitel, V.; Donner, M.; Winandy, S.; Kubitz, R.; Häussinger, D. Expression and Function of the Bile Acid Receptor TGR5 in Kupffer Cells. *Biochem Biophys Res Commun* **2008**, *372* (1), 78–84. https://doi.org/10.1016/j.bbrc.2008.04.171.

(98) Wang, Y.-D.; Chen, W.-D.; Yu, D.; Forman, B. M.; Huang, W. The G-Protein-Coupled Bile Acid Receptor, Gpbar1 (TGR5), Negatively Regulates Hepatic Inflammatory Response through Antagonizing Nuclear Factor Kappa Light-Chain Enhancer of Activated B Cells (NF-KB) in Mice. *Hepatology* **2011**, *54* (4), 1421–1432. https://doi.org/10.1002/hep.24525.

(99) Pols, T. W. H.; Noriega, L. G.; Nomura, M.; Auwerx, J.; Schoonjans, K. The Bile Acid Membrane Receptor TGR5 as an Emerging Target in Metabolism and Inflammation. *J Hepatol* **2011**, *54* (6), 1263–1272. https://doi.org/10.1016/j.jhep.2010.12.004.

(100) Guo, C.; Xie, S.; Chi, Z.; Zhang, J.; Liu, Y.; Zhang, L.; Zheng, M.; Zhang, X.; Xia, D.; Ke, Y.; Lu, L.; Wang, D. Bile Acids Control Inflammation and Metabolic Disorder through Inhibition of NLRP3 Inflammasome. *Immunity* **2016**, *45* (4), 802–816. https://doi.org/10.1016/j.immuni.2016.09.008.

(101) Tacke, F. Targeting Hepatic Macrophages to Treat Liver Diseases. *J Hepatol* **2017**, *66* (6), 1300–1312. https://doi.org/10.1016/j.jhep.2017.02.026.

(102) McMahan, R. H.; Wang, X. X.; Cheng, L. L.; Krisko, T.; Smith, M.; el Kasmi, K.; Pruzanski, M.; Adorini, L.; Golden-Mason, L.; Levi, M.; Rosen, H. R. Bile Acid Receptor Activation Modulates Hepatic Monocyte Activity and Improves Nonalcoholic Fatty Liver Disease. *Journal of Biological Chemistry* **2013**, *288* (17), 11761–11770. https://doi.org/10.1074/jbc.M112.446575.

(103) Reich, M.; Klindt, C.; Deutschmann, K.; Spomer, L.; Häussinger, D.; Keitel, V. Role of the G Protein-Coupled Bile Acid Receptor TGR5 in Liver Damage. *Digestive Diseases* **2017**, *35* (3), 235–240. https://doi.org/10.1159/000450917.

(104) Thomas, C.; Gioiello, A.; Noriega, L.; Strehle, A.; Oury, J.; Rizzo, G.; Macchiarulo, A.; Yamamoto, H.; Mataki, C.; Pruzanski, M.; Pellicciari, R.; Auwerx, J.; Schoonjans, K. TGR5-Mediated Bile Acid Sensing Controls Glucose Homeostasis. *Cell Metab* **2009**, *10* (3), 167–177. https://doi.org/10.1016/j.cmet.2009.08.001.

(105) Chávez-Talavera, O.; Tailleux, A.; Lefebvre, P.; Staels, B. Bile Acid Control of Metabolism and Inflammation in Obesity, Type 2 Diabetes, Dyslipidemia, and Nonalcoholic Fatty Liver Disease. *Gastroenterology* **2017**, *152* (7), 1679-1694.e3. https://doi.org/10.1053/j.gastro.2017.01.055.

(106) Nevens, F.; Andreone, P.; Mazzella, G.; Strasser, S. I.; Bowlus, C.; Invernizzi, P.; Drenth, J. P. H.; Pockros, P. J.; Regula, J.; Beuers, U.; Trauner, M.; Jones, D. E.; Floreani, A.; Hohenester, S.; Luketic, V.; Shiffman, M.; van Erpecum, K. J.; Vargas, V.; Vincent, C.; Hirschfield, G. M.; Shah, H.; Hansen, B.; Lindor, K. D.; Marschall, H.-U.; Kowdley, K. v.; Hooshmand-Rad, R.; Marmon, T.; Sheeron, S.; Pencek, R.; MacConell, L.; Pruzanski, M.; Shapiro, D. A Placebo-Controlled Trial of Obeticholic Acid in Primary Biliary Cholangitis. *New England Journal of Medicine* **2016**, *375* (7), 631–643. https://doi.org/10.1056/NEJMoa1509840.

(107) Trauner, M.; Nevens, F.; Shiffman, M. L.; Drenth, J. P. H.; Bowlus, C. L.; Vargas, V.; Andreone, P.; Hirschfield, G. M.; Pencek, R.; Malecha, E. S.; MacConell, L.; Shapiro, D. Long-Term Efficacy and Safety of Obeticholic Acid for Patients with Primary Biliary Cholangitis: 3-Year Results of an International Open-Label Extension Study. *Lancet Gastroenterol Hepatol* **2019**, *4* (6), 445–453. https://doi.org/10.1016/S2468-1253(19)30094-9.

(108) Harms, M. H.; Hirschfield, G. M.; Floreani, A.; Mayo, M. J.; Parés, A.; Liberman, A.; Malecha, E. S.; Pencek, R.; MacConell, L.; Hansen, B. E. Obeticholic Acid Is Associated with Improvements in AST-to-Platelet Ratio Index and GLOBE Score in Patients with Primary Biliary Cholangitis. *JHEP Reports* **2021**, *3* (1), 100191. https://doi.org/10.1016/j.jhepr.2020.100191.

(109) Pellicciari, R.; Fiorucci, S.; Camaioni, E.; Clerici, C.; Costantino, G.; Maloney, P. R.; Morelli, A.; Parks, D. J.; Willson, T. M. 6α-Ethyl-Chenodeoxycholic Acid (6-ECDCA), a Potent and Selective FXR Agonist Endowed with Anticholestatic Activity. *J Med Chem* **2002**, *45* (17), 3569–3572. https://doi.org/10.1021/jm025529g.

(110) Ali, A. H.; Carey, E. J.; Lindor, K. D. Recent Advances in the Development of Farnesoid X Receptor Agonists. *Ann Transl Med* **2015**, *3* (1), 5. https://doi.org/10.3978/j.issn.2305-5839.2014.12.06.

(111) Yu, D. D.; Sousa, K. M.; Mattern, D. L.; Wagner, J.; Fu, X.; Vaidehi, N.; Forman, B. M.; Huang, W. Stereoselective Synthesis, Biological Evaluation, and Modeling of Novel Bile Acid-Derived G-Protein Coupled Bile Acid Receptor 1 (GP-BAR1, TGR5) Agonists. *Bioorg Med Chem* **2015**, *23* (7), 1613–1628. https://doi.org/10.1016/j.bmc.2015.01.048.

(112) Kumar, D. P.; Asgharpour, A.; Mirshahi, F.; Park, S. H.; Liu, S.; Imai, Y.; Nadler, J. L.; Grider, J. R.; Murthy, K. S.; Sanyal, A. J. Activation of Transmembrane Bile Acid Receptor TGR5 Modulates Pancreatic Islet α Cells to Promote Glucose Homeostasis. *Journal of Biological Chemistry* **2016**, *291* (13), 6626–6640. https://doi.org/10.1074/jbc.M115.699504.

(113) Festa, C.; Renga, B.; D'Amore, C.; Sepe, V.; Finamore, C.; de Marino, S.; Carino, A.; Cipriani, S.; Monti, M. C.; Zampella, A.; Fiorucci, S. Exploitation of Cholane Scaffold for the Discovery of Potent and Selective Farnesoid X Receptor (FXR) and G-Protein Coupled Bile Acid Receptor 1 (GP-BAR1) Ligands. *J Med Chem* **2014**, *57* (20), 8477–8495. https://doi.org/10.1021/jm501273r.

(114) Carino, A.; Cipriani, S.; Marchianò, S.; Biagioli, M.; Scarpelli, P.; Zampella, A.; Monti, M. C.; Fiorucci, S. Gpbar1 Agonism Promotes a Pgc-1α-Dependent Browning of White Adipose Tissue and Energy Expenditure and Reverses Diet-Induced Steatohepatitis in Mice OPEN. https://doi.org/10.1038/s41598-017-13102-y.

(115) Sorcini, A.; Zampella, S. F.; Francisci, S.; Marchianò, P.; Scarpelli, D. M.; Biagioli, A.; Carino, S.; Cipriani, D. Rescues Mice from Murine Colitis Macrophages and Activation of GPBAR1 the M1/M2 Phenotype of Intestinal The Bile Acid Receptor GPBAR1 Regulates. **2022**. https://doi.org/10.4049/jimmunol.1700183.

(116) Xu, Y. Recent Progress on Bile Acid Receptor Modulators for Treatment of Metabolic Diseases. *J Med Chem* **2016**, *59* (14), 6553–6579. https://doi.org/10.1021/acs.jmedchem.5b00342.

(117) Biagioli, M.; Carino, A.; Marchianò, S.; Roselli, R.; di Giorgio, C.; Bordoni, M.; Fiorucci, C.; Sepe, V.; Conflitti, P.; Limongelli, V.; Distrutti, E.; Baldoni, M.; Zampella, A.; Fiorucci, S. Identification of Cysteinyl-Leukotriene-Receptor 1 Antagonists as Ligands for the Bile Acid Receptor GPBAR1. *Biochem Pharmacol* **2020**, *177*, 113987. https://doi.org/10.1016/j.bcp.2020.113987.

(118) Sarau, H. M.; Ames, R. S.; Chambers, J.; Ellis, C.; Elshourbagy, N.; Foley, J. J.; Schmidt, D. B.; Muccitelli, R. M.; Jenkins, O.; Murdock, P. R.; Herrity, N. C.; Halsey, W.; Sathe, G.; Muir, A. I.; Nuthulaganti, P.; Dytko, G. M.; Buckley, P. T.; Wilson, S.; Bergsma, D. J.; Hay, D. W. P. Identification, Molecular Cloning, Expression, and Characterization of a Cysteinyl Leukotriene Receptor. *Mol Pharmacol* **1999**, *56* (3), 657–663. https://doi.org/10.1124/mol.56.3.657.

(119) Christie, W. W.; Harwood, J. L. Oxidation of Polyunsaturated Fatty Acids to Produce Lipid Mediators. *Essays Biochem* **2020**, *64* (3), 401–421. https://doi.org/10.1042/EBC20190082.

(120) Kanaoka, Y.; Maekawa, A.; Austen, K. F. Identification of GPR99 Protein as a Potential Third Cysteinyl Leukotriene Receptor with a Preference for Leukotriene E4 Ligand. *J Biol Chem* **2013**, *288* (16), 10967–10972. https://doi.org/10.1074/jbc.C113.453704.

(121) Capra, V.; Thompson, M. D.; Sala, A.; Cole, D. E.; Folco, G.; Rovati, G. E. Cysteinyl-Leukotrienes and Their Receptors in Asthma and Other In£ammatory Diseases: Critical Update and EmergingTrends. *Med Res Rev* **2007**, *27* (4), 469–527. https://doi.org/10.1002/med.20071.

(122) Rovati, G. E.; Capra, V. Cysteinyl-Leukotriene Receptors and Cellular Signals. *ScientificWorldJournal* **2007**, *7*, 1375–1392. https://doi.org/10.1100/tsw.2007.185.

(123) Savari, S. Cysteinyl Leukotrienes and Their Receptors: Bridging Inflammation and Colorectal Cancer. *World J Gastroenterol* **2014**, *20* (4), 968. https://doi.org/10.3748/wjg.v20.i4.968.

(124) Madrid, L. v.; Mayo, M. W.; Reuther, J. Y.; Baldwin, A. S. Akt Stimulates the Transactivation Potential of the RelA/P65 Subunit of NF-KB through Utilization of the IκB Kinase and Activation of the Mitogen-Activated Protein Kinase P38.

Journal of Biological Chemistry **2001**, *276* (22), 18934–18940. https://doi.org/10.1074/jbc.M101103200.

(125) Thompson, C.; Cloutier, A.; Bossé, Y.; Poisson, C.; Larivée, P.; McDonald, P. P.; Stankova, J.; Rola-Pleszczynski, M. Signaling by the Cysteinyl-Leukotriene Receptor 2. *Journal of Biological Chemistry* **2008**, *283* (4), 1974–1984. https://doi.org/10.1074/jbc.M608197200.

(126) Hennen, S.; Wang, H.; Peters, L.; Merten, N.; Simon, K.; Spinrath, A.; Blättermann, S.; Akkari, R.; Schrage, R.; Schröder, R.; Schulz, D.; Vermeiren, C.; Zimmermann, K.; Kehraus, S.; Drewke, C.; Pfeifer, A.; König, G. M.; Mohr, K.; Gillard, M.; Müller, C. E.; Lu, Q. R.; Gomeza, J.; Kostenis, E. Decoding Signaling and Function of the Orphan G Protein–Coupled Receptor GPR17 with a Small-Molecule Agonist. *Sci Signal* **2013**, *6* (298). https://doi.org/10.1126/scisignal.2004350.

(127) Magi, S.; Takemoto, Y.; Kobayashi, H.; Kasamatsu, M.; Akita, T.; Tanaka, A.; Takano, K.; Tashiro, E.; Igarashi, Y.; Imoto, M. 5-Lipoxygenase and Cysteinyl Leukotriene Receptor 1 Regulate Epidermal Growth Factor-induced Cell Migration through <scp>T</Scp> Iam1 Upregulation and <scp>R</Scp> Ac1 Activation. *Cancer Sci* **2014**, *105* (3), 290–296. https://doi.org/10.1111/cas.12340.

(128) Pu, S.; Liu, Q.; Li, Y.; Li, R.; Wu, T.; Zhang, Z.; Huang, C.; Yang, X.; He, J. Montelukast Prevents Mice Against Acetaminophen-Induced Liver Injury. *Front Pharmacol* **2019**, *10*. https://doi.org/10.3389/fphar.2019.01070.

(129) Anzini, M.; Braile, C.; Valenti, S.; Cappelli, A.; Vomero, S.; Marinelli, L.; Limongelli, V.; Novellino, E.; Betti, L.; Giannaccini, G.; Lucacchini, A.; Ghelardini, C.; Norcini, M.; Makovec, F.; Giorgi, G.; Ian Fryer, R. Ethyl 8-Fluoro-6-(3-Nitrophenyl)-4 *H* -Imidazo[1,5- *a*][1,4]Benzodiazepine-3-Carboxylate as Novel, Highly Potent, and Safe Antianxiety Agent. *J Med Chem* **2008**, *51* (15), 4730–4743. https://doi.org/10.1021/jm8002944.

(130) Anzini, M.; Valenti, S.; Braile, C.; Cappelli, A.; Vomero, S.; Alcaro, S.; Ortuso, F.; Marinelli, L.; Limongelli, V.; Novellino, E.; Betti, L.; Giannaccini, G.; Lucacchini, A.; Daniele, S.; Martini, C.; Ghelardini, C.; di Cesare Mannelli, L.; Giorgi, G.; Mascia, M. P.; Biggio, G. New Insight into the Central Benzodiazepine Receptor–Ligand Interactions: Design, Synthesis, Biological Evaluation, and Molecular Modeling of 3-Substituted 6-Phenyl-4 *H* -Imidazo[1,5- *a*][1,4]Benzodiazepines and Related Compounds. *J Med Chem* **2011**, *54* (16), 5694–5711. https://doi.org/10.1021/jm2001597.

(131) Nuti, E.; Casalini, F.; Avramova, S. I.; Santamaria, S.; Fabbi, M.; Ferrini, S.; Marinelli, L.; la Pietra, V.; Limongelli, V.; Novellino, E.; Cercignani, G.; Orlandini, E.; Nencetti, S.; Rossello, A. Potent Arylsulfonamide Inhibitors of Tumor Necrosis Factor-α Converting Enzyme Able to Reduce Activated Leukocyte Cell Adhesion Molecule Shedding in Cancer Cell Models. *J Med Chem* **2010**, *53* (6), 2622–2635. https://doi.org/10.1021/jm901868z.

(132) Limongelli, V. Ligand Binding Free Energy and Kinetics Calculation in 2020. *WIREs Computational Molecular Science* **2020**, *10* (4). https://doi.org/10.1002/wcms.1455.

(133) Halgren, T. A.; Murphy, R. B.; Friesner, R. A.; Beard, H. S.; Frye, L. L.; Pollard, W. T.; Banks, J. L. Glide: A New Approach for Rapid, Accurate Docking and Scoring. 2. Enrichment Factors in Database Screening. *J Med Chem* **2004**, *47* (7), 1750–1759. https://doi.org/10.1021/jm030644s.

(134) Friesner, R. A.; Banks, J. L.; Murphy, R. B.; Halgren, T. A.; Klicic, J. J.; Mainz, D. T.; Repasky, M. P.; Knoll, E. H.; Shelley, M.; Perry, J. K.; Shaw, D. E.; Francis, P.; Shenkin, P. S. Glide: A New Approach for Rapid, Accurate Docking and Scoring. 1. Method and Assessment of Docking Accuracy. *J Med Chem* **2004**, *47* (7), 1739–1749. https://doi.org/10.1021/jm0306430.

(135) Luginina, A.; Gusach, A.; Marin, E.; Mishin, A.; Brouillette, R.; Popov, P.; Shiriaeva, A.; Besserer-Offroy, É.; Longpré, J.-M.; Lyapina, E.; Ishchenko, A.; Patel, N.; Polovinkin, V.; Safronova, N.; Bogorodskiy, A.; Edelweiss, E.; Hu, H.; Weierstall, U.; Liu, W.; Batyuk, A.; Gordeliy, V.; Han, G. W.; Sarret, P.; Katritch, V.; Borshchevskiy, V.; Cherezov, V. Structure-Based Mechanism of Cysteinyl Leukotriene Receptor Inhibition by Antiasthmatic Drugs. *Sci Adv* **2019**, *5* (10). https://doi.org/10.1126/sciadv.aax2518.

(136) D'Amore, C.; di Leva, F. S.; Sepe, V.; Renga, B.; del Gaudio, C.; D'Auria, M. V.; Zampella, A.; Fiorucci, S.; Limongelli, V. Design, Synthesis, and Biological Evaluation of Potent Dual Agonists of Nuclear and Membrane Bile Acid Receptors. *J Med Chem* **2014**, *57* (3), 937–954. https://doi.org/10.1021/jm401873d.

(137) Sepe, V.; Renga, B.; Festa, C.; D'Amore, C.; Masullo, D.; Cipriani, S.; di Leva, F. S.; Monti, M. C.; Novellino, E.; Limongelli, V.; Zampella, A.; Fiorucci, S. Modification on Ursodeoxycholic Acid (UDCA) Scaffold. Discovery of Bile Acid Derivatives As Selective Agonists of Cell-Surface G-Protein Coupled Bile Acid Receptor 1 (GP-BAR1). *J Med Chem* **2014**, *57* (18), 7687–7701. https://doi.org/10.1021/jm500889f.

(138) de Marino, S.; Carino, A.; Masullo, D.; Finamore, C.; Marchianò, S.; Cipriani, S.; di Leva, F. S.; Catalanotti, B.; Novellino, E.; Limongelli, V.; Fiorucci, S.; Zampella, A. Hyodeoxycholic Acid Derivatives as Liver X Receptor α and G-Protein-Coupled Bile Acid Receptor Agonists. *Sci Rep* **2017**, *7* (1), 43290. https://doi.org/10.1038/srep43290.

(139) di Leva, F. S.; Festa, C.; Carino, A.; de Marino, S.; Marchianò, S.; di Marino, D.; Finamore, C.; Monti, M. C.; Zampella, A.; Fiorucci, S.; Limongelli, V. Discovery of ((1,2,4-Oxadiazol-5-Yl)Pyrrolidin-3-Yl)Ureidyl Derivatives as Selective Non-Steroidal Agonists of the G-Protein Coupled Bile Acid Receptor-1. *Sci Rep* **2019**, *9* (1), 2504. https://doi.org/10.1038/s41598-019-38840-z.

(140) Scheja, L.; Heeren, J. Metabolic Interplay between White, Beige, Brown Adipocytes and the Liver. *J Hepatol* **2016**, *64* (5), 1176–1186. https://doi.org/10.1016/j.jhep.2016.01.025.

(141) Sepe, V.; Renga, B.; Festa, C.; D'Amore, C.; Masullo, D.; Cipriani, S.; di Leva, F. S.; Monti, M. C.; Novellino, E.; Limongelli, V.; Zampella, A.; Fiorucci, S. Modification on Ursodeoxycholic Acid (UDCA) Scaffold. Discovery of Bile Acid Derivatives As Selective Agonists of Cell-Surface G-Protein Coupled Bile Acid Receptor 1 (GP-BAR1). *J Med Chem* **2014**, *57* (18), 7687–7701. https://doi.org/10.1021/jm500889f.

(142) di Leva, F. S.; Festa, C.; Renga, B.; Sepe, V.; Novellino, E.; Fiorucci, S.; Zampella, A.; Limongelli, V. Structure-Based Drug Design Targeting the Cell Membrane Receptor GPBAR1: Exploiting the Bile Acid Scaffold towards Selective Agonism. *Sci Rep* **2015**, *5* (1), 16605. https://doi.org/10.1038/srep16605.

(143) de Marino, S.; Carino, A.; Masullo, D.; Finamore, C.; Marchianò, S.; Cipriani, S.; di Leva, F. S.; Catalanotti, B.; Novellino, E.; Limongelli, V.; Fiorucci, S.; Zampella, A. Hyodeoxycholic Acid Derivatives as Liver X Receptor α and G-

Protein-Coupled Bile Acid Receptor Agonists. *Sci Rep* **2017**, *7* (1), 43290. https://doi.org/10.1038/srep43290.

(144) di Leva, F. S.; Festa, C.; Carino, A.; de Marino, S.; Marchianò, S.; di Marino, D.; Finamore, C.; Monti, M. C.; Zampella, A.; Fiorucci, S.; Limongelli, V. Discovery of ((1,2,4-Oxadiazol-5-Yl)Pyrrolidin-3-Yl)Ureidyl Derivatives as Selective Non-Steroidal Agonists of the G-Protein Coupled Bile Acid Receptor-1. *Sci Rep* **2019**, *9* (1), 2504. https://doi.org/10.1038/s41598-019-38840-z.

(145) Fiorucci, S.; Distrutti, E.; Carino, A.; Zampella, A.; Biagioli, M. Bile Acids and Their Receptors in Metabolic Disorders. *Prog Lipid Res* **2021**, *82*, 101094. https://doi.org/10.1016/j.plipres.2021.101094.

(146) Chiang, J. Y. L.; Ferrell, J. M. Up to Date on Cholesterol 7 Alpha-Hydroxylase (CYP7A1) in Bile Acid Synthesis. *Liver Res* **2020**, *4* (2), 47–63. https://doi.org/10.1016/j.livres.2020.05.001.

(147) Liu, H.; Pathak, P.; Boehme, S.; Chiang, JohnY. L. Cholesterol 7α-Hydroxylase Protects the Liver from Inflammation and Fibrosis by Maintaining Cholesterol Homeostasis. *J Lipid Res* **2016**, *57* (10), 1831–1844. https://doi.org/10.1194/jlr.M069807.

(148) Biagioli, M.; Marchianò, S.; di Giorgio, C.; Roselli, R.; Bordoni, M.; Bellini, R.; Fiorillo, B.; Sepe, V.; Catalanotti, B.; Cassiano, C.; Monti, M. C.; Distrutti, E.; Zampella, A.; Fiorucci, S. Combinatorial Targeting of G-protein-coupled Bile Acid Receptor 1 and Cysteinyl Leukotriene Receptor 1 Reveals a Mechanistic Role for Bile Acids and Leukotrienes in Drug-induced Liver Injury. *Hepatology* **2022**. https://doi.org/10.1002/hep.32787.

(149) Cipriani, S.; Mencarelli, A.; Chini, M. G.; Distrutti, E.; Renga, B.; Bifulco, G.; Baldelli, F.; Donini, A.; Fiorucci, S. The Bile Acid Receptor GPBAR-1 (TGR5) Modulates Integrity of Intestinal Barrier and Immune Response to Experimental Colitis. https://doi.org/10.1371/journal.pone.0025637.

(150) Biagioli, M.; Carino, A.; Cipriani, S.; Francisci, D.; Marchianò, S.; Scarpelli, P.; Sorcini, D.; Zampella, A.; Fiorucci, S. The Bile Acid Receptor GPBAR1 Regulates the M1/M2 Phenotype of Intestinal Macrophages and Activation of GPBAR1 Rescues Mice from Murine Colitis. *The Journal of Immunology* **2017**, *199* (2), 718–733. https://doi.org/10.4049/jimmunol.1700183.

(151) Keitel, V.; Stindt, J.; Häussinger, D. Bile Acid-Activated Receptors: GPBAR1 (TGR5) and Other G Protein-Coupled Receptors; 2019; pp 19–49. https://doi.org/10.1007/164_2019_230.

(152) Burris, T. P.; Busby, S. A.; Griffin, P. R. Targeting Orphan Nuclear Receptors for Treatment of Metabolic Diseases and Autoimmunity. *Chem Biol* **2012**, *19* (1), 51–59. https://doi.org/10.1016/j.chembiol.2011.12.011.

(153) Jetten Corresponding Author, A. M. Retinoid-Related Orphan Receptors (RORs): Critical Roles in Development, Immunity, Circadian Rhythm, and Cellular Metabolism. **2009**. https://doi.org/10.1621/nrs.07003.

(154) Huh, J. R.; Leung, M. W. L.; Huang, P.; Ryan, D. A.; Krout, M. R.; Malapaka, R. R. v; Chow, J.; Manel, N.; Ciofani, M.; Kim, S. v; Cuesta, A.; Santori, F. R.; Lafaille, J. J.; Xu, H. E.; Gin, D. Y.; Rastinejad, F.; Littman, D. R. Digoxin and Its Derivatives Suppress T H 17 Cell Differentiation by Antagonizing RORct Activity. **2011**. https://doi.org/10.1038/nature09978.

(155) Ladurner, A.; Schwarz, P. F.; Dirsch, V. M. Natural Products as Modulators of Retinoic Acid Receptor-Related Orphan Receptors (RORs). **2021**. https://doi.org/10.1039/d0np00047g.

(156) Fauber, B. P.; Magnuson, S. Modulators of the Nuclear Receptor Retinoic Acid Receptor-Related Orphan Receptor-γ (RORγ or RORc). **2014**. https://doi.org/10.1021/jm401901d.
(157) Jin, L.; Martynowski, D.; Zheng, S.; Wada, T.; Xie, W.; Li, Y. Structural Basis for Hydroxycholesterols as Natural Ligands of Orphan Nuclear Receptor RORγ. *Molecular Endocrinology* **2010**, *24* (5), 923–929. https://doi.org/10.1210/me.2009-0507.
(158) Fiorillo, B.; Sepe, V.; Conflitti, P.; Roselli, R.; Biagioli, M.; Marchianò, S.; de Luca, P.; Baronissi, G.; Rapacciuolo, P.; Cassiano, C.; Catalanotti, B.; Zampella, A.; Limongelli, V.; Fiorucci, S. Structural Basis for Developing Multitarget Compounds Acting on Cysteinyl Leukotriene Receptor 1 and G-Protein-Coupled Bile Acid Receptor 1. *J Med Chem* **2021**, *64* (22), 16512–16529. https://doi.org/10.1021/acs.jmedchem.1c01078.
(159) Fiorucci, S.; Rapacciuolo, P.; Fiorillo, B.; Roselli, R.; Marchianò, S.; di Giorgio, C.; Bordoni, M.; Bellini, R.; Cassiano, C.; Conflitti, P.; Catalanotti, B.; Limongelli, V.; Sepe, V.; Biagioli, M.; Zampella, A. Discovery of a Potent and Orally Active Dual GPBAR1/CysLT1R Modulator for the Treatment of Metabolic Fatty Liver Disease. *Front Pharmacol* **2022**, *13*. https://doi.org/10.3389/fphar.2022.858137.
(160) Gertzen, C. G. W.; Spomer, L.; Smits, S. H. J.; Häussinger, D.; Keitel, V.; Gohlke, H. Mutational Mapping of the Transmembrane Binding Site of the G-Protein Coupled Receptor TGR5 and Binding Mode Prediction of TGR5 Agonists. *Eur J Med Chem* **2015**, *104*, 57–72. https://doi.org/10.1016/j.ejmech.2015.09.024.
(161) Bain, C. C.; Mowat, A. M. The Monocyte-Macrophage Axis in the Intestine. *Cell Immunol* **2014**, *291* (1–2), 41–48. https://doi.org/10.1016/j.cellimm.2014.03.012.
(162) Na, Y. R.; Stakenborg, M.; Seok, S. H.; Matteoli, G. Macrophages in Intestinal Inflammation and Resolution: A Potential Therapeutic Target in IBD. *Nat Rev Gastroenterol Hepatol* **2019**, *16* (9), 531–543. https://doi.org/10.1038/s41575-019-0172-4.
(163) Fiorucci, S.; Biagioli, M.; Zampella, A.; Distrutti, E. Bile Acids Activated Receptors Regulate Innate Immunity. *Front Immunol* **2018**, *9*. https://doi.org/10.3389/fimmu.2018.01853.
(164) Fiorucci, S.; Carino, A.; Baldoni, M.; Santucci, L.; Costanzi, E.; Graziosi, L.; Distrutti, E.; Biagioli, M. Bile Acid Signaling in Inflammatory Bowel Diseases. *Dig Dis Sci* **2021**, *66* (3), 674–693. https://doi.org/10.1007/s10620-020-06715-3.
(165) Cook, D. N.; Kang, H. S.; Jetten, A. M. Retinoic Acid-Related Orphan Receptors (RORs): Regulatory Functions in Immunity, Development, Circadian Rhythm, and Metabolism. *Nucl Receptor Res* **2015**, *2*. https://doi.org/10.11131/2015/101185.
(166) Wallace, K. L. Immunopathology of Inflammatory Bowel Disease. *World J Gastroenterol* **2014**, *20* (1), 6. https://doi.org/10.3748/wjg.v20.i1.6.
(167) Shibata, A.; Uga, K.; Sato, T.; Sagara, M.; Igaki, K.; Nakamura, Y.; Ochida, A.; Kono, M.; Shirai, J.; Yamamoto, S.; Yamasaki, M.; Tsuchimori, N. Pharmacological Inhibitory Profile of TAK-828F, a Potent and Selective Orally Available RORγt Inverse Agonist. *Biochem Pharmacol* **2018**, *150*, 35–45. https://doi.org/10.1016/j.bcp.2018.01.023.
(168) Buchele, V.; Abendroth, B.; Büttner-Herold, M.; Vogler, T.; Rothamer, J.; Ghimire, S.; Ullrich, E.; Holler, E.; Neurath, M. F.; Hildner, K. Targeting Inflammatory T Helper Cells via Retinoic Acid-Related Orphan Receptor

Gamma t Is Ineffective to Prevent Allo-Response-Driven Colitis. *Front Immunol* **2018**, *9*. https://doi.org/10.3389/fimmu.2018.01138.

(169) Biagioli, M.; Marchianò, S.; Carino, A.; di Giorgio, C.; Santucci, L.; Distrutti, E.; Fiorucci, S. Bile Acids Activated Receptors in Inflammatory Bowel Disease. *Cells* **2021**, *10* (6), 1281. https://doi.org/10.3390/cells10061281.

(170) Ono, Y.; Kanai, T.; Sujino, T.; Nemoto, Y.; Kanai, Y.; Mikami, Y.; Hayashi, A.; Matsumoto, A.; Takaishi, H.; Ogata, H.; Matsuoka, K.; Hisamatsu, T.; Watanabe, M.; Hibi, T. T-Helper 17 and Interleukin-17–Producing Lymphoid Tissue Inducer-Like Cells Make Different Contributions to Colitis in Mice. *Gastroenterology* **2012**, *143* (5), 1288–1297. https://doi.org/10.1053/j.gastro.2012.07.108.

(171) Biagioli, M.; Carino, A.; Cipriani, S.; Francisci, D.; Marchianò, S.; Scarpelli, P.; Sorcini, D.; Zampella, A.; Fiorucci, S. The Bile Acid Receptor GPBAR1 Regulates the M1/M2 Phenotype of Intestinal Macrophages and Activation of GPBAR1 Rescues Mice from Murine Colitis. *The Journal of Immunology* **2017**, *199* (2), 718–733. https://doi.org/10.4049/jimmunol.1700183.

(172) Gorbalenya, A. E.; Baker, S. C.; Baric, R. S.; de Groot, R. J.; Drosten, C.; Gulyaeva, A. A.; Haagmans, B. L.; Lauber, C.; Leontovich, A. M.; Neuman, B. W.; Penzar, D.; Perlman, S.; M Poon, L. L.; Samborskiy, D. v; Sidorov, I. A.; Sola, I.; Ziebuhr, J. The Species Severe Acute Respiratory Syndrome-Related Coronavirus: Classifying 2019-NCoV and Naming It SARS-CoV-2. https://doi.org/10.1038/s41564-020-0695-z.

(173) Perlman, S.; Netland, J. Coronaviruses Post-SARS: Update on Replication and Pathogenesis. *Nat Rev Microbiol* **2009**, *7* (6), 439–450. https://doi.org/10.1038/nrmicro2147.

(174) Hoffmann, M.; Kleine-Weber, H.; Schroeder, S.; Krüger, N.; Herrler, T.; Erichsen, S.; Schiergens, T. S.; Herrler, G.; Wu, N.-H.; Nitsche, A.; Müller, M. A.; Drosten, C.; Pöhlmann, S. SARS-CoV-2 Cell Entry Depends on ACE2 and TMPRSS2 and Is Blocked by a Clinically Proven Protease Inhibitor. *Cell* **2020**, *181* (2), 271-280.e8. https://doi.org/10.1016/j.cell.2020.02.052.

(175) Yan, R.; Zhang, Y.; Li, Y.; Xia, L.; Guo, Y.; Zhou, Q. Structural Basis for the Recognition of SARS-CoV-2 by Full-Length Human ACE2. *Science (1979)* **2020**, *367* (6485), 1444–1448. https://doi.org/10.1126/science.abb2762.

(176) Hoffmann, M.; Kleine-Weber, H.; Pöhlmann, S. A Multibasic Cleavage Site in the Spike Protein of SARS-CoV-2 Is Essential for Infection of Human Lung Cells. *Mol Cell* **2020**, *78* (4), 779-784.e5. https://doi.org/10.1016/j.molcel.2020.04.022.

(177) Turner, A. J.; Hooper, N. M. The Angiotensin–Converting Enzyme Gene Family: Genomics and Pharmacology. *Trends Pharmacol Sci* **2002**, *23* (4), 177–183. https://doi.org/10.1016/S0165-6147(00)01994-5.

(178) Tipnis, S. R.; Hooper, N. M.; Hyde, R.; Karran, E.; Christie, G.; Turner, A. J. A Human Homolog of Angiotensin-Converting Enzyme. *Journal of Biological Chemistry* **2000**, *275* (43), 33238–33243. https://doi.org/10.1074/jbc.M002615200.

(179) Donoghue, M.; Hsieh, F.; Baronas, E.; Godbout, K.; Gosselin, M.; Stagliano, N.; Donovan, M.; Woolf, B.; Robison, K.; Jeyaseelan, R.; Breitbart, R. E.; Acton, S. A Novel Angiotensin-Converting Enzyme–Related Carboxypeptidase (ACE2) Converts Angiotensin I to Angiotensin 1-9. *Circ Res* **2000**, *87* (5). https://doi.org/10.1161/01.RES.87.5.e1.

(180) Imai, Y.; Kuba, K.; Rao, S.; Huan, Y.; Guo, F.; Guan, B.; Yang, P.; Sarao, R.; Wada, T.; Leong-Poi, H.; Crackower, M. A.; Fukamizu, A.; Hui, C.-C.; Hein, L.; Uhlig, S.; Slutsky, A. S.; Jiang, C.; Penninger, J. M. Angiotensin-Converting Enzyme 2 Protects from Severe Acute Lung Failure. *Nature* **2005**, *436* (7047), 112–116. https://doi.org/10.1038/nature03712.

(181) Dikalova, A.; Clempus, R.; Lassègue, B.; Cheng, G.; McCoy, J.; Dikalov, S.; Martin, A. S.; Lyle, A.; Weber, D. S.; Weiss, D.; Taylor, W. R.; Schmidt, H. H. H. W.; Owens, G. K.; Lambeth, J. D.; Griendling, K. K. Nox1 Overexpression Potentiates Angiotensin II-Induced Hypertension and Vascular Smooth Muscle Hypertrophy in Transgenic Mice. *Circulation* **2005**, *112* (17), 2668–2676. https://doi.org/10.1161/CIRCULATIONAHA.105.538934.

(182) Jones, E. S.; Vinh, A.; McCarthy, C. A.; Gaspari, T. A.; Widdop, R. E. AT2 Receptors: Functional Relevance in Cardiovascular Disease. *Pharmacol Ther* **2008**, *120* (3), 292–316. https://doi.org/10.1016/j.pharmthera.2008.08.009.

(183) Marchesi, C.; Paradis, P.; Schiffrin, E. L. Role of the Renin–Angiotensin System in Vascular Inflammation. *Trends Pharmacol Sci* **2008**, *29* (7), 367–374. https://doi.org/10.1016/j.tips.2008.05.003.

(184) Wang, Y.; Wang, Y.; Luo, W.; Huang, L.; Xiao, J.; Li, F.; Qin, S.; Song, X.; Wu, Y.; Zeng, Q.; Jin, F.; Wang, Y. A Comprehensive Investigation of the MRNA and Protein Level of ACE2, the Putative Receptor of SARS-CoV-2, in Human Tissues and Blood Cells. *Int J Med Sci* **2020**, *17* (11), 1522–1531. https://doi.org/10.7150/ijms.46695.

(185) Zou, X.; Chen, K.; Zou, J.; Han, P.; Hao, J.; Han, Z. Single-Cell RNA-Seq Data Analysis on the Receptor ACE2 Expression Reveals the Potential Risk of Different Human Organs Vulnerable to 2019-NCoV Infection. *Front Med* **2020**, *14* (2), 185–192. https://doi.org/10.1007/s11684-020-0754-0.

(186) Zhuang, M.; Cheng, Y.; Zhang, J.; Jiang, X.; Wang, L.; Deng, J.; Wang, P. Increasing Host Cellular Receptor—Angiotensin-converting Enzyme 2 Expression by Coronavirus May Facilitate 2019-nCoV (or SARS-CoV-2) Infection. *J Med Virol* **2020**, *92* (11), 2693–2701. https://doi.org/10.1002/jmv.26139.

(187) Ziegler, C. G. K.; Allon, S. J.; Nyquist, S. K.; Mbano, I. M.; Miao, V. N.; Tzouanas, C. N.; Cao, Y.; Yousif, A. S.; Bals, J.; Hauser, B. M.; Feldman, J.; Muus, C.; Wadsworth, M. H.; Kazer, S. W.; Hughes, T. K.; Doran, B.; Gatter, G. J.; Vukovic, M.; Taliaferro, F.; Mead, B. E.; Guo, Z.; Wang, J. P.; Gras, D.; Plaisant, M.; Ansari, M.; Angelidis, I.; Adler, H.; Sucre, J. M. S.; Taylor, C. J.; Lin, B.; Waghray, A.; Mitsialis, V.; Dwyer, D. F.; Buchheit, K. M.; Boyce, J. A.; Barrett, N. A.; Laidlaw, T. M.; Carroll, S. L.; Colonna, L.; Tkachev, V.; Peterson, C. W.; Yu, A.; Zheng, H. B.; Gideon, H. P.; Winchell, C. G.; Lin, P. L.; Bingle, C. D.; Snapper, S. B.; Kropski, J. A.; Theis, F. J.; Schiller, H. B.; Zaragosi, L.-E.; Barbry, P.; Leslie, A.; Kiem, H.-P.; Flynn, J. L.; Fortune, S. M.; Berger, B.; Finberg, R. W.; Kean, L. S.; Garber, M.; Schmidt, A. G.; Lingwood, D.; Shalek, A. K.; Ordovas-Montanes, J.; Banovich, N.; Barbry, P.; Brazma, A.; Desai, T.; Duong, T. E.; Eickelberg, O.; Falk, C.; Farzan, M.; Glass, I.; Haniffa, M.; Horvath, P.; Hung, D.; Kaminski, N.; Krasnow, M.; Kropski, J. A.; Kuhnemund, M.; Lafyatis, R.; Lee, H.; Leroy, S.; Linnarson, S.; Lundeberg, J.; Meyer, K.; Misharin, A.; Nawijn, M.; Nikolic, M. Z.; Ordovas-Montanes, J.; Pe'er, D.; Powell, J.; Quake, S.; Rajagopal, J.; Tata, P. R.; Rawlins, E. L.; Regev, A.; Reyfman, P. A.; Rojas, M.; Rosen, O.; Saeb-Parsy, K.; Samakovlis, C.; Schiller, H.; Schultze, J. L.; Seibold, M. A.; Shalek, A. K.; Shepherd, D.; Spence, J.; Spira,

A.; Sun, X.; Teichmann, S.; Theis, F.; Tsankov, A.; van den Berge, M.; von Papen, M.; Whitsett, J.; Xavier, R.; Xu, Y.; Zaragosi, L.-E.; Zhang, K. SARS-CoV-2 Receptor ACE2 Is an Interferon-Stimulated Gene in Human Airway Epithelial Cells and Is Detected in Specific Cell Subsets across Tissues. *Cell* **2020**, *181* (5), 1016-1035.e19. https://doi.org/10.1016/j.cell.2020.04.035.

(188) Williamson, E. J.; Walker, A. J.; Bhaskaran, K.; Bacon, S.; Bates, C.; Morton, C. E.; Curtis, H. J.; Mehrkar, A.; Evans, D.; Inglesby, P.; Cockburn, J.; McDonald, H. I.; MacKenna, B.; Tomlinson, L.; Douglas, I. J.; Rentsch, C. T.; Mathur, R.; Wong, A. Y. S.; Grieve, R.; Harrison, D.; Forbes, H.; Schultze, A.; Croker, R.; Parry, J.; Hester, F.; Harper, S.; Perera, R.; Evans, S. J. W.; Smeeth, L.; Goldacre, B. Factors Associated with COVID-19-Related Death Using OpenSAFELY. *Nature* **2020**, *584* (7821), 430–436. https://doi.org/10.1038/s41586-020-2521-4.

(189) Ashraf, U. M.; Abokor, A. A.; Edwards, J. M.; Waigi, E. W.; Royfman, R. S.; Abdul-Moiz Hasan, S.; Smedlund, K. B.; Maria Gregio Hardy, A.; Chakravarti, R.; Gerard Koch, L. SARS-CoV-2, ACE2 Expression, and Systemic Organ Invasion. **2021**. https://doi.org/10.1152/physiolgenomics.00087.2020.

(190) Surguchov, A.; Surgucheva, I.; Stec, J.; Bizzarri, R.; Saponaro, F.; Rutigliano, G.; Sestito, S.; Bandini, L.; Storti, B.; Zucchi, R. ACE2 in the Era of SARS-CoV-2: Controversies and Novel Perspectives. **2020**. https://doi.org/10.3389/fmolb.2020.588618.

(191) Shyh, G. I.; Nawarskas, J. J.; Cheng-Lai, A. Angiotensin-Converting Enzyme Inhibitors and Angiotensin Receptor Blockers in Patients With Coronavirus Disease 2019. *Cardiol Rev* **2020**, *28* (4), 213–216. https://doi.org/10.1097/CRD.0000000000000319.

(192) Heurich, A.; Hofmann-Winkler, H.; Gierer, S.; Liepold, T.; Jahn, O.; Pöhlmann, S. TMPRSS2 and ADAM17 Cleave ACE2 Differentially and Only Proteolysis by TMPRSS2 Augments Entry Driven by the Severe Acute Respiratory Syndrome Coronavirus Spike Protein. *J Virol* **2014**, *88* (2), 1293–1307. https://doi.org/10.1128/JVI.02202-13.

(193) Lambert, D. W.; Yarski, M.; Warner, F. J.; Thornhill, P.; Parkin, E. T.; Smith, A. I.; Hooper, N. M.; Turner, A. J. Tumor Necrosis Factor-α Convertase (ADAM17) Mediates Regulated Ectodomain Shedding of the Severe-Acute Respiratory Syndrome-Coronavirus (SARS-CoV) Receptor, Angiotensin-Converting Enzyme-2 (ACE2). *Journal of Biological Chemistry* **2005**, *280* (34), 30113–30119. https://doi.org/10.1074/jbc.M505111200.

(194) Prada, J. A. H.; Ferreira, A. J.; Katovich, M. J.; Shenoy, V.; Qi, Y.; Santos, R. A. S.; Castellano, R. K.; Lampkins, A. J.; Gubala, V.; Ostrov, D. A.; Raizada, M. K.; Mcknight, B.; Institute, J. A. H. P.; Genomics, F. Structure-Based Identification of Small-Molecule Angiotensin-Converting Enzyme 2 Activators as Novel Antihypertensive Agents. **2008**. https://doi.org/10.1161/HYPERTENSIONAHA.107.108944.

(195) Kulemina, L. v.; Ostrov, D. A. Prediction of Off-Target Effects on Angiotensin-Converting Enzyme 2. *SLAS Discovery* **2011**, *16* (8), 878–885. https://doi.org/10.1177/1087057111413919.

(196) Qaradakhi, T.; Gadanec, L. K.; McSweeney, K. R.; Tacey, A.; Apostolopoulos, V.; Levinger, I.; Rimarova, K.; Egom, E. E.; Rodrigo, L.; Kruzliak, P.; Kubatka, P.; Zulli, A. The Potential Actions of Angiotensin-converting Enzyme II (ACE2) Activator Diminazene Aceturate (DIZE) in Various Diseases. *Clin Exp Pharmacol Physiol* **2020**, *47* (5), 751–758. https://doi.org/10.1111/1440-1681.13251.

(197) Shenoy, V.; Ferreira, A. J.; Katovich, M.; Raizada, M. K. Angiotensin-Converting Enzyme 2/Angiotensin-(1-7)/Mas Receptor Axis. In *The Protective Arm of the Renin Angiotensin System (RAS)*; Elsevier, 2015; pp 269–274. https://doi.org/10.1016/B978-0-12-801364-9.00038-9.

(198) Qi, Y.; Zhang, J.; Cole-Jeffrey, C. T.; Shenoy, V.; Espejo, A.; Hanna, M.; Song, C.; Pepine, C. J.; Katovich, M. J.; Raizada, M. K. Diminazene Aceturate Enhances Angiotensin-Converting Enzyme 2 Activity and Attenuates Ischemia-Induced Cardiac Pathophysiology. *Hypertension* **2013**, *62* (4), 746–752. https://doi.org/10.1161/HYPERTENSIONAHA.113.01337.

(199) Rajapaksha, I. G.; Mak, K. Y.; Huang, P.; Burrell, L. M.; Angus, P. W.; Herath, C. B. The Small Molecule Drug Diminazene Aceturate Inhibits Liver Injury and Biliary Fibrosis in Mice. *Sci Rep* **2018**, *8* (1), 10175. https://doi.org/10.1038/s41598-018-28490-y.

(200) Hasan, H. F.; Elgazzar, E. M.; Mostafa, D. M. Diminazene Aceturate Extenuate the Renal Deleterious Consequences of Angiotensin-II Induced by γ-Irradiation through Boosting ACE2 Signaling Cascade. *Life Sci* **2020**, *253*, 117749. https://doi.org/10.1016/j.lfs.2020.117749.

(201) Nicolau, L. A. D.; Nolêto, I. R. S. G.; Medeiros, J. V. R. Could a Specific ACE2 Activator Drug Improve the Clinical Outcome of SARS-CoV-2? A Potential Pharmacological Insight. *Expert Rev Clin Pharmacol* **2020**, *13* (8), 807–811. https://doi.org/10.1080/17512433.2020.1798760.

(202) Baldissera, M. D.; Sagrillo, M. R.; Grando, T. H.; Rosa, L. D.; de Sá, M. F.; da Luz, S. C. A.; Silveira, S. O.; Nascimento, K.; Peres, D. S.; Copetti, P. M.; da Silva, A. S.; Stefani, L. M.; Monteiro, S. G. Cytotoxic and Genotoxic Effects of the Trypanocidal Drug Diminazene Aceturate. *Comp Clin Path* **2017**, *26* (1), 219–227. https://doi.org/10.1007/s00580-016-2373-3.

(203) Towler, P.; Staker, B.; Prasad, S. G.; Menon, S.; Tang, J.; Parsons, T.; Ryan, D.; Fisher, M.; Williams, D.; Dales, N. A.; Patane, M. A.; Pantoliano, M. W. ACE2 X-Ray Structures Reveal a Large Hinge-Bending Motion Important for Inhibitor Binding and Catalysis. *Journal of Biological Chemistry* **2004**, *279* (17), 17996–18007. https://doi.org/10.1074/jbc.M311191200.

(204) Carino, A.; Moraca, F.; Fiorillo, B.; Marchianò, S.; Sepe, V.; Biagioli, M.; Finamore, C.; Bozza, S.; Francisci, D.; Distrutti, E.; Catalanotti, B.; Zampella, A.; Fiorucci, S. Hijacking SARS-CoV-2/ACE2 Receptor Interaction by Natural and Semi-Synthetic Steroidal Agents Acting on Functional Pockets on the Receptor Binding Domain. *Front Chem* **2020**, *8*. https://doi.org/10.3389/fchem.2020.572885.

(205) Girisa, S.; Henamayee, S.; Parama, D.; Rana, V.; Dutta, U.; Kunnumakkara, A. B. Targeting Farnesoid X Receptor (FXR) for Developing Novel Therapeutics against Cancer. *Molecular biomedicine* **2021**, *2* (1), 21. https://doi.org/10.1186/s43556-021-00035-2.

(206) Festa, C.; Renga, B.; D'Amore, C.; Sepe, V.; Finamore, C.; de Marino, S.; Carino, A.; Cipriani, S.; Monti, M. C.; Zampella, A.; Fiorucci, S. Exploitation of Cholane Scaffold for the Discovery of Potent and Selective Farnesoid X Receptor (FXR) and G-Protein Coupled Bile Acid Receptor 1 (GP-BAR1) Ligands. *J Med Chem* **2014**, *57* (20), 8477–8495. https://doi.org/10.1021/jm501273r.

(207) Cipriani, S.; Renga, B.; D'amore, C.; Simonetti, M.; de Tursi, A. A.; Carino, A.; Monti, M. C.; Sepe, V.; Zampella, A.; Fiorucci, S. Impaired Itching Perception in Murine Models of Cholestasis Is Supported by Dysregulation of GPBAR1 Signaling. **2015**. https://doi.org/10.1371/journal.pone.0129866.

(208) Carino, A.; Cipriani, S.; Marchianò, S.; Biagioli, M.; Santorelli, C.; Donini, A.; Zampella, A.; Monti, M. C.; Fiorucci, S. BAR502, a Dual FXR and GPBAR1 Agonist, Promotes Browning of White Adipose Tissue and Reverses Liver Steatosis and Fibrosis OPEN. *Nature Publishing Group* **2017**. https://doi.org/10.1038/srep42801.

(209) Carino, A.; Marchianò, S.; Biagioli, M.; Fiorucci, C.; Zampella, A.; Monti, M. C.; Morretta, E.; Bordoni, M.; Giorgio, C. di; Roselli, R.; Ricci, P.; Distrutti, E.; Fiorucci, S. Transcriptome Analysis of Dual FXR and GPBAR1 Agonism in Rodent Model of NASH Reveals Modulation of Lipid Droplets Formation. https://doi.org/10.3390/nu11051132.

(210) Manikandan, P.; Nagini, S. Cytochrome P450 Structure, Function and Clinical Significance: A Review. *Curr Drug Targets* **2018**, *19* (1). https://doi.org/10.2174/1389450118666170125144557.

(211) Guengerich, F. P.; Waterman, M. R.; Egli, M. Recent Structural Insights into Cytochrome P450 Function. *Trends Pharmacol Sci* **2016**, *37* (8), 625–640. https://doi.org/10.1016/j.tips.2016.05.006.

(212) Zanger, U. M.; Schwab, M. Cytochrome P450 Enzymes in Drug Metabolism: Regulation of Gene Expression, Enzyme Activities, and Impact of Genetic Variation. *Pharmacol Ther* **2013**, *138* (1), 103–141. https://doi.org/10.1016/j.pharmthera.2012.12.007.

(213) Hill, H. A. O.; Röder, A.; Williams, R. J. P. The Chemical Nature and Reactivity of Cytochrome P-450; 1970; pp 123–151. https://doi.org/10.1007/3-540-05257-7_3.

(214) Isin, E. M.; Guengerich, F. P. Complex Reactions Catalyzed by Cytochrome P450 Enzymes. *Biochimica et Biophysica Acta (BBA) - General Subjects* **2007**, *1770* (3), 314–329. https://doi.org/10.1016/j.bbagen.2006.07.003.

(215) Hrycay, E. G.; Bandiera, S. M. Monooxygenase, Peroxidase and Peroxygenase Properties and Reaction Mechanisms of Cytochrome P450 Enzymes; 2015; pp 1–61. https://doi.org/10.1007/978-3-319-16009-2_1.

(216) Congiu, M.; Mashford, M. L.; Slavin, J. L.; Desmond, P. v. Coordinate Regulation of Metabolic Enzymes and Transporters by Nuclear Transcription Factors in Human Liver Disease. *J Gastroenterol Hepatol* **2009**, *24* (6), 1038–1044. https://doi.org/10.1111/j.1440-1746.2009.05800.x.

(217) Hofmann, A. F.; Zakko, S. F.; Lira, M.; Clerici, C.; Hagey, L. R.; Lambert, K. K.; Steinbach, J. H.; Schteingart, C. D.; Olinga, P.; Groothuis, G. M. M. Novel Biotransformation and Physiological Properties of Norursodeoxycholic Acid in Humans. *Hepatology* **2005**, *42* (6), 1391–1398. https://doi.org/10.1002/hep.20943.

(218) Cheallaigh, A. Preparation of Methyl 1,2,3,4-Tetra-O-Acetyl-β-D-Glucopyranuronate. *Organic Syntheses* **2016**, *93*, 200–209. https://doi.org/10.15227/orgsyn.093.0200.

(219) Engstrom, K. M.; Daanen, J. F.; Wagaw, S.; Stewart, A. O. Gram Scale Synthesis of the Glucuronide Metabolite of ABT-724. **2006**. https://doi.org/10.1021/jo0611972.

(220) D'Amore, C.; di Leva, F. S.; Sepe, V.; Renga, B.; del Gaudio, C.; D'Auria, M. V.; Zampella, A.; Fiorucci, S.; Limongelli, V. Design, Synthesis, and Biological Evaluation of Potent Dual Agonists of Nuclear and Membrane Bile Acid Receptors. *J Med Chem* **2014**, *57* (3), 937–954. https://doi.org/10.1021/jm401873d.

(221) Biagioli, M.; Carino, A.; Marchianò, S.; Roselli, R.; di Giorgio, C.; Bordoni, M.; Fiorucci, C.; Sepe, V.; Conflitti, P.; Limongelli, V.; Distrutti, E.; Baldoni, M.; Zampella, A.; Fiorucci, S. Identification of Cysteinyl-Leukotriene-Receptor 1 Antagonists as Ligands for the Bile Acid Receptor GPBAR1. *Biochem Pharmacol* **2020**, *177*, 113987. https://doi.org/10.1016/j.bcp.2020.113987.

(222) Shelley, J. C.; Cholleti, A.; Frye, L. L.; Greenwood, J. R.; Timlin, M. R.; Uchimaya, M. Epik: A Software Program for PK a Prediction and Protonation State Generation for Drug-like Molecules. *J Comput Aided Mol Des* **2007**, *21* (12), 681–691. https://doi.org/10.1007/s10822-007-9133-z.

(223) Banks, J. L.; Beard, H. S.; Cao, Y.; Cho, A. E.; Damm, W.; Farid, R.; Felts, A. K.; Halgren, T. A.; Mainz, D. T.; Maple, J. R.; Murphy, R.; Philipp, D. M.; Repasky, M. P.; Zhang, L. Y.; Berne, B. J.; Friesner, R. A.; Gallicchio, E.; Levy, R. M. Integrated Modeling Program, Applied Chemical Theory (IMPACT). *J Comput Chem* **2005**, *26* (16), 1752–1780. https://doi.org/10.1002/jcc.20292.

Acknowledgements

First and foremost, I would like to express my immense gratitude to *Prof. Valentina Sepe*. She has supervised me in the amazing yet crazy journey my PhD course has been. I thank her for interceding in my favour for the MSCO exam in 2016, for the blind faith and trust she gives me in every single aspect of my work every day, for supporting and promoting me, for all the imminent shipments to Perugia and Bangalore, for sharing every difficult moment, for our long conversations, for always being open and kind, for her precision I so much appreciate, for her humbleness. I am also deeply glad to have witnessed her career advancement as associate professor. I have grown and matured so much professionally while working with her.

I'm extremely grateful to *Prof. Angela Zampella*, for acknowledging my merits and my work, for being a strict and stern team leader, for all the projects she included me in.

Thanks to both of them, I end my PhD studies with the certainty to have outdone myself yet again.

This endeavour would not have been possible without the support of *Prof. Maria Valeria D'Auria*, my Master thesis supervisor. I want to thank her for always believing in my talent and skills, for the immense respect she has for me, for introducing me to the world of research, for our conversations about cooking, for her motherly care and for all the tips.

Words cannot express my gratitude to *Dr. Chiara Cassiano*. I want to deeply thank her for making my PhD journey so special. I thank her for being a friend, an ally other than just a colleague. For firmly respecting me, for every compliment, for all our cigarette breaks, for every ride home, for all our chitchats over coffee, for trusting me, for listening to me every time I needed to talk. I still thank her for the endless trust I was able to

build in her, for all the nicknames, for our depressive moments, for teaching me how to work with a mass spectrometer, for all the suggestions and support, for all the time spent to figure out mass spectra, for all the times she saw me in tears, for tolerating the times I was angry and frustrated, for her witty humour and earnest opinions. For everything.

I would like to extend my sincere thanks to two amazing women who shared part of their PhD journey with me. I thank *Dr. Giuliana Baronissi* for livening up the lab with our laughter, for all the singing along, for all our conversations, for every time she helped me lighten the work.

I want to equally thank *Dr. Rosa De Gregorio* for being a trusted and trustful friend, for tolerating my bulky, weird personality, for never getting angry at me, for feeling free to cry in front of me, for her kindness, for always paying attention to details, for always trusting my opinions and suggestions, for every morning coffee. I am so happy and honoured to accompany her in her PhD course, to work with her every day in the same lab. She is a great lab companion.

Special thanks to *Dr. Ilenia Alfano*, for sharing our PhD adventure, for being so similar to me, for every time we burst into laughter for our own jokes, for livening up the whole II floor with our loud voices, for all the fun, for all the gossiping, for her honesty and respect, for being a good friend, for understanding and sharing my humour, for all the TikTok hits we kept repeating all day long. I am very glad to have had the chance to share this adventure with her, I can only say one last thing, “top amio”. I wish her all the best.

I am undoubtedly thankful to *Dr. Claudia Finamore, Prof. Carmen Festa* and *Prof. Simona De Marino* for being such an irreplaceable and unique part of our research team together with *Dr. Giuliano Napolitano.*

Still, I want to thank all the intern students I had the pleasure to work with throughout these three great years. I also want to extend my thanks to the professors on the II floor, especially *Prof. Margherita Brindisi* for her kindness. A special thanks also to *Prof. Daniela Marasco* and *Dr. Sara La Manna* who share our labs.

I am deeply thankful to *Prof. Dr. Burkhard König*, for hosting me in his research group at the University of Regensburg. For all the subgroup and lunchtime meetings, for letting me dive into photochemistry, for his kindness and affability. I also want to thank all the PhDs and Post-Docs I had the pleasure to meet during my stay at Regensburg, I want to thank the guys I had the pleasure to work with, *Dr. Alejandro Heredero Sánchez* for all the time we spent together, for every unsuccessful reaction we planned, for every morning we walked together to the lab, for every dinner, for all our Spanish conversations; and *Dr. Lea Müller*, for being so nice and welcoming, for all the German chitchats, for showing me "Stoff und Schnaps", for sharing with me part of her PhD journey.

I cannot help but also thank *Dr. Michela Marcon* for all the time we spent singing together in the lab, for becoming such a great friend, for all the times we danced over the tables, for all the help, for all the kindness, for all the beer and wine we shared, for our cultural exchange, for being so strong and unapologetic. I wish her all the best in the world.

I still want to wholeheartedly thank *Dr. Giorgia Barison* for being such a kind and unique friend, for all the trust she gave me, for all our coffee breaks, for all the walks, for all the videocalls, for the times we spoke privately, for everything. I hope to visit Venice soon with her. In the end, I also want to thank *Dr. Anurag-Nitin Chinchole* for being such a great person, for his niceness, for being such a "jalebi baby", for all the respect he had for me and *Alberto Nunez Bendinelli* for all the parties at his place,

for all the time we shared, for all his craziness, for all the fun. I also want to thank *Dr. Marco Henriquez Toro* and *Dr. Camilo Verdugo***.** Words feel inappropriate to express how much grateful I am to all of them, they made my stay in Regensburg worth living a thousand times, I love them and really hope I get to meet them all once again.

In the end I want to thank my amazing housemates, *Dr. Lucio Spinelli* for being such a nice guy, for all the fun we have at work, for sharing dinner every day, for all the animes and movies I have not watched yet, for all the depression and all the nice moments; *Johanna Bretschneider*, for our Italian-German exchange conversations, for all the singing together, for all the Nimm2 she gave me and all the Elfer Raus games we played together, for being so nice, *danke schön*! And *Rosa Evangelista*, for all the times I gave her cooking suggestions, for all the after-dinner chitchats. Thanks a lot, to them for making special and nicer the time I spent writing my thesis.

I want to thank all my friends, those who stayed and those who did not, thanks especially to *Alessia, Fabio, Francesca,* and *Mario*, just for loving me for who I am.

I owe infinite thanks to my family, my mother *Francesca*, my father *Aniello*, and my sister *Rosalinda*, for the unconditional love and support, for their pride, for literally everything. Thanks also to all my uncles and aunts for all the love they gave me. At the very end of this long list of thanks, a final acknowledgement has to be expressed to one last person, for the love and passion for what he does, for never giving up, for his curiosity, for his inner fights, for the persistence and determination, for becoming living proof of meritocracy, for having learnt who he truly is, for accepting himself, for every time he loved and hated himself, for the patience and strength. He reached a spectacular goal in life, he outdid his

own expectations once again, and with the hope he will never lose the spirit that dragged him up to this point in life, I thank myself.

È di nuovo tra noi, in un bicchiere di latte. È inserito in una lunga catena, molto complessa, tuttavia tale che quasi tutti i suoi anelli sono accetti al corpo umano. Viene ingoiato: e poiché ogni struttura vivente alberga una selvaggia diffidenza verso ogni apporto di altro materiale di origine vivente, la catena viene meticolosamente frantumata, e i frantumi, uno per uno, accettati o respinti. Uno, quello che ci sta a cuore, varca la soglia intestinale ed entra nel torrente sanguigno: migra, bussa alla porta di una cellula nervosa, entra e soppianta un altro carbonio che ne faceva parte. Questa cellula appartiene a un cervello, e questo è il mio cervello, di me che scrivo, e la cellula in questione, ed in essa l'atomo in questione, è addetta al mio scrivere, in un gigantesco minuscolo gioco che nessuno ha ancora descritto. È quella che in questo istante, fuori da un labirintico intreccio di sì e di no, fa sì che la mia mano corra in un certo cammino sulla carta, la segni di queste volute che sono segni; un doppio scatto, in su e in giù, fra due livelli d'energia guida questa mia mano ad imprimere sulla carta questo punto: questo.

Primo Levi, "Carbonio", Il Sistema periodico